AWARD NUMBER: **W81XWH-20-1-0630**

TITLE: **Cathartocytosis: A Novel Cellular Process Essential for Metaplastic Dedifferentiation**

PRINCIPAL INVESTIGATOR: **Jeffrey W. Brown, M.D., Ph.D.**

CONTRACTING ORGANIZATION: **Washington University**

REPORT DATE: **AUGUST 2021**

TYPE OF REPORT: **Annual Progress Report**

PREPARED FOR: U.S. Army Medical Research and Development Command
Fort Detrick, Maryland 21702-5012

DISTRIBUTION STATEMENT: Approved for Public Release;
Distribution Unlimited

The views, opinions and/or findings contained in this report are those of the author(s) and should not be construed as an official Department of the Army position, policy or decision unless so designated by other documentation.

REPORT DOCUMENTATION PAGE

Form Approved
OMB No. 0704-0188

Public reporting burden for this collection of information is estimated to average 1 hour per response, including the time for reviewing instructions, searching existing data sources, gathering and maintaining the data needed, and completing and reviewing this collection of information. Send comments regarding this burden estimate or any other aspect of this collection of information, including suggestions for reducing this burden to Department of Defense, Washington Headquarters Services, Directorate for Information Operations and Reports (0704-0188), 1215 Jefferson Davis Highway, Suite 1204, Arlington, VA 22202-4302. Respondents should be aware that notwithstanding any other provision of law, no person shall be subject to any penalty for failing to comply with a collection of information if it does not display a currently valid OMB control number. **PLEASE DO NOT RETURN YOUR FORM TO THE ABOVE ADDRESS.**

1. REPORT DATE	2. REPORT TYPE	3. DATES COVERED
AUGUST 2021	Annual	07/15/2020-07/14/2021

4. TITLE AND SUBTITLE
Cathartocytosis: A Novel Cellular Process Essential for Metaplastic Dedifferentiation

5a. CONTRACT NUMBER
W81XWH-20-1-0630

5b. GRANT NUMBER
CA191105

5c. PROGRAM ELEMENT NUMBER

6. AUTHOR(S)
Jeffrey W. Brown, M.D., Ph.D.

E-Mail: brownjw@wustl.edu

5d. PROJECT NUMBER

5e. TASK NUMBER

5f. WORK UNIT NUMBER

7. PERFORMING ORGANIZATION NAME(S) AND ADDRESS(ES)

Washington University
CB8124, 660 South Euclid Ave.
St. Louis, MO 63110-1010

8. PERFORMING ORGANIZATION REPORT NUMBER

9. SPONSORING / MONITORING AGENCY NAME(S) AND ADDRESS(ES)

U.S. Army Medical Research and Development Command
Fort Detrick, Maryland 21702-5012

10. SPONSOR/MONITOR'S ACRONYM(S)

11. SPONSOR/MONITOR'S REPORT NUMBER(S)

12. DISTRIBUTION / AVAILABILITY STATEMENT

Approved for Public Release; Distribution Unlimited

13. SUPPLEMENTARY NOTES

14. ABSTRACT

I have discovered that the epitope recognized by mAb Das-1 and which is aberrantly expressed in foregut metaplasia and cancer is 3'-Sulfo-Le^A. The manuscript describing these findings has been uploaded to BioRXIV and revisions have been submitted to Scientific Reports. Based on this knowledge we have made significant progress in molecularly characterizing the process of cathartocytosis annotated by this antigen. Our studies have also suggested that this epitope may actually play a functional role in cathartocytosis and thus inhibiting its synthesis in high-risk metaplasia and cancer from synthesizing this antigen may have therapeutic potential for esophageal, gastric, and pancreatic cancer. I were happy with the progress during the first year of this grant and I am sure I will have more exciting findings to report over the next two years. In addition to these discoveries, I have also published 4 additional primary research papers, 2 abstracts, given an oral presentation at Digestive Disease Week, and received three additional smaller grants. Support from this grant has been acknowledged where appropriate.

15. SUBJECT TERMS
Esophageal cancer, gastric cancer, pancreatic cancer, glycosylation, 3'-Sulfo-LeA, cathartocytosis, paligenosis.

16. SECURITY CLASSIFICATION OF:			17. LIMITATION OF ABSTRACT	18. NUMBER OF PAGES	19a. NAME OF RESPONSIBLE PERSON
a. REPORT	b. ABSTRACT	c. THIS PAGE			USAMRMC
Unclassified	Unclassified	Unclassified	Unclassified	140	19b. TELEPHONE NUMBER *(include area code)*

TABLE OF CONTENTS

	Page
1. Introduction	4
2. Keywords	4
3. Accomplishments	4
4. Impact	7
5. Changes/Problems	9
6. Products	10
7. Participants & Other Collaborating Organizations	13
8. Special Reporting Requirements	15
9. Appendices	15

1. **INTRODUCTION:** *Narrative that briefly (one paragraph) describes the subject, purpose and scope of the research.*

The experiments proposed here serve to antigenically and molecular characterize the cellular changes that occur as a mature cell becomes metaplastic. The first Aim of this grant was to determine the epitope recognized by the mAb Das-1 that is widely expressed specifically in metaplasia and cancer of the gastrointestinal foregut and elsewhere. The second Aim was to molecularly characterize the cellular protein machinery that orchestrates cathartocytosis.

2. **KEYWORDS:** *Provide a brief list of keywords (limit to 20 words).*

Gastric Cancer, Pancreatic Cancer, Esophageal Cancer, Barrett's Esophagus, Cathartocytosis, 3'-Sulfo Lewis A, Metaplasia

3. **ACCOMPLISHMENTS:** *The PI is reminded that the recipient organization is required to obtain prior written approval from the awarding agency grants official whenever there are significant changes in the project or its direction.*

What were the major goals of the project?
List the major goals of the project as stated in the approved SOW. If the application listed milestones/target dates for important activities or phases of the project, identify these dates and show actual completion dates or the percentage of completion.

Specific Aim 1

Major Task 1: Determine the glycosylation epitope recognized by mAb Das-1

Subtask 1: Submit Das-1 IgM and IgG to NCFG to be run on their comprehensive mammalian glycan array. Target Date: 7/2020

-100% Complete, Manuscript under review

Subtask 2: Validate hits with competitive ELISAs, western blots, and IHC/IF. Target Date: 12/2020

-100% Complete, Manuscript under review

Subtask 3: Determine the importance of this glycosylation epitope by knocking down the relevant glycosylation enzymes in cell culture Target Date: 12/2021

-75% Complete

Milestone: Identification and confirmation of the glycosylation epitope recognized by mAb Das-1. Target Date: 12/2021

-99% Complete, Manuscript under review

Specific Aim 2

Major Task 2: Identifying the subcellular trajectories membrane takes in the process of cathartocytosis in cell culture

Subtask 1: Clone shRNA vectors to knock down proteins essential to autophagy (canonical and noncanonical), multivesicular body, and autophagolysosome. Target Date 9/2020

-100% Complete

Subtask 2: Validate efficacy of the cloned shRNA vectors. Target Date: 9/2020

-50% Complete

Subtask 3: Tandem protein mass spectroscopy of membrane secreted by LS174T and LS180 cell lines. Target Date: 12/2020

-50% Complete

Continued

Subtask 4: Determine the effect of knockdown on membrane secretion *in vitro* using ELISA and western blot. 7/2021

-85% Complete

Milestone Achieved: Identification of membrane shuttling pathways essential to cathartocytosis

-85% Complete

Major Task 3: Validate the importance of the identified proteins in our established murine models of metaplasia using genetic knockouts Subtask 1: Obtain IACUC and DoD approval for animal use

-Washington University IACUC Approval: March 19, 2020

-DoD ACURO Approval: June 4, 2020

-100% Complete

Subtask 2: Obtain and breed genetic knockouts, heterozygotes, and control littermates based on *in vitro* cell culture results. Target Date: 7/2023

-50% Complete

Subtask 3: Validate that these genetic knockouts block cathartocytosis in our established murine models of induced metaplasia Milestone Achieved: Identification and confirmation of the glycosylation epitope recognized by mAb Das-1. Target Date: 7/2023

-50% Complete

Milestone Achieved: Publish 1-2 manuscripts presenting the molecular details of cathartocytosis that advance the field of cancer biology. Target Date: 7/2023

-0% Complete

What was accomplished under these goals?

For this reporting period describe: 1) major activities; 2) specific objectives; 3) significant results or key outcomes, including major findings, developments, or conclusions (both positive and negative); and/or 4) other achievements. Include a discussion of stated goals not met. Description shall include pertinent data and graphs in sufficient detail to explain any significant results achieved. A succinct description of the methodology used shall be provided. As the project progresses to completion, the emphasis in reporting in this section should shift from reporting activities to reporting accomplishments.

Major Activities:

Specific Aim 1

-I have identified the clinically important epitope aberrantly expressed in cancer and recognized by the monoclonal antibody Das-1 is 3'-Sulfo Lewis A and the afucosylated form 3'-Sulfo Lewis C.

-The vast majority of Specific Aim 1 and the data was presented at the 2021 Digestive Disease Week (abstract selected for an oral presentation). The manuscript detailing these findings is under review (the preprint is available on BioRXIV and provided in the appendix).

Specific Aim 2

-Using cell culture and colocalization in murine tissue, I have narrowed down the subcellular trajectory significantly. Our data has suggested that the membrane is initially enveloped in a autophagosome, which fuses with the lysosome to form the autophagolysosome.

Continued

Subsequently the autophagolysosome is sorted through the multivesicular body which then fuses with the apical membrane to release the membrane permitting rapid dedifferentiation.

By way of identifying the antigen (Specific Aim 1), I have determined that galectins play a key role in cathartocytosis. I have obtained three global galectin knockouts (Galectin-3, Galectin-4, and Galectin-8) that preferentially bind 3'-Sulfated Galactose containing glycans and these have very interesting phenotypes that I am currently characterizing.

-Galectin-3 knockout blocks cathartocytosis
-Galectin-8 knockout has a significantly delayed maturation of the gastric chief cells

I am in the process of completely characterizing these knockouts in cell culture as well as in murine models of metaplasia. The interaction of sulfomucins with Galectin knockouts have not been described and as such this is a novel mechanism used by cells to dedifferentiate in the process of metaplasia and oncogenesis.

I have also obtained two additional murine alleles. I have generated the Gal3st2$^{fl/fl}$ mouse, to specifically knockout the enzyme that adds the 3'-Sulfate to 3'-Sulfo-Le^{A}. I have also obtained the Papss2$^{fl/fl}$ mouse from Dr. Xie (University of Pittsburgh), which will allow me to conditionally delete the enzyme that creates 3'-Phosphoadenosine-5'-Phosphosulfate (PAPS), an essential precursor to all sulfation reactions. These two murine alleles will allow me to determine the precise function of the sulfation reaction to metaplasia and cancer

What opportunities for training and professional development has the project provided?
If the project was not intended to provide training and professional development opportunities or there is nothing significant to report during this reporting period, state "Nothing to Report."

Describe opportunities for training and professional development provided to anyone who worked on the project or anyone who was involved in the activities supported by the project. "Training" activities are those in which individuals with advanced professional skills and experience assist others in attaining greater proficiency. Training activities may include, for example, courses or one-on-one work with a mentor. "Professional development" activities result in increased knowledge or skill in one's area of expertise and may include workshops, conferences, seminars, study groups, and individual study. Include participation in conferences, workshops, and seminars not listed under major activities.

Subtask 1 Peer review:
-In the last year, I have acted as *Ad hoc* reviewer for Cellular and Molecular Gastroenterology and Hepatology, PLoS One, and Experimental Physiology, and Gut

Subtask 2 Presentation at local and national conferences:
-Abstract selected for oral presentation at 2021 Digestive Disease Week
-An additional abstract (other research project) presented at Digestive Disease Week

Subtask Review abstracts for & sit on a committee for Digestive Disease Week:
-Abstract reviewer for the Midwest Clinical and Translational Research Meeting of CSCTR as well as 2021 Digestive Disease Week

Continued

<u>Subtask 4 Grantsmanship</u>
-I have been awarded three additional research grants:

[1] AGA2021-5101 Role: Principal Investigator 8/3/2020-12/31/2021
AGA-Takeda COVID-19 Rapid Response Research Award

[2] R21 AI156236 Role: Subsite PI 7/1/2021-6/30/2023
National Institutes of Health

[3] DDFRCS Role: Principal Investigator 7/1/2021-6/30/2022
Intramural / Doris Duke Fund to Retain Clinical Scientists

Details including title, dates, effort, contacts, etc are listed below

How were the results disseminated to communities of interest?
If there is nothing significant to report during this reporting period, state "Nothing to Report."

Describe how the results were disseminated to communities of interest. Include any outreach activities that were undertaken to reach members of communities who are not usually aware of these project activities, for the purpose of enhancing public understanding and increasing interest in learning and careers in science, technology, and the humanities.

I have disseminated my results by formally presenting the data at local and national conferences as well as in publications (listed below).

What do you plan to do during the next reporting period to accomplish the goals?
If this is the final report, state "Nothing to Report."

Describe briefly what you plan to do during the next reporting period to accomplish the goals and objectives.

I will continue to both present my research at local and national conferences as well as publish my findings. I will also plan on developing a website for my laboratory.

4. **IMPACT:** D*escribe distinctive contributions, major accomplishments, innovations, successes, or any change in practice or behavior that has come about as a result of the project relative to:*

What was the impact on the development of the principal discipline(s) of the project?
If there is nothing significant to report during this reporting period, state "Nothing to Report."

Describe how findings, results, techniques that were developed or extended, or other products from the project made an impact or are likely to make an impact on the base of knowledge, theory, and research in the principal disciplinary field(s) of the project. Summarize using language that an intelligent lay audience can understand (Scientific American style).

I have published the antigen expressed by metaplasia and cancers throughout the GI foregut and elsewhere. Knowledge of this antigen will permit alternative approaches to assaying for this antigen beyond the antibody Das-1.

We are working with Interpace biosciences to commercialize an assay to risk stratify pancreatic cyst based on data generated and published prior to this award.

What was the impact on other disciplines?
If there is nothing significant to report during this reporting period, state "Nothing to Report."

Describe how the findings, results, or techniques that were developed or improved, or other products from the project made an impact or are likely to make an impact on other disciplines.

Nothing to report

What was the impact on technology transfer?
If there is nothing significant to report during this reporting period, state "Nothing to Report."

Describe ways in which the project made an impact, or is likely to make an impact, on commercial technology or public use, including:

- *transfer of results to entities in government or industry;*
- *instances where the research has led to the initiation of a start-up company; or*
- *adoption of new practices.*

Nothing to report

What was the impact on society beyond science and technology?
If there is nothing significant to report during this reporting period, state "Nothing to Report."

Describe how results from the project made an impact, or are likely to make an impact, beyond the bounds of science, engineering, and the academic world on areas such as:

- *improving public knowledge, attitudes, skills, and abilities;*
- *changing behavior, practices, decision making, policies (including regulatory policies), or social actions; or*
- *improving social, economic, civic, or environmental conditions.*

Nothing to report

5. **CHANGES/PROBLEMS:** *The PD/PI is reminded that the recipient organization is required to obtain prior written approval from the awarding agency grants official whenever there are significant changes in the project or its direction. If not previously reported in writing, provide the following additional information or state, "Nothing to Report," if applicable:*

Changes in approach and reasons for change
Describe any changes in approach during the reporting period and reasons for these changes. Remember that significant changes in objectives and scope require prior approval of the agency.

As reported to my scientific officer (Chinmayi Chandrasekhara), my primary mentor Jason Mills has moved from Washington University to Baylor College of Medicine. We continue to work closely together and have weekly meetings via Zoom. Thus, this is simply a change in location and does not affect the research moving forward.

Actual or anticipated problems or delays and actions or plans to resolve them
Describe problems or delays encountered during the reporting period and actions or plans to resolve them.

Nothing to report

Changes that had a significant impact on expenditures
Describe changes during the reporting period that may have had a significant impact on expenditures, for example, delays in hiring staff or favorable developments that enable meeting objectives at less cost than anticipated.

Nothing to report

Significant changes in use or care of human subjects, vertebrate animals, biohazards, and/or select agents
Describe significant deviations, unexpected outcomes, or changes in approved protocols for the use or care of human subjects, vertebrate animals, biohazards, and/or select agents during the reporting period. If required, were these changes approved by the applicable institution committee (or equivalent) and reported to the agency? Also specify the applicable Institutional Review Board/Institutional Animal Care and Use Committee approval dates.

Nothing to report

Significant changes in use or care of vertebrate animals

I have changed the PI on the vertebrates protocol from Jason Mills to myself (Jeffrey W. Brown). ACURO has approved the addendum to the protocol.

Significant changes in use of biohazards and/or select agents

Nothing to report

6. **PRODUCTS:** *List any products resulting from the project during the reporting period. If there is nothing to report under a particular item, state "Nothing to Report."*

- **Publications, conference papers, and presentations**
  Report only the major publication(s) resulting from the work under this award.

  Journal publications. *List peer-reviewed articles or papers appearing in scientific, technical, or professional journals. Identify for each publication: Author(s); title; journal; volume: year; page numbers; status of publication (published; accepted, awaiting publication; submitted, under review; other); acknowledgement of federal support (yes/no).*

Miao Z-F, Lewis MA, Cho CJ, Adkins-Threats M, Park D, **Brown JW**, Sun J-X, Burclaff JR, Kennedy S, Lu J, Mahar M, Vietor I, Huber LA, Davidson NO, Cavalli V, Rubin DC, Wang Z-N, Mills JC. A Dedicated Molecular Network Licenses Differentiated Cells to Return to the Cell Cycle. *Developmental Cell* 2020: 55:1-17. PMID: 32768422. ‡Cover Article.
Published, Acknowledgement of Federal Support: Yes (But not this grant)

Jin RU,* **Brown JW**,*† Li QK, Bayguinov PO, Wang JS, Mills JC.† Tropism of SARS-CoV-2 for Barrett's Esophagus may Increase Susceptibility to Developing COVID-19. *Gastroenterology* 2021: 160: 2165-8. *Co-First Author, †Co-Corresponding Author. PMID: 33484686.
Published, Acknowledgement of Federal Support: Yes

Das KK, **Brown JW**, Fernandez-del Castillo C, Huynh T, Mills JC, Matsuda Y, Das KM, Mino-Kenudson M. mAb Das-1 Identifies Pancreatic Adenocarcinoma and High-grade Pancreatic Intraepithelial Neoplasm (PanIN) with High Specificity. *Human Pathology* 2021: 111:36-44. PMID: 33524436. ‡Cover Article.
Published, Acknowledgement of Federal Support: Yes

Radyk MD, Peña BL, Spatz LB, **Brown JW**, Cho CJ, Shih C-C, Fitzpatrick JAJ, Mills JC. ATF3 Governs the Initial, Autodegradative Phase of Paligenosis, the Conserved Cellular Program that Converts Mature Cells to Progenitors. *EMBO Reports, Accepted, in press.*
Under review, Acknowledgement of Federal Support: Yes

CONTINUED

Brown JW,† Das KK, Kalas V, Das KM, Mills JC.† 3'-Sulfated Lewis A is a Biomarker for Metaplastic and Carcinomatous Transformation of Several Gastrointestinal Epithelia. *Under review*. †Co-Corresponding Author. [Uploaded to BioRXIV]
Under review, Acknowledgement of Federal Support: Yes

Brown JW,* Cho CJ,* Mills JC. Paligenosis: Cellular Remodeling During Tissue Repair. *Annual Reviews in Physiology*, submitted for volume 84 (2022), Under Review *Co-First Author
Under Review, Acknowledgement of Federal Support: Yes

Books or other non-periodical, one-time publications. *Report any book, monograph, dissertation, abstract, or the like published as or in a separate publication, rather than a periodical or series. Include any significant publication in the proceedings of a one-time conference or in the report of a one-time study, commission, or the like. Identify for each one-time publication: author(s); title; editor; title of collection, if applicable; bibliographic information; year; type of publication (e.g., book, thesis or dissertation); status of publication (published; accepted, awaiting publication; submitted, under review; other); acknowledgement of federal support (yes/no).*

Brown JW & Al Ismail G. Chapter 4. Constipation in Washington Manual of Gastroenterology Subspecialty Consult. 4th Edition. *Ed.* C. Prakash Gyawali. Lippincott Williams & Wilkins. September 29, 2020.
Published, Acknowledgement of Federal Support: No

Other publications, conference papers and presentations. *Identify any other publications, conference papers and/or presentations not reported above. Specify the status of the publication as noted above. List presentations made during the last year (international, national, local societies, military meetings, etc.). Use an asterisk (*) if presentation produced a manuscript.*

Jin RU, **Brown JW**, Meeker A, Li QK, Bayguinov PO, Wang JS, Fitzpatrick J, Whelan S, Mills JC. Tropism of SARS-CoV-2 for Barrett's Esophagus may Increase Susceptibility to Developing COVID-19. Virtual Meeting (May, 2021) *Poster of Distinction*
Reference: *Gastroenterology* 2021: 160(6): S430.

Brown JW, Das KK, Kalas V, Das KM, Mills JC. 3'-Sulfated Lewis A is a Biomarker for Metaplastic and Carcinomatous Transformation of Several Gastrointestinal Epithelia. Virtual Meeting (May, 2021) *Selected For Oral Presentation at DDW.
Reference: *Gastroenterology* 2021: 160(6): S71.

- **Website(s) or other Internet site(s)**
  List the URL for any Internet site(s) that disseminates the results of the research activities. A short description of each site should be provided. It is not necessary to include the publications already specified above in this section.

Nothing to report

- **Technologies or techniques**
  Identify technologies or techniques that resulted from the research activities. Describe the technologies or techniques were shared.

Nothing to report

- **Inventions, patent applications, and/or licenses**
  Identify inventions, patent applications with date, and/or licenses that have resulted from the research. Submission of this information as part of an interim research performance progress report is not a substitute for any other invention reporting required under the terms and conditions of an award.

Nothing to report

- **Other Products**
  Identify any other reportable outcomes that were developed under this project. Reportable outcomes are defined as a research result that is or relates to a product, scientific advance, or research tool that makes a meaningful contribution toward the understanding, prevention, diagnosis, prognosis, treatment and /or rehabilitation of a disease, injury or condition, or to improve the quality of life. Examples include:
  - *data or databases;*
  - *physical collections;*
  - *audio or video products;*
  - *software;*
  - *models;*
  - *educational aids or curricula;*
  - *instruments or equipment;*
  - *research material (e.g., Germplasm; cell lines, DNA probes, animal models);*
  - *clinical interventions;*
  - *new business creation; and*
  - *other.*

Nothing to report

7. PARTICIPANTS & OTHER COLLABORATING ORGANIZATIONS

What individuals have worked on the project?

Provide the following information for: (1) PDs/PIs; and (2) each person who has worked at least one person month per year on the project during the reporting period, regardless of the source of compensation (a person month equals approximately 160 hours of effort). If information is unchanged from a previous submission, provide the name only and indicate "no change".

Name:	Jeffrey W. Brown, M.D., Ph.D.
Project Role:	Principal Investigator
Researcher Identifier (e.g. ORCID ID):	0000-0002-3992-9613
Nearest person month worked:	6
Contribution to Project:	Jeffrey W. Brown oversees the completion and participates in all aspects of the project.
Funding Support:	Department of Defense W81XWH-20-1-0630 American Gastroenterological Association: AGA2021-5101 National Institutes of Health: R21 AI156236 Washington University Division Funds
Name:	Xiaobo Lin, Ph.D.
Project Role:	Senior Scientist
Researcher Identifier (e.g. ORCID ID):	0000-0003-1422-0568
Nearest person month worked:	2
Contribution to Project:	Xiaobo Lin manages the mouse colony and performs many of the mouse experiments
Funding Support:	Division Funds
Name:	Yan-Alexander Kefalov
Project Role:	Research Technician
Researcher Identifier (e.g. ORCID ID):	N/A
Nearest person month worked:	12
Contribution to Project:	Yan-Alexander Kefalov clones constructs and performs cell culture experiments.
Funding Support:	W81XWH-20-1-0630

Has there been a change in the active other support of the PD/PI(s) or senior/key personnel since the last reporting period?
If there is nothing significant to report during this reporting period, state "Nothing to Report."

If the active support has changed for the PD/PI(s) or senior/key personnel, then describe what the change has been. Changes may occur, for example, if a previously active grant has closed and/or if a previously pending grant is now active. Annotate this information so it is clear what has changed from the previous submission. Submission of other support information is not necessary for pending changes or for changes in the level of effort for active support reported previously. The awarding agency may require prior written approval if a change in active other support significantly impacts the effort on the project that is the subject of the project report.

Other Support:

****NEW ACTIVE****
Title: Evaluating the Infective Potential of the Metaplastic GI Foregut
Funding: American Gastrological Association-Takeda COVID-19 Rapid Response Research Award
Project Goals: The goals of this project are to antigenically characterize the expression of ACE2 and TMPRSS2 in the metaplastic GI foregut and utilize our novel organoid system for Barrett's esophagus to study infection with SARS-Cov-2 using a chimeric BSL-2 virus. We will develop a high throughput system to screen for drugs that inhibit viral entry via a tandem GFP-RFP conjugated to the soluble spike protein.
Project Start and End Dates: 8/3/2020-12/31/2021
Level of Effort (%) in the project: 10%
Contact at the Funding Agency: Nick Tomeo, ntomeo@gastro.org

Title: Exploiting the Salivary Arsenal to Inhibit Diarrheal Disease
Funding: NIH/NIAID R21 AI156236 (PI: Bullitt, Subsite PI Jeffrey W. Brown)
Project Goals: This project expands upon our prior report [Brown *et al*., *Journal of Infectious Diseases* 2018: 217(9): 1435-41] where we were the first to demonstrate that a component of saliva (Histatin-5) was able to inhibit adhesion of Enterotoxigenic *E. coli* (ETEC, traveler's diarrhea) to the intestinal epithelium by making its pili rigid. The project proposes to solve the cryo-EM structure of Histatin-5 bound to CFA/I pili from ETEC as well as to evaluate the efficacy of other salivary peptides on inhibiting bacterial adhesion. As subsite PI, I would be responsible with determining whether these peptides inhibit adherence to Caco-2 cells as well as human intestinal monolayers.
Project Start and End Dates: 2/22/2021-1/31/2023
Level of Effort (%) in the project: 5%
Contact at the Funding Agency: Shaun Gratton, shaun.gratton@nih.gov

****NEW ACTIVE** CONTINUED**:

Title: Das-1 Reactivity as a Serologic and Biliary Biomarker for Inflammatory Strictures
Funding: Doris Duke Fund to Retain Clinical Scientists
Project Goals: The goal of pilot project is to use our established Das-1 sandwich ELISA of serum and bile (obtained during ERCP) as a means of (1) diagnosing primary sclerosing cholangitis, potentially at a timepoint before macroscopic fibrotic disease has occurred (2) risk stratifying dominant biliary strictures as malignant v. benign. The basis of this proposal derives from 3'-Sulfo-Le^A being shed from inflamed biliary epithelium (detected with the antibody Das-1), while intrahepatic hepatomas and cholangiocarcinomas do not express this antigen. The ultimate goals of this pilot study are to address two short comings in diagnosing the stricturing biliary disease: (1) the poor sensitivity of cytology / FISH in diagnosing malignant strictures *i.e.* a negative Das-1 ELISA would suggest that the stricture should be resampled at a shorter interval (2) the inability to diagnose PSC prior to macroscopic fibrotic stricturing disease that inevitably leads to cirrhosis and cholangiocarcinoma. While no drug has been shown to prolong transplant-free survival in PSC it is unclear whether this is due to the drug being used or delivering the drug only after end-stage, irreversible, fibrotic disease has occurred.

Project Start and End Dates: 7/1/2021-6/30/2022
Level of Effort (%) in the project: 3%
Contact at the Funding Agency: Jennifer Mosher, mosherj@wustl.edu

What other organizations were involved as partners?
If there is nothing significant to report during this reporting period, state "Nothing to Report."

Describe partner organizations – academic institutions, other nonprofits, industrial or commercial firms, state or local governments, schools or school systems, or other organizations (foreign or domestic) – that were involved with the project. Partner organizations may have provided financial or in-kind support, supplied facilities or equipment, collaborated in the research, exchanged personnel, or otherwise contributed.

Provide the following information for each partnership:
Organization Name:
Location of Organization: (if foreign location list country)
Partner's contribution to the project (identify one or more)

- *Financial support;*
- *In-kind support (e.g., partner makes software, computers, equipment, etc., available to project staff);*
- *Facilities (e.g., project staff use the partner's facilities for project activities);*
- *Collaboration (e.g., partner's staff work with project staff on the project);*
- *Personnel exchanges (e.g., project staff and/or partner's staff use each other's facilities, work at each other's site); and*
- *Other.*

Nothing to Report

8. SPECIAL REPORTING REQUIREMENTS

COLLABORATIVE AWARDS: *For collaborative awards, independent reports are required from BOTH the Initiating Principal Investigator (PI) and the Collaborating/Partnering PI. A duplicative report is acceptable; however, tasks shall be clearly marked with the responsible PI and research site. A report shall be submitted to* ***https://ebrap.org/eBRAP/public/index.htm*** *for each unique award.*

QUAD CHARTS: *If applicable, the Quad Chart (available on https://www.usamraa.army.mil/Pages/Resources.aspx) should be updated and submitted with attachments.*

9. **APPENDICES:** *Attach all appendices that contain information that supplements, clarifies or supports the text. Examples include original copies of journal articles, reprints of manuscripts and abstracts, a curriculum vitae, patent applications, study questionnaires, and surveys, etc.*

CURRICULUM VITAE - Jeffrey Wade Brown, M.D., Ph.D.



DATE: May 12th, 2021

PERSONAL INFORMATION:

Sex: Male
Date of Birth:
Place of Birth: Detroit, MI
Married:
Children:

CITIZENSHIP:

United States of America

ADDRESS AND TELEPHONE NUMBERS:

Office: Washington University School of Medicine
Division of Gastroenterology, Box 8124
660 S. Euclid Ave
St. Louis, MO 63110

Home:

PRESENT POSITION:

2018-Present Instructor in Medicine, Division of Gastroenterology, Department of Medicine
Washington University School of Medicine, St. Louis, MO

EDUCATION:

1999-2003	B.A.	Colgate University, Hamilton, NY
2003-2012	M.D., Ph.D.	Boston University School of Medicine, Boston, MA
2012-2013	Internship	University of Pittsburgh Medical Center, Pittsburgh, PA
2013-2015	Residency	University of Pittsburgh Medical Center, Pittsburgh, PA
2015-2018	Fellowship	Washington University School of Medicine, St. Louis, MO

ACADEMIC POSITIONS / EMPLOYMENT:

2012-2013 Internal Medicine Intern, University of Pittsburgh Medical Center, Pittsburgh, PA

2013-2015 Internal Medicine Resident, University of Pittsburgh Medical Center, Pittsburgh, PA

2015-2018 Gastroenterology Fellow, Washington University in St. Louis, School of Medicine, St. Louis, MO

2018-Present Instructor in Medicine, Division of Gastroenterology, Department of Medicine
Washington University in St. Louis, School of Medicine, St. Louis, MO

MEDICAL LICENSURE AND BOARD CERTIFICATION:

2015-present State of Missouri, Medical License #2018009071
2015-present American Board of Internal Medicine, Internal Medicine #359447
2019-present American Board of Internal Medicine, Gastroenterology #359447

HONORS AND AWARDS:

1999-2003	Deans Award for Academic Excellence (x8)
2000	Phi Eta Sigma National Honor Society
2000	Haskell-Schiff Prize for Excellence in Chemistry
2001	Lawrence Chemical Prize for Excellence in Chemistry
2001-3	Charles A. Dana Scholar (x3)
2001	Highest Academic Standing for a Fraternity New Member
2002	Edwin Foster Kingsbury Prize for Excellence in Chemistry
2003	Phi Scholar of the Year
2003	Bernard and Sydell Citron Pre-Medical Scholastic Prize
2003	Roy Burnett Smith Prize for Excellence in Chemistry
2003	Beta Beta Beta Biological Honor Society
2009	Henry I. Russek Graduate Student Achievement Award
2017-8	Graduate Medical Education Committee, Fellow Representative
2017	Tour Physician for the St. Louis Symphony, Spain
2019	DDW Basic Science Travel Award

EDITORIAL RESPONSIBILITIES:

2015 *Ad hoc* reviewer for Journal of Clinical Case Reports

2018 *Ad hoc* reviewer for Annals of Internal Medicine (x2)
Ad hoc reviewer for Cellular and Molecular Gastroenterology and Hepatology
Ad hoc reviewer for Cell Communication and Signaling

2019 *Ad hoc* reviewer for Cellular and Molecular Gastroenterology and Hepatology
Ad hoc reviewer for Journal of Physiology

2020 *Ad hoc* reviewer for Cellular and Molecular Gastroenterology and Hepatology
Ad hoc reviewer for PLoS One
Ad hoc reviewer for Experimental Physiology

2021 *Ad hoc* reviewer for Gut
Ad hoc reviewer for Experimental Physiology

FUNDING AGENCY REVIEW COMMITTEES:

2018 *Ad hoc* reviewer for the UK Medical Research Council. Clinical Research Training Fellowship Application

OTHER REVIEWS:

2020 Abstract reviewer for the Midwest Clinical and Translational Research Meeting of AFMR / CSCTR

2021 Abstract reviewer for the 2021 American Gastroenterological Association Digestive Disease Week

TEACHING / LECTURES:
GI Pathophysiology to 2nd Year Medical Students, Washington University School of Medicine

PROFESSIONAL SOCIETIES AND ORGANIZATIONS:
1999-present Massachusetts Medical Society
1999-present American Medical Association
2016-present American Gastroenterological Association
2018-present Central Society for Clinical and Translational Research
2019-present American Physiological Society

RESEARCH SUPPORT:

Completed

Merck Fellow	Summer Undergraduate Research Fellow, Colgate University, Mentor: Quang Shen, Ph.D. (2001)	
Schlichting Fellow	Summer Undergraduate Research Fellow, Colgate University, Mentor: Quang Shen, Ph.D. (2002)	
Boston University Graduate Student Research Fellowship	Pre-Doctoral Student, Boston University School of Medicine, Mentor: C. James McKnight, Ph.D. (2008)	
NIH NIDDK T32 DK007130	Ruth Kirschstein NRSA Institutional Research Training Grant (T32), Post-Doctoral Fellow, Mentor: Jason Mills, M.D., Ph.D. (7/1/2016-6/30/2018)	
DDRCC Pilot & Feasibility	Principal Investigator Washington University, Digestive Disease Research Core Center under the parent grant P30-DK052574	5/1/2018-6/30/2020

Current

DoD W81XWH-20-1-0630	Principal Investigator PRCRP Career Development Award	7/15/2020-7/14/2023
AGA2021-5101	Principal Investigator AGA-Takeda COVID-19 Rapid Response Research Award	8/3/2020-12/31/2021
R21 AI156236	Subsite PI National Institutes of Health	2/22/2021-1/31/2023
DDFRCS	Principal Investigator Doris Duke Fund to Retain Clinical Scientists	7/1/2021-6/30/2022

MAJOR INVITED LECTURESHIPS:

2009 Young Investigator Platform Speaker, 23rd Symposium of the Protein Society, Boston, MA

2009 Platform Speaker, Henry I. Russek Student Achievement Day, Boston, MA

2009 Platform Speaker, 53rd Annual Meeting of the Biophysical Society, Boston, MA

2012 Chief of Medicine Conference, VA Pittsburgh Healthcare System, Pittsburgh, PA

2014 Chief of Medicine Conference, VA Pittsburgh Healthcare System, Pittsburgh, PA

2015 Grand Rounds, University of Pittsburgh Medical Center, Pittsburgh, PA

2016 Galaxy of Gastroenterology, St. Louis, MO

2016 Grand Rounds, WUSM Division of Gastroenterology, St. Louis, MO

2017 Galaxy of Gastroenterology, St. Louis, MO

2017 Grand Rounds, WUSM Division of Gastroenterology, St. Louis, MO

2019 Plenary Speaker, 50th Annual Digestive Disease Week, San Diego, CA

2019 Speaker, 2019 Midwest DDRCC Alliance Meeting, Chicago, IL

2021 Speaker, Gastric Neoplasm Session, 52nd Annual Digestive Disease Week, Virtual.

BIBLIOGRAPHY:

Scientific Identifier: orcid.org/0000-0002-3992-9613

Pubmed: www.ncbi.nlm.nih.gov/sites/myncbi/1VqcsShymbl/bibliography/40300079/public

Thesis & Dissertation:

1. Thesis: **Brown JW**. Structure and Conformational Composition of Several Alpha-Substituted Nitroalkanes as Determined by *Ab initio* Molecular Orbital Computations and Gas-Phase Electron Diffraction. (2003) Advisor: Quang Shen, Ph.D.

2. Dissertation: **Brown JW**. Structure, Function, Dynamics, and Cellular Localization of Villin-Type Headpiece Domains. (2010) Advisor: C. James McKnight, Ph.D.

Poster and Oral Presentations:

1. **Brown JW**, Vardar D, Luna E, McKnight CJ. Designing Actin-Binding Activity into Supervillin Headpiece, a Homolog of Villin. Boston University's Science and Engineering Research Symposium, Boston, MA, (April, 2007)

2. **Brown JW**, Vardar D, Luna E, McKnight CJ. Designing Actin-Binding Activity into Supervillin Headpiece, a Homolog of Villin. Henry I. Russek Student Achievement Day, Boston, MA, (May, 2007)

3. **Brown JW**, Vardar D, McKnight CJ. Using Surface Potentials to Design Novel Functionality into Homologous Proteins. 21st Symposium of the Protein Society, Boston, MA, (July, 2007)

Reference: *Protein Sci* 2007. 16(S1): 110.

4. **Brown JW**, Vardar D, McKnight CJ. Using Surface Potentials to Design Novel Functionality into Homologous Proteins. Boston University's Science and Engineering Research Symposium, Boston, MA, (April, 2008)
5. **Brown JW**, McKnight CJ. A Near-Atomic Resolution Model of the Microvillus. Henry I. Russek Student Achievement Day, Boston, MA (May, 2008)
6. **Brown JW**, McKnight CJ. A Near-Atomic Resolution Model of the Microvillar Cytoskeleton and the Organization of the Brush Border. 23rd Symposium of the Protein Society, Boston, MA (July, 2009)
   Reference: *Protein Sci* 2009: 18(1): 157
7. **Brown JW**, McKnight CJ. A Near-Atomic Resolution Model of the Microvillar Cytoskeleton and the Organization of the Brush Border. 54th Annual Meeting of the Biophysical Society, San Francisco, CA (February, 2010)
   Reference: *Biophys J* 2010: 96(3, S1): 210a.
8. **Brown JW**, McKnight CJ. A "Chinese Finger Trap" Model of Spectrin. Boston University's Science and Engineering Research Symposium, Boston, MA (March, 2010)
9. **Brown JW**, McKnight CJ. A Near-Atomic Resolution Model of the Microvillar Cytoskeleton and the Organization of the Brush Border. 6th Annual Meeting of the American Physician Scientist Association, Chicago, IL (April, 2010)
10. **Brown JW**, McKnight CJ. A Near-Atomic Resolution Model of the Microvillar Cytoskeleton and the Organization of the Brush Border. Henry I. Russek Student Achievement Day, Boston, MA (May, 2010)
11. **Brown JW**, Bullitt E, McKnight CJ. A "Chinese Finger-Trap" Model of Spectrin. 25th Symposium of the Protein Society, Boston, MA, (July, 2011)
    Reference: *Protein Sci* 2011: 20(S1): 86.
12. **Brown JW**, Badahdah A, Bullitt E. A Role for Salivary Peptides in the Defense Against Enterotoxigenic *Escherichia coli.* UPMC Department of Medicine's 12th Annual Research Day, Pittsburgh, PA (May, 2014)
13. Yadlapati Y, Keswani RN, Ciolino JD, Grande D, Listernick Z, Carlson DA, Castell DO, Dunbar KB, Gawron AJ, Gyawali CP, Katz P, Lacy B, Spechler SJ, Vela MF, Adler JM, Alghamdi S, Ali M, Atiq O, Bill J, **Brown JW**, Guentner A, Horner B, Horsley-Silva JL, Laing P, Martin DJ, Martin J, Pham T, Platovsky A, Schowalter J, Silon B, Singh G, Sleesman B, Sloan JA, Vance J, Pandolfino J. Development of High Resolution Esophageal Manometry (HREM) Training System Identifies Significant Variation in HREM Learning Curves. Digestive Disease Week, San Diego, CA (May, 2016)
    Reference: *Gastroenterology* 2016: 151(1): S460-61.
14. Cassell BE, Walker T, Alghamdi S, Bill J, Blais P, Boutte H, **Brown JW**, Sayuk GS, Gyawali CP Do Consultants Follow-up on Tests They Recommend? Insights From an Academic Inpatient Gastrointestinal Consult Service Digestive Disease Week, Chicago, IL (May, 2016)
    Reference: *Gastroenterology* 2016: 151(1): S199.

15. **Brown JW**, Badahdah A, Bullitt E. A Role for Salivary Peptides in the Defense Against Enterotoxigenic *Escherichia coli.* Digestive Disease Week, Chicago, IL (May, 2017)
    Reference: *Gastroenterology* 2017: 152(5): S807.
16. **Brown JW**, Badahdah A, Iticovici M, Vickers TJ, Alvarado DM, Helmerhorst EJ, Oppenheim FG, Mills JC, Ciorba MA, Fleckenstein JM, Bullitt E. A Role for Salivary Peptides in the Innate Defense Against Enterotoxigenic *Escherichia coli*. FASEB Gastrointestinal Tract XVII, Steamboat Springs, CO (August, 2017)
17. **Brown JW**, Das KK, Willet SG, Radyk MD, Burclaff J, Mills JC. Cathartocytosis, A Novel Cellular Process Essential for Metaplastic Dedifferentiation. Keystone Symposium: Cellular Plasticity: Reprogramming, Regeneration, and Metaplasia. Keystone, CO (January, 2019)
18. **Brown JW**, Das KK, Willet SG, Radyk MD, Burclaff J, Mills JC. Cathartocytosis, A Novel Cellular Process Essential for Metaplastic Dedifferentiation. Midwest Clinical & Translational Research Meeting of the CSCTR and MWAFMR. Chicago, IL (April, 2019)
    Reference: *Journal of Investigative Medicine* 2019: 67:908.
19. **Brown JW**, Das KK, Willet SG, Radyk MD, Burclaff J, Mills JC. Cathartocytosis, A Novel Cellular Process Essential for Metaplastic Dedifferentiation. Digestive Disease Week. San Diego, CA (May, 2019) *Selected for a Plenary at DDW.
    Reference: *Gastroenterology* 2019: 156(6): S82.
20. **Brown JW**, Das KK, Willet SG, Radyk MD, Burclaff J, Mills JC. Cathartocytosis, A Novel Cellular Process Essential for Metaplastic Dedifferentiation. FASEB: The Gastrointestinal Tract XVIII Conference. Integrated Biology of the GI Super-Organ. Steamboat Springs, CO (July, 2019)
21. **Brown JW**, Das KK, Willet SG, Radyk MD, Burclaff J, Mills JC. Cathartocytosis, A Novel Cellular Process Essential for Metaplastic Dedifferentiation. DDRCC Symposium. San Francisco, CA (Feb, 2020)
22. Jin RU, **Brown JW**, Meeker A, Li QK, Bayguinov PO, Wang JS, Fitzpatrick J, Whelan S, Mills JC. Tropism of SARS-CoV-2 for Barrett's Esophagus may Increase Susceptibility to Developing COVID-19. Virtual Meeting (May, 2021) *Poster of Distinction*
    Reference: *Gastroenterology* 2021: 160(6): S430.
23. **Brown JW**, Das KK, Kalas V, Das KM, Mills JC. 3'-Sulfated Lewis A is a Biomarker for Metaplastic and Carcinomatous Transformation of Several Gastrointestinal Epithelia. Virtual Meeting (May, 2021) *Selected For Oral Presentation at DDW.
    Reference: *Gastroenterology* 2021: 160(6): S71.
24. Soleymanjahi, S, Blanc V, Quasebarth E, Ciorba MA, Alvarado DM, Mills JC, **Brown JW**, Rubin DC, Davidson NO. Intestinal Rbm47 Deletion Promotes Spontaneous Polyposis Through Up-Regulated Epithelial Proliferation, Alternative Splicing of ZO-1 But Mitigates Colitis-Associated Tumorigenesis Via Anti-Oxidative Adapatation and Reduced Inflammation. Virtual Meeting (May, 2021) *Selected For Plenary at DDW.
    Reference: *Gastroenterology* 2021: 160(6): S357.

Invited Commentaries, Reviews, & Book Chapters:

1. **Brown JW**, Mills JC. Implantable Synthetic Organoid Matrices for Intestinal Regeneration. *Nature Cell Biology* 2017: 19(11): 1307-8. PMID: 29087385.
2. **Brown JW** & Al Ismail G. Chapter 4. Constipation in Washington Manual of Gastroenterology Subspecialty Consult. 4th Edition. *Ed.* C. Prakash Gyawali. Lippincott Williams & Wilkins. September 29, 2020.
3. Cho CJ,* **Brown JW**,* Mills JC. Paligenosis – A Risky, but Necessary Endeavor. *EMBO Journal*, *in preparation* *Co-First Author
4. **Brown JW**,* Cho CJ,* Mills JC. Paligenosis: Cellular Remodeling During Tissue Repair. *Annual Reviews in Physiology*, submitted for volume 84 (2022), Under Review *Co-First Author

Peer-Reviewed Manuscripts:

1. Shen Q, **Brown JW**, Malona JA, Cochran JC, & Richardson AD. Molecular Structure and Conformation of Chloronitromethane as Determined by Gas-Phase Electron Diffraction and Theoretical Calculations. *Journal of Physical Chemistry A* 2006: 110(23): 7491-5. PMID: 16759140.
2. Shen Q, **Brown JW**, Richardson AD, & Hagen K. The Molecular Structure and Conformation of Trichloronitromethane as Determined by Gas-Phase Electron Diffraction and Theoretical Calculations. *Journal of Molecular Structure* 2007: 830(1-3): 204-7.
3. Grasko JM, Hooper AJ, **Brown JW**, McKnight CJ, & Burnett JR. A Novel Missense *HGD* Gene Mutation, K57N, in a Patient with Alkaptonuria. *Clinica Chimica Acta* 2009: 403(1-2): 254-6. PMID: 19306858.
4. **Brown JW**, Vardar D, & McKnight CJ. How to Arm a Supervillin: Designing F-actin Binding Activity into Supervillin Headpiece. *Journal of Molecular Biology* 2009: 393(3): 608-18. PMID: 19683541, PMC2760644.
5. **Brown JW**, & McKnight CJ. Identifying Competitive Protein Antagonists for F-actin with Reverse-Phase HPLC. *Analytical Biochemistry* 2010: 398(1): 117-9. PMID: 19932072, PMC2812587.
6. **Brown JW**, & McKnight CJ. Molecular Model of the Microvillar Cytoskeleton and Organization of the Brush Border. *PLoS ONE* 2010: 5(2; e9406): 1-11. PMID: 20195380, PMC2827561.
7. **Brown JW**, Farelli JD, & McKnight CJ. On Unsatisfied Hydrogen Bonds in the N-terminal Subdomain of Villin Headpiece. *Journal of Molecular Biology* 2011: 413(3): 543-7. PMID: 21903098, PMC3196028.
8. **Brown JW**, Farelli JD, & McKnight CJ. On the Unyielding Hydrophobic Core of Villin Headpiece. *Protein Science* 2012: 21(5): 647-54. PMID: 22467489, PMC3403462.
9. Dworkis DA, Brown SA, Gaeta JM, **Brown JW**, Gonzalez MH. Barriers to Outpatient Respiratory Therapy Among Adult Residents of Emergency Shelters. *Annals of Internal Medicine* 2012: 157(9): 679-680. PMID: 23128875.

10. Chen L,* **Brown JW**,* Mok Y-F, Hatters DM, & McKnight CJ. The Allosteric Mechanism Induced by Protein Kinase A (PKA) Phosphorylation of Dematin (Band 4.9). *Journal of Biological Chemistry* 2013: 288(12): 8313-20. PMID: 23355471, PMC3605649. *Co-First Authors.

11. Mitsche MA, Packer LE, **Brown JW**, Jiang ZG, McKnight CJ, Small DM. Surface Tensiometry of Apolipoprotein B Domains at Lipid Interfaces Suggests a New Model for the Initial Steps in Triacylglyceride-Rich Lipoprotein Assembly. *Journal of Biological Chemistry* 2014: 289(13): 9000-12. PMID: 24515109, PMC3979410.

12. **Brown JW**. Thwarting Antibiotic Resistance by Concealing the Host. *Journal of Postdoctoral Research* 2014: 2(5): 37-40.

13. **Brown JW**, Bullitt E, Sriswasdi S, Harper S, Speicher DW, & McKnight CJ. The Physiological Molecular Shape of Spectrin: a Compact Supercoil Resembling a Chinese Finger Trap. *PLoS Computational Biology* 2015: 11(6; e1004302): 1-20. PMID: 26067675, PMC4466138.

14. **Brown JW**, Vipperla K, Vattikutti S, Kancherla D. An Unusual Cause of Dyspnea in a Patient with Rheumatoid Arthritis. *JSM Clinical Case Reports* 2016: 4(2, 1098): 1-2. ‡Cover Article.

15. Cassell BE, Walker T, Alghamdi S, Bill J, Blais P, Boutte H, **Brown JW**, Sayuk GS, Gyawali CP. Do Consultants Follow-up on Tests They Recommend? Insights from an Academic Inpatient Gastrointestinal Consult Service. *Digestive Diseases and Sciences* 2017: 62: 1448-54. PMID: 28391419, PMC5890923.

16. **Brown JW**,* Badahdah A,* Iticovici M, Vickers TJ, Alvarado DM, Helmerhorst EJ, Oppenheim FG, Mills JC, Ciorba MA, Fleckenstein JM, Bullitt E. A Role for Salivary Peptides in the Innate Defense Against Enterotoxigenic *Escherichia coli*. *Journal of Infectious Diseases* 2018: 217(9): 1435-41. PMID: 29528423, PMC5894089. *Co-First Author

17. Das KK, Geng X, **Brown JW**, Morales-Oyarvide V, Huynh T, Pergolini I, Pitman M, Ferrone C, Al Efishat M, Haviland D, Thompson E, Wolfgang C, Lennon AM, Allen P, Lillemoe K, Fields RC, Hawkins WF, Li J, Fernandez-del Castillo C, Das KM, Mino-Kenudson M. Cross Validation of the Monoclonal Antibody Das-1 in the Identification of High-risk Mucinous Pancreatic Cystic Lesions. *Gastroenterology* 2019: 157(3):720-30. PMID: 31175863, PMC6707850.

18. Miao Z-F, Lewis MA, Cho CJ, Adkins-Threats M, Park D, **Brown JW**, Sun J-X, Burclaff JR, Kennedy S, Lu J, Mahar M, Vietor I, Huber LA, Davidson NO, Cavalli V, Rubin DC, Wang Z-N, Mills JC. A Dedicated Molecular Network Licenses Differentiated Cells to Return to the Cell Cycle. *Developmental Cell* 2020: 55:1-17. PMID: 32768422. ‡Cover Article.

19. Jin RU,* **Brown JW**,*† Li QK, Bayguinov PO, Wang JS, Mills JC.† Tropism of SARS-CoV-2 for Barrett's Esophagus may Increase Susceptibility to Developing COVID-19. *Gastroenterology* 2021: 160: 2165-8. *Co-First Author, †Co-Corresponding Author. PMID: 33484686.

20. Das KK, **Brown JW**, Fernandez-del Castillo C, Huynh T, Mills JC, Matsuda Y, Das KM, Mino-Kenudson M. mAb Das-1 Identifies Pancreatic Adenocarcinoma and High-grade Pancreatic Intraepithelial Neoplasm (PanIN) with High Specificity. *Human Pathology* 2021: 111:36-44. PMID: 33524436. ‡Cover Article.

21. Radyk MD, Peña BL, Spatz LB, **Brown JW**, Cho CJ, Shih C-C, Fitzpatrick JAJ, Mills JC. ATF3 Governs the Initial, Autodegradative Phase of Paligenosis, the Conserved Cellular Program that Converts Mature Cells to Progenitors. *EMBO Reports* 2021*, Accepted, in press.*

22. **Brown JW**,† Das KK, Kalas V, Das KM, Mills JC.† 3'-Sulfated Lewis A is a Biomarker for Metaplastic and Carcinomatous Transformation of Several Gastrointestinal Epithelia. *Under review*. †Co-Corresponding Author. [Uploaded to BioRXIV]

CellPress

Developmental Cell

Article

A Dedicated Evolutionarily Conserved Molecular Network Licenses Differentiated Cells to Return to the Cell Cycle

Zhi-Feng Miao,[1,2,7] Mark A. Lewis,[1,7] Charles J. Cho,[1,7] Mahliyah Adkins-Threats,[1] Dongkook Park,[1] Jeffrey W. Brown,[1] Jing-Xu Sun,[1,2] Joseph R. Burclaff,[1] Susan Kennedy,[1] Jianyun Lu,[1] Marcus Mahar,[3] Ilja Vietor,[4] Lukas A. Huber,[4] Nicholas O. Davidson,[1,5] Valeria Cavalli,[3] Deborah C. Rubin,[1,5] Zhen-Ning Wang,[2,*] and Jason C. Mills[1,5,6,8,*]

[1]Division of Gastroenterology, Department of Medicine, Washington University School of Medicine, St. Louis, MO 63110, USA
[2]Department of Surgical Oncology and General Surgery, Key Laboratory of Precision Diagnosis and Treatment of Gastrointestinal Tumors, First Hospital of China Medical University, Shenyang 110001, China
[3]Department of Neuroscience, Washington University School of Medicine, St. Louis, MO, USA
[4]Division of Cell Biology, Biocenter, Medical University of Innsbruck, Innsbruck, Austria
[5]Department of Developmental Biology, Washington University School of Medicine, St. Louis, MO, USA
[6]Department of Pathology and Immunology, Washington University School of Medicine, St. Louis, MO, USA
[7]These authors contributed equally
[8]Lead Contact
*Correspondence: josieon826@sina.cn (Z.-N.W.), jmills@wustl.edu (J.C.M.)
https://doi.org/10.1016/j.devcel.2020.07.005

SUMMARY

Differentiated cells can re-enter the cell cycle to repair tissue damage via a series of discrete morphological and molecular stages coordinated by the cellular energetics regulator mTORC1. We previously proposed the term ''paligenosis'' to describe this conserved cellular regeneration program. Here, we detail a molecular network regulating mTORC1 during paligenosis in both mouse pancreatic acinar and gastric chief cells. DDIT4 initially suppresses mTORC1 to induce autodegradation of differentiated cell components and damaged organelles. Later in paligenosis, IFRD1 suppresses p53 accumulation. *Ifrd1*$^{-/-}$ cells do not complete paligenosis because persistent p53 prevents mTORC1 reactivation and cell proliferation. *Ddit4*$^{-/-}$ cells never suppress mTORC1 and bypass the IFRD1 checkpoint on proliferation. Previous reports and our current data implicate DDIT4/IFRD1 in governing paligenosis in multiple organs and species. Thus, we propose that an evolutionarily conserved, dedicated molecular network has evolved to allow differentiated cells to re-enter the cell cycle (i.e., undergo paligenosis) after tissue injury.

INTRODUCTION

As early as 1900, pathologists observed that adult tissue damage was often repaired by mature cells recruited back into the cell cycle (Adami, 1900). They speculated that this cellular ''reprogramming'' must involve cells switching from using energy for physiological function (like secretion) to fueling proliferation. We now know that the reversion to a proliferative, regenerative state can occur in various contexts, such as during regeneration of limbs in amphibians or when tissue transforms into the precancerous state known as metaplasia (Burclaff and Mills, 2018a). Metaplasia itself can be regenerative, fully restoring cellular architecture, or it can persist chronically, increasing risk for cancer (Sáenz and Mills, 2018; Goldenring, 2018). In stomach, for example, spasmolytic polypeptide-expressing metaplasia (SPEM, also known as pseudopyloric metaplasia) can be induced in a synchronous, reversible fashion in mice by drugs like high-dose tamoxifen (Huh et al., 2012; Keeley et al., 2019). In humans infected with the bacterium *H. pylori*, SPEM can be chronic and increase risk for progression to cancer (Sáenz and Mills, 2018). Similarly, the drug cerulein can induce metaplasia of mature digestive-enzyme-secreting pancreatic acinar cells in mice to model acinar-to-ductal metaplasia (ADM). In humans, ADM can progress to pancreatic intraepithelial neoplasia (PanIN) and pancreatic cancer (Burclaff and Mills, 2018a).

We previously showed that injury-induced regeneration in various contexts and organs can occur via the same discrete series of cellular and molecular changes (Willet et al., 2018). We reasoned that—just as dying cells, independent of species and tissue type, can access the same apoptotic cellular program—differentiated cells that need to re-enter the cell cycle to regenerate lost tissue would also have access to a conserved molecular-cellular program. We termed this program ''paligenosis'' and showed that it required biphasic regulation of the metabolic sensor and protein translation effector complex mTORC1 (Willet et al., 2018; Mills et al., 2019). We showed that paligenosis proceeds by discrete, sequential stages: (1) mTORC1 is quenched

 2020 Elsevier Inc.

as cells massively upregulate lysosomes and autophagy; (2) cells induce a cohort of embryonic and fetal progenitor genes (like *Sox9*); and (3) mTORC1 is reactivated to power cell-cycle re-entry(Willet et al., 2018). Cells require lysosome activity to clear stage 1. Without mTORC1, they are blocked in G1/S phase and do not enter stage 3. We proposed that multicellular organisms evolved paligenosis to allow the vast majority of cells to be harnessed for physiological function during homeostasis without sacrificing them as a potential reservoir of potential progenitors to repair large-scale tissue damage.

Here, we sought to identify a conserved molecular machinery that might govern mTORC1 during paligenosis. We expect paligenosis genes to be: (1) conserved across species, (2) induced upon paligenosis-causing injury in multiple tissues, and (3) largely dispensable for normal development or stem cell homeostasis. We identify two highly conserved genes, DNA damage-induced transcript 4 (DDIT4) and interferon-related developmental regulator 1 (IFRD1), that are increased specifically following injury that induces paligenosis. We show in gastric chief and pancreatic acinar cells that DDIT4 causes the initial suppression of mTORC1 observed in paligenosis. p53 continues mTORC1 suppression as DDIT4 expression is lost. IFRD1 then suppresses p53 to relieve the mTORC1 blockade and allow cells to re-enter the cell cycle. Previously published data, coupled with our findings here, indicate that IFRD1 and DDIT4 function similarly in multiple organs and across animal phyla. The data are consistent with a model wherein differentiated cells have access to specific genes largely dedicated to governing cell-cycle re-entry, conceptually similar to how they have genes (e.g., caspases, BCL-2 family) dedicated to executing cell death.

RESULTS

Induction of DDIT4 and IFRD1 in Paligenosis and Requirement for IFRD1 in Paligenosis Are Conserved across Tissue and Phyla

To decode the molecular network regulating mTORC1 in paligenosis, we determined the intersection of a published set of mTOR-associated genes with sets of transcripts upregulated in mice in 4 organs we and others previously have shown undergo a paligenotic response (Willet et al., 2018) (Figure 1A; Table S1). Only two transcripts, *Ifrd1* (encoding interferon-related developmental regulator 1) and *Ddit4* (also called *Redd1*, encoding DNA damage-induced transcript 4) were at the intersection of all 5 gene sets. We next analyzed publicly available data from a published single-cell RNA sequencing (RNA-seq) analysis of the regenerative injury induced by amputation in the amphibian axolotl (Figure 1B) (Gerber et al., 2018). Just as in mouse paligenosis, the fraction of cells in the regenerating wound bed expressing *DDIT4* and *IFRD1* transcripts increased. *DDIT4* increased slightly immediately after amputation and then decreased. The fraction of cells expressing *IFRD1* increased after *DDIT4* and continued to rise until the stages of regeneration characterized by maximal recruitment of mature cells back into the cell cycle (marked by expression of the cell-cycle transcript *AURKA*).

DDIT4 has been previously characterized as an injury-activated scaffold that suppresses mTORC1 activity via induction of the TSC1/TSC2 complex from *Drosophila* to humans. (DeYoung et al., 2008; Kimball et al., 2008) However, IFRD1 conservation has not been reported. We found that nearly the entire IFRD1 protein is conserved from the fission yeast *Schizosaccharomyces pombe* to humans (Figures S1A and S1B) with similar likely secondary structure involving extensive alpha-helical character into an armadillo (or alpha-solenoid) fold (Figures S1A and S1C), similar to the non-injury-induced paralog IFRD2 (Brown et al., 2018). The yeast ortholog of IFRD1 has not been specifically characterized, but various transcriptomic and mutant screens indicate it is injury-induced and not required for vegetative growth (Lock et al., 2019). A recent paper similarly identified the *dictyostelium Ifrd1* ortholog as mediating dedifferentiation from the multicellular slime mold to unicellular state (Nichols et al., 2020).

Likewise, the *Drosophila melanogaster* ortholog of *Ifrd1*, CG31694, had not been specifically characterized but had been shown to be rapidly induced following injuries that induce proliferation in the gut (Vodovar et al., 2005; Bou Sleiman et al., 2015). We confirmed that *difrd1* increased following intestinal stem-cell-recruiting stress using GFP driven by the *difrd1* promoter (Figure 1C). Various injuries induce *Drosophila* enterocytes to re-enter the cell cycle to help fuel proliferative repair. Two hypomorphic *difrd1 Drosophila* pedigrees showed no homeostatic abnormalities but complete loss of proliferation in response to injury (Figure 1D), consistent with requirement for dIFRD1 in paligenosis.

We also surveyed the requirement for IFRD1 in regeneration after injury in various other mouse tissues. In nerves following axotomy, a model of regeneration that resembles paligenosis in that neurons dedifferentiate to regenerate axons (Vercellino et al., 2007; Stierli et al., 2018), regeneration was markedly retarded by knockdown of *Ifrd1* (Figures 1E and 1F). Similarly, *Ifrd1*$^{-/-}$ livers showed nearly 2-fold reduction in paligenotic proliferation post-partial hepatectomy (Figures 1G and 1H). Thus, evidence points to DDIT4 and IFRD1 as injury-induced genes that may have an evolutionarily conserved role in paligenosis.

IFRD1 and DDIT4 Are Increased in Gastric and Pancreatic Paligenosis, with IFRD1 Dispensable for Early Stages

Of the 4 organs in Figure 1A, the stomach is unique because injury can cause both increased proliferation of the constitutively active adult progenitor cells in the isthmus and neck of the gland (nearer the gastric lumen), while also recruiting the normally mitotically quiescent digestive-enzyme-secreting chief cells in the base of the gland as progenitors via paligenosis (Stange et al., 2013; Radyk et al., 2018; Sáenz and Mills, 2018; Willet et al., 2018). Consistent with a role specifically in paligenosis, after injury with regeneration-inducing doses (250 mg/kg) of tamoxifen (hereafter, "TAM") (Huh et al., 2012; Burclaff et al., 2017; Keeley et al., 2019), *Ifrd1* was increased in the chief cells but not other cells in the epithelium (Figures 2A and 2B). Induction of *Ifrd1* specifically within chief cells was substantial enough to be detectable via western blot and qRT-PCR by 12 and 48 h. DDIT4/*Ddit4* increased more modestly, peaking at 12 h and dropping below baseline by 24 h onward (Figures 2C and 2D). The pattern of earlier, modest *Ddit4* increase with later, more dramatic *Ifrd1* induction, was similar to that seen during axolotl regeneration.

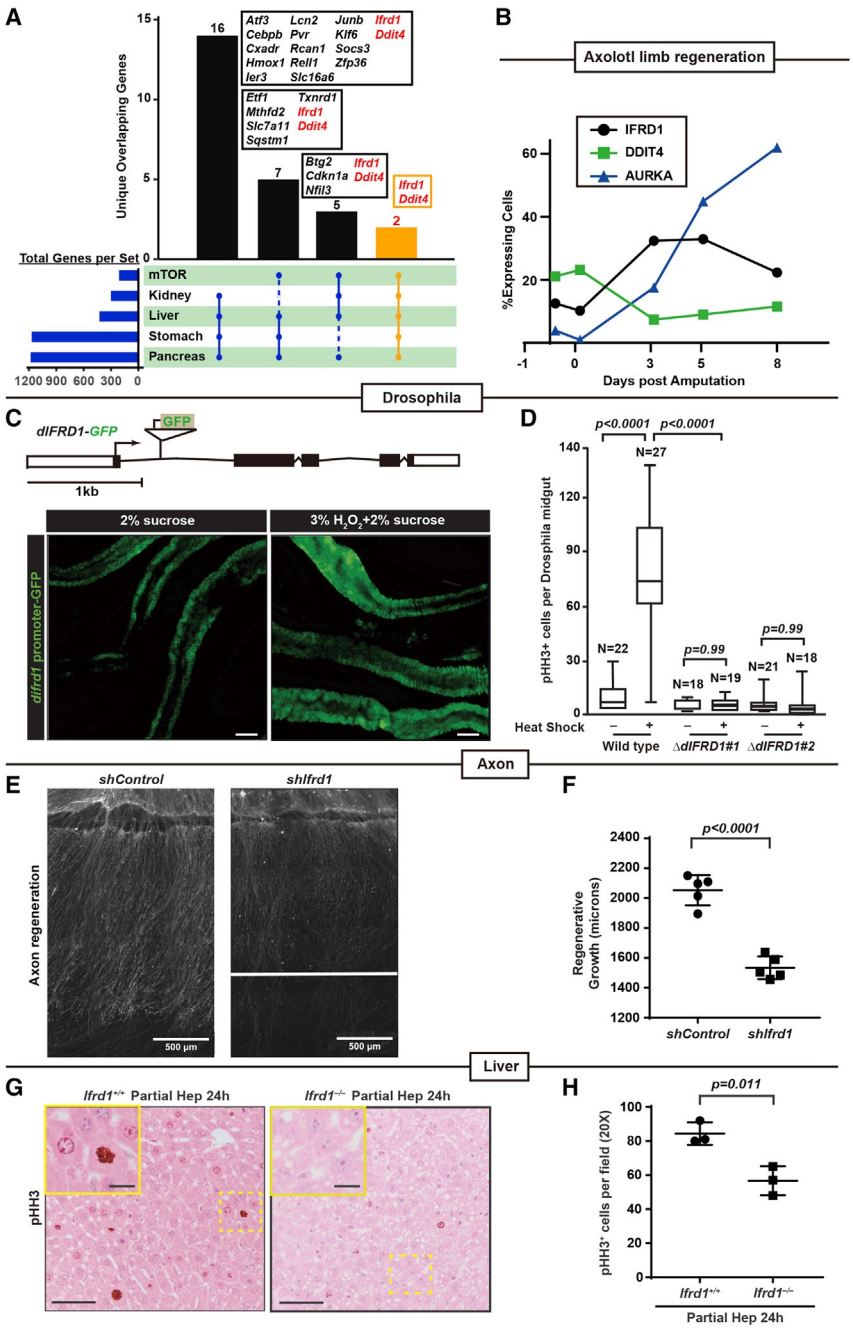


Figure 1. IFRD1 and DDIT4 Are mTORC1-Associated Genes Induced during Paligenosis, and IFRD1 Is Required for Paligenosis in Multiple Tissues and Species

(A) Intersection of transcripts upregulated by paligenotic injury in 4 organs with genes in the HALLMARK_MTORC1_SIGNALING Gene Set from Broad GSEA. Only intersections of gene sets R4 and transcripts unique for that intersection intersections are depicted.

(B) Fraction of cells expressing *DDIT4* and *IFRD1* in previously published single-cell RNA-seq of regenerating cells after axolotl limb amputation. *AURKA* is representative of a cohort of cell-cycle transcripts upregulated at ≥ paligenosis stage 3.

(C) GFP under regulation of *difrd1* promoter in *Drosophila melanogaster* intestine at baseline and after stem-cell recruiting oxidative stress. Scale bar, 100 mm. Above: genomic map of GFP P-element insertion in *difrd1* locus.

(D) Total phospho-histone H3+ (pHH3+) cells of wild type untreated (n = 22), wild type with heat shock (n = 27), DdIFRD1 #1 untreated (n = 18), DdIFRD1 #1 with heat shock (n = 19), DdIFRD1 #2 untreated (n = 21) and DdIFRD1 #2 with heat shock (n = 18) *Drosophila* mid-gut. DdIFRD1 #1 and #2 are *difrd1* hypomorphic alleles. Variance plotted as mean ± SD with significance estimated by one-way ANOVA with Dunnett post hoc test to the *Ifrd*$^{+/+}$ control.

(E) Regenerating mouse dorsal root ganglion neurites visualized by anti-SCG10 following axotomy *ex vivo* of control and shRNA knockdown of *Ifrd1* (shIfrd1). Panels are divided at maximal extension of neurite regeneration. Scale bar, 500 mm.

(F) Axon regeneration quantified following axotomy from *Ifrd1*$^{+/+}$ (n = 5) and *Ifrd1*$^{-/-}$ (n = 5) mice. Each data point: mean ± SEM maximal axon regeneration length for an individual culture from an individual mouse with significance estimated by unpaired, two-tailed t test.

(G) Immunohistochemical staining for mitotic marker pHH3 in regenerating liver 24 h following partial resection (''Partial Hep''). Scale bar, 50 mm; boxed area insert, 25 mm.

(H) Quantification of data as for (G) from *Ifrd1*$^{+/+}$ (n = 3) and *Ifrd1*$^{-/-}$ mice (n = 3). Each data point: mean ± SEM counts of R10 fields in a single mouse with significance estimated by unpaired, two-tailed t test.

We first focus on IFRD1 following gastric and pancreatic injury. *Ifrd1*$^{-/-}$ stomachs were defective in paligenosis, with markedly decreased proliferation induction (Figures 2E, 2F, and S2A). To confirm paligenosis specificity of IFRD1, we killed acid-secreting parietal cells in *HK-iDTR;Ifrd1*$^{-/-}$ mice with diphtheria toxin, an injury that induces proliferation of the existing stem and progenitor cells in the neck of the gastric unit but ''not'' paligenosis in the chief cells in the base of the unit (Burclaff et al., 2017). Activation of the constitutive progenitors was not affected by loss of IFRD1 (Figures S2B and S2C), furthering the interpretation that IFRD1 is required only for chief cells to proliferate by paligenotic induction of proliferation.

We have previously shown that paligenosis occurs via 3 stages: (1) massive activation of autophagy and lysosomal activity as mTORC1 is extinguished; (2) re-expression of progenitor or embryonic markers (e.g., SOX9 or the epitope for the lectin GSII, normally found exclusively in progenitor cells of the isthmus and neck zones); (3) induction of high-level mTORC1 with cell-cycle entry. Chief cells not only return to the cell cycle during paligenosis but return to a progenitor-like phenotype (Nam et al., 2010; Stange et al., 2013; Weis et al., 2017; Willet et al., 2018; Burclaff et al., 2020). Induction of lysosomal activity still occurred in *Ifrd1*$^{-/-}$ mice at 24 h post-TAM (Figures S2D and S2E), and SOX9 was still induced at later time points (Figure S2F), though

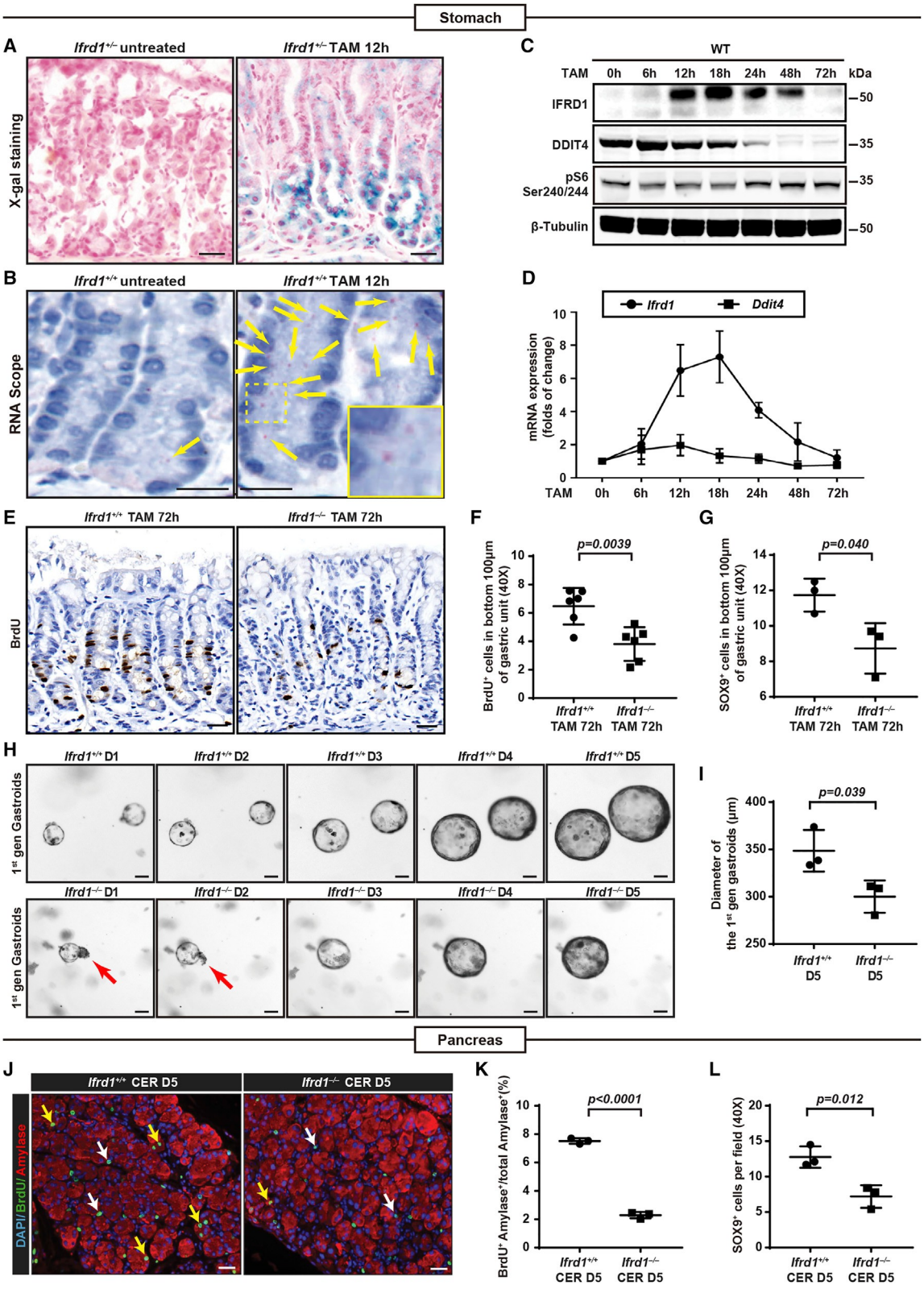


Figure 2. IFRD1 and DDIT4 Are Induced in Murine Gastric and Pancreatic Paligenosis; IFRD1 Is Required Cell-Autonomously

Figure360▷ For a Figure360 author presentation of this figure, see https://doi.org/10.1016/j.devcel.2020.07.005.

(A) Expression of lacZ knocked into the null allele of *Ifrd1*$^{+/-}$ mice after TAM showing induction of expression in basal chief cells early in paligenosis. Scale bar, 50 mm.

(legend continued on next page)

overall census of SOX9+, paligenotic cells was reduced by 72 h (Figure 2G). The reduction of SOX9+ cells was roughly equivalent to the overall loss of paligenotic cells in *Ifrd1*$^{-/-}$ mice (e.g., Figure S2A), so we interpret the results as indicating IFRD1 is largely dispensable for stages 1 and 2.

We next determined if IFRD1 was required in a cell-autonomous way within chief cells by growing organoids from stomach bodies, which are established from the epithelium, initially from both normal epithelial progenitors and proliferation of paligenotic chief cells (Stange et al., 2013; Moore et al., 2015). As expected, organoids generated from *Ifrd1*$^{-/-}$ mice were delayed in their outgrowth (Figures 2H and 2I), consistent with IFRD1 being specifically required for paligenotic growth intrinsically within chief cells. Thus, our results collectively showed: chief-cell-specific *Ifrd1* expression (Figures 2A and 2B) induced during paligenosis; lack of phenotype in injured *HK-iDTR;Ifrd1*$^{-/-}$ mice in which chief cell paligenosis does not occur (Figures S2B and S2C); and slower outgrowth from epithelial organoids that depend in part on proliferation from paligenotic chief cells.

In pancreas, as in stomach, proliferating, paligenotic acinar cells induced by cerulein injury were greatly reduced in *Ifrd1*$^{-/-}$ mice, while proliferating cells in the stroma were largely unaffected (Figures 2J, 2K, and S3A). Likewise, stage 1 autophagic induction and stage 2 SOX9 induction still occurred (Figures S3B and S3C). As in stomach, SOX9+ cells overall were reduced (Figures 2L and S3C). However, in *Ifrd1*$^{-/-}$ mice at peak paligenosis (72 h), 35% ± 2% of gastric units showed cell loss in gland bases versus only 7.0% ± 2.6% of control units (n = 3–4 mice per genotype, p = 0.0004 by two-tailed Student's t test; see also Figure S2A), so loss of SOX9+ cells correlates with overall cell death in the absence of IFRD1 (as we observed previously in stomach). Thus, overall, in pancreas and stomach, IFRD1 is largely required for the final, proliferative and regenerative stage of paligenosis.

IFRD1 Loss Causes p53 Stabilization and Failed mTORC1 Reinduction in Stage 3 of Paligenosis

The proliferative/regenerative stage 3 of paligenosis requires the reinduction of mTORC1 activity to drive paligenotic cells into S phase of the cell cycle (Willet et al., 2018). *Ifrd1*$^{-/-}$ stomachs showed the usual induction of mTORC1 activity in non-paligenotic isthmal and neck progenitor cells (Figure 3A), as measured by expression of phosphorylated S6 ribosomal protein (pS6), a critical downstream target of mTORC1 (which we have previously vetted as a proxy for mTORC1 activity in tissue) (Willet et al., 2018). In contrast, even in regions of more limited cell loss at day 3 post-TAM, there was marked reduction in paligenotic reinduction of mTORC1 in the absence of IFRD1 (Figure 3A). p53 suppresses mTORC1 activity by various routes (Hasty et al., 2013; Akeno et al., 2015; Deng et al., 2016; Liu et al., 2019a) and, thus, could be a key mechanism for mTORC1 suppression and failed paligenotic proliferation as well as potentially contribute to the increased cell loss seen in *Ifrd1*$^{-/-}$ mice. Accordingly, we observed increased p53 in the base of *Ifrd1*$^{-/-}$ gastric units (Figures 3B and 3C).

IFRD1 is thought to act as a scaffold that helps coordinate deacetylation of lysines of various proteins (Micheli et al., 2011; Tummers et al., 2015). IFRD1 effects on p53 have not been previously shown, yet it is known that acetylation promotes p53 transcriptional activity and blocks its degradation (Tang et al., 2008; Wang et al., 2016; Yun et al., 2016; Liu et al., 2019b). *Ifrd1*$^{-/-}$ mice exhibited increased expression of p53 acetylated on lysine 379 in paligenotic cells (Figures 3D and S2G). The effects of IFRD1 were, as expected, at the post-translational level, as *Trp53* mRNA levels were not affected by loss of IFRD1 (Figure 3E). The increased p53 protein in *Ifrd1*$^{-/-}$ mice correlated in western blots with the immunohistochemical results, with decreased phosphorylation of S6 kinase target: serine residues 240 and 244 of S6 ribosomal protein (Figure 3F) (Hutchinson et al., 2011). Note that p53 and pS6 are all also expressed in non-paligenotic cells (i.e., in cells that do not express IFRD1), so differences on western blot of the entire body of the stomach are not as dramatic as changes in expression detected by immunohistochemistry specifically in paligenotic cells. DDIT4 protein was slightly increased by loss of IFRD1 at day 3 (Figures 3F and S2H).

Results in the pancreas were similar. Gene set enrichment analysis (GSEA) of *Ifrd1*$^{-/-}$ mice ± cerulein at day 5 showed substantial de-enrichment of multiple proliferation-associated gene sets in *Ifrd1*$^{-/-}$ mice (Figures 3G and S3G), consistent with IFRD1 requirement for stage 3 of paligenosis. Unbiased analysis of expression patterns using the entire Broad Institute "Hallmark" collection of GSEA datasets (a compendium of gene sets designed for unbiased screens; Subramanian et al., 2005) further highlighted de-enrichment of cell-cycle-related gene

(B) RNAScope shows *Ifrd1* mRNA in chief cells after TAM. Scale bar; inset highlights two red puncta from boxed area; arrows indicate other puncta; scale bar, 50 mm.
(C) Western blot for DDIT4 and IFRD1 and mTORC1 proxy pS6 240/244, tubulin as loading control.
(D) qRT-PCR for *Ifrd1* and *Ddit4*. Each data point represents mean ± SEM from n = 3 mice cohorts.
(E) Proliferation measured by BrdU 72 h after TAM. Scale bar, 50 mm.
(F) Data as in (E) quantified, focusing on the basal 100 mm gastric of *Ifrd1*$^{+/+}$ (n = 6) and *Ifrd1*$^{-/-}$ (n = 6) mice gastric unit. Data point: mean ± SEM of R 40 glands quantified per mouse with significance estimated by unpaired, two-tailed t test.
(G) As per (F) but for SOX9+ progenitor cells of *Ifrd1*$^{+/+}$ (n = 3) and *Ifrd1*$^{-/-}$ (n = 3) mice.
(H) Organoids from stomach body at various days after isolation. Scale bar, 100 mm. Initial outgrowth of wild-type organoids occurs throughout the gastric unit, whereas the bases (arrow) of *Ifrd1*$^{-/-}$ mice do not expand, slowing overall organoid growth
(I) Data as in (H), quantified for organoid diameter after 5 day in culture of *Ifrd1*$^{+/+}$ (n = 3) and *Ifrd1*$^{-/-}$ (n = 3) mice. Data point: mean ± SEM of R 100 gastroids per mouse with significance estimated by unpaired, two-tailed t test.
(J) BrdU (green) identifying proliferating acinar cells 5 days post cerulein-injury-induced paligenosis (acinar cells labeled by digestive enzyme amylase, red). Yellow arrows, representative paligenotic cells; white arrows, non-epithelial cells. Scale bar, 50 mm
(K) Paligenotic (i.e., amylase positive) proliferative (i.e., BrdU+) cells of *Ifrd1*$^{+/+}$ (n = 3) and *Ifrd1*$^{-/-}$ (n = 3) mice from (J) are quantified. Data point: mean ± SEM of R10 random fields per mouse with significance estimated by unpaired, two-tailed Student's t test.
(L) As per (K) but with quantification of SOX9+ progenitor cells of *Ifrd1*$^{+/+}$ (n = 3) and *Ifrd1*$^{-/-}$ (n = 3) mice.

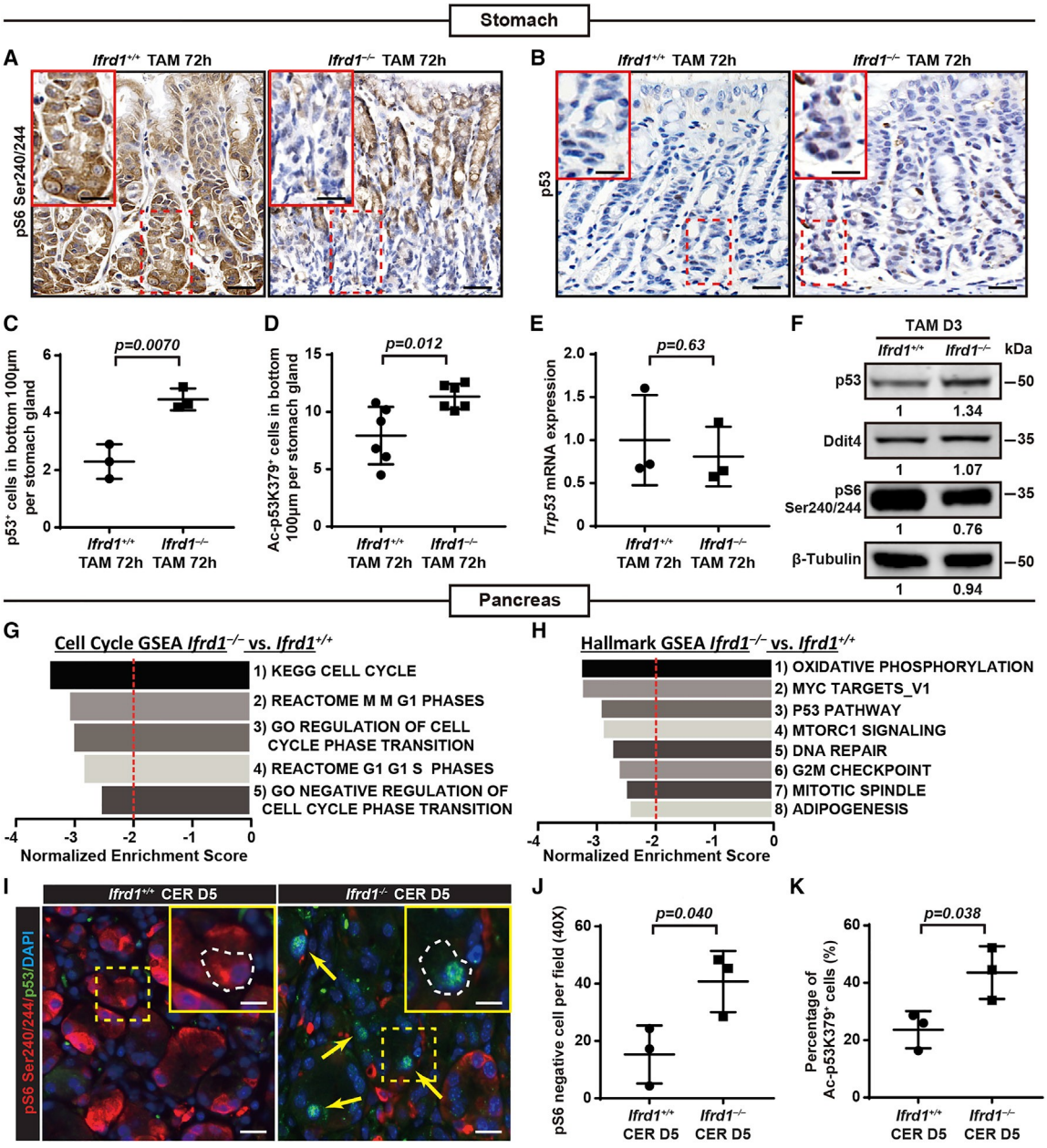


Figure 3. Loss of IFRD1 Causes p53 Stabilization and Failed mTORC1 Reinduction in Stage 3 of Paligenosis

(A) Anti-S6 phosphorylated on serines 240/244 (mTORC1 activity proxy) showing most surviving, paligenotic (i.e., basal) *Ifrd1*$^{-/-}$ cells are pS6-negative. Non-paligenotic cells higher in the unit are unaffected by IFRD1 loss. Scale bar, 50 mm; boxed area insert, 25 mm.

(B) As for (A) with anti-p53. Scale bar, 50 mm; boxed area insert, 25 mm.

(C) Data as for (B) quantified but focusing on the basal 100 mm of *Ifrd1*$^{+/+}$ (n = 3) and *Ifrd1*$^{-/-}$(n = 3) mice, where paligenosis occurs. Data point: mean ± SEM of R40 glands quantified per mouse with significance estimated by unpaired, two-tailed t test.

(D) As per (C) but quantifying anti-p53 acetylated on lysine residue 379 (Ac-p53K379) of *Ifrd1*$^{+/+}$ (n = 6) and *Ifrd1*$^{-/-}$(n = 6) mice.

(E) Quantitative real-time PCR of *Ifrd1*$^{+/+}$ (n = 3) and *Ifrd1*$^{-/-}$(n = 3) mice stomach bodies 72 h after TAM injury. Data point: mean ± SEM of 3 technical replicates per mouse, significance by unpaired, two-tailed t test.

(F) Western blot for mouse stomach body extracts 72 h after TAM. Tubulin as loading control. Numbers under bands indicate relative expression of null to control.

(G) GSEA of global mRNA expression profiling from whole pancreas using cell-cycle-related gene sets from Broad Institute. All statistically significant cell-cycle gene sets (false discovery rate [FDR] and p value < 0.001) exhibiting a normalized enrichment score (NES) %−2.0 (dashed red line) in *Ifrd1*$^{-/-}$ versus *Ifrd*$^{+/+}$ mice are depicted.

(H) Unbiased GSEA using all gene sets in Broad "Hallmark" compilation. All statistically significant gene sets with NES %−2.0 *Ifrd1*$^{-/-}$versus *Ifrd*$^{+/+}$ mice depicted.

(I) Phospho-S6 (red) and p53 (green) after 5 days of cerulein. Arrows highlight representative p53-positive and pS6-negative cells. Scale bar, 50 mm; boxed area insert, 25 mm. Note *Ifrd1*$^{-/-}$ mice have increased nuclear p53 and decreased pS6, individual p53+ cells lack pS6.

(legend continued on next page)

sets and highlighted p53 and mTORC1 alterations (Figures 3H and S3H). Moreover, as in stomach, paligenotic acinar cells at day 5 showed increased nuclear p53 and decreased pS6, and we noted that individual p53+ cells generally lacked pS6 expression, indicating p53 and mTORC1 activity were mutually exclusive during paligenosis as predicted (Figures 3I, 3J, S3D, and S3E). As in stomach, K379-acetylated p53 increased in paligenotic acinar cells (Figures 3K and S3F).

We further confirmed the role of IFRD1 in p53 stability by inducing IFRD1 via tunicamycin stress (Zhao et al., 2010) in p53-competent, intestinal L174 cells in tissue culture. As IFRD1 was induced, p53 acetylated on K382 (the human equivalent of mouse K379) decreased. When IFRD1 was stably knocked down, acetylated-p53 was elevated at both baseline and under stress (Figure S3I). Thus, overall the results are consistent with IFRD1 acting to destabilize p53.

p53 Is Required for Suppression of mTORC1 after Stage 1 of Paligenosis

To further dissect the relationship between p53 and mTORC1, we induced paligenosis in *Trp53*$^{-/-}$ mice with TAM (Figure S4A). Induction of autophagy in stage 1 could still be seen at 24 h (Figures S4B and S4C) in *Trp53*$^{-/-}$ mice; however, as predicted based on the known role of p53 as a suppressor of mTORC1 (Hasty et al., 2013; Akeno et al., 2015; Deng et al., 2016), the dynamics of mTORC1 suppression were aberrant (Figures 4A and 4B). mTORC1 was extinguished in both *Trp53*$^{-/-}$ and control paligenotic cells at 6 h; however, while it remained diminished in control cells at 12 h, it was already increasing in the absence of p53 (Figures 4A–4C). The more rapid reinduction of mTORC1 correlated predictably with an earlier and more robust increase in paligenotic proliferation, starting by 24 h and continuing through peak paligenosis at 72 h (Figures 4D and S4D). Loss of p53 stimulated re-entry into all stages of the cell cycle, as the number of chief cells (labeled via gastric intrinsic factor [GIF]) remaining quiescent (i.e., remaining negative for the cell-cycle marker Ki-67) was dramatically reduced in *Trp53*$^{-/-}$ mice (Figures 4E and 4F). *Trp53*$^{-/-}$ stomachs showed the expected decrease in the p53-induced, cell-cycle suppressor p21 and increase in the cell-cycle proteins Cyclins D1 (Figure 4G). Gastroids generated from Trp53$^{-/-}$ mice also showed increased outgrowth (Figures 4H and 4I), consistent with an epithelial cell-autonomous mechanism.

Results in pancreas were equivalent with significantly increased BrdU+ and reduced p21+ cells by day 5 after cerulein (Figures 4J–4L, S4E, and S4F). Overall, the results show that loss of p53 leads to briefer mTORC1 diminishment that did not substantially affect induction of autodegradation of mature cell architecture but did lead to premature mTORC1 reinduction causing aberrant mTORC1-reactivation-mediated transition from stage 2 to stage 3 of paligenosis.

Previously, we showed mTORC1 inhibition with rapamycin during TAM treatment specifically blocks stage 3 cell-cycle entry (Willet et al., 2018). If the principal reason for the increased paligenotic proliferation in *Trp53*$^{-/-}$ mice were due to dysregulated mTORC1 at that stage, then rapamycin should render the *Trp53*$^{-/-}$ phenotype equivalent to that of rapamycin-treated wild-type mice (Figure S5A). Accordingly, rapamycin caused near complete loss of pS6 in *Trp53*$^{-/-}$ and wild-type stomachs following TAM (Figure S5B). Consistent with our hypothesis, it also blocked not only paligenotic S phase entry in wild-type mice (confirming previous results) but also in *Trp53*$^{-/-}$ mice (Figures S5C and S5D). We previously showed that rapamycin inhibits progression specifically from G1 to S phase (Willet et al., 2018). Consistent with that observation, rapamycin did not significantly affect Ki-67-positive cells (which include G1 phase cells) in wild-type mice (Figures S5E and S5F). *Trp53*$^{-/-}$ mice, however, showed increased Ki-67+ cell census (Figures S5E and S5F), consistent with the increased early mTORC1 in *Trp53*$^{-/-}$ mice affecting not just S phase entry in stage 3 but also causing more efficient paligenotic recruitment of cells overall into all phases of the cell cycle. This increased efficiency of paligenosis was also mTORC1 dependent, as it was corrected by rapamycin.

Because IFRD1 works to destabilize p53 in the stage 2 to 3 transition, the *Ifrd1*$^{-/-}$ phenotype should be corrected by loss of p53. Accordingly, *Ifrd1*$^{-/-}$;*Trp53*$^{-/-}$ stomachs (Figures S6A–S6C) showed a phenotype statistically indistinguishable from that of wild type in terms of: paligenotic induction of proliferating progenitors (Figures 5A–5F and S6A) and mTORC1 activity at 72 h (FigureS6B). p21 expression was even lower than in wild type (Figures 5G and S6D). The pancreas showed similar rescue of mTORC1 activity and suppression of p21 (Figures 5H–5K and S6E–S6H). Summing the above results: p53 works to maintain mTORC1 suppression after the initial decrease in stage 1 of paligenosis, so when IFRD1 destabilizes p53, the mTORC1 blockade is removed so that cells can enter the cell cycle in stage 3.

The Initial Suppression of mTORC1 in Paligenosis Stage 1 Depends on DDIT4

The results so far explain the molecular machinery dictating the transition from stage 2 through stage 3. However, neither loss of IFRD1 nor p53 prevented the initial decrease in mTORC1 and the massive induction of autophagy and lysosomes seen in stage 1. We reasoned DDIT4, as a known suppressor of mTORC1 and the other gene identified by our initial screen (Figure 1A), could be the key gene to initiate stage 1.

In accordance with DDIT4 being required for mTORC1 suppression early in paligenosis, DDIT4 was expressed only in chief cells and only early in paligenosis, coinciding with the nadir (4–12 h, stage 1) of mTORC1 in TAM-treated mouse stomachs (Figures 6A and 6B). Conversely, DDIT4 was lost as paligenosis progressed to the proliferative stage 3 (48–72 h) when mTORC1 was reinduced to suprabasal levels (Figures 2C, 6A, and 6B). The loss of mTORC1 that occurs specifically in paligenotic chief cells by 12 h after TAM was substantial enough to result in consistent decrease of 57% ± 7% in western blots of the entire stomach body (Figures 6C and 6D). In contrast, mTORC1 in *Ddit4*$^{-/-}$ mice was nearly unchanged or increased at all time points by western blot (Figures 6C and 6D), and immunohistochemistry showed that mTORC1 at 12 h persisted aberrantly specifically in the

(J) pS6-negative cells of *Ifrd1*$^{+/+}$ (n = 3) and *Ifrd1*$^{-/-}$(n = 3) mice from experiments such as in (I) quantified by HALO™ automated cell counting and image-normalizing software. Data point: mean ± SEM of R10 random fields quantified per mouse with significance estimated by unpaired, two-tailed t test.
(K) As per (J) but with acetylated-p53 K379+ cells of *Ifrd1*$^{+/+}$ (n = 3) and *Ifrd1*$^{-/-}$(n = 3) mice as a fraction of total paligenotic cells.

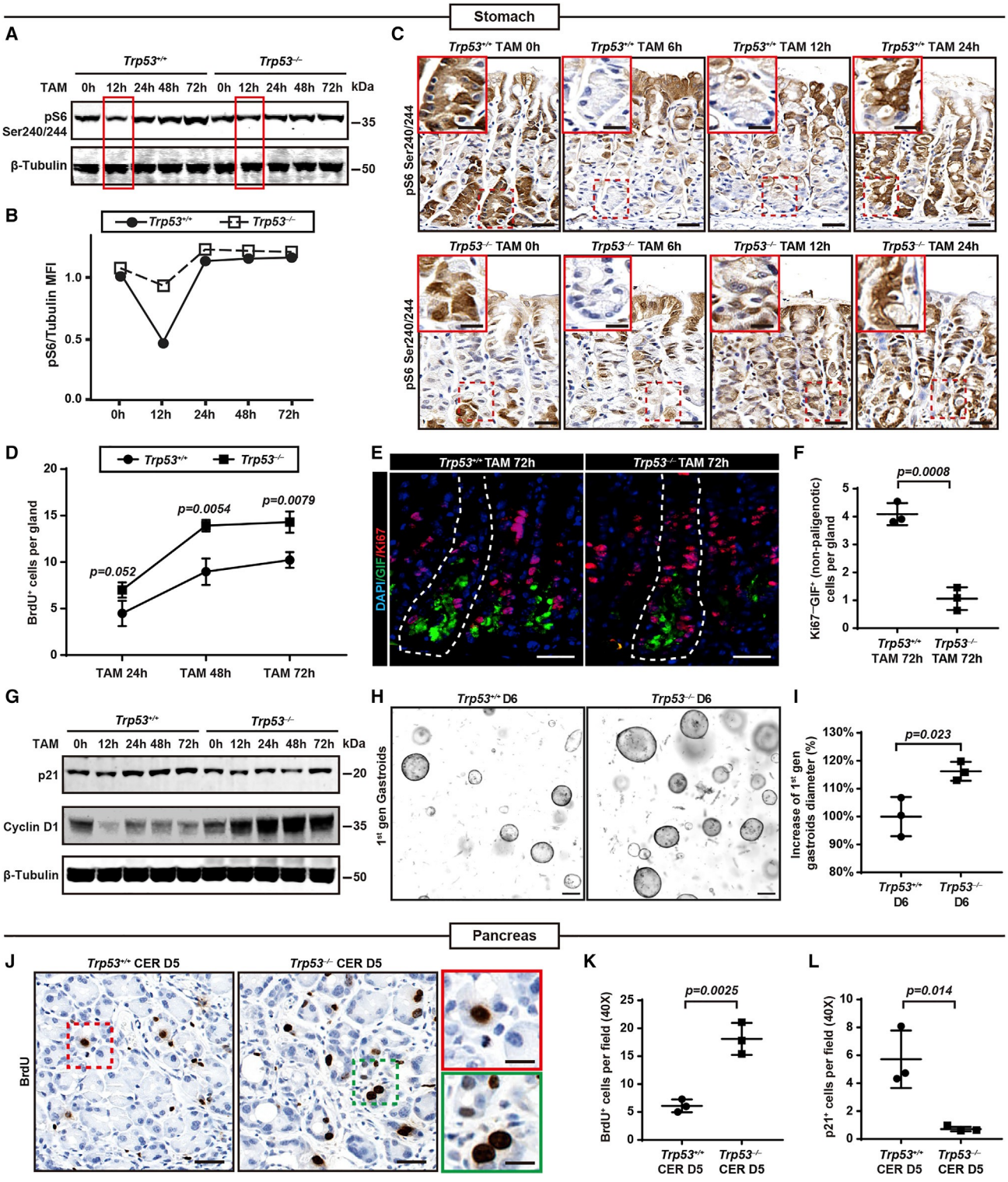


Figure 4. p53 Is Required to Delay mTORC1 Reactivation during Stages 2–3 of Paligenosis

(A) Western blot showing pS6 240/244 (i.e., mTORC1 activity) is restored earlier (at 12 h) in *Trp53*$^{-/-}$ mouse versus control.

(B) Quantification of pS6 240/244 versus tubulin intensity from the blot in (A) from n = 1 mouse cohort.

(C) Anti-pS6 240/244 with insets highlighting paligenotic cells in the base showing that pS6 is lost in basal cells in both genotypes but reappears prematurely in *Trp53*$^{-/-}$ cells by 12 h. Because non-paligenotic cells also express pS6, pS6 western blots in (A) do not show complete loss of pS6. Scale bar, 50 mm; boxed area insert, 25 mm.

(legend continued on next page)

paligenotic cells in *Ddit4*$^{-/-}$ stomachs and in pancreas at the 24 h time point after cerulein, when mTORC1 is lowest in pancreas (Willet et al., 2018) (Figures 6B and 6L). Thus, the results indicate DDIT4 is activated early in paligenosis to perform the initial suppression of mTORC1 that is later maintained by p53.

Autophagic and Lysosomal Recycling of Cell Architecture in Stage 1 Depends on DDIT4 Suppression of mTORC1, and Rapamycin Rescues the *Ddit4*$^{-/-}$ Phenotype

We have shown that decreased mTORC1 in stage 1 is required for the induction of the massive autophagic and lysosomal activity that governs eventual turnover of mature cell architecture (Willet et al., 2018). Accordingly, in *Ddit4*$^{-/-}$ mice, the failure to suppress mTORC1 in stage 1 correlated with greatly decreased induction of lysosomes and autophagosomes (Figures S7A–S7C), indicating aberrant autodegradation in stage 1. The failure of stage 1 correlated subsequently with aberrant cells at 72 h (i.e., stage 3, peak metaplasia): many cells still preserved key aspects of chief cell morphology, including large size, abundant apical cytoplasm, well-formed secretory granules containing GIF (Figures 6E–6G and S7D) (Willet et al., 2018). Loss of mTORC1 downregulation in stage 1 also led to earlier and more dramatic increase in the number of paligenotic cells entering the cell cycle in stage 3 (Figures 6G–6I). Furthermore, organoids derived from *Ddit4*$^{-/-}$ stomach bodies showed significantly increased growth, consistent with a paligenotic-cell-autonomous effect on proliferation due to sustained mTORC1 activation (Figures 6J and 6K).

The results so far indicated that, in the absence of DDIT4, mTORC1 in stage 2 paligenotic cells is already elevated because it does not get suppressed in stage 1. Thus, *Ddit4*$^{-/-}$ cells can complete paligenosis and progress to stage 3 regardless of the IFRD1-regulated p53 checkpoint. That is because p53 works to suppress only reactivation of mTORC1 in stage 2 to 3 progression, so this checkpoint is irrelevant if mTORC1 never decreases in stage 1. Accordingly, IFRD1 abundance was not affected by loss of DDIT4. Corroborating the gastric results, *Ddit4*$^{-/-}$ acinar cells also preserved mature cell features during peak stage 3 paligenosis and showed increased proliferation (Figures 6M–6O).

To confirm that the increased proliferation and persistent mature cell architecture in *Ddit4*$^{-/-}$ mice were due to failure to suppress mTORC1, we treated *Ddit4*$^{-/-}$ mice with rapamycin to force mTORC1 inactivation. As expected, rapamycin suppressed mTORC1 in *Ddit4*$^{-/-}$ mice as measured by decreased phosphorylation of S6 and the mTORC1 direct target S6 kinase (Figures 7A and 7B). Similarly, the mTORC1 suppressive protein TSC2—which, as expected, was decreased in *Ddit4*$^{-/-}$ mice—was increased by rapamycin (Figure 7B). Reducing mTORC1 with rapamycin administration in *Ddit4*$^{-/-}$ mice corrected the stage 3 hyperproliferation and mature-architecture-retention phenotypes in both stomach (Figures 7A, 7C, 7D, S7E, and S7F) and pancreas (Figures 7G, 7H, and S7G). Consistent with the key role of DDIT4 in paligenosis being to suppress mTORC1, rapamycin administration in *Ddit4*$^{-/-}$ mice did not affect SOX9 expression (stage 2–3 marker) in either stomach or pancreas (Figures 7E, 7F, S7H, and S7I). Overall, thus, DDIT4 is required for the autophagic/lysosomal recycling of cell architecture that characterizes stage 1, and, because rapamycin completely rescues the stage 1 defects caused by *Ddit4*$^{-/-}$, DDIT4 regulates stage 1 via mTORC1 suppression.

DISCUSSION

We summarize the molecular logic of DDIT4 and IFRD1 action in the conserved cellular dedifferentiation program we have termed paligenosis as follows: a stressor that may eventually cause differentiated cells to return to the cell cycle causes acute activation of DDIT4 along with a more gradual accumulation of IFRD1 and p53. The DDIT4 activation is required for the initial suppression of mTORC1 activity during stage 1, as *Ddit4*$^{-/-}$ mice never substantially decrease mTORC1 and largely do not activate the autodegradative machinery to turnover mature cell features. Passage into stage 3 depends on mTORC1 reactivation as we show here and in prior studies (Willet et al., 2018). Thus, *Ddit4*$^{-/-}$ cells, which maintain constitutively high mTORC1, do not need to wait for mTORC1 reactivation because mTORC1 is never deactivated, and they become proliferative more rapidly. DDIT4 protein decreases dramatically by the end of stage 1, so its direct role is limited to the initial mTORC1 decline.

As stage 1 progresses, the massive activation of lysosomes would be expected to begin to reactivate mTORC1 via liberation of amino acids and other products of lysosome digestion. During most of stage 1, DDIT4 suppresses mTORC1 despite this reactivation pressure. But as DDIT4 decreases, mTORC1 still does

(D) Quantification of BrdU-positive (i.e., proliferative) cells from *Trp53*$^{+/+}$ (TAM 24 h, n = 3; TAM 48 h, n = 3; TAM 72 h, n = 3) and *Trp53*$^{-/-}$ (TAM 24 h, n = 3; TAM 48 h, n = 3; TAM 72 h, n = 3) mice shows cell proliferation increases in *Trp53*$^{-/-}$ mice as early as 24 h. Data point: mean ± SEM of ℝ40 glands quantified per mouse with significance estimated by unpaired, two-tailed t test.

(E) Cell-cycle marker Ki67 (red) and chief cell lineage marker GIF (green) shows decreased Ki67^{-}/GIF^{+} cells (i.e., chief cells that are non-paligenotic in *Trp53*$^{-/-}$ mice. Scale bar, 50 mm.

(F) Non-paligenotic cells from *Trp53*$^{+/+}$ (n = 3) and *Trp53*$^{-/-}$ (n = 3) mice as in (E) were quantified. Data point: mean ± SEM of ℝ40 glands quantified per mouse with significance estimated by unpaired, two-tailed t test.

(G) Western blots from stomach body for p53 activated target proliferation-suppressing p21 and p53 repressed target proliferation-promoting Cyclin D1.

(H) Organoids at day 6 after culturing from *Trp53*$^{-/-}$ and *Trp53*$^{+/+}$ mice. Scale bar, 100 mm.

(I) Data as in (H) from *Trp53*$^{+/+}$ (n = 3) and *Trp53*$^{-/-}$ (n = 3) mice, quantified for organoid diameter. Data point: mean ± SEM of ℝ100 gastroids per mouse with significance estimated by unpaired, two-tailed t test.

(J) Anti-BrdU pancreas 5 days after cerulein injury showing markedly increased proliferation of *Trp53*$^{-/-}$ acinar cell paligenosis. Scale bar, 50 mm; boxed area insert, 25 mm.

(K) BrdU-positive cells as in (J) from *Trp53*$^{+/+}$ (n = 3) and *Trp53*$^{-/-}$ (n = 3) mice were quantified. Data point: mean ± SEM of ℝ10 random fields quantified per mouse with significance estimated by unpaired, two-tailed Student's t test.

(L) As per (K) but quantifying p21+ cell-cycle-arrested cells of *Trp53*$^{+/+}$ (n = 3) and *Trp53*$^{-/-}$ (n = 3) mice.

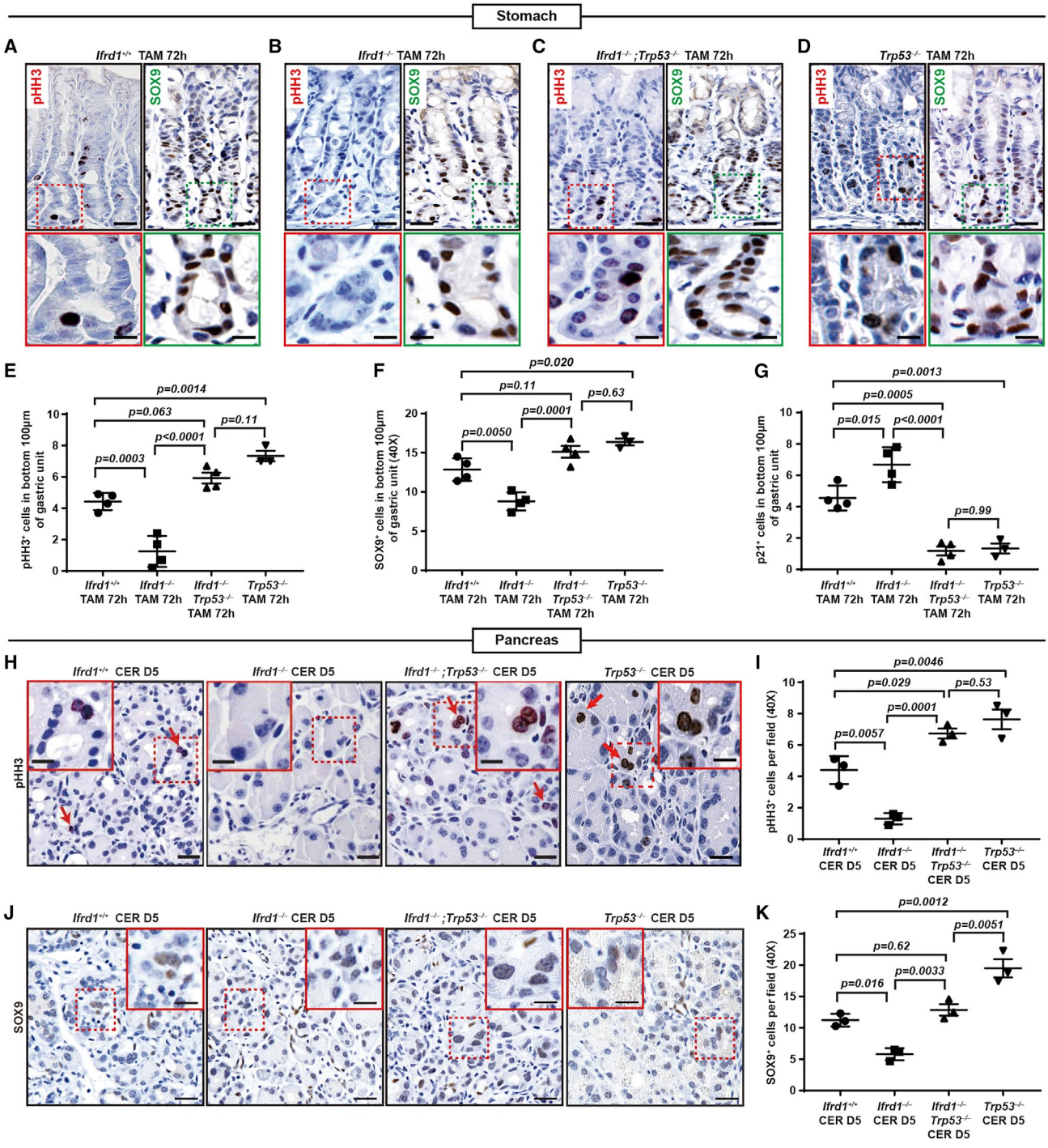


Figure 5. Loss of p53 Rescues the *Ifrd1*$^{-/-}$ Phenotype, Indicating IFRD1 Destabilizes p53

Figure360▷ For a Figure360 author presentation of this figure, see https://doi.org/10.1016/j.devcel.2020.07.005.

(A) Anti-phospho-histone H3 (pHH3), marking mitotic cells and SOX9 (progenitor cells) in control mice, TAM day 3; bottom: higher magnification of bases where paligenosis occurs. Scale bar, 30 mm; boxed area insert, 15 mm.

(B) As for (A) but with *Ifrd1*$^{-/-}$ mice.

(C) As for (A) but with *Ifrd1*$^{-/-}$;*Trp53*$^{-/-}$ mice.

(D) As for (A) but with *Trp53*$^{-/-}$ mice.

(E) pHH3 quantified from paligenotic bases of *Ifrd1*$^{+/+}$ (n = 4), *Ifrd1*$^{-/-}$ (n = 4), *Ifrd1*$^{-/-}$;*Trp53*$^{-/-}$ (n = 4), and *Trp53*$^{-/-}$ (n = 3) mice as in bottoms of (A–D). Data point: mean ± SEM of R40 glands quantified per mouse with significance estimated by one-way ANOVA with multiple comparisons to *Ifrd*$^{+/+}$ control (Dunnett post hoc test).

(F) As per (E) but quantifying SOX9+ progenitor cells of *Ifrd1*$^{+/+}$ (n = 4), *Ifrd1*$^{-/-}$ (n = 4), *Ifrd1*$^{-/-}$;*Trp53*$^{-/-}$ (n = 4), and *Trp53*$^{-/-}$ (n = 3) mice induced in the base.

(legend continued on next page)

not reactivate because p53 peaks during this time period. We know p53 is critical for suppressing mTORC1 reactivation and not its initial deactivation, because *Trp53*$^{-/-}$ cells still undergo stage 1 autodegradation and mTORC1 deactivation. Loss of p53 only makes that phase more transient with earlier mTORC1 reactivation. Eventually, late in stage 2, p53 begins to decrease, allowing full mTORC1 reactivation with progression through the cell cycle. The p53 decrease is abetted by IFRD1 which promotes the less active, deacetylated form of p53. *Ifrd1*$^{-/-}$ cells have hyperactive p53 in stage 2 and 3, and they largely fail to upregulate mTORC1, with many simply dying.

Thus, initial loss of mTORC1 is via DDIT4 while reactivation is via IFRD1 suppressing p53-mediated inhibition of mTORC1. The two phases of mTORC1 regulation appear relatively autonomous. Loss of DDIT4 does not affect IFRD1 abundance. Loss of IFRD1 does cause increased DDIT4 but does not affect stage 1, indicating it has no effect on DDIT4 function. The mTORC1 reactivation in stage 2 to 3 appears to be a critical checkpoint, as rapamycin leads to a dramatic blockade in paligenosis, with cells all expressing progenitor markers like SOX9 but unable to divide (Willet et al., 2018). Thus, the actions of IFRD1 and p53 may help ensure fidelity of cells before they undertake the drastic final step of going from a quiescent, mature state (which they might have been in for weeks to even years) back into the cell cycle. We saw some evidence of the importance of this step because loss of DDIT4 maintained high levels of mTORC1, which correlated with cells carrying DNA damage into stage 3. Thus, loss of either DDIT4 or p53 may promote tumorigenesis because both mutants would bypass the cell-cycle fidelity check in stage 3. Accordingly, it has been reported in other tissues that loss of DDIT4 mimics loss of p53 in increasing tumorigenesis risk because mice lacking either gene fail to respond appropriately to DNA damage (Janic et al., 2018).

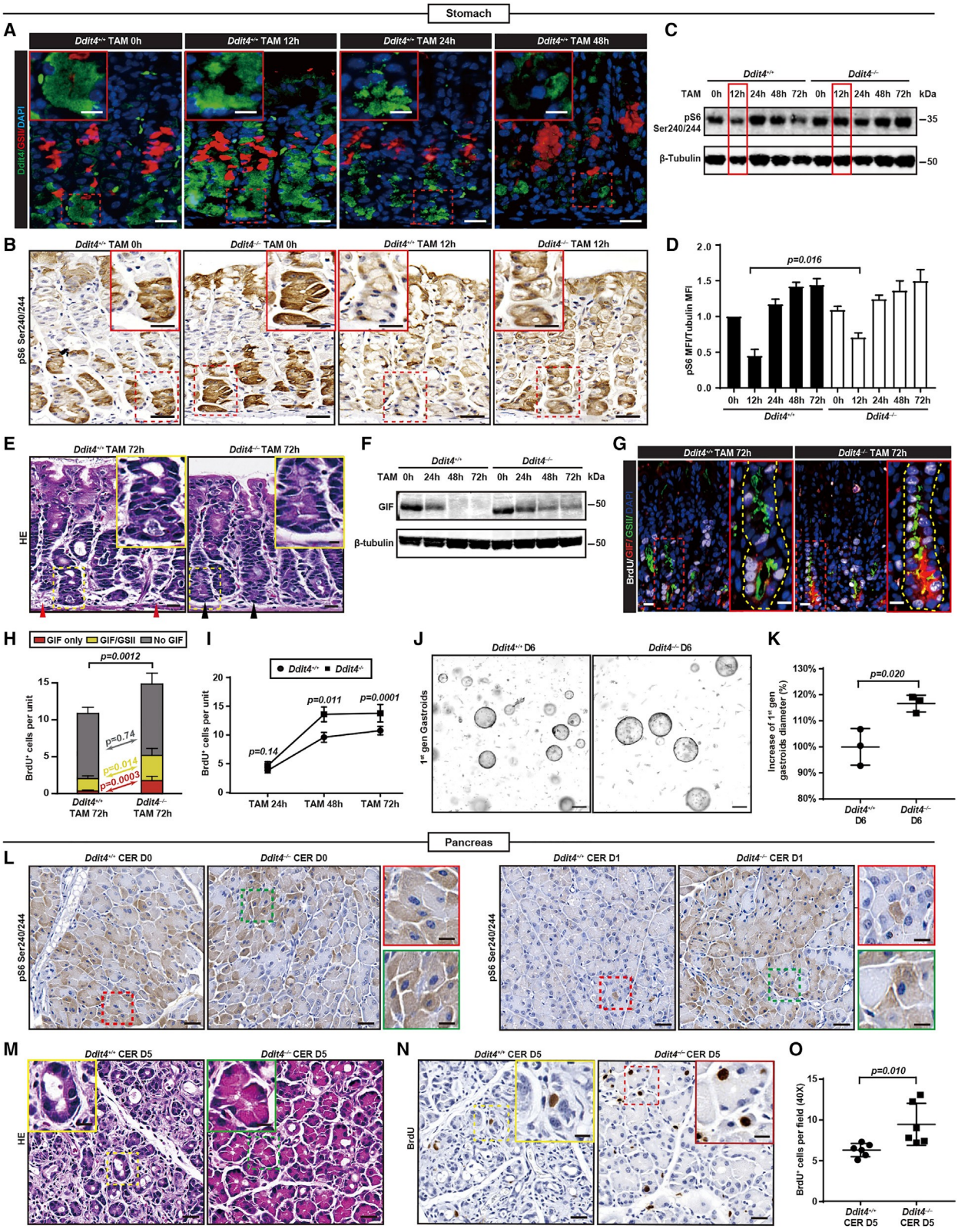
The mechanisms DDIT4 and IFRD1 use to regulate mTORC1 appear to be confined to injury-induced proliferation of mature or quiescent cells (i.e., paligenosis) and do not apply to constitutively active stem and progenitor cells or to proliferation during development. DDIT4 and IFRD1 are typically injury induced in all organisms and tissues where they have so far been studied, and mice null for *Ddit4* and *Ifrd1* develop normally and have normal adult stem cell activity. Previous reports have implicated DDIT4 in recruiting hematopoietic stem cells for regeneration after 5-FU with DDIT4 suppressing mTORC1 and helping to mediate scavenging of reactive oxygen species until cells are ready to renter the cell cycle, potentially an analogous process to what we observe in the current study (Basu, 2014). IFRD1 has also been shown to be required for skeletal muscle regeneration (Micheli et al., 2011), and for recruitment of quiescent myogenic stem cells after muscle crush injury (Vadivelu et al., 2004), and is induced during *dictyostelium* dedifferentiation (Nichols et al., 2020). We previously showed that *Ifrd1*$^{-/-}$ mice do not efficiently recruit stem cells for intestinal repair after resection (Garcia et al., 2014). In all these earlier studies, the cells that get recruited to eventually become stem cells must first emerge from mitotic quiescence. Moreover, in some cases, their emergence is known to require first suppression and then reactivation of mTORC1 (Basu, 2014). In our studies and in the extant literature, the mechanism of action of IFRD1 and DDIT4 in regulating injury-induced proliferation is cell autonomous (e.g., both genes are induced in chief cells and govern paligenosis in chief cells).

We are only just beginning to understand the dynamic, cell biological differences between constitutively dividing stem and progenitor cells (like LGR5+ crypt-base intestinal cells or isthmal gastric epithelial cells [Miao et al., 2020] and so-called reserve or quiescent ''stem cells''). It has been proposed that many of the so-called reserve stem cells recruited to proliferate in the intestine after injury to the constitutively dividing stem cells (e.g., via doxorubicin or radiation) may be differentiated cells like Paneth cells (Mills and Sansom, 2015; Burclaff and Mills, 2018b; Yu et al., 2018; Jones et al., 2019). Thus, the role for mTORC1 in nutritional and metabolic regulation of stem cell activity and tumorigenesis (Faller et al., 2015; Beyaz et al., 2016; Mihaylova et al., 2018; Miao et al., 2020) may involve effects on paligenotic recruitment of new stem cells from quiescent or mature cells. Recent reports have also implicated reactive oxygen species, the Cystine/Glutamate antiporter (xCT) and changes in DNA methylation specifically in recruiting mature chief cells – but not isthmal stem cells - during injury-induced tissue regeneration (Meyer et al., 2019; Shimuzu et al., 2020). It will be interesting to determine how those pathways intersect with the mTORC1-regulating molecular circuitry we identify here.

Overall, we argue that DDIT4 and IFRD1 are conserved elements of the paligenotic program that mature cells (and perhaps mitotically quiescent cells in general) use after injury to become regenerative. Their role seems principally to be to legislate the biphasic mTORC1 changes. It is too early to argue whether they are universal elements, as there may be different forms of injury-induced reprogramming (besides paligenosis), just as apoptosis is only one form of programed cell death. We also cannot argue yet that they have evolved exclusively to regulate paligenosis, as evolution constantly repurposes genes, just as genes that are core elements of mitosis, apoptosis, and autophagy are also used by cells in other contexts. However, we expect that the elucidation of this core machinery involving DDIT4, IFRD1, p53, and mTORC1 will play out in numerous cellular and tissue contexts.

Multicellular organisms can dedicate the vast majority of cells to specific functions; however, paligenosis also allows those cells to act as a large reservoir of potential progenitors to repair damage of organs throughout life. In the absence of tissue stem cells, the inability to undergo paligenosis can be catastrophic because regeneration cannot occur. For example, if we continue cerulein injury for 2 weeks in *Ifrd1*$^{-/-}$ mice, there is near complete loss of exocrine pancreatic tissue (unpublished observations). There are

(G) As per (E) but quantifying p21+ cell-cycle-arrested cells of *Ifrd1*$^{+/+}$ (n = 4), *Ifrd1*$^{-/-}$ (n = 4), *Ifrd1*$^{-/-}$;*Trp53*$^{-/-}$ (n = 4), and *Trp53*$^{-/-}$ (n = 3) mice induced in the base.
(H) Anti-pHH3 in *Ifrd*$^{+/+}$, *Ifrd1*$^{-/-}$, *Ifrd1*$^{-/-}$;*Trp53*$^{-/-}$, and *Trp53*$^{-/-}$ mice pancreases 5 days after cerulein. Scale bar, 50 mm; boxed area insert, 25 mm.
(I) pHH3 quantified as from (H) of *Ifrd1*$^{+/+}$ (n = 3), *Ifrd1*$^{-/-}$ (n = 3), *Ifrd1*$^{-/-}$;*Trp53*$^{-/-}$ (n = 3), and *Trp53*$^{-/-}$ (n = 3) mice. Data point: mean ± SEM of R10 random fields quantified per mouse with significance estimated by one-way ANOVA with multiple comparisons to the *Ifrd*$^{+/+}$ control (Dunnett post hoc test).
(J) Anti-SOX9 in *Ifrd*$^{+/+}$, *Ifrd1*$^{-/-}$, *Ifrd1*$^{-/-}$;*Trp53*$^{-/-}$, and *Trp53*$^{-/-}$ mice pancreases 5 days after cerulein. Scale bar, 50 mm; boxed area insert, 25 mm.
(K) As per (I) but for SOX9+ progenitor cells of *Ifrd1*$^{+/+}$ (n = 3), *Ifrd1*$^{-/-}$ (n = 3), *Ifrd1*$^{-/-}$;*Trp53*$^{-/-}$ (n = 3), and *Trp53*$^{-/-}$ (n = 3) mice.



(legend on next page)

risks, however, in allowing long-lived cells to cycle between replicative and differentiated states because mutations could potentially accumulate over time increasing risk for accumulation of oncogenic mutations with each paligenotic event (Burclaff and Mills, 2018a, 2018b). Accordingly, the pathologists and cell biologists of over a century ago who first recognized that mature cells could be recruited back into the cell cycle also noted that this process likely fueled lesions like metaplasia that increase risk for tumorigenesis (Adami, 1900). The IFRD1 and p53 cell-cycle licensing we show here that occurs in stage 3 of paligenosis may be one reason why p53 evolved in multicellular organisms and not yeast (Wahl and Carr, 2001; Wylie et al., 2014): multicellular organisms can afford to waste damaged cells via apoptosis to avoid cancer risk.

Because paligenosis is at the heart of regeneration and tumorigenesis—but not a part of normal homeostasis—delineating the paligenosis machinery may lead to druggable targets that can inhibit cancer progression or spur regeneration without affecting homeostatic processes like the proliferation of constitutively active tissue stem cells.

STAR+METHODS

Detailed methods are provided in the online version of this paper and include the following:

- KEY RESOURCES TABLE
- RESOURCE AVAILABILITY
  - Lead Contact
  - Materials Availability
  - Data and Code Availability
- EXPERIMENTAL MODEL AND SUBJECT DETAILS
  - Human Cancer Cell
  - Mice
  - Drosophila
  - Gastroid
- METHOD DETAILS
  - Drug Treatments
  - Imaging and Tissue Analysis
  - Quantitative PCR
  - Western Blots
  - Axon Regeneration
  - Electron Microscopy
- QUANTIFICATION AND STATISTICAL ANALYSIS
  - Imaging and Quantifications
  - Bioinformatics, Microarray and *In Silico* Screening
  - Statistics

SUPPLEMENTAL INFORMATION

Supplemental Information can be found online at https://doi.org/10.1016/j.devcel.2020.07.005.

Figure 6. The Initial Suppression of mTORC1 and Autophagic/Lysosomal Recycling of Cell Architecture in Paligenosis Stage 1 Depends on DDIT4

(A) DDIT4 (green) is confined to gastric chief cells, increasing in stage 1 (4–24 h) then lost later. GSII (red, a progenitor marker) labels stages 2–3 paligenotic chief cells at base of gland and normal progenitor cells higher in the gland. As paligenotic cells become GSII+, they lose DDIT4, indicating DDIT4 is in homeostatic chief cells, increased in stage 1 and lost thereafter. Blue, nuclei. Scale bar, 30 mm; boxed area insert highlighting base, 15 mm.

(B) Anti-pS6 240/244 showing that at mid-Stage 1 (12 h), *Ddit4*$^{-/-}$ paligenotic cells fail to extinguish mTORC1. Scale bar, 30 mm; boxed area insert highlighting base, 15 mm.

(C) Representative western blot for pS6 240/244 showing decreased mTORC1 in stage 1 (12 h) only in *Ddit4*$^{+/+}$ mice. Note pS6 is also in non-paligenotic cells, so a blot of whole stomach body registers only partial decrease. This blot is one of those quantified in (D).

(D) Western blots quantified from n = 3 independent mouse cohorts represented as mean ± SEM, significance estimated by unpaired, two-tailed Student's t test at the 12 h time point.

(E) H&E staining of stomachs in *Ddit4*$^{+/+}$ and *Ddit4*$^{-/-}$ mice at 72 h after TAM injury (TAM 72 h). Red arrows show representative glands with dropout (i.e., the cells at the base of units are lost) in *Ddit4*$^{+/+}$ control. Note that cells are mostly cuboidal/columnar. There is no dropout apparent in *Ddit4*$^{-/-}$ mice; black arrows show representative bases with most chief cells preserving their cytoplasm 72 h after TAM injury. Scale bar, 30 mm; boxed area insert, 15 mm.

(F) Western blot of GIF and b-tubulin control expression from whole corpus protein extracts of *Ddit4*$^{+/+}$ and *Ddit4*$^{-/-}$ mice at various time points after TAM injury.

(G) GIF (red, chief cells), GSII (green, progenitor or paligenotic cells), BrdU (white), DAPI (blue). Note paligenotic cells *Ddit4*$^{-/-}$ mice are both more proliferative (BrdU+) and have more GIF^{+} granules, indicating failed stage 1 downscaling. Scale bar, 30 mm; boxed area insert, 15 mm.

(H) Proliferating (BrdU+) cells of *Ddit4*$^{+/+}$ (n = 3) and *Ddit4*$^{-/-}$ (n = 3) mice quantified by cell type in stage 3, proliferative paligenosis (72 h TAM). GIF-negative cells lack chief cell markers so are non-paligenotic: i.e., derived from GSII+ progenitors from neck (green) or progenitors even higher in the unit (gray); GIF+GSII− cells aberrantly retain chief cell features without inducing progenitor markers, indicating failed stage 1. *Ddit4*$^{-/-}$ mice have significantly increased paligenotic (GIF+GSII+) and aberrant paligenotic cells (GIF+) but no difference in non-paligenotic proliferating cells. Data point: mean ± SEM across R40 fields, significance estimated between paired cell types by unpaired, two-tailed t test.

(I) Total BrdU^{+} (proliferating) cells from *Ddit4*$^{+/+}$ (TAM 24 h, n = 3; TAM 48 h, n = 3; TAM 72 h, n = 8) and *Ddit4*$^{-/-}$ (TAM 24 h, n = 3; TAM 48 h, n = 3; TAM 72 h, n = 8) mice per unit were quantified, Data point: mean ± SEM of R 40 glands quantified per mouse, significance estimated by unpaired, two-tailed t test at each time point.

(J) Organoids at day 6 after culturing from *Ddit4*$^{-/-}$ and *Ddit4*$^{+/+}$ mice. Scale bar, 100 mm.

(K) Data as in (J), quantifying organoid diameter from *Ddit4*$^{+/+}$ (n = 3) and *Ddit4*$^{-/-}$ (n = 3) mice. Data point: mean ± SEM of R100 gastroids per mouse with significance estimated by unpaired, two-tailed t test.

(L) Anti-pS6 240/244 showing normal, homeostatic mTORC1 in *Ddit4*$^{+/+}$ and *Ddit4*$^{-/-}$ pancreas, with *Ddit4*$^{-/-}$ acinar cells failing to extinguish mTORC1 at cerulein injury day 1 (mid-stage 1 in pancreas); inset in *Ddit4*$^{+/+}$ highlights a rare pS6+ cell, whereas most cells are positive in the absence of DDIT4. Scale bar, 30 mm; boxed area insert, 15 mm.

(M) H&E staining of *Ddit4*$^{+/+}$ and *Ddit4*$^{-/-}$ pancreas after 5 days of cerulein treatment (CER D5). Most acinar cells preserve their cytoplasm in *Ddit4*$^{-/-}$ mice, consistent with failure of stage 1 turnover of mature cell architecture. Scale bar, 30 mm; boxed area insert, 15 mm.

(N) Anti-BrdU of pancreas 5 days after CER injury. Note increased BrdU+ cells in *Ddit4*$^{-/-}$ mice and failed downscaling of cell architecture. Scale bar, 30 mm; boxed area insert, 15 mm.

(O) BrdU-positive cells from *Ddit4*$^{+/+}$ (n = 6) and *Ddit4*$^{-/-}$ (n = 6) mice as in (N) quantified. Data point: mean ± SEM of R10 random fields quantified per mouse with significance estimated by unpaired, two-tailed Student's t test.

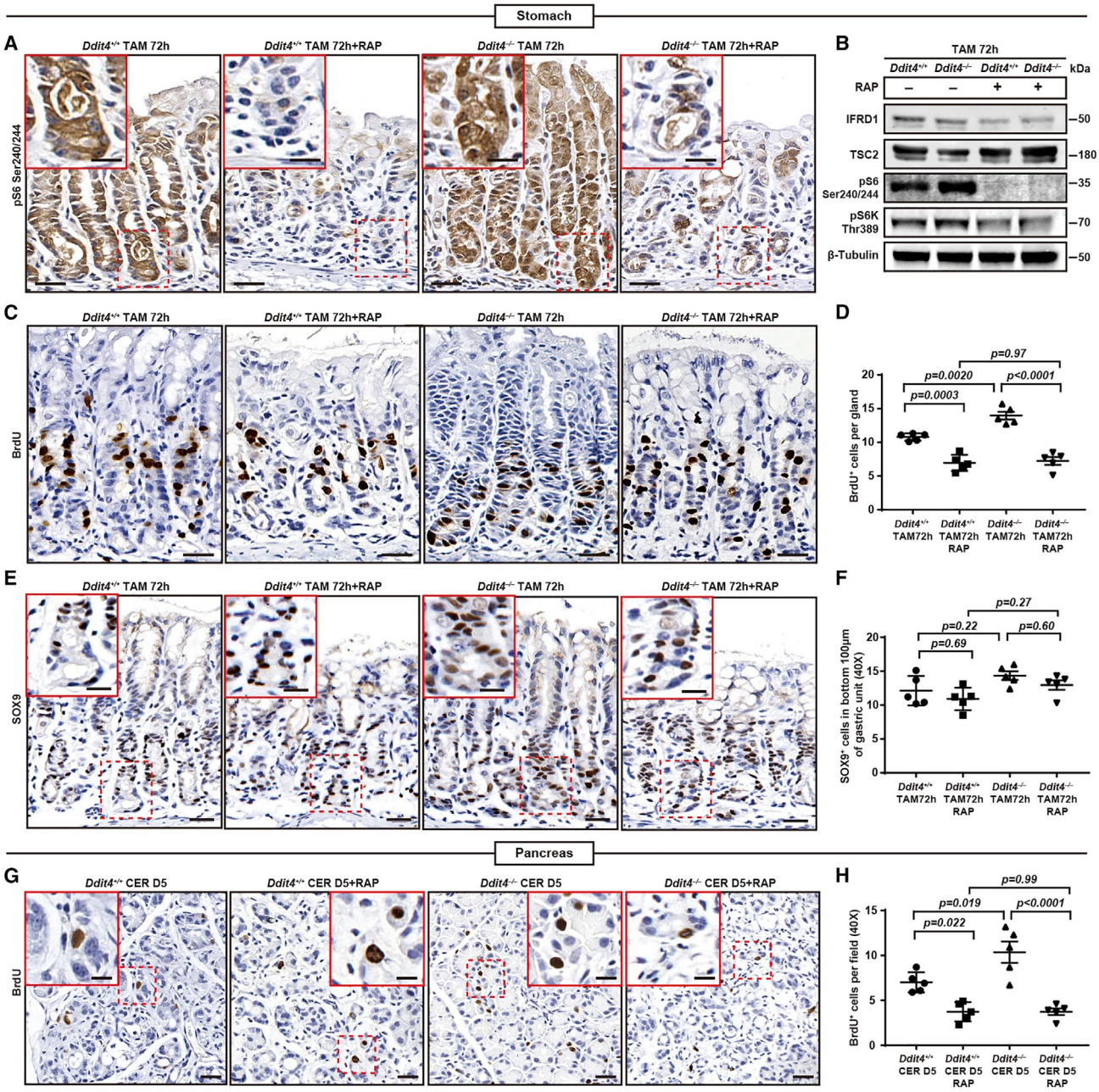


Figure 7. mTORC1 Inhibition Rescues *Ddit4*$^{-/-}$ Stage 1 Phenotype

(A) Rapamycin blocks pS6 (mTORC1) in *Ddit4*$^{-/-}$ and *Ddit4*$^{+/+}$ mice. Scale bar, 30 mm; boxed area highlighting bases of units where paligenosis occurs; inset, 15 mm.

(B) Western blot of whole corpus ± rapamycin. Note IFRD1 is less abundant at 72 h, so exposure was longer than for Figure 2C.

(C) As in (A) but with anti-BrdU. Paligenotic proliferation (BrdU) in *Ddit4*$^{-/-}$ stomachs is corrected by rapamycin, such that both genotypes have the usual loss of proliferation upon mTORC1 reactivation. Scale bar, 30 mm; boxed area insert, 15 mm.

(D) Data from *Ddit4*$^{+/+}$ (n = 5), *Ddit4*$^{-/-}$ (n = 5), *Ddit4*$^{+/+}$+ rapamycin (n = 5), and *Ddit4*$^{-/-}$+ rapamycin (n = 5) mice as for (C) were quantified. Note rapamycin does not significantly affect non-paligenotic proliferation, so only paligenotic proliferation is inhibited. Data point: mean ± SEM of R40 glands quantified per mouse, significance by one-way ANOVA, Dunnett post hoc to *Ddit4*$^{+/+}$ control.

(E) Immunohistochemistry images of SOX9 staining after 5 days cerulein injury (CER D5) ± rapamycin (RAP).

(F) Quantification of immunostaining depicted in (E) from *Ddit4*$^{+/+}$ (n = 5), *Ddit4*$^{-/-}$ (n = 5), *Ddit4*$^{+/+}$+ rapamycin (n = 5), and *Ddit4*$^{-/-}$+ rapamycin (n = 5) mice. Each data point is the mean of R10 random field quantified per mouse. Variance is plotted as standard error of the mean with significance estimated by one-way ANOVA with multiple comparisons to the *Ifrd*$^{+/+}$ control (Dunnett post hoc test).

(G) BrdU in pancreas. Boxes: individual proliferating cells. Proliferating cells after rapamycin are stromal, not paligenotic acinar cells. Scale bar, 30 mm; boxed area inset, 15 mm.

(H) Data from *Ddit4*$^{+/+}$ (n = 5), *Ddit4*$^{-/-}$ (n = 5), *Ddit4*$^{+/+}$+ rapamycin (n = 5), and *Ddit4*$^{-/-}$+ rapamycin (n = 5) mice as in (G) quantified. Data point: mean ± SEM of R 10 random fields quantified per mouse, significance as per (D).

A video abstract is available at https://doi.org/10.1016/j.devcel.2020.07.005#mmc6.

ACKNOWLEDGMENTS

We thank Quark Pharmaceuticals Inc for allowing the opportunity to use the *Ddit4*$^{tm1.1\ (KOMP)Vlcg/J}$ (*Ddit4*$^{-/-}$) mice. We thank Dr. Elena Feinstein (Quark Pharmaceuticals, Inc) and Prof. Rubin Tuder (University of Colorado Denver) for providing the *Ddit4*$^{tm1.1\ (KOMP)Vlcg/J}$ (*Ddit4*$^{-/-}$) mice. We thank Dr. Paul Taghert and Dr. Craig Micchelli for *Drosophila* food and reagents and for *Drosophila*, which were also obtained from the Bloomington Drosophila Stock Center (NIH P40OD018537). We are deeply grateful to Spencer G. Willet (Washington University in St Louis) for critically revising the manuscript and figures. We thank the lab of David Denardo for training and use of HALO software. We acknowledge the AITAC of the Washington University Digestive Disease Center (DDRCC: P30 DK052574) and the NIH Shared Instrumentation Grant S10 RR0227552 (for NanoZoomer slide scanning). M.A.L. was funded by T32-DK077653 (NIH, NIDDK) by the DeNardo Education & Research Foundation Grant and a supplement to R01-DK094989 (NIH NIDDK); M.A.-T. by T32-DK077653 (NIH, NIDDK) and R25-GM103757 (NIGMS, NIH); J.W.B. by T32-DK007130 (NIH NIDDK); C.J.C. by T32-CA009547(NIH NCI); J.B. by T32-GM007067 (NIGMS, NIH) and the Philip and Sima Needleman Student Fellowship in Regenerative Medicine; N.O.D. by R01s HL38180 (NIH NHBLI), DK112378, and DK56260 (NIH NIDDK); D.C.R. by R01-DK106382 (NIH NIDDK); Z.N.-W. by National Key R&D Program of China (MOST-2017YFC0908300), National Natural Science Foundation of China (81961128026 and U1908207), and Major Scientific and Technological Special Project of Liaoning Province of China (2019020176-JH1/103); and J.C.M. by DK094989, DK105129, and DK110406, by the Alvin J. Siteman Cancer Center–Barnes Jewish Hospital Foundation Cancer Frontier Fund, NIH National Cancer Institute P30 CA091842 and R01 CA246208, and the Barnard Trust.

AUTHOR CONTRIBUTIONS

Z.-F.M. designed and performed experiments, analyzed and interpreted data, performed statistical analyses, and drafted and revised the manuscript; M.A.L. designed and performed experiments and bioinformatic analyses, analyzed and interpreted data, and performed statistical analyses; C.J.C. designed and performed experiments, analyzed and interpreted data, and performed statistical analyses; M.A.-T. performed experiments, analyzed and interpreted data, performed statistical analyses, and revised the manuscript; D.P. designed and performed experiments, analyzed and interpreted data, and performed statistical analyses; J.W.B. performed computational work on evolutionary conservation and structure-function analysis; J.-X.S. performed experiments, analyzed and interpreted data, and performed statistical analyses; J.R.B., S.K., and J.L. performed experiments and analyzed data; M.M. designed and performed experiments and analyzed data; I.V. and L.A.H. provided critical reagent and revised manuscript; N.O.D. provided funding and critical reagent; V.C. provided funding, a critical reagent, and revised manuscript; D.C.R. provided funding, interpreted data, and revised the manuscript; Z.N.-W. provided funding and human samples for the study and drafted and revised the manuscript; J.C.M. designed the experiments, provided funding for the study, performed bioinformatic analyses, generated data, and drafted and revised the manuscript.

DECLARATION OF INTERESTS

The authors declare no competing interests.

Received: May 6, 2020
Revised: June 4, 2020
Accepted: July 11, 2020
Published: August 7, 2020

REFERENCES

Adami, J.G. (1900). On growth and overgrowth. In festschrift" in Honor of Abraham Jacobi, MD, LLD: To Commemorate the Seventieth Anniversary of His Birth, May Sixth, 1900 (Knickerbocker Press), pp. 422–432.

Akeno, N., Miller, A.L., Ma, X., and Wikenheiser-Brokamp, K.A. (2015). p53 suppresses carcinoma progression by inhibiting mTOR pathway activation. Oncogene *34*, 589–599.

Barker, N., Huch, M., Kujala, P., van de Wetering, M., Snippert, H.J., van Es, J.H., Sato, T., Stange, D.E., Begthel, H., van den Born, M., et al. (2010). Lgr5+ve stem cells drive self-renewal in the stomach and build long-lived gastric units in vitro. Cell Stem Cell *6*, 25–36.

Basu, S. (2014). A complex interplay between PGC-1 co-activators and mTORC1 regulates hematopoietic recovery following 5-fluorouracil treatment. Stem Cell Res. *12*, 178–193.

Beyaz, S., Mana, M.D., Roper, J., Kedrin, D., Saadatpour, A., Hong, S.J., Bauer-Rowe, K.E., Xifaras, M.E., Akkad, A., Arias, E., et al. (2016). High-fat diet enhances stemness and tumorigenicity of intestinal progenitors. Nature *531*, 53–58.

Blanc, V., Sessa, K.J., Kennedy, S., Luo, J., and Davidson, N.O. (2010). Apobec-1 complementation factor modulates liver regeneration by post-transcriptional regulation of interleukin-6 mRNA stability. J. Biol. Chem. *285*, 19184–19192.

Bou Sleiman, M.S., Osman, D., Massouras, A., Hoffmann, A.A., Lemaitre, B., and Deplancke, B. (2015). Genetic, molecular and physiological basis of variation in Drosophila gut immunocompetence. Nat. Commun. *6*, 7829.

Brown, A., Baird, M.R., Yip, M.C., Murray, J., and Shao, S. (2018). Structures of translationally inactive mammalian ribosomes. eLife *7*, e40486.

Brugarolas, J., Lei, K., Hurley, R.L., Manning, B.D., Reiling, J.H., Hafen, E., Witters, L.A., Ellisen, L.W., and Kaelin, W.G., Jr. (2004). Regulation of mTOR function in response to hypoxia by REDD1 and the TSC1/TSC2 tumor suppressor complex. Genes Dev *18*, 2893–904.

Burclaff, J., and Mills, J.C. (2018a). Plasticity of differentiated cells in wound repair and tumorigenesis, part I: stomach and pancreas. Dis. Model. Mech. *11*, dmm033373.

Burclaff, J., and Mills, J.C. (2018b). Plasticity of differentiated cells in wound repair and tumorigenesis, part II: skin and intestine. Dis. Model. Mech. *11*.

Burclaff, J., Osaki, L.H., Liu, D., Goldenring, J.R., and Mills, J.C. (2017). Targeted apoptosis of parietal cells is insufficient to induce metaplasia in stomach. Gastroenterology *152*, 762–766.e7.

Burclaff, J., Willet, S.G., Sáenz, J.B., and Mills, J.C. (2020). Proliferation and differentiation of gastric mucous neck and chief cells during homeostasis and injury-induced metaplasia. Gastroenterology *158*, 598–609.e5.

Cho, Y., and Cavalli, V. (2012). HDAC5 is a novel injury-regulated tubulin deacetylase controlling axon regeneration. EMBO J. *31*, 3063–3078.

Conway, J.R., Lex, A., and Gehlenborg, N. (2017). UpSetR: an R package for the visualization of intersecting sets and their properties. Bioinformatics *33*, 2938–2940.

Deng, W., Cha, J., Yuan, J., Haraguchi, H., Bartos, A., Leishman, E., Viollet, B., Bradshaw, H.B., Hirota, Y., and Dey, S.K. (2016). p53 coordinates decidual sestrin 2/AMPK/mTORC1 signaling to govern parturition timing. J. Clin. Invest. *126*, 2941–2954.

DeYoung, M.P., Horak, P., Sofer, A., Sgroi, D., and Ellisen, L.W. (2008). Hypoxia regulates TSC1/2-mTOR signaling and tumor suppression through REDD1-mediated 14-3-3 shuttling. Genes Dev. *22*, 239–251.

Drozdetskiy, A., Cole, C., Procter, J., and Barton, G.J. (2015). JPred4: a protein secondary structure prediction server. Nucleic Acids Res. *43*, W389–W394.

Fahling, M., Mathia, S., Paliege, A., Koesters, R., Mrowka, R., Peters, H., Persson, P.B., Neumayer, H.H., Bachmann, S., and Rosenberger, C. (2013). Tubular von Hippel-Lindau knockout protects against rhabdomyolysis-induced AKI. J. Am. Soc. Nephrol. *24*, 1806–1819.

Faller, W.J., Jackson, T.J., Knight, J.R., Ridgway, R.A., Jamieson, T., Karim, S.A., Jones, C., Radulescu, S., Huels, D.J., Myant, K.B., et al. (2015).

mTORC1-mediated translational elongation limits intestinal tumour initiation and growth. Nature *517*, 497–500.

Garcia, A.M., Wakeman, D., Lu, J., Rowley, C., Geisman, T., Butler, C., Bala, S., Swietlicki, E.A., Warner, B.W., Levin, M.S., and Rubin, D.C. (2014). Tis7 deletion reduces survival and induces intestinal anastomotic inflammation and obstruction in high-fat diet-fed mice with short bowel syndrome. Am. J. Physiol. Gastrointest. Liver Physiol. *307*, G642–G654.

Gerber, T., Murawala, P., Knapp, D., Masselink, W., Schuez, M., Hermann, S., Gac-Santel, M., Nowoshilow, S., Kageyama, J., Khattak, S., et al. (2018). Single-cell analysis uncovers convergence of cell identities during axolotl limb regeneration. Science *362*, eaaq0681.

Goldenring, J.R. (2018). Pyloric metaplasia, pseudopyloric metaplasia, ulcer-associated cell lineage and spasmolytic polypeptide-expressing metaplasia: reparative lineages in the gastrointestinal mucosa. J Pathol *245*, 132–137.

Gu, Z., Eils, R., and Schlesner, M. (2016). Complex heatmaps reveal patterns and correlations in multidimensional genomic data. Bioinformatics *32*, 2847–2849.

Hasty, P., Sharp, Z.D., Curiel, T.J., and Campisi, J. (2013). mTORC1 and p53: clash of the gods? Cell Cycle *12*, 20–25.

Huh, W.J., Khurana, S.S., Geahlen, J.H., Kohli, K., Waller, R.A., and Mills, J.C. (2012). Tamoxifen induces rapid, reversible atrophy, and metaplasia in mouse stomach. Gastroenterology *142*, 21–24.e7.

Hutchinson, J.A., Shanware, N.P., Chang, H., and Tibbetts, R.S. (2011). Regulation of ribosomal protein S6 phosphorylation by casein kinase 1 and protein phosphatase 1. J. Biol. Chem. *286*, 8688–8696.

Janic, A., Valente, L.J., Wakefield, M.J., Di Stefano, L., Milla, L., Wilcox, S., Yang, H., Tai, L., Vandenberg, C.J., Kueh, A.J., et al. (2018). DNA repair processes are critical mediators of p53-dependent tumor suppression. Nat. Med. *24*, 947–953.

Jones, J.C., Brindley, C.D., Elder, N.H., Myers, M.G., Jr., Rajala, M.W., Dekaney, C.M., McNamee, E.N., Frey, M.R., Shroyer, N.F., and Dempsey, P.J. (2019). Cellular plasticity of Defa4Cre-expressing Paneth cells in response to Notch activation and intestinal injury. Cell. Mol. Gastroenterol. Hepatol. *7*, 533–554.

Keeley, T.M., Horita, N., and Samuelson, L.C. (2019). Tamoxifen-induced gastric injury: effects of dose and method of administration. Cell. Mol. Gastroenterol. Hepatol. *8*, 365–367.

Kimball, S.R., Do, A.N., Kutzler, L., Cavener, D.R., and Jefferson, L.S. (2008). Rapid turnover of the mTOR complex 1 (mTORC1) repressor REDD1 and activation of mTORC1 signaling following inhibition of protein synthesis. J. Biol. Chem. *283*, 3465–3475.

Kowalik, A.S., Johnson, C.L., Chadi, S.A., Weston, J.Y., Fazio, E.N., and Pin, C.L. (2007). Mice lacking the transcription factor Mist1 exhibit an altered stress response and increased sensitivity to caerulein-induced pancreatitis. Am. J. Physiol. Gastrointest. Liver Physiol. *292*, G1123–G1132.

Lex, A., Gehlenborg, N., Strobelt, H., Vuillemot, R., and Pfister, H. (2014). UpSet: visualization of intersecting sets. IEEE Trans. Vis. Comput. Graph. *20*, 1983–1992.

Liberzon, A., Birger, C., Thorvaldsdóttir, H., Ghandi, M., Mesirov, J.P., and Tamayo, P. (2015). The molecular signatures database (MSigDB) hallmark gene set collection. Cell Syst. *1*, 417–425.

Liu, J., Zhang, C., Hu, W., and Feng, Z. (2019a). Tumor suppressor p53 and metabolism. J. Mol. Cell Biol. *11*, 284–292.

Liu, Y., Tavana, O., and Gu, W. (2019b). p53 modifications: exquisite decorations of the powerful guardian. J. Mol. Cell Biol. *11*, 564–577.

Lock, A., Rutherford, K., Harris, M.A., Hayles, J., Oliver, S.G., Bähler, J., and Wood, V. (2019). PomBase 2018: user-driven reimplementation of the fission yeast database provides rapid and intuitive access to diverse, interconnected information. Nucleic Acids Res. *47*, D821–D827.

Meyer, A.R., Engevik, A.C., Willet, S.G., Williams, J.A., Zou, Y., Massion, P.P., Mills, J.C., Choi, E., and Goldenring, J.R. (2019). Cystine/glutamate antiporter (xCT) is required for chief cell plasticity after gastric injury. Cell Mol Gastroenterol Hepatol *8*, 379–405.

Miao, Z.F., Adkins-Threats, M., Burclaff, J.R., Osaki, L.H., Sun, J.X., Kefalov, Y., He, Z., Wang, Z.N., and Mills, J.C. (2020). A metformin-responsive metabolic pathway controls distinct steps in gastric progenitor fate decisions and maturation. Cell Stem Cell *26*, 910–925.e6.

Micheli, L., Leonardi, L., Conti, F., Maresca, G., Colazingari, S., Mattei, E., Lira, S.A., Farioli-Vecchioli, S., Caruso, M., and Tirone, F. (2011). PC4/Tis7/IFRD1 stimulates skeletal muscle regeneration and is involved in myoblast differentiation as a regulator of MyoD and NF-kappaB. J. Biol. Chem. *286*, 5691–5707.

Mihaylova, M.M., Cheng, C.W., Cao, A.Q., Tripathi, S., Mana, M.D., Bauer-Rowe, K.E., Abu-Remaileh, M., Clavain, L., Erdemir, A., Lewis, C.A., et al. (2018). Fasting activates fatty acid oxidation to enhance intestinal stem cell function during homeostasis and aging. Cell Stem Cell *22*, 769–778.e4.

Mills, J.C., and Sansom, O.J. (2015). Reserve stem cells: differentiated cells reprogram to fuel repair, metaplasia, and neoplasia in the adult gastrointestinal tract. Sci. Signal. *8*, re8.

Mills, J.C., Stanger, B.Z., and Sander, M. (2019). Nomenclature for cellular plasticity: are the terms as plastic as the cells themselves? EMBO J. *38*, e103148.

Moore, B.D., Jin, R.U., Osaki, L., Romero-Gallo, J., Noto, J., Peek, R.M., Jr., and Mills, J.C. (2015). Identification of alanyl aminopeptidase (CD13) as a surface marker for isolation of mature gastric zymogenic chief cells. Am. J. Physiol. Gastrointest. Liver Physiol. *309*, G955–G964.

Nagy, A., Gertsenstein, M., Vintersten, K., and Behringer, R. (2007). Staining frozen mouse embryo sections for {beta}-galactosidase (lacZ) activity. CSH Protoc. *2007*, pdb.prot4726.

Nam, K.T., Lee, H.J., Sousa, J.F., Weis, V.G., O'Neal, R.L., Finke, P.E., Romero-Gallo, J., Shi, G., Mills, J.C., Peek, R.M., Jr., et al. (2010). Mature chief cells are cryptic progenitors for metaplasia in the stomach. Gastroenterology *139*, 2028–2037.e9.

Nichols, J.M., Antolović, V., Reich, J.D., Brameyer, S., Paschke, P., and Chubb, J.R. (2020). Cell and molecular transitions during efficient dedifferentiation. eLife *9*, e55435.

Osaki, L.H., Bockerstett, K.A., Wong, C.F., Ford, E.L., Madison, B.B., DiPaolo, R.J., and Mills, J.C. (2019). Interferon-gamma directly induces gastric epithelial cell death and is required for progression to metaplasia. J. Pathol. *247*, 513–523.

Otu, H.H., Naxerova, K., Ho, K., Can, H., Nesbitt, N., Libermann, T.A., and Karp, S.J. (2007). Restoration of liver mass after injury requires proliferative and not embryonic transcriptional patterns. J. Biol. Chem. *282*, 11197–11204.

Radyk, M.D., Burclaff, J., Willet, S.G., and Mills, J.C. (2018). Metaplastic cells in the stomach arise, independently of stem cells, via dedifferentiation or transdifferentiation of chief cells. Gastroenterology *154*, 839–843.e2.

Ramsey, V.G., Doherty, J.M., Chen, C.C., Stappenbeck, T.S., Konieczny, S.F., and Mills, J.C. (2007). The maturation of mucus-secreting gastric epithelial progenitors into digestive-enzyme secreting zymogenic cells requires Mist1. Development *134*, 211–222.

Rudolf, A., Buttgereit, D., Rexer, K.H., and Renkawitz-Pohl, R. (2012). The syncytial visceral and somatic musculature develops independently of b3-tubulin during Drosophila embryogenesis, while maternally supplied b1-tubulin is stable until the early steps of myoblast fusion. Eur. J. Cell Biol. *91*, 192–203.

Sáenz, J.B., and Mills, J.C. (2018). Acid and the basis for cellular plasticity and reprogramming in gastric repair and cancer. Nat. Rev. Gastroenterol. Hepatol. *15*, 257–273.

Shimuzu, T., Sohn, Y., Choi, E., Petersen, C.P., Prasad, N., and Goldenring, J.R. (2020). Decrease in mir-148a expression during initiation of chief cell transdifferentiation. Cell Mol Gastroenterol Hepatol *9*, 61–78.

Sievers, F., and Higgins, D.G. (2018). Clustal omega for making accurate alignments of many protein sequences. Protein Sci *27*, 135–145.

Stange, D.E., Koo, B.K., Huch, M., Sibbel, G., Basak, O., Lyubimova, A., Kujala, P., Bartfeld, S., Koster, J., Geahlen, J.H., et al. (2013). Differentiated Troy+ chief cells act as reserve stem cells to generate all lineages of the stomach epithelium. Cell *155*, 357–368.

Stierli, S., Napoli, I., White, I.J., Cattin, A.L., Monteza Cabrejos, A., Garcia Calavia, N., Malong, L., Ribeiro, S., Nihouarn, J., Williams, R., et al. (2018).

The regulation of the homeostasis and regeneration of peripheral nerve is distinct from the CNS and independent of a stem cell population. Development *145*.

Subramanian, A., Tamayo, P., Mootha, V.K., Mukherjee, S., Ebert, B.L., Gillette, M.A., Paulovich, A., Pomeroy, S.L., Golub, T.R., Lander, E.S., and Mesirov, J.P. (2005). Gene set enrichment analysis: a knowledge-based approach for interpreting genome-wide expression profiles. Proc. Natl. Acad. Sci. USA *102*, 15545–15550.

Tang, Y., Zhao, W., Chen, Y., Zhao, Y., and Gu, W. (2008). Acetylation is indispensable for p53 activation. Cell *133*, 612–626.

Tummers, B., Goedemans, R., Pelascini, L.P., Jordanova, E.S., van Esch, E.M., Meyers, C., Melief, C.J., Boer, J.M., and van der Burg, S.H. (2015). The interferon-related developmental regulator 1 is used by human papillomavirus to suppress NFkappa B activation. Nat. Commun. *6*, 6537.

Vadivelu, S.K., Kurzbauer, R., Dieplinger, B., Zweyer, M., Schafer, R., Wernig, A., Vietor, I., and Huber, L.A. (2004). Muscle regeneration and myogenic differentiation defects in mice lacking TIS7. Mol. Cell. Biol. *24*, 3514–3525.

Vercellino, M., Merola, A., Piacentino, C., Votta, B., Capello, E., Mancardi, G.L., Mutani, R., Giordana, M.T., and Cavalla, P. (2007). Altered glutamate reuptake in relapsing-remitting and secondary progressive multiple sclerosis cortex: correlation with microglia infiltration, demyelination, and neuronal and synaptic damage. J. Neuropathol. Exp. Neurol. *66*, 732–739.

Vodovar, N., Vinals, M., Liehl, P., Basset, A., Degrouard, J., Spellman, P., Boccard, F., and Lemaitre, B. (2005). Drosophila host defense after oral infection by an entomopathogenic Pseudomonas species. Proc. Natl. Acad. Sci. USA *102*, 11414–11419.

Wahl, G.M., and Carr, A.M. (2001). The evolution of diverse biological responses to DNA damage: insights from yeast and p53. Nat. Cell Biol. *3*, E277–E286.

Wang, D., Kon, N., Lasso, G., Jiang, L., Leng, W., Zhu, W.G., Qin, J., Honig, B., and Gu, W. (2016). Acetylation-regulated interaction between p53 and SET reveals a widespread regulatory mode. Nature *538*, 118–122.

Weis, V.G., Petersen, C.P., Weis, J.A., Meyer, A.R., Choi, E., Mills, J.C., and Goldenring, J.R. (2017). Maturity and age influence chief cell ability to transdifferentiate into metaplasia. Am. J. Physiol. Gastrointest. Liver Physiol. *312*, G67–G76.

Willet, S.G., Lewis, M.A., Miao, Z.F., Liu, D., Radyk, M.D., Cunningham, R.L., Burclaff, J., Sibbel, G., Lo, H.G., Blanc, V., et al. (2018). Regenerative proliferation of differentiated cells by mTORC1-dependent paligenosis. EMBO J. *37*, e98311.

Wylie, A., Lu, W.J., D'Brot, A., Buszczak, M., and Abrams, J.M. (2014). p53 activity is selectively licensed in the Drosophila stem cell compartment. eLife *3*, e01530.

Yu, S., Tong, K., Zhao, Y., Balasubramanian, I., Yap, G.S., Ferraris, R.P., Bonder, E.M., Verzi, M.P., and Gao, N. (2018). Paneth cell multipotency Induced by Notch Activation following Injury. Cell Stem Cell *23*, 46–59.e5.

Yun, T., Yu, K., Yang, S., Cui, Y., Wang, Z., Ren, H., Chen, S., Li, L., Liu, X., Fang, M., and Jiang, X. (2016). Acetylation of p53 protein at lysine 120 up-regulates Apaf-1 protein and sensitizes the mitochondrial apoptotic pathway. J. Biol. Chem. *291*, 7386–7395.

Zhao, C., Datta, S., Mandal, P., Xu, S., and Hamilton, T. (2010). Stress-sensitive regulation of IFRD1 mRNA decay is mediated by an upstream open reading frame. J. Biol. Chem. *285*, 8552–8562.

STAR+METHODS

KEY RESOURCES TABLE

REAGENT or RESOURCE	SOURCE	IDENTIFIER
Antibodies		
Rabbit anti-Ddit4	Protein Tech	Cat#10638-1-AP; RRID: AB_2245711
Goat anti-Ddit4	Santa Cruz	Cat# sc-46034; RRID: AB_2292589
Rabbit anti-Ki67	Abcam	Cat# ab15580; RRID: AB_443209
Rabbit anti-pS6 240/244	Cell Signaling	Cat#2215; RRID: AB_331682
Rabbit anti-pS6k 389	Cell Signaling	Cat#9205; RRID: AB_330944
Rabbit anti-TSC2	Cell Signaling	Cat#4308; RRID: AB_10547134
Mouse anti-b-tubulin	Abcam	Cat# ab21057; RRID: AB_727043
Mouse anti-BrdU	DHSB (G3G4)	Cat# G3G4; RRID:AB_2618097
Rabbit anti-human gastric intrinsic factor	Gift of Dr. David Alpers, Washington University	N/A
Sheep anti-Pepsinogen	Abcam	Cat# ab31464; RRID: AB_2160912
Rabbit anti-Sox9	Millipore	Cat# AB5535; RRID: AB_2239761
Rabbit anti-LC3B	Cell Signaling	Cat#2775; RRID: AB_915950
Rabbit anti-Amylase	Sigma-Aldrich	Cat# A8273; RRID: AB_258380
Rat anti-Lamp1	DHSB	Cat#1D4B; RRID: AB_528127
Rabbit anti-pHH3	Cell Signaling	Cat#9701; RRID: AB_331535
Mouse anti-P53	Cell Signaling	Cat#2524; RRID: AB_331743
Rabbit anti-P53	Proteintech	Cat#10442-1-AP; RRID: AB_2206609
Rabbit anti-Acetyl p53 379	Cell Signaling	Cat#2570; RRID: AB_823591
Rabbit anti-Acetyl p53 382	Cell Signaling	Cat#2525; RRID: AB_330083
Mouse anti-P21	Santa Cruz	Cat# sc-6246; RRID: AB_628073
Mouse anti-cyclin D1	Santa Cruz	Cat# sc-8396; RRID: AB_627344
Rabbit anti-IFRD1	Novus Biologicals	Cat# NBP1-87327; RRID: AB_11052376
Ifrd1 Probe-RNAscope 2.5 HD-RED	ACD	Cat#569021
Bacterial and Virus Strains		
XL-10 Gold	Agilent	Cat #200317

(*Continued on next page*)

Continued

REAGENT or RESOURCE	SOURCE	IDENTIFIER
Chemicals, Peptides, and Recombinant Proteins		
Tamoxifen	Toronto Research Chemicals Inc	Cat#T00600
5-Bromo-2-deoxyuridine (BrdU)	Sigma-Aldrich	Cat#B5002
EDTA	Thermo-fisher	Cat#AM2691
DTT	Gold Biotechnology	Cat#DTT10
BSA	Sigma-Aldrich	Cat#A7906
Matrigel	Corning	Cat#354234
Triton X-100	Lab Chem	Cat#LC262801
Advanced DMEM/F12	Invitrogen	Cat#12634-010
HEPES	Gibco	Cat#15630-080
Glutamax	Gibco	Cat#35050-061
N- Acetylcysteine	Sigma-Aldrich	Cat#A9165
EGF	Peprotech	Cat#315-09
FGF10	Peprotech	Cat#100-26
Gastrin	Sigma-Aldrich	Cat#G9020
ROCK Inhibitor (y-27632)	Sigma-Aldrich	Cat#Y0503
N-2	Gibco	Cat#17502-048
B27	Gibco	Cat#17504-044
Primocin	Invivogen	Cat#ant-pm-1,2
trypLE Express	Gibco	Cat#12605-028
DPBS	Gibco	Cat#14190-136
Isothesia	Henry Schein Animal Health	Cat#NDC11695-6776-2
Tween20	Sigma-Aldrich	Cat#P5927
ProLong Gold antifade mountant with DAPI	Molecular Probes	Cat#P36930
Permount Mounting Medium	Fisher Chemical	Cat#SP150
DNase I	Invitrogen	Cat# 18047019
SuperScript III	Invitrogen	Cat# 11752050
PowerUp SYBR Green Master Mix	ThermoFisher	Cat# A25742
RNA Protect Reagent	Qiagen	Cat# 76526
T-PER Tissue Protein Extraction Reagent	ThermoFisher	Cat#78510
DC protein assay	BioRad	Cat# 5000111
Pierce™ BCA Protein Assay Kit	ThermoFisher	Cat# 23225
SuperSignal™ West Pico PLUS Chemiluminescent Substrate	ThermoFisher	Cat#34580
5-fluoro-2'-deoxyuridine	Sigma-Aldrich	Cat# F0503
Potassium hexacyanoferrate(III)	Sigma-Aldrich	Cat# 244023
Potassium hexacyanoferrate(II) trihydrate	Sigma-Aldrich	Cat# 455989
N,N-Dimethylformamide	Sigma-Aldrich	Cat# 227056
5-Bromo-4-chloro-3-indolyl b-D-galactopyranoside	Sigma-Aldrich	Cat# B4252
DMEM	Gibco	Cat# 11965084
RIPA Lysis and Extraction Buffer	Thermo Scientific	Cat# 89900
Tunicamycin	Sigma-Aldrich	Cat# T7765
Cerulein	Bachem	Cat# H-3220
Rapamycin	LC Laboratories	Cat# R-5000
Halt™ Protease and Phosphatase Inhibitor Single-Use Cocktail, EDTA-Free (100X)	Thermo Scientific	Cat# 78443

(*Continued on next page*)

Continued

REAGENT or RESOURCE	SOURCE	IDENTIFIER
Critical Commercial Assays		
RNeasy Micro Kit	Qiagen	Cat#74004
Vectastain Elite ABC HRP Kit	Vector Laboratories	Cat#PK6100
DAB Substrate Kit	Thermo Scientific	Cat#36000
RNeasy Mini Kit	Qiagen	Cat#74104
GeneChip™ Mouse Gene 2.0 ST Array	Affymetrix	Cat#902119
Deposited Data		
Microarray data files (High dose tamoxifen induced SPEM)	NBCI Gene Expression	GSE71580
Microarray data files (Cerulein induced pancreatitis)	NBCI Gene Expression	GSE3644
Microarray data files (Acute kidney injury)	NBCI Gene Expression	GSE44925
Microarray data files (Liver regeneration)	NBCI Gene Expression	GSE6998
Microarray data files (*Ifrd1*$^{+/+}$ and *Ifrd1*$^{-/-}$ pancreas ± Cerulein at D5)	NBCI Gene Expression	GSE121925
Experimental Models: Cell Lines		
LS174T	ATCC	Cat# CL-188; RRID:CVCL_1384
Experimental Models: Organisms/Strains		
Mouse: *Ddit4*$^{tm1.1\ (KOMP)Vlcg/J}$	Generated by Quark Pharmaceuticals Inc, (Brugarolas et al., 2004)	N/A
Mouse: *Trp53*^{tm1Tyj}/J	Jackson laboratories	RRID: IMSR_JAX:002101
Mouse: *Ifrd1*^{tm1Lah}	Generated by Dr. Lukas Huber Medical University of Innsbruck	RRID: MGI:3043558
Mouse: Wild type C57BL/6	Jackson laboratories	RRID: IMSR_JAX:000664
Mouse: *Atp4b-cre: B6.FVB-Tg(Atp4b-cre) 1Jig/JcmiJ*	Jackson Laboratories	RRID: IMSR_ JAX: 030656
Mouse: Gt(ROSA)26Sor$^{tm1\ (HBEGF)Awai}$	Jackson Laboratories	RRID: IMSR_JAX:007900
D. melanogaster, Canton -S	Bloomington Drosophila Stock Center	BDSC:64349; flybaseID: FBsn0000274
D. melanogaster, DIFRD1#1 yw;CG31694[EY11632]	Bloomington Drosophila Stock Center	BDSC:20811; flybaseID: FBst0020811
D. melanogaster, DIFRD1#2; yw;CG31694 [CA07748]	Bloomington Drosophila Stock Center	BDSC:51520; flybaseID: FBst0051520
D. melanogaster, IFRD1-GFP yw;CG31694 [CA07748].	Bloomington Drosophila Stock Center	BDSC:51520; flybaseID: FBst0051520
D. melanogaster, w1118	Bloomington Drosophila Stock Center	BDSC: 3605; FlybaseID: FBal0018186
Oligonucleotides		
Primers for qPCR, see Table S4	This paper	N/A
Primers for mouse genotyping, see Table S2	This paper	N/A
Recombinant DNA		
IFRD1 shRNA (TRCN0000151595)	This paper	N/A
Software and Algorithms		
QuantStudio3 Design and Analysis Software	ThermoFisher	https://www.thermofisher.com/us/en/home/technical-resources/software-downloads/ab-quantstudio-3-and-5-real-time-pcr-system.html
Photoshop CS6	Adobe	RRID:SCR_014199; https://www.adobe.com/downloads.html

(*Continued on next page*)

Continued

REAGENT or RESOURCE	SOURCE	IDENTIFIER
Partek Genomic Suite 6.6	Partek Incorporated	RRID: SCR_011860; http://www.partek.com/partek-genomics-suite/
GSEA-P Software	Broad Institute	RRID:SCR_003199; http://software.broadinstitute.org/gsea/index.jsp
NDP.View2	Hamamatsu Photonics	Cat#U12388-01
Prism 3	GraphPad	RRID:SCR_002798; https://www.graphpad.com/scientific-software/prism/
Cytation 3 cell imaging multi-mode reader	BioTek	Cat# BTCYT3MV
Image J	NIH	RRID: SCR_003070; https://imagej.nih.gov/ij/
AxioVision 4.9.1	Zeiss	https://www.zeiss.com/microscopy/us/downloads/axiovision-downloads.html

RESOURCE AVAILABILITY

Lead Contact

Further information and requests for resources and reagents should directed to, and will be fulfilled by the Lead Contact, Jason Mills (jmills@wustl.edu).

Materials Availability

This study did not generate new unique reagents.

Data and Code Availability

The accession number for the microarray data files reported in this paper is NCBI GEO: GSE71580, GSE3644, GSE44925, GSE6998 and GSE121925

https://www.ncbi.nlm.nih.gov/geo/query/acc.cgi?acc=GSE71580
https://www.ncbi.nlm.nih.gov/geo/query/acc.cgi?acc=GSE3644
https://www.ncbi.nlm.nih.gov/geo/query/acc.cgi?acc=GSE44925
https://www.ncbi.nlm.nih.gov/geo/query/acc.cgi?acc=GSE6998
https://www.ncbi.nlm.nih.gov/geo/query/acc.cgi?acc=GSE121925.

EXPERIMENTAL MODEL AND SUBJECT DETAILS

Human Cancer Cell

LS174T Cells (ATCC) grown under standard conditions (DMEM, 10%FBS, and Primocin at 37°C and 5%CO2) were cotransfected with a transposon expressing shRNA against IFRD1 (TRCN0000151595) under a U6 promoter as well as a plasmid expressing Hyperactive piggyBac transposase to stably incorporate the shRNA vector into the genome. After selection with puromycin, passaged cells were treated with tunicamycin (4 ug/mL; Sigma T7765) for 15-18 hours, lysed with RIPA buffer, and analyzed via western blot. Effect of IFRD1 knockdown was compared to LS174T cells stably transfected with an empty vector and treated in an identical manner in parallel.

Mice

All experiments using vertebrate animals followed protocols approved by the Washington University School of Medicine or China Medical University Animal Studies Committees. WT C57BL/6 and *Trp53*$^{tm1Tyj/J}$ (*Trp53*$^{-/-}$) mice were purchased from Jackson Laboratories (Bar Harbor, ME). *Ifrd1*^{tm1Lah} (*Ifrd1*$^{-/-}$) mice were previously described(Vadivelu et al., 2004). *Ddit4*$^{tm1.1\ (KOMP)Vlcg/J}$ (*Ddit4*$^{-/-}$) mice were the property of Quark Pharmaceuticals Inc and were generated by Lexicon Inc by Quark's request. *Atp4b-Cre;LSL-DTR* mice were generated as described previously(Burclaff et al., 2017). All strains of mice in these studies were maintained in a specified pathogen-free barrier facility under a 12-hour light cycle with free access to standard chow pellets and water. Each mouse used was genotyped by PCR amplification. For full list of genotyping primers, see Table S2.

Experimental and control groups each contained at least three mice, with representatives from both genders. There were no differences in results observed between male and female mice. All mice used were between 8-12 weeks old. When possible, mice of equivalent age and gender (littermate controls) were used for experimental and control groups otherwise, mice were randomly chosen and sorted into experimental groups.

Drosophila

The mammalian *ifrd1* orthologue is CG31694 (*difrd1* here). *Drosophila* stocks were obtained from the Bloomington Drosophila stock center. yw; P(EPgy2)EY11632 (BL#20811; designated as difrd1 #1), yw; P(PTT-GA)CA07748 (BL#52520; designated as difrd1 #2 or ifrd1-GFP). w1118 or Canton-S are used as wild types(Rudolf et al., 2012). All *Drosophila* were cultured on yeast-molasses based on food at the room temperature.

Gastroid

Gastric organoids (gastroids) collected from the gastric glands in the corpus of the stomach were isolated from Wildtype, *Ifrd1*$^{-/-}$, *Trp53*$^{-/-}$ *and Ddit4*$^{-/-}$ mice. After dissecting the stomach, flush stomachs with PBS and cut the forestomach and the antrum off. Wash the corpus with cold chelating solution, remove the muscle layer and cut the mucosa into small pieces. Immerse the small pieces in chelating solution + 10 mM EDTA for 3hours with gently shaking as described previously(Barker et al., 2010; Osaki et al., 2019). Approximately 100 gastric glands were mixed with 50 ㎖ of Matrigel (Corning), plated in 24-well plates and cultured in Advanced DMEM/F12 medium (Invitrogen), 50% Wnt3a conditioned medium, 10% R-Spondin1 and Noggin conditioned medium(Osaki et al., 2019) supplemented with 10mM HEPES, 1X N-2, 1X B27, 1X glutamax (Invitrogen), 1.25 mM N-Acetylcysteine (Sigma-Aldrich), 50 ng/mL EGF, 100 ng/mL FGF10 (Peprotech), 10 nM gastrin (Sigma-Aldrich) and 0.1% Primocin (Invivogen). 10 ㎜ ROCK inhibitor (Y-27632, Sigma-Aldrich) was provided for the first generation gastroids to prevent anoikis. Conditioned medium was changed every 3 days.

METHOD DETAILS

Drug Treatments

STOMACH SPEM was induced by Tamoxifen (5 mg/20 g body weight; Toronto Research Chemicals) dissolved in 10% ethanol and 90% sunflower oil, injected intraperitoneally (IP) daily. Mice were euthanized at 6-72h post Tamoxifen treatment as described previously(Huh et al., 2012). Pancreatic ADM was induced by 6 hourly IP injections of 50 ㎎/kg cerulein (Sigma-Aldrich) given every other day for 1-14 days as described previously(Willet et al., 2018). Rapamycin (60 ㎎/20 g body weight; LC Laboratories) was injected IP in 0.25% Tween-20, 0.25% polyethylene glycol in PBS daily for 3-7 days pre-treatment and throughout the injury time course. Partial hepatectomy was performed as previously described(Blanc et al., 2010). Mice were given an intraperitoneal injection containing 5-bromo-2'-deoxyuridine (BrdU; 120 mg/kg) and 5-fluoro-2'-deoxyuridine (12 mg/kg) in sterile water 90 min before sacrifice for all BrdU labeling experiments. Mice were anesthetized with isothesia (Henry Schein Animal Health) and sacrificed via cervical dislocation. Mouse stomachs were immediately excised and flushed with PBS after sacrifice and fixed in freshly prepared 10% formalin overnight and moved to 70% ethanol before preparation for embedding. Stomach were cut into rings or strips, embedded in 3% agar in a tissue cassette, and underwent routine paraffin processing. Tissue was sectioned 5㎜ thick and mounted on glass slides.

For *Drosophila* heat shock stress, female *Drosophila* were incubated at 37°C for 90 minutes and recovered for more than 2 days at room temperature. For *Drosophila* oxidative stress, female *Drosophila* were raised in vials containing 1 mL of 2% sucrose solution with or without 3% hydrogen peroxide for overnight. *Drosophila* guts were dissected in saline and fixed (7% picric acid/4% paraformaldehyde, 1X PBS) for 60 min.

Imaging and Tissue Analysis

For immunohistochemistry staining, sections were deparaffinized in Histo-Clear (National Diagnostics) and rehydrated in a gradient of ethanol, then blocked with 5% normal serum in 0.15% triton X-100 and incubated overnight with primary antibodies. The following day, sections were washed in PBS and incubated for 1 h with biotin conjugated secondary antibodies then incubated with avidin/biotin complex (ABC, Vector) reagent for 30 min at room temperature. Sections were developed with DAB for desired time then counterstained in hematoxylin prior to mounting. For antibodies used in this study, see Table S3. For immunofluorescence staining, sections were deparaffinized in xylene and rehydrated, then blocked with 1% BSA in 0.15% triton X-100 and incubated overnight with primary antibodies. Primary antibodies were detected with Alexa-fluor (Invitrogen) secondary antibodies and 4',6-Diamidino-2-phenylindole (DAPI) was used to detect nuclei in immunofluorescence images. For X-gal staining, fresh mouse tissue was embedded in OCT and sectioned using a frozen microtome (Leica). Tissue frozen sections were immersed in 1 mg/ml X-gal staining solution overnight at 37°C in the dark. The following day, slides were post-fixed in 4% PFA for 10 min, then rinsed in PBS for 10 min and counterstained with Nuclear Fast Red(Nagy et al., 2007). *In Situ* hybridization was used to detect RNA expression of *IFRD1* using RNAscope 2.5 HD-Brown kit according to manufacturer's instructions (Advanced Cell Diagnostics). To reduce background staining in parietal cell, slides were pretreated with 0.3M hydrochloric acid for 30 minutes. Negative controls were used according to manufacturer's instructions.

Drosophila midguts were dissected in *Drosophila* saline (182mM KCl, 46mM NaCl, 10mM Tris Base, 3mM $CaCl_2$, pH adjusted to 7.2 with 1N HCl) and transferred to fixation solution (4% formaldehyde, 7% picric acid in 1X PBS) for 1h at room temperature while shaking. All samples were washed by Washing buffer (1X PBT: 1x PBS and 0.3% Triton X-100) several times for 1h and blocked in the pre-incubation buffer (1X PBT containing 1% BSA and 1% normal goat serum, 0.01% Sodium Azide). Primary antibodies were diluted in the same buffer. Midguts were incubated in antisera overnight at 4°C with shaking. After intensive washing, midguts were incubated with secondary antibodies for 1h at room temperature. After washing twice for 15 minutes, midguts were stained with 1 ㎎/mL DAPI in 1x PBT for 15 min, followed twice more washing and mounted in Vectashield medium (Vector Laboratories).

Quantitative PCR

Total RNA was extracted from the corpus of the stomach and isolated using RNeasy Mini Kit (Qiagen) per the manufacturer's protocol. Quality of mRNA was verified with a BioTek Take3 spectrophotometer. RNA was treated with DNase I (Invitrogen), and 1 mg RNA was reverse-transcribed to make cDNA with SuperScript III (Invitrogen) following the manufacturer's protocol. qRT-PCR was performed using PowerUp SYBR Green Master Mix (ThermoFisher) and gene specific primers on a QuantStudio 3 PCR System (ThermoFisher) and data analyzed using QuantStudio Design & Analysis Software. Every run was standardized to TATA Box Binding Protein (TBP) primers and all samples were run in triplicate. All primers were exon-spanning when possible, (i.e. for genes having multiple exons of sufficient length). For full list of qPCR primers, see Table S4.

Western Blots

Approximately 100 mg of mouse stomach corpus tissue or LS174T Cells were lysed in T-PER Tissue Protein Extraction Reagent (Thermo) or RIPA Lysis and Extraction Buffer (Thermo) with 13 protease/phosphatase inhibitor cocktail (Thermo). Protein concentrations were measured using the DC protein assay (BioRad) or Pierce™ BCA Protein Assay Kit (Thermo). 20-50 mg protein was separated using a 10% SDS-polyacrylamide gel electrophoresis (SDS-PAGE) gel (Thermo), then transferred to PVDF membranes (Millipore). Membranes were blocked in TBS/Tween containing 3% BSA, and subsequently incubated with primary antibody overnight at 4°C then with either infrared fluorescent dye-conjugated secondary antibodies (LI-COR Biosciences) or horseradish peroxidase (HRP)-conjugated secondary antibody (Jackson ImmunoResearch) for one hour. Protein signal intensities were normalized against a tubulin loading control for each sample. Fluorescent intensity values were determined and quantified using Image Studio Lite Ver 5.2 software (LI-COR Biosciences). When HRP secondary antibody was used, immunoreactive bands were visualized with SuperSignal™ West Pico PLUS Chemiluminescent Substrate (Thermo). Antibody sources and dilutions are listed in Table S3.

Axon Regeneration

Embryonic DRG neurons were cultured as previously described(Cho and Cavalli, 2012). Briefly, e13.5 DRG neurons were dissected from wildtype mice, trypsinized (.05%) for 25 minutes, and triturated 60x to dissociate the cells. Neurons were resuspended in neuronal media consisting of Neurobasal, 1x B27, 1x Glutamax, FDU, and pen/strep, and were plated in spots of 10,000 neurons on plates coated with poly-d-lysine and laminin. Lentivirus containing FCIV-Bclxl was added at DIV2 and shIFRD1 at DIV4. At DIV 9, spots were axotomized with an 8mm long microtome blade and fixed 48 hours after injury. Spots were immunostained for SCG10 and regenerative growth was measured from the blade mark to the axon tips. The experiments were completed in technical triplicate with 8 biological replicates.

Electron Microscopy

Stomach corpus tissue was collected as described above, fixed overnight at 4℃ in modified Karnovsky's fixative, and sectioned into rings. Tissue rings were processed for EM by the Washington University in St. Louis Department of Pathology and Immunology Electron Microscopy Facility.

QUANTIFICATION AND STATISTICAL ANALYSIS

Imaging and Quantifications

Fluorescence microscopy was performed using a Zeiss Axiovert 200 microscope with an Axiocam MRM camera and Apotome II instrument for grid-based optical sectioning. Immunofluorescence images were taken on a Zeiss Apotome (Zeiss). Bright field images were taken on a 2.0 HT Nanozoomer (Hamamatsu) whole slide scanner or Olympus BX43 light microscope. For imaging of RNAscope samples, individual images were taken at 40x and stitched together digitally. Images were analyzed and post-imaging adjustments were performed with Adobe Photoshop CS6. All time points and treatments were quantified with at least three mice, with representatives from both genders.

Human sample immunohistochemstry staining was scored on the following scale: 0, no staining; 1, minimal staining in less than 20% of cells; 2, moderate to strong staining in at least 20% of cells; 3, strong staining in at least 50% of cells. The scoring system was designed and independently verified by two human pathologists.

Quantification of pancreatic proliferation and SOX9+ cells was done by counting at least 10 randomly sampled whole 403 fields per condition, representing 500 mm in maximal dimension. Tissue preparation and imaging for electron microscopy were as previously described(Ramsey et al., 2007). For counts of paligenotic cells in immunohistochemically stained tissue, we used a method previously described(Willet et al., 2018), in which we counted cells only in the bottom 100 mM of each well-oriented gastric unit. For all genotypes in the current study, we have calculated from n=3 mice of 10 fields each (as well as years of previous experience) that this method is 99.9% sensitive and 80% specific for paligenotic cells (meaning almost no paligenotic cells are uncounted, but 20% might be miscounted as paligenotic, though there is no systemic bias that would affect comparisons across genotypes).

Autophagosome area was calculated by outlining the full regions of autophagosomes in each zymogenic cell cytoplasm and calculating that as a fraction of total cytoplasmic area using ImageJ (NIH). HALO image analysis platform (Indica Labs) was used in some cases to quantify intensity of fluorescent staining (eg for phospho-S6 in CER pancreases). We selected 10 random pancreas images

per *Ifrd1*$^{-/-}$ and control animals that exhibited pathological ADM. Exposure times were kept constant across all samples, and images were analyzed based on the intensity of fluorescence per cell. The staining threshold was set based on control tissue for positive staining.

Bioinformatics, Microarray and *In Silico* Screening

Microarray data from this manuscript have previously been deposited in the National Center for Biotechnology Gene Expression Omnibus (GEO): Stomach (TAM-treated, 12h, GSE71580)(Moore et al., 2015); Pancreas (Cerulein, 24h, GSE3644)(Kowalik et al., 2007); Kidney (Glycerol, 24h, GSE44925)(Fahling et al., 2013, Liver (Hepatectomy, 6h, GSE6998)(Otu et al., 2007). Genes whose expression was increased 1.5-fold (stomach sample) or 2-fold (other organs) with unadjusted p-value of <0.05, were selected, and those with unique, official Gene Symbols were analyzed for intersections with the Gene Set called ''mTORC1-associated Hallmark'' gene set from the Broad GSEA(Liberzon et al., 2015). Analysis of intersection among the 5 gene sets was performed in R (version 3.6.1) using the UpSetR(Conway et al., 2017) and ComplexHeatMap(Gu et al., 2016) implementations of the UpSet(Lex et al., 2014) approach to data visualization. Intersections were depicted in ''distinct'' mode, meaning lists of intersecting transcripts represent those that are exclusive to that intersection of gene sets (eg, *Ifrd1*, and *Ddit4* are the only transcripts in all 5 gene sets and are also, consequently, members of the intersection of ''Stomach'', ''Pancreas'', ''Liver'', ''Kidney''; however, because they are classified in the 5 set intersection, they are not also listed as part of the intersection of ''Stomach'', ''Pancreas'', ''Liver'', ''Kidney''). Intersections that contained no transcripts unique to that intersection were not plotted.

GSEA(Subramanian et al., 2005) was done using default 3.0 GSEA app settings, except: ''Permutation type'' was set to ''gene_set'' and ''Metric for ranking genes'' was set to: ''Diff_of_Classes''. GMX files were made using microarray data generated de novo from *Ifrd1*$^{+/+}$ and *Ifrd1*$^{-/-}$ pancreas tissue ± treatment with cerulein at d5 (GSE121925, publically available November 1, 2019). RNA to generate expression profiles for GSEA was isolated using the RNEasy Micro Kit (Qiagen) following the manufacturers' instructions. Mouse Gene 2.0 ST Array (Affymetrix) Genechips were used to determine mRNA expression, and Partek Genomic Suite 6.6 was used to determine normalized expression for GMX files. Multisequence alignments and phylogenetic analysis are presented as uncurated results from Clustal Omega Webserver(Sievers and Higgins, 2018). Secondary structure prediction was computed with the JPred4 webserver(Drozdetskiy et al., 2015) using the sequence of human IFRD1.

Axolotl data were downloaded(Gerber et al., 2018) and fraction of cells expressing each gene at each time point calculated by formulas in Microsoft Excel.

Statistics

Statistical analyses were performed in GraphPad Prism 7 (La Jolla, CA). In cases involving more than two samples to compare, ANOVA with post-hoc correction (Tukey) was used to assess statistical significance if multiple conditions were compared; Dunnett post-hoc when comparing multiple samples to a single control. Otherwise unpaired, two tailed Student's t test was used unless otherwise stated. Most data (eg cell counts) were first analyzed as mean values of measurements from multiple fields across multiple sections of an organ for each animal, and then the mean of those means was plotted. Area measurement analysis was done using Student's t test (for data that showed presumptive normal distribution). Almost all data were expressed as mean of the means from each mouse ± standard error of mean (SEM) or, when noted, standard deviation (SD) when only a sample mean is plotted.

Human Pathology (2021) 111, 36e44



Human PATHOLOGY

www.elsevier.com/locate/humpath

Original contribution

mAb Das-1 identifies pancreatic ductal adenocarcinoma and high-grade pancreatic intraepithelial neoplasia with high accuracy*,**



Koushik K. Das MD [a,**], Jeffrey W. Brown MD, PhD [a], Carlos Fernandez del-Castillo MD [b], Tiffany Huynh MSN, NP-BC [c], Jason C. Mills MD, PhD [a], Yoko Matsuda MD, PhD [d], Kiron M. Das MD [e], Mari Mino-Kenudson MD [c,f,*]

[a] *Division of Gastroenterology, Washington University, St. Louis, 63110, USA*
[b] *Department of Surgery, Massachusetts General Hospital and Harvard Medical School, Boston, 02114, USA*
[c] *Department of Pathology, Massachusetts General Hospital, Boston, 02114, USA*
[d] *Oncology Pathology, Department of Pathology and Host-Defense, Faculty of Medicine, Kagawa, 761-0793, Japan*
[e] *Division of Gastroenterology, Rutgers-Robert Wood Johnson Medical School, New Brunswick, 08901, USA*
[f] *Department of Pathology, Harvard Medical School, Boston, 02115, USA*

Received 23 September 2020; revised 15 January 2021; accepted 18 January 2021

Available online 30 January 2021

Keywords:
Pancreatic intraepithelial neoplasia (PanIN);
mAb Das-1;
Pancreatic adenocarcinoma;
Biomarker;
CEP

Summary Pancreatic intraepithelial neoplasia (PanIN) is a microscopic precursor lesion to pancreatic ductal adenocarcinoma (PDAC); however, there are few biomarkers that segregate high-grade PanIN/PDAC from low-grade PanIN lesions. mAb Das-1 is a monoclonal antibody against a colonic epithelial antigen that is reactive to premalignant conditions of the upper gastrointestinal tract including Barrett's esophagus, incomplete-type gastric intestinal metaplasia, and intraductal papillary mucinous neoplasm of the pancreas at high risk of malignancy. We sought to examine a role for Das-1 expression in differentiating high-grade PanIN/PDAC from low-grade PanIN lesions. We examined surgical specimens from 86 patients and 2 autopsied pancreata (74 with and 14 without PDAC) with 107 distinct PanIN lesions, 74 PDAC cases, and 32 associated lymph node metastases, with internal controls of normal

* Competing interests: A patent for the use of mAb Das-1 in detection of precancerous lesions of the esophagus has been awarded (K.M.D.) and a patent for its possible use in detection of pancreatic cancer is currently pending (K.K.D., M.M.-K., K.M.D.). These patents have not been licensed, and these authors hold no commercial interests at this time.

** Funding/Support: This work was supported by the American Society for Gastrointestinal Endoscopy (K.K.D.), National Pancreas Foundation (K.M.D.), National Institutes of Health (NIH)/National Institute of Diabetes and Digestive and Kidney Diseases (NIDDK) T32DK007130-41, and Digestive Diseases Research Core Centers Pilot & Feasibility Grant as part of P30 DK052574 (J.W.B.). Development of mAb Das-1 was supported in part by research grants NIDDK, R01 DK47673, and R01 DK63618 to K.M.D. J.W.B. was also supported by the Department of Defense, through the PRCRP program (W81XWH-20-1-0630).

* Corresponding author. Massachusetts General Hospital, 55 Fruit St., Warren 122, Boston, MA 02114, USA.
** Corresponding author. 660 South Euclid Avenue, Campus Box 8124, St. Louis, MO 63110, USA.
E-mail addresses: k.das@wustl.edu (K.K. Das), mminokenudson@partners.org (M. Mino-Kenudson).

https://doi.org/10.1016/j.humpath.2021.01.003
0046-8177/© 2021 Elsevier Inc. All rights reserved.

pancreatic ducts observed in 56 cases. All of the normal pancreatic duct controls (0/56) and low-grade PanIN (0/95) lesions were nonreactive to Das-1. Das-1 expression among high-grade PanIN (7/12, 58%), PDAC (55/74, 74%), and lymph node metastasis (21/32, 66%) cases was significantly higher ($p < 0.0001$). Clinicopathologically, Das-1 reactivity was significantly correlated with nodal metastasis (pZ0.021). Overall, the sensitivity, specificity, and accuracy of Das-1 in segregating high-grade PanIN/PDAC from low-grade PanIN lesions and normal ducts were 72%, 100%, and 90%, respectively. Thus, mAb Das-1 reacts with high specificity with high-grade PanIN and PDAC and may help in preoperative diagnosis and/or clinical risk stratification.
© 2021 Elsevier Inc. All rights reserved.

1. Introduction

Pancreatic ductal adenocarcinoma (PDAC) is projected to become the second leading cause of cancer death in the United States by 2030 [1]. Unfortunately, the vast majority of patients present with locally advanced or metastatic disease, and only if the patient's cancer is small and confined to the pancreas, or ideally preinvasive, will post-surgical overall survival be meaningfully improved [2]. Thus, biomarkers to identify PDAC, preferably in its preinvasive stage, are of utmost clinical need.

Pancreatic intraepithelial neoplasia (PanIN) is a precursor lesion to PDAC that is confined to pancreatic ducts and is 5 mm or less in diameter. PanIN typically exhibits a gastric epithelial morphology and is currently classified into two grades: low-grade PanIN (PanIN-1 and PanIN-2) and high-grade PanIN (PanIN-3). The latter demonstrates pronounced cytologic and architectural atypia, equivalent to *in situ* carcinoma [3e5]. Morphological progression from low-grade to high-grade PanIN lesions is marked by successive accumulation of alterations in cancer-associated genes including *KRAS*, *p16/CDKN2A*, *TP53*, and *SMAD4/DPC4* [3]. Clinically, the presence of high-grade PanIN may impact the decision for pancreatic resection, and if it is found in the context of a patient with hereditary pancreatitis, for example, it is an indication for total pancreatectomy [6]. Unfortunately, there is significant interobserver variability in morphologic grading of PanIN [7,8], creating the need for additional approaches for molecular grading. Indeed, given the high prevalence of low-grade PanIN lesions that are unlikely to progress to clinically important neoplasm in the general population [4,7,9], markers are needed not only to help differentiate neoplastic from non-neoplastic pancreatic lesions but also to identify high-grade PanIN that often accompanies invasive carcinoma or might indicate a future pancreatic cancer risk.

Although genetic and/or epigenetic alterations of several genes such as *KRAS*, *TP53*, and *DPC/SMAD4* and expression of several biomarkers such as COX2, S100A4, and survivin have been identified and correlated with outcomes in PDAC, studies have not been able to show that their expression reliably identifies cancer at an early or preinvasive stage with high sensitivity or specificity [10]. Many markers are confounded by their expression in chronic pancreatitis (CP), from which PDAC may emerge. Even critical markers such as *KRAS*, which is found in the vast majority of PDACs, are ubiquitous in low-grade PanIN as well as in individuals who smoke, those with CP, and in non-neoplastic ductal hyperplasia [11e13]. Available screening modalities may have difficulty in distinguishing mass-forming CP from PDAC, not only because PDAC may arise in the background of CP but also because clinical signs and symptoms of the conditions can be quite similar.

Using a colon epithelial protein (CEP), we have previously developed a novel murine monoclonal antibody, mAb Das-1 (formerly known as $7E_{12}H_{12}$, IgM isotype), that reacts specifically with normal colonic epithelium [14]. Both via immunoperoxidase and immunofluorescence assays, we and others have independently demonstrated that mAb Das-1 specifically reacts with both non**e**goblet and goblet cell colonic epithelium, but not with normal small intestinal enterocytes from the duodenum, jejunum, or ileum [14,15]. Although reactivity of mAb Das-1 is similarly absent from the normal pancreatic, gastric, and esophageal mucosa, it is strongly expressed in preneoplastic and intestinal phenotypic changes in these organs. Indeed, it has been shown that mAb Das-1 is both highly sensitive and specific for detection of Barrett's esophagus, incomplete-type gastric intestinal metaplasia, and cancer developed therefrom [16e19]. We have reported that mAb Das-1 expression serves as a sensitive and highly specific marker segregating high-risk lesions of intraductal papillary mucinous neoplasm (IPMN) of the pancreas from low-risk lesions. While normal pancreatic ducts and low-grade (low- and intermediate-grade) gastric-type IPMN were minimally reactive, mAb Das-1 was significantly more reactive in high-risk/malignant lesions including intestinal-type IPMN, high-grade dysplasia of any epithelial subtype, and IPMN-associated carcinoma [20]. In a large, multicenter validation study with cyst fluid from 169 patients with resected pancreatic cystic lesions, enzyme-linked immunosorbent assay for Das-1 identified high-risk lesions (those lesions warranting surgical resection) with

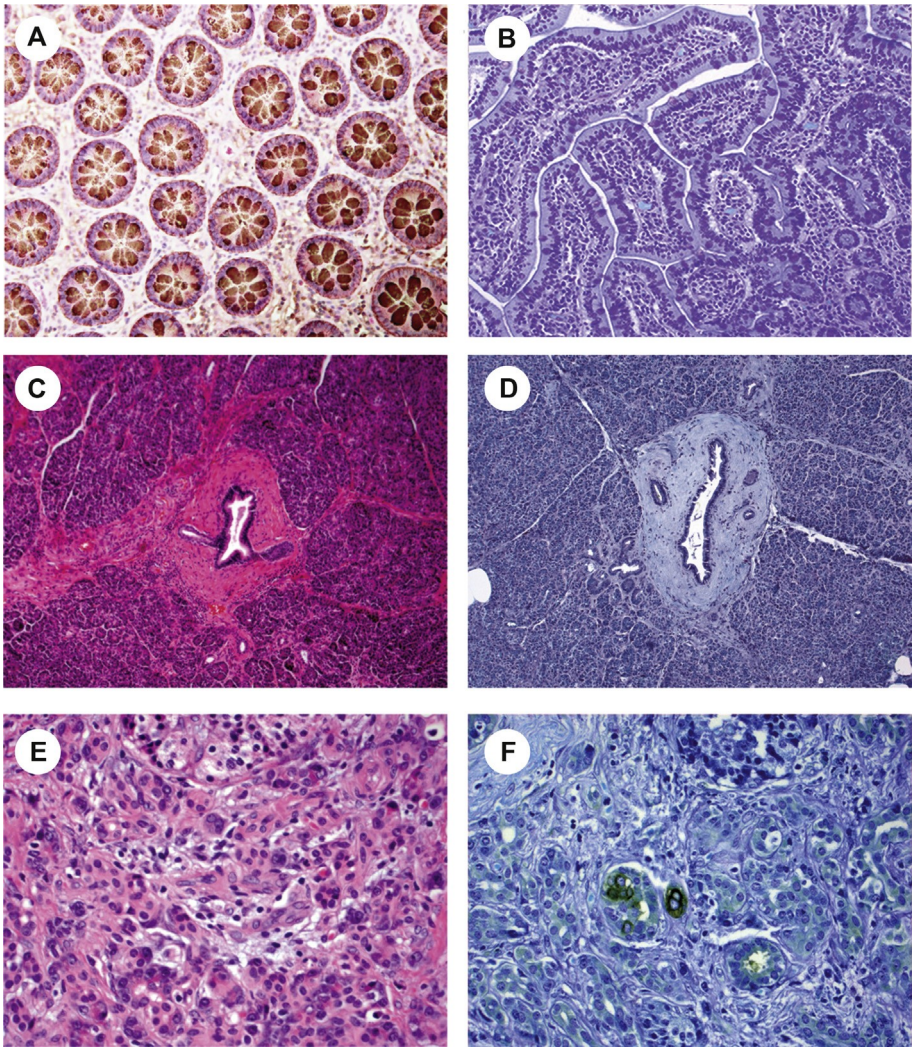


Fig. 1 Normal colonic mucosa exhibits cytoplasmic expression of Das-1 (A), whereas normal small intestinal mucosa is negative for Das-1 (B). Similarly, normal pancreatic parenchyma including pancreatic ducts is nonreactive to Das-1: H&E staining (C), Das-1 immunohistochemistry (D). Interestingly, rare small foci with acinar to ductal metaplasia in the setting of chronic pancreatitis secondary to pancreatic ductal adenocarcinoma show strong membranous and/or cytoplasmic Das-1 expression: H&E staining (E), Das-1 immunohistochemistry (F). H&E, hematoxylin and eosin.

88% sensitivity, 99% specificity, and 95% accuracy, which was significantly more accurate than any available clinical guideline [21].

In the present study, we explore the ability of mAb Das-1 to distinguish non-neoplastic pancreatic ducts and low-grade PanIN from high-grade lesions. To that end, we examined reactivity of the mAb by immunohistochemistry against tissue with all grades of PanIN, associated PDAC, and matched lymph node (LN) metastasis.

2. Materials and methods

2.1. Case selection

The Massachusetts General Hospital Institutional Review Board approved this study. The surgical pathology file of Massachusetts General Hospital was queued for pancreatic resections for PDAC between 2005 and 2007. After exclusion of postneoadjuvant therapy resections and those with insufficient materials, the remaining 74 cases as well as 10 pancreatic resections for mass-forming CP, 2 pancreatic resections for pancreatic duct stricture with associated CP, and 2 autopsied pancreata with PanIN lesions formed our study cohort (n Z 88). Of these, representative sections with various grades of PanIN, invasive adenocarcinoma, and/or associated LN metastasis were evaluated via Das-1 immunohistochemistry. All blocks were formalin fixed, paraffin embedded, and routine serial 5-mm sections were obtained. Hematoxylin and eosin-stained sections were reviewed to ensure the presence of representative lesions in the same block.

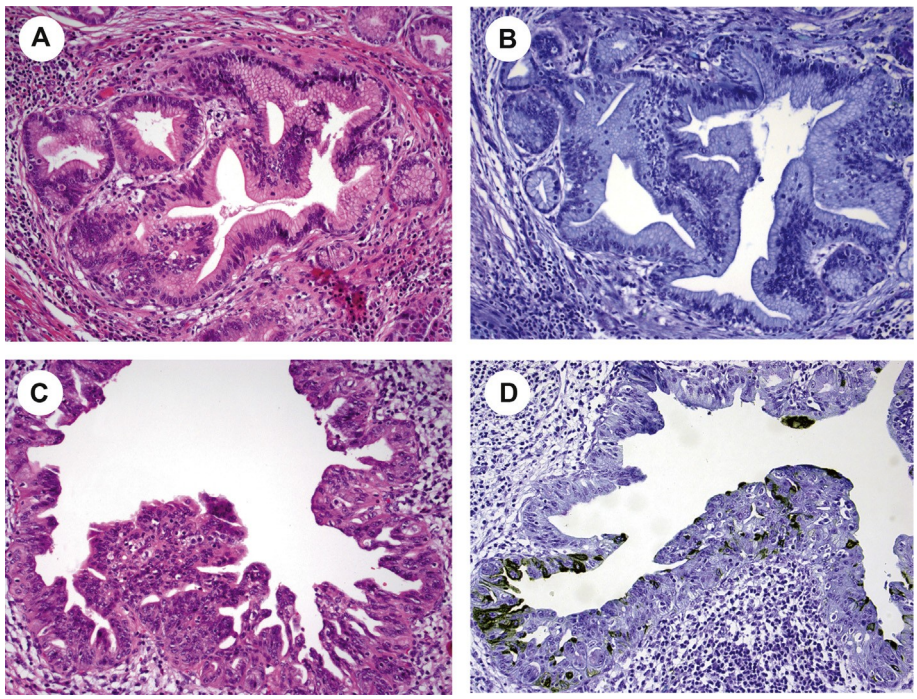


Fig. 2 Low-grade PanIN (PanIN-1 and PanIN-2) are nonreactive to Das-1 [H&E staining (A), Das-1 immunohistochemistry (B)], while cytoplasmic and/or membranous patterns of Das-1 expression is seen in the majority of high-grade PanIN (PanIN-3) lesions [H&E staining (C), Das-1 immunohistochemistry (D)]. H&E, hematoxylin and eosin.

For the purpose of this study, PanIN lesions were classified into low-grade PanIN (PanIN-1 and PanIN-2) and high-grade PanIN (PanIN-3) using previously accepted criteria [4]. In brief, PanIN-1 is defined as either a flat (PanIN-1A) or papillary/micropapillary (PanIN-1B) epithelial lesion composed of columnar cells with basally located nuclei, abundant cytoplasmic mucin, and essentially no cytologic atypia. PanIN-2 is predominantly papillary and exhibits mild to moderate nuclear atypia, nuclear crowding, hyperchromatism, and pseudostratification. In contrast, PanIN-3 has pronounced architectural and cytologic atypia equivalent to carcinoma *in situ* that is usually papillary or micropapillary and demonstrates a loss of polarity with prominent nucleoli and mitoses.

2.2. Immunohistochemistry using mAb Das-1

Tissue sections from each lesion were examined with mAb Das-1 using a sensitive immunoperoxidase assay, as described previously [14,16,17,20]. Each experiment included at least two slides of normal colon and duodenal tissue sections as positive and negative controls, respectively (Fig. 1A and B). Reactivity to mAb Das-1 was considered positive if a dark green to crisp golden brown staining was present and was graded based on the percentage of affected cells that were positive: grade 0 (negative), <5%; grade 1, 5**e**25%; grade 2, 25**e**50%; and grade 3, >50%. Two of the authors (K.K.D. and M.M.-K.) who were blinded to the clinical data evaluated and scored each section. There was agreement among the investigators in the vast majority of cases, and in the cases with discordant scores, the final score was determined after discussion.

2.3. Statistical analysis

Das-1 expression in high-grade PanIN, PDAC, and LN metastases was compared against low-grade PanIN and normal pancreatic ducts using Fisher's exact test. Das-1 reactivity was also correlated with the other clinicopathological parameters using Fisher's Exact test. $P < 0.05$ was considered statistically significant.

3. Results

3.1. mAb Das-1 expression in non-neoplastic pancreatic parenchyma

Non-neoplastic pancreatic ducts and pancreatic parenchyma including CP were essentially nonreactive in all the samples examined (Fig. 1C and D). Notably, tumor-associated CP and stroma were essentially negative except in areas with nests of tumor cells or immediately adjacent, which may indicate localized extravasation. Das-1 expression was observed in rare, small foci with acinar to ductal metaplasia (ADM) in CP secondary to PDAC (Fig. 1E and F).

Table 1 Clinicopathological features of patients with pancreatic ductal adenocarcinoma stratified by Das-1 expression.

Clinical or pathologic feature	Total, N	Das-1 expression		*P*value
		Negative	Positive	
All cases	74	19	55	
Gender				0.785
Male	28	8 (42%)	20 (36%)	
Female	46	11 (58%)	35 (64%)	
Age (years)				0.100
Mean	65.8	62.5	67.0	
SD	10.2	9.7	10.3	
Tumor size (cm)				0.446
Mean	3.1	2.9	3.1	
SD	0.9	0.9	0.9	
Tumor stage				0.671
pT1	1	0 (0%)	1 (1.8%)	
pT2	7	1 (5.3%)	6 (11%)	
pT3	65	18 (95%)	47 (85%)	
pT4	1	0 (0%)	1 (1.8%)	
Nodal stage				0.021
pN0	16	8 (42%)	8 (11%)	
pN1	58	11 (58%)	47 (89%)	
Stage				1.000
IA	1	0 (0%)	1 (1.8%)	
IB	1	0 (0%)	1 (1.8%)	
IIA	14	8 (42%)	6 (11%)	
IIB	57	11 (58%)	46 (84%)	
III	1	0 (0%)	1 (1.8%)	
Histological grade[a]				
Low	35	10 (53%)	25 (45%)	0.606
High	39	9 (47%)	30 (55%)	
Lymphatic invasion				
(–)	25	8 (42%)	17 (31%)	0.408
(þ)	49	11 (58%)	38 (69%)	
(–)	26	9 (47%)	17 (31%)	0.266
(þ)	48	10 (53%)	38 (69%)	
(–)	6	1 (5.3%)	5 (9.1%)	1.000
(þ)	68	18 (95%)	50 (91%)	
Negative	26	11 (58%)	15 (27%)	0.259
Positive	48	8 (42%)	40 (73%)	

SD, standard deviation.
[a] Low grade: well and moderately differentiated, high grade: poorly differentiated and undifferentiated.

3.2. mAb Das-1 is specific for high-grade PanIN lesions and PDAC

In total, the PanIN lesions consisted of 95 low-grade PanIN (58 PanIN-1 and 37 PanIN-2) and 12 high-grade PanIN lesions. The former included 16 low-grade PanIN (10 PanIN-1 and 6 PanIN-2) lesions from pancreatic resections for mass-forming CP, and the latter included 4 high-grade PanIN lesions in the pancreata that did not show invasive carcinoma. Of the low-grade PanIN lesions, no lesions were reactive to Das-1 (Fig. 2A and B) (Table 2). Compared with non-neoplastic pancreatic ducts (present in 56 individual sections) and low-grade PanIN lesions, Das-1 expression among high-grade PanIN was significantly higher ($P < 0.0001$), with 7 of 12 (58%) staining positive (Grade 1: n = 5, Grade 2: n = 0; Grade 3: n = 2). Of note, 2 (50%) of 4 high-grade PanIN lesions identified in the pancreata without PDAC were immunoreactive to Das-1. When reactive to mAb Das-1, the lesional epithelium exhibited intense staining in cytoplasmic and/or membranous patterns (Fig. 2C and D). Within samples demonstrating various PanIN grades, mAb Das-1 preferentially

Table 2 Das-1 expression in pancreatic ducts, PanIN, and pancreatic adenocarcinomas.

Das-1 expression	Non-neoplastic pancreatic duct	Low-grade PanIN	High-grade PanIN	PDAC	LN metastasis
Total	56	95	12	74	32
Das-1 (%)	0 (0%)	0 (0%)	7 (58%)	55 (74%)	21 (66%)
Grade 1[1]	0	0	5	10	6
Grade 2[2]	0	0	0	14	2
Grade 3[3]	0	0	2	31	13
p-value	NS	NS	<0.0001[a]	<0.0001[a]	<0.0001[a]

Performance for high-grade PanIN/PDAC: sensitivity 72%, specificity 100%.
Abbreviations: PanIN, pancreatic intraepithelial neoplasia; PDAC, pancreatic ductal adenocarcinoma; LN, lymph node.
[1]Grade 1: Das-1 expression was seen in 5–25% of tumor cells.
[2]Grade 2: Das-1 expression was positive in 25–50% of tumor cells.
[3]Grade 3: Das-1 was expressed in >50% of tumor cells.
[a] Each category was compared with low-grade PanIN lesions and non-neoplastic pancreatic duct controls.

reacted with high-grade PanIN and was absent in low-grade lesions.

3.3. mAb Das-1 expression in PDAC

In total, 55 of 74 (74%) invasive carcinomas were considered positive (Tables 1 and 2). Das-1 staining was often diffuse (Grade 1: n = 10; Grade 2: n = 14; Grade 3: n = 31), and mostly cytoplasmic in the invasive ducts (Fig. 3), and also highlighted perineural lymphatic, and venous invasion, and cancerization of the duct (intraductal spread of carcinoma) (Fig. 4A–C, Table 2). Overall, the sensitivity and specificity of Das-1 in segregating high-grade PanIN/PDAC from non-neoplastic ducts and low-grade PanIN lesions were 72% (95% CI: 0.62–0.81) and 100% (95% CI: 0.98–1.00), respectively, with an accuracy of 90%.

Compared to Das-1 negative tumors, those with Das-1 expression were more likely to have nodal metastasis (58% vs. 89%, $p = 0.021$), but there was no association between Das-1 expression and other clinicopathological features including age, gender, pathologic T stage and AJCC stage, histologic grade of the tumor, lymphovascular and perineural invasion and resection margin status (Table 1). There was no difference in overall survival between the two groups as well. Two-year overall survival rate was 56% for those with negative Das-1 expression and 47% for those with positive Das-1 expression ($p = 0.313$).

3.4. mAb Das-1 reactivity in nodal metastases

mAb Das-1 was also examined in 32 LNs with metastatic deposits, distant from the primary PDAC in 30 cases. Reactivity was evident in 21 of 32 (66%) of the LNs (grade 1: n = 6, grade 2: n = 2; grade 3: n = 13) in these cases (Table 2). Staining was specific for metastatic adenocarcinoma tissue within the LN (Fig. 4D). Among the primary tumors in these cases, 25 of 30 (83%) were positive for Das-1, and in no case was a LN reactive when a primary tumor was not. Only in 4 cases was Das-1 expression present in the primary tumor but absent in the nodal metastasis. Interestingly, in one case, a primary tumor exhibiting Das-1 expression had one LN that was focally positive for Das-1 and another that was negative for Das-1.

4. Discussion

In this study, we show that mAb Das-1 is a potential novel biomarker to specifically identify high-grade PanIN and PDAC, but not non-neoplastic pancreatic ducts and low-grade PanIN lesions. Indeed, in our cohort, mAb Das-1 was able to distinguish high-grade PanIN/PDAC, with 72% sensitivity, 100% specificity, and 90% accuracy. While mAb Das-1 was completely nonreactive with low-grade PanIN, expression among high-grade PanIN was significantly higher at 58% (7/12). With regard to the performance of the immunohistochemistry assay, 55% of positive samples stained at a grade 3 level (>50% of affected glands staining positive), and the vast majority (75%) of samples stained at a grade 2 level or higher (at least 25% of affected glands stained positive).

While low-grade PanIN lesions are commonly identified in benign pancreata and associated with few genetic alterations [9,22,23], high-grade PanIN lesions are usually confined to the immediate vicinity of an infiltrating carcinoma with a genetic profile similar to that of PDAC [24–27]. In addition, we have recently demonstrated in a large autopsy study of 173 patients who did not die with any evidence of PDAC or IPMN, a frequency of 77% of PanIN-1 and of 28% of PanIN-2 in comparison with a frequency of 4% of PanIN-3 [9]. Given the ubiquity of these asymptomatic, low-grade PanIN lesions, the ability to make the distinction between PanIN-2 and PanIN-3 lesions is clinically crucial. However, as with many features in surgical pathology that one attempts to stratify into ordinal categories, the features that separate PanIN-3 from PanIN-2 lie on a continuum, resulting in ambiguity in delineating PanIN-2 and PanIN-3 lesions [4]. Indeed, even expert pancreatic pathologists disagree in diagnosing high-grade dysplasia versus low-grade dysplasia in 16% of cases [8]. Thus, the development of biomarkers that can specifically delineate high-grade PanIN, but not low-grade PanIN, may

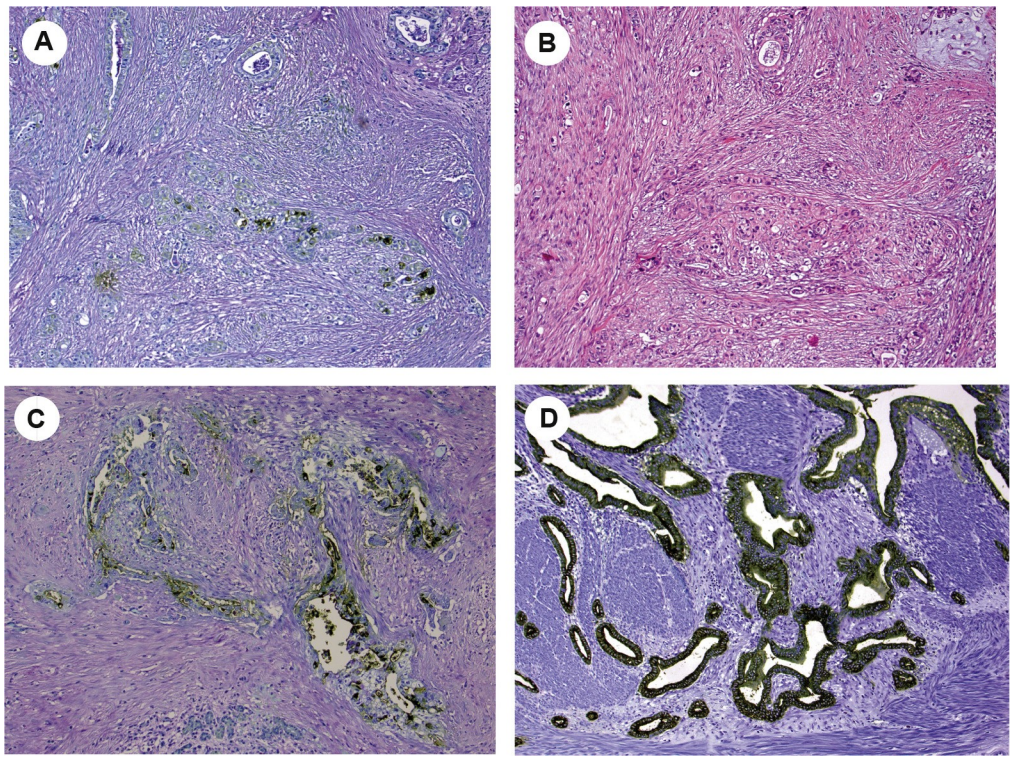


Fig. 3 Examples of pancreatic ductal adenocarcinomas with grade 1 (A and B), grade 2 (C), and grade 3 (D) Das-1 expression (panels A, C, and D: Das-1 immunohistochemistry, panel B: H&E staining). H&E, hematoxylin and eosin.

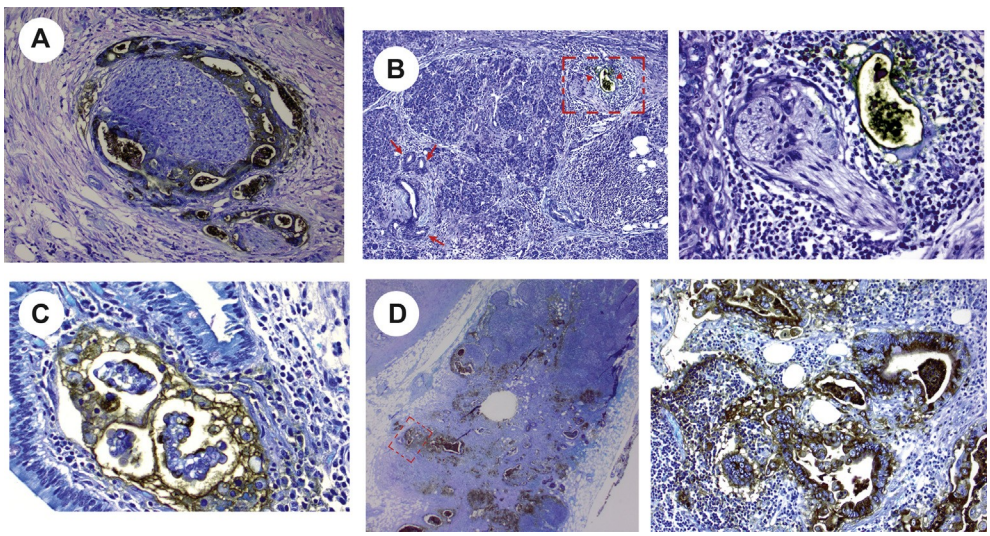


Fig. 4 Das-1 staining highlighting perineural invasion (A). A malignant duct in the vicinity of neural tissue is positive for Das-1 (arrow heads; an area marked by a rectangle is magnified in the second image), whereas normal interlobular duct and low-grade PanIN lesions are nonreactive to Das-1 (arrows) (B). Lymphatic invasion with Das-1 expression (C). An example of lymph node metastasis with grade 3 Das-1 expression (an area marked by a rectangle is magnified in the second image) (D).

help to confidently grade lesions and optimally manage early PDAC.

Mass-forming CP including autoimmune pancreatitis can clinically mimic PDAC. Initial assessment of pancreatic masses frequently involves endoscopic ultrasound-guided, transduodenal/transgastric fine needle aspiration. As such, pathologic evaluation of cytologic materials is often contaminated with gastric or duodenal glandular epithelium. Furthermore, CP frequently exhibits low-grade PanIN lesions that may be difficult to distinguish from

well-differentiated PDAC. As mAb Das-1 is nonreactive in normal gastric, duodenal, and pancreatic epithelium, as well as in pancreatitis and low-grade PanIN lesions, its reactivity may be helpful in these initial evaluations. A few immunohistochemistry markers including SMAD4 (loss of expression), p53 (aberrant expression), and IPM3 have been evaluated for the differentiation of PDAC and/or high-grade PanIN from non-neoplastic pancreatic tissue and low-grade PanIN [28,29]. Of these, IPM3 is expressed in 96% of PDACs, but its expression in high-grade PanIN lesions appears to be limited (<60%) [28]. Thus, a panel of immunohistochemical stains including mAb Das-1 and IPM3, for example, may allow for more confident discrimination between well-differentiated PDAC and/or high-grade PanIN from gastric or duodenal epithelium and/or low-grade PanIN lesions.

Evidence in mouse models has suggested that ADM is a likely antecedent to the development of PanIN and subsequently PDAC [30]. ADM also may be a site of increased epithelial-to-mesenchymal transformation (EMT) in models of pancreatic cancer [31]. In our study, we found a few instances of ADM with strong membranous and cytoplasmic expression of mAb Das-1. Further evaluation in lineage-labeled models of EMT may elucidate at what stage mAb Das-1 expression becomes apparent as well as whether gastric and/or intestinal programming is activated concurrently.

Previous studies of mAb Das-1 reactivity in fetal tissues by Badve et al. [32] demonstrated expression of the Das-1 antigen in organs arising from the primitive gut, ureteric bud, and several other sites of ectodermal, mesodermal, and endodermal origin. Subsequently, it has been shown that although Das-1 is expressed in the fetal esophagus, stomach, and small intestine, it is lost in the respective adult organs and reappears in precancerous and cancerous conditions such as Barrett's esophagus/esophageal adenocarcinoma [16,33], incomplete-type gastric intestinal metaplasia/gastric adenocarcinoma [17,19], and small intestinal adenoma/small intestinal adenocarcinoma [34]. These findings suggest that mAb Das-1 may be a novel oncofetal marker. While expression of Das-1 is present in fetal pancreatic tissue and absent in adult pancreata [32], we now demonstrate that expression returns in high-grade PanIN and PDAC. Furthermore, the reactivity remains upon metastasis into LNs in the vast majority of PDACs.

We have previously described the expression of mAb Das-1 in high-grade IPMN lesions including those of the gastric epithelial type, as well as associated invasive carcinoma [20,21]. It is not certain why this colonic specific marker would be expressed in dysplastic lesions of the pancreas and PDAC. As the antigen of the Das-1 antibody, CEP, has not been fully characterized and its function has not been elucidated, further research is ongoing to assess the functional significance of the expression of this marker in these pre-invasive and invasive conditions of the pancreas.

There are several limitations in our study. First, as our surgical specimens were entirely from a single tertiary referral center, there may be a referral or treatment access bias. In addition, our PDAC cases were chosen non-randomly on the basis of availability of tissue samples from sequentially resected PDACs. This selection should not bias our sample as all cases by definition contained a combination of preneoplastic and neoplastic lesions, and analysis was completed on a per-lesional basis. Second, the numbers of PanIN lesions in individual histologic categories, particularly high-grade PanIN lesions, were small. However, the differences in reactivity among low-grade PanIN and high-grade PanIN were still highly statistically significant ($p < 0.001$). Third, additional biomarkers and clinicopathologic parameters such as biliary obstruction/jaundice and plasma CA19-9 levels were not available to correlate with mAb Das-1 expression. Nevertheless, we have demonstrated that expression of mAb Das-1 segregates high-grade PanIN/PDAC from low-grade PanIN via immunohistochemical analysis.

In conclusion, mAb Das-1 is a sensitive and highly specific biomarker for high-grade PanIN and PDAC. The inclusion of the Das-1 marker in the analysis of tissue may aid in the preoperative diagnosis and/or risk stratification of patients with a pancreatic mass lesion.

Acknowledgments

The authors would like to thank Kelly Walton for her technical advice for immunohistochemical staining. K.K.D., J.W.B., and M.M.-K. contributed to conceptualization, data curation, formal analysis, investigation, methodology, and writing; K.M.D. and C.F.d.-C. contributed to conceptualization and writing; T.H. and Y.M. contributed to data curation.

References

[1] Rahib L, Smith BD, Aizenberg R, Rosenzweig AB, Fleshman JM, Matrisian LM. Projecting cancer incidence and deaths to 2030: the unexpected burden of thyroid, liver, and pancreas cancers in the United States. Canc Res 2014;74:2913**e**21.

[2] Siegel R, Ward E, Brawley O, Jemal A. Cancer statistics, 2011. CA Cancer J Clin 2011;61:212**e**36.

[3] Hruban RH, Goggins M, Parsons J, Kern SE. Progression model for pancreatic cancer. Clin Canc Res 2000;6:2969**e**72.

[4] Hruban RH, Takaori K, Klimstra DS, et al. An illustrated consensus on the classification of pancreatic intraepithelial neoplasia and intraductal papillary mucinous neoplasms. Am J Surg Pathol 2004; 28:977**e**87.

[5] Basturk O, Hong SM, Wood LD, et al. A revised classification system and recommendations from the Baltimore consensus meeting for neoplastic precursor lesions in the pancreas. Am J Surg Pathol 2015; 39:1730**e**41.

[6] Rebours V, Lévy P, Mosnier JF, et al. Pathology analysis reveals that dysplastic pancreatic ductal lesions are frequent in patients with hereditary pancreatitis. Clin Gastroenterol Hepatol 2010;8:206**e**12.

[7] Hruban RH, Adsay NV, Albores-Saavedra J, et al. Pancreatic intraepithelial neoplasia: a new nomenclature and classification system for pancreatic duct lesions. Am J Surg Pathol 2001;25:579**e**86.

[8] Longnecker DS, Adsay NV, Fernandez-del Castillo C, et al. Histopathological diagnosis of pancreatic intraepithelial neoplasia and intraductal papillary-mucinous neoplasms: interobserver agreement. Pancreas 2005;31:344**e**9.

[9] Matsuda Y, Furukawa T, Yachida S, et al. The prevalence and clinicopathological characteristics of high-grade pancreatic intraepithelial neoplasia: autopsy study evaluating the entire pancreatic parenchyma. Pancreas 2017;46:658**e**64.

[10] Ansari D, Rosendahl A, Elebro J, Andersson R. Systematic review of immunohistochemical biomarkers to identify prognostic subgroups of patients with pancreatic cancer. Br J Surg 2011;98:1041**e**55.

[11] Kanda M, Matthaei H, Wu J, et al. Presence of somatic mutations in most early-stage pancreatic intraepithelial neoplasia. Gastroenterology 2012;142:730**e**3. e739.

[12] Luttges J, Diederichs A, Menke MA, Vogel I, Kremer B, Kloppel G. Ductal lesions in patients with chronic pancreatitis show K-ras mutations in a frequency similar to that in the normal pancreas and lack nuclear immunoreactivity for p53. Cancer 2000;88:2495**e**504.

[13] Berger DH, Chang H, Wood M, et al. Mutational activation of K-ras in nonneoplastic exocrine pancreatic lesions in relation to cigarette smoking status. Cancer 1999;85:326**e**32.

[14] Das KM, Sakamaki S, Vecchi M, Diamond B. The production and characterization of monoclonal antibodies to a human colonic antigen associated with ulcerative colitis: cellular localization of the antigen by using the monoclonal antibody. J Immunol 1987;139:77**e**84.

[15] Halstensen TS, Das KM, Brandtzaeg P. Epithelial deposits of immunoglobulin G1 and activated complement colocalise with the M(r) 40 kD putative autoantigen in ulcerative colitis. Gut 1993;34:650**e**7.

[16] Das KM, Prasad I, Garla S, Amenta PS. Detection of a shared colon epithelial epitope on Barrett epithelium by a novel monoclonal antibody. Ann Intern Med 1994;120:753**e**6.

[17] Mirza ZK, Das KK, Slate J, et al. Gastric intestinal metaplasia as detected by a monoclonal antibody is highly associated with gastric adenocarcinoma. Gut 2003;52:807**e**12.

[18] Piazuelo MB, Haque S, Delgado A, Du JX, Rodriguez F, Correa P. Phenotypic differences between esophageal and gastric intestinal metaplasia. Mod Pathol 2004;17:62**e**74. an official journal of the United States and Canadian Academy of Pathology, Inc.

[19] Watari J, Moriichi K, Tanabe H, et al. Biomarkers predicting development of metachronous gastric cancer after endoscopic resection: an analysis of molecular pathology of Helicobacter pylori eradication. Int J Canc2012;130:2349**e**58.

[20] Das KK, Xiao H, Geng X, et al. mAb Das-1 is specific for high-risk and malignant intraductal papillary mucinous neoplasm (IPMN). Gut 2014;63:1626**e**34.

[21] Das KK, Geng X, Brown JW, et al. Cross validation of the monoclonal antibody Das-1 in identification of high-risk mucinous pancreatic cystic lesions. Gastroenterology 2019;157:720**e**30. e722.

[22] Luttges J, Galehdari H, Brocker V, et al. Allelic loss is often the first hit in the biallelic inactivation of the p53 and DPC4 genes during pancreatic carcinogenesis. Am J Pathol 2001;158:1677**e**83.

[23] Andea A, Sarkar F, Adsay VN. Clinicopathological correlates of pancreatic intraepithelial neoplasia: a comparative analysis of 82 cases with and 152 cases without pancreatic ductal adenocarcinoma. Mod Pathol 2003;16:996**e**1006.

[24] Kozuka S, Sassa R, Taki T, et al. Relation of pancreatic duct hyperplasia to carcinoma. Cancer 1979;43:1418**e**28.

[25] Hisa T, Suda K, Nobukawa B, et al. Distribution of intraductal lesions in small invasive ductal carcinoma of the pancreas. Pancreatology 2007;7:341**e**6.

[26] Wilentz RE, Iacobuzio-Donahue CA, Argani P, et al. Loss of expression of Dpc4 in pancreatic intraepithelial neoplasia: evidence that DPC4 inactivation occurs late in neoplastic progression. Canc Res 2000;60:2002**e**6.

[27] Yamano M, Fujii H, Takagaki T, Kadowaki N, Watanabe H, Shirai T. Genetic progression and divergence in pancreatic carcinoma. Am J Pathol 2000;156:2123**e**33.

[28] Yantiss RK, Woda BA, Fanger GR, et al. KOC (K homology domain containing protein overexpressed in cancer): a novel molecular marker that distinguishes between benign and malignant lesions of the pancreas. Am J Surg Pathol 2005;29:188**e**95.

[29] Maitra A, Adsay NV, Argani P, et al. Multicomponent analysis of the pancreatic adenocarcinoma progression model using a pancreatic intraepithelial neoplasia tissue microarray. Mod Pathol 2003;16:902**e**12. an official journal of the United States and Canadian Academy of Pathology, Inc.

[30] Reichert M, Rustgi AK. Pancreatic ductal cells in development, regeneration, and neoplasia. J Clin Invest 2011;121:4572**e**8.

[31] Rhim AD, Mirek ET, Aiello NM, et al. EMT and dissemination precede pancreatic tumor formation. Cell 2012;148:349**e**61.

[32] Badve S, Logdberg L, Sokhi R, et al. An antigen reacting with das-1 monoclonal antibody is ontogenically regulated in diverse organs including liver and indicates sharing of developmental mechanisms among cell lineages. Pathobiology 2000;68:76**e**86.

[33] Griffel LH, Amenta PS, Das KM. Use of a novel monoclonal antibody in diagnosis of Barrett's esophagus. Dig Dis Sci 2000;45:40**e**8.

[34] Onuma EK, Amenta PS, Jukkola AF, Mohan V, Borra S, Das KM. A phenotypic change of small intestinal epithelium to colonocytes in small intestinal adenomas and adenocarcinomas. Am J Gastroenterol 2001;96:2480**e**5.

Tropism of Severe Acute Respiratory Syndrome Coronavirus 2 for Barrett's Esophagus May Increase Susceptibility to Developing Coronavirus Disease 2019

Ramon U. Jin,[1,*] Jeffrey W. Brown,[2,*] Qing Kay Li,[3] Peter O. Bayguinov,[4] Jean S. Wang,[2] and Jason C. Mills[2,5,6]

[1]*Division of Oncology, Department of Medicine, Washington University in St Louis, School of Medicine, St Louis, Missouri;* [2]*Division of Gastroenterology, Department of Medicine, Washington University in St Louis, School of Medicine, St Louis, Missouri;* [3]*Department of Pathology, Johns Hopkins Medical Institutions, Baltimore, Maryland;* [4]*Washington University Center for Cellular Imaging, Washington University School of Medicine, St Louis, Missouri;* [5]*Department of Pathology and Immunology, Washington University in St Louis, School of Medicine, St Louis, Missouri; and* [6]*Department of Developmental Biology, Washington University in St Louis, School of Medicine, St Louis, Missouri*

Coronavirus disease 2019 (COVID-19), caused by severe acute respiratory syndrome coronavirus 2 (SARS-CoV-2), is a global pandemic, spurring the exigent need for determining how the virus is transmitted and what increases disease susceptibility.

Gastrointestinal (GI) symptoms are prominent in COVID-19, and live virus is detected along the GI tract and in stool.[1] SARS-CoV-2 enters host cells via its transmembrane spike glycoproteins that bind host angiotensin-converting enzyme 2 (ACE-2) protein on the cell surface, an interaction facilitated by spike protein cleavage catalyzed by host type II transmembrane serine protease (TMPRSS2).[2] Thus, concurrent cellular expression of ACE-2 and TMPRSS2 determines cellular tropism for SARS-CoV-2. Surveys of ACE-2 and TMPRSS2 in GI tissues have shown abundant expression in human intestines.[3] However, the low pH of gastric secretions[4] and the emulsifying conditions[3] of the small and large intestines inactivate the virus, limiting access of infective virus to distal GI tissues via the GI tract lumen.

Here, we show that individuals with intestinal metaplasia (ie, ectopic intestine-like cells in their esophagus as in Barrett's esophagus) would have increased potential for viable, ingested virus to interact with a receptive host epithelium. Thus, intestinal metaplasia could present a previously unappreciated orogastric route for viral entry in individuals with this condition.

Methods

All human tissue blocks were collected from the archives of The Johns Hopkins School of Medicine Bayview Medical Campus Department of Pathology. Barrett's esophagus organoids were derived from deidentified tissue from patients who were undergoing surveillance esophagogastroduodenoscopy for previously identified nondysplastic Barrett's esophagus and who provided informed consent through the Washington University School of Medicine Digestive Disease Research Core Center. Human tissue collection was approved by the review boards of each institution. Organoid cultures were infected with a chimeric virus expressing the SARS-CoV-2 spike protein (recombinant vesicular stomatitis virus [rVSV]–enhanced green fluorescent protein [eGFP]–SARS-CoV-2). Both fixed and live cells were imaged by light, epifluorescence, and live confocal microscopy.

Results

To test whether intestinal-type metaplasias of the proximal GI foregut might be receptive to SARS-CoV-2 infection, we determined ACE-2 and TMPRSS2 expression in a series of esophageal and gastric biopsies harboring intestinal metaplasia (Supplementary Table 1). Unlike normal esophageal and gastric tissue, intestinal-type metaplasia of the esophagus and stomach strongly expressed both ACE-2 and TMPRSS2 on epithelial cells with ACE-2 predominantly localized to the apical plasma membranes (Figure 1*A*, Supplementary Figure 1A, and Supplementary Table 1). The findings were corroborated by analyses of previous global surveys of RNA expression[5] showing that unlike normal esophageal and gastric tissue, intestinal-type metaplasias of these tissues aberrantly express *ACE2* and *TMPRSS2* messenger RNA.

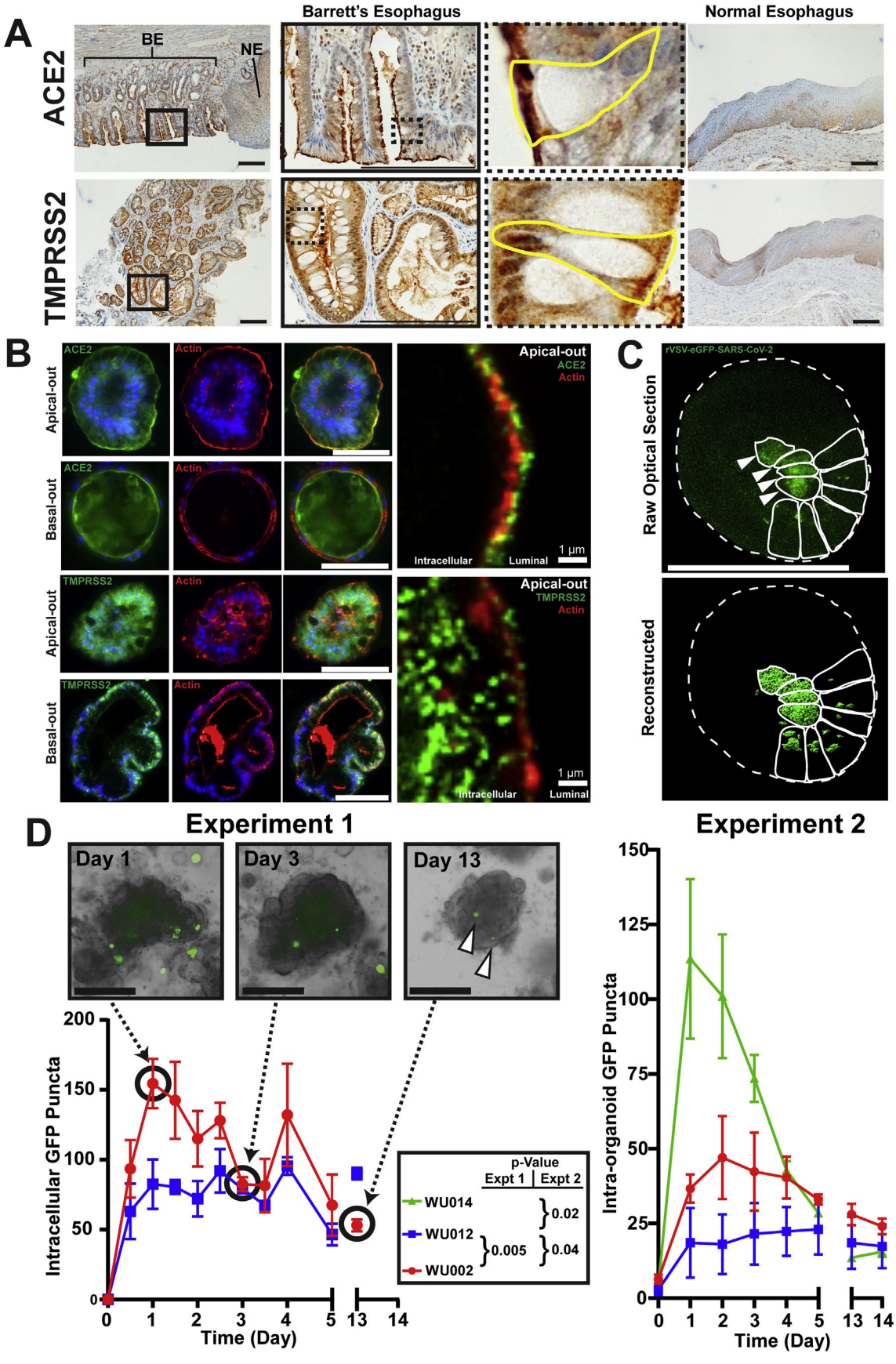
To test whether Barrett's metaplasia is susceptible to infection by SARS-CoV-2, we chose an ex vivo model: organoids derived from patients with Barrett's esophagus. We first demonstrated that organoids generated from biopsies of Barrett's esophagus faithfully reproduce the in vivo histopathologic characteristics (Supplementary Figure 1*B*). Specifically, they form a columnar monolayer that is low in expression of the foregut transcription factor SOX2, high in expression of the mid and hindgut transcription factor CDX2, reactive to the histochemical goblet cell mucin stain

*Authors share co-first authorship.

Abbreviations used in this paper: ACE-2, angiotensin-converting enzyme 2; COVID-19, coronavirus disease 2019; eGFP, enhanced green fluorescent protein; GI, gastrointestinal; rVSV, recombinant vesicular stomatitis virus; SARS-CoV-2, severe acute respiratory syndrome coronavirus 2; TMPRSS2, transmembrane protease, serine 2; VSV, vesicular stomatitis virus.

Most current article

© 2021 by the AGA Institute
0016-5085/$36.00
https://doi.org/10.1053/j.gastro.2021.01.024


A
Barrett's Esophagus
Normal Esophagus
ACE2
TMPRSS2
BE
NE
B
Apical-out
Basal-out
ACE2
Actin
TMPRSS2
Intracellular
Luminal
1 μm
C
rVSV-eGFP-SARS-CoV-2
Raw Optical Section
Reconstructed
D
Experiment 1
Experiment 2
Day 1
Day 3
Day 13
Intracellular GFP Puncta
Intra-organoid GFP Puncta
Time (Day)
p-Value
Expt 1 | Expt 2
WU014
WU012
WU002
0.02
0.005
0.04

Alcian blue, and, importantly for this study, maintain the apical expression of ACE-2 and TMPRSS2 (Figure 1*B* and Supplementary Figure 1*B* and *C*).

We incubated 3 Barrett's esophageal organoid lines (WU014, WU002, and WU012) harboring unique intestinal characteristics (Supplementary Figure 1*B*) with a chimeric virus (rVSV–eGFP–SARS-CoV-2) in which the SARS-CoV-2 spike protein replaces the VSV glycoprotein G and the eGFP gene is carried within viral RNA to report on intracellular translation of viral proteins. Thus, this chimeric virus exhibits the same tropism and cell invasion behavior of actual SARS-CoV-2 but can be studied in a Biosafety Level 2 facility. rVSV–eGFP–SARS-CoV-2 infected cells within 12 hours, and the GFP signal, indicating active translation of viral RNA, persisted until our last time point 2 weeks later (Figure 1*C* and *D*; Supplementary Figure 1*D*). We observed in an initial experiment (Experiment 1, Figure 1*D*) that although both patient organoid lines were efficiently infected, the line with increased intestinalization (ie, lower SOX2-to-CDX2 ratio; Supplementary Figure 1*B*) was more extensively infected. We thus repeated the experiment (Experiment 2, Figure 1*D*)but added an additional line (WU0014) featuring even greater intestinal features (Supplementary Figure 1*B*). In Experiment 2, we also reasoned virus in patients would encounter intact epithelium, so we scored only those infected cells within organoids above a threshold size. Together, these organoid results show that Barrett's esophagus may serve as a novel in vivo niche for SARS-CoV-2 and that viral entry may increase with increasing intestinalization (Figure 1*D*).

Discussion

Esophageal and gastric metaplasia are caused by chronic injury and predispose individuals to developing adenocarcinoma of the respective tissue.[6,7] However, the data presented here suggest that these metaplasias may also have other unanticipated consequences.

We show that intestinal-type metaplasia of the esophagus and stomach aberrantly express the proteins critical for binding and invasion by SARS-CoV-2: ACE-2 and TMPRSS2. Recent studies have demonstrated that the low pH of the stomach and the luminal fluid of the small and large intestines greatly attenuate the infectivity of SARS-CoV-2 that is present in swallowed oral secretions and refluxed respiratory sputum.[3,4] Thus, the ectopic, proximal expression of ACE-2 and TMPRSS2 may become salient because it means host receptors for SARS-CoV-2 are located in a region of the digestive tract where higher viable viral titers exist after ingestion. Moreover, individuals with known Barrett's esophagus are almost universally treated with proton pump inhibitors, and those with gastric intestinal metaplasia almost invariably have loss of acid-secreting parietal cells.[6,7] Thus, the decreased ability for the stomach to produce acid either by pharmacologic inhibition or loss of acid-secreting cells may compound the risk due to increased gastric pH that could result in increased viral titers and prolonged exposure. In addition, epidemiologically, intestinal metaplasia increases with age and male sex, paralleling demographics of those most susceptible to COVID-19.[8]

Previous work indicated that viable virus infects cells via SARS-CoV-2 spike protein interaction with apical ACE-2 receptor. Two factors in our cultures increased apical exposure of cells to virus: (1) we administered virus immediately after passaging (ie, after dissociating organoids to single cells exposing all cell surfaces), and (2) as new Barrett's organoids form, many wholly or partially orient "apical-out," that is, with cell apices exposed to the culture medium (Figure 1*B*). Importantly, all 3 organoid lines had equivalent distribution of apical-out, basal-out, and hybrid orientations (data not shown) indicating orientation did not affect infectivity.

Figure 1. Barrett's esophagus expresses ACE-2 and TMPRSS2 and is readily infected by rVSV–eGFP–SARS-CoV-2. (*A*) Human Barrett's esophagus immunohistochemistry shows expression of apical ACE-2, the host receptor for the SARS-CoV-2 spike protein, and TMPRSS2, the necessary protease. Insets highlight individual goblet cells outlined in yellow with apical ACE-2 and TMPRSS2 expression patterns. Normal esophagus does not express apical ACE-2 or TMPRSS2. Scale bars, 200 μm. BE, area of Barrett's esophagus; NE, adjacent area of normal squamous esophagus. (*B*) Barrett's organoids grow with various mixtures of "apical-out" and "basal-out" arrangements. Epifluorescence imaging of fixed organoids demonstrates apical ACE-2 staining (*green*) and TMPRSS2 staining (*green*) with b-actin staining (*red*) highlighting the apical surface. Confocal imaging using an Airyscan detector in SR mode showing super-resolution co-localization of ACE-2 (*green*) and TMPRSS2 (*green*) with apical b-actin (*red*); intracellular and luminal spaces are highlighted. Scale bars, 100 μm or as indicated. (*C*) Z-stack still image of live confocal microscopy of infected Barrett's organoids with raw optical section and 3-dimensional reconstruction shown. Organoid outer surface marked by *dotted line*, and individual green infected cells are outlined with a *solid line* in each organoid, showing diffuse cytoplasmic (*arrowheads*) and punctate vesicular GFP patterns. Scale bars, 100 μm. (*D*) Incubation of Barrett's esophagus organoids (WU014 with mostly intestinal features, WU002 with mixed intestinal–gastric features, and WU012 with mostly gastric features; see Supplementary Figure 1*B*) with rVSV–eGFP–SARS-CoV-2. Experiment 1: quantification of all intracellular punctate GFP foci in Barrett's organoids (2 independent cultures); Experiment 2: only GFP puncta within organoids > 10 μm scored (3–6 independent cultures) at specified time points for 2 weeks. Live-cell brightfield and fluorescence imaging of WU002 Barrett's organoids at time points indicated. Note: A single field of organoids is followed serially in each panel. Persistently infected (green from GFP translated from rVSV–eGFP–SARS-CoV-2 virus) cells are indicated at the day 13 time point (*arrowheads*). Scale bars, 200 μm. *P*-values by 2-tailed, paired Student's *t* test (Experiment 1) and by analysis of variance with Dunnett multiple comparison test to WU012 as control (Experiment 2) of the area under the curve at each time point from the first time point to day 5 (see Supplementary Methods).

Overall, our data suggest that individuals with intestinal-type metaplasias of the proximal GI tract (eg, Barrett's esophagus, in particular) are potentially at higher risk for developing or experiencing a more severe presentation of COVID-19 relative to the general population. Future studies to determine the additional risk posed by ectopic proximal expression of ACE-2 and TMPRSS2 should include infection of a much broader panel of organoids of varying intestinal differentiation and, eventually, large-scale retrospective database analyses correlated with autopsy series to analyze COVID-19 outcome vs viral load and extent of metaplasia.

Supplementary Material

Note: To access the supplementary material accompanying this article, visit the online version of *Gastroenterology* at www.gastrojournal.org, and at https://doi.org/10.1053/j.gastro.2021.01.024.

References

1. Xiao F, et al. Gastroenterology 2020;158:1831–1833.
2. Hoffman M, et al. Cell 2020;181:271–280.
3. Zang R, Castro MFG, et al. Sci Immunol 2020;5:eabc3582.
4. Zang R, Castro MFG, et al. BioRXiv 2020.
5. di Pietro M, et al. Proc Natl Acad Sci 2012;109:9077–9082.
6. Spechler SJ, et al. N Engl J Med 2014;371:836–845.
7. Amieva M, et al. Gastroenterology 2016;150:64–78.
8. Wu Z, et al. JAMA 2020;323:1239–1242.

Author names in bold are co–first authors.

Received September 3, 2020. Accepted January 10, 2021.

Correspondence
Address correspondence to: Jason C. Mills, MD, PhD, Washington University in St Louis, School of Medicine, 660 South Euclid Avenue, Campus Box 8124, St Louis, MO 63110. e-mail: jmills@wustl.edu; or Jeffrey W. Brown, M.D., Ph.D. Washington University in St. Louis, School of Medicine 660 S. Euclid Avenue, Campus Box 8124 St. Louis, MO 63110. e-mail: brownjw@wustl.edu.

Acknowledgments
The authors thank Sean P. J. Whelan, PhD, and James A. J. Fitzpatrick, PhD, from the Washington University School of Medicine, St Louis, and Alan K. Meeker, MAT, PhD, from the Johns Hopkins Medical Institutions, Baltimore, for their collaboration on this article.

CRediT Authorship Contributions
Ramon U. Jin, MD, PhD (Conceptualization: Equal). Jeffrey W. Brown, MD, PhD (Writing – original draft: Equal). Qing Kay Li, MD, PhD (Investigation: Supporting). Peter O. Bayguinov, PhD (Investigation: Supporting). Jean S. Wang, MD, PhD (Resources: Supporting). Jason C Mills, MD, PhD (Conceptualization: Equal; Investigation: Supporting; Resources: Equal; Supervision: Lead).

Conflicts of interest
The authors disclose no conflicts.

Funding
This study was supported by the American Gastroenterological Association Foundation AGA-Takeda COVID-19 Rapid Response Research Award AGA2021-5101 and the Department of Defense through the Peer Reviewed Cancer Research Program (PRCRP) program under award no. W81XWH-20-1-0630 to Jeffrey W. Brown; the Washington University Center for Cellular Imaging (supported by Washington University School of Medicine), the Children's Discovery Institute of Washington University and St Louis Children's Hospital (CDI-CORE-2015-505 and CDI-CORE-2019-813), the Foundation for Barnes-Jewish Hospital (3770 and 4642), and the Alvin J. Siteman Cancer Center at Barnes-Jewish Hospital and Washington University School of Medicine (P30 CA091842) to Peter O. Bayguinov and James A. J. Fitzpatrick (collaborator); the Advanced Imaging and Tissue Analysis Core of the Washington University Digestive Disease Research Core Center (P30 DK052574) and the Oncology Tissue Core at JHU (P30 CA006973); grant T32HL007088 to Ramon U. Jin; the BETRNet (NCI U54CA163060) to Ramon U. Jin and Jason C. Mills; and NIH grants R21DK111369, R01DK105129, and R01DK110406 to Jason C. Mills.

Supplementary Methods

Human Sample Collection, Immunohistochemistry, and Quantification

Formalin-fixed paraffin-embedded tissue blocks of the esophagus (n ¼ 26) and stomach (n ¼ 5) were from The Johns Hopkins School of Medicine Bayview Medical Campus Department of Pathology with Institutional Review Board approval. Formalin-fixed paraffin-embedded blocks were cut into 4-mm sections, deparaffinized, and rehydrated before incubation with primary antibodies.

For manual ACE-2 immunostaining, heat-induced antigen retrieval was via a steamer using Antigen Unmasking Solution (H-3300; Vector Laboratories) with blocking of endogenous peroxidase and phosphatase (S2003; Dako). Anti-ACE2 (1:2000 dilution, Ab15348; Abcam) was detected by horseradish peroxidase (HRP)-labeled anti-rabbit secondary antibody (PV6119; Leica Microsystems), visualized with 3,3^0-diaminobenzidine (D4293; Sigma-Aldrich), and counterstained with Mayer's hematoxylin. ACE-2 autostaining used a Ventana Discovery Ultra autostainer (Roche Diagnostics) with antigen retrieval performed by Ventana Ultra CC1 buffer (no. 6414575001; Roche Diagnostics). Primary antibody was detected with an anti-rabbit HQ detection system (nos. 7017936001 and 7017812001; Roche), visualized with the Chromomap DAB IHC detection kit (no. 5266645001; Roche) and counterstained with hematoxylin. For TMPRSS2 immunostaining, autostaining was done as above with anti-TMPRSS2 (1:12,000 dilution, Ab92323; Abcam) primary antibody detected with the same anti-rabbit HQ detection system (nos. 7017936001 and 7017812001; Roche), visualized by the Chromomap DAB IHC kit (no. 5266645001; Roche Diagnostics), and counterstained with hematoxylin.

ACE2 and TMPRSS2 staining were quantified in areas of Barrett's esophagus or gastric intestinal metaplasia through review of hematoxylin and eosin histology. ACE-2 and TMPRSS2 stained serial sections were scored as follows: 0 ¼ no apical staining; 1 ¼ <50% of apical staining, 2 ¼ >50% apical staining in 20× fields of view in areas of Barrett's esophagus or gastric intestinal metaplasia and adjacent tissue controls when available.

Human Barrett's Esophagus Organoid Culture System

Barrett's esophagus organoids were derived from deidentified tissue from patients who were undergoing Barrett's esophagus surveillance esophagogastroduodenoscopy for previously identified nondysplastic Barrett's esophagus, approved by the Institutional Review Board of Washington University School of Medicine, and who provided informed consent through the Washington University School of Medicine Digestive Disease Research Core Center. In brief, Barrett's esophagus organoids were cultured with L-WRN-conditioned media[1] supplemented with 10 nM gastrin (Sigma-Aldrich), 10 mM nicotinamide (Sigma-Aldrich), 500 nM A83-01 (Tocris), 10 mM SB202190 (Sigma-Aldrich), 200 ng/mL FGF10 (Peprotech), 10 mM Y-27632 (Sigma-Aldrich), and Primocin (Invivogen) in 3D Matrigel (Corning) in 24-well plates.[2] Organoids were expanded and passaged every 7–10 days (except for virus infection experiments, see below) by mechanical dissociation from Matrigel, dispersed using TrypLE (Thermo Fisher) and manual pipetting, and transferred into new Matrigel and plated in 24-well plates.

Human Barrett's Esophagus Organoid Immunofluorescence/Immunohistochemical Staining

Human Barrett's esophagus organoids were pelleted and fixed in 10% formalin at 4°C for 1 hour. Organoids were washed, moved to 70% ethanol, mounted in 3% agar, and embedded in paraffin. Blocks were cut into 7-mm sections. For immunofluorescence, tissue microtome sections underwent a standard deparaffinization with xylene and rehydration protocol and were antigen retrieved in sodium citrate buffer (2.94 g sodium citrate, 500 mL Tween 20, pH 6.0) using a pressure cooker. Sections were blocked in 1% bovine serum albumin, 0.3% Triton X-100 in phosphate-buffered saline, and incubated with primary antibodies: anti-ACE-2 (1:100 dilution, catalog no. Ab15348; Abcam), anti-TMPRSS2 (1:100 dilution, catalog no. HPA035787; Sigma-Aldrich), and anti-b-Actin (1:200 dilution, catalog no. A1978; Sigma-Aldrich). Fluorescent secondary antibodies were applied, and slides were mounted using ProLong Gold antifade reagent with DAPI (Molecular Probes). For immunohistochemistry, the same manual staining procedure for anti-ACE-2 staining and autostaining procedure for TMPRSS2 was used as described above.

Viral Infection of Human Barrett's Esophagus Organoids and Quantification

rVSV–eGFP–SARS-CoV-2 chimeric virus (eGFP reporter encoded in the viral RNA) was constructed by 2 collaborating authors (P.W. Rothlauf and S.P.J. Whelan) using the SARS-CoV-2 Wuhan-Hu-1 spike and the VSV Indiana strain.[3] The virus was generated and recovered according to previous published methods[4] and propagated in MA104 cells (ATCC). Organoids were infected with 2.5 × 10^5 plaque forming units (PFU) of infectious rVSV–eGFP–SARS-CoV-2 (muliplicity of infection [MOI] ¼ 0.5) for long-term infection assays or for 48 hours before live confocal imaging.

For long-term organoid viral quantification experiments, 75,000 Barrett's esophagus cells were seeded into 48-well plates before viral infections as described. Brightfield and fluorescent imaging was performed using the BioTek Lionheart Cell Imaging Multimode Reader as described below every 12 hours for 312 hours total or every day for 14 days. Visible green punctate per well was counted for Experiment 1, and visible green puncta in organoids larger than 10 mm were counted for Experiment 2. These data were then graphed and analyzed using GraphPad Prism 8.1.1. For statistical analysis that incorporated the repeated, sequential measures of the same cultures over time, data were transformed by measuring the area under the curve for each time point until day 5 (the time point in both

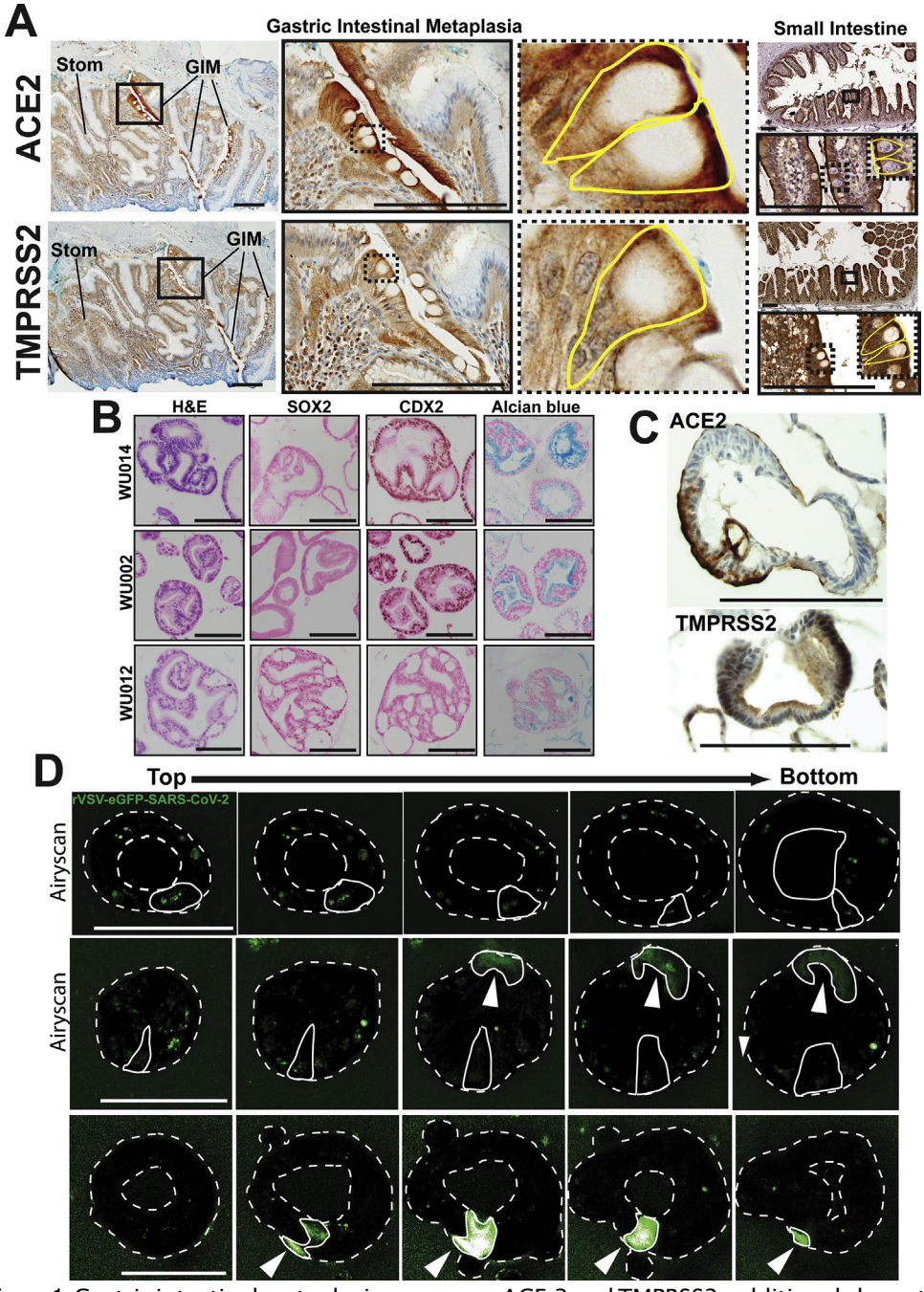
experiments when peak viral entry returned toward a steady-state, baseline in all organoid lines). Statistical significance was calculated from the transformed data (ie, the area under the curve calculations). For the 2 organoid lines in Experiment 1, a paired 2-tailed Student's t test was used. Statistical significance for Experiment 2 was calculated using paired analysis of variance of mean area under the curve values with post hoc Dunnett correction where WU012 was considered the control. Alpha was 0.05 for all approaches.

Imaging

Fluorescence microscopy was performed using a Zeiss Axiovert 200 microscope with an Axiocam MRM camera and Apotome II instrument for grid-based optical sectioning. Immunofluorescence images were taken on a Zeiss Apotome. Brightfield images were taken on an Olympus BX43 light microscope. Long-term infection organoid fluorescent imaging was performed on a BioTek Lionheart Cell Imaging Multimode Reader. Live confocal imaging was performed at the Washington University Center for Cellular Imaging using a Zeiss LSM880 Confocal Microscope with Airyscan unit and Pecon stage-top incubator. Images were analyzed and postimaging adjustments were performed with Adobe Photoshop CS6, and line art was generated in Adobe Illustrator CS6.

References

1. VanDussen KL, S, et al. Stem Cell Res 2019;37:101430.
2. Sato T, et al. Gastroenterology 2011;141:1762–1772.
3. Case JB, et al. Cell Host Microbe 2020;28:475–485.
4. Whelan SP, et al. Proc Natl Acad Sci USA 1995;92:8388–8392.



Supplementary Figure 1. Gastric intestinal metaplasia expresses ACE-2 and TMPRSS2; additional characterization of Barrett's esophagus organoids. (*A*) Immunohistochemistry of human gastric intestinal metaplasia (*GIM*) and adjacent stomach (*Stom*) shows apical expression of ACE-2 and TMPRSS2. Small intestine staining for both proteins shown as a positive control. Insets highlight individual goblet cells outlined in *yellow* with apical ACE-2 and TMPRSS2 expression patterns. Scale bars, 200 ㎜. (*B*) Hematoxylin and eosin images demonstrating the distinct columnar epithelium morphology and immunohistochemical staining of SOX2 (*brown* nuclear pattern), CDX2 (*brown* nuclear pattern), and Alcian blue (*blue* vesicular cytoplasmic pattern) for 3 human Barrett's esophagus organoid lines (WU014, WU002, and WU012). Scale bars, 100 ㎜. (*C*) Immunohistochemical staining of ACE-2 (*brown* apical cytoplasmic) and TMPRSS2 (*brown* diffuse cytoplasmic) for the intestinal WU002 human Barrett's esophagus organoid line. Scale bars, 100 ㎜. (*D*) Three-dimensional confocal Z-stack series ("top" of the organoid to the "bottom") with Airyscan detector used as indicated of live Barrett's organoids infected with rVSV–eGFP–SARS-CoV-2 demonstrating diffuse cytoplasmic (*arrowheads*) and punctate vesicular green GFP patterns. The organoid lumen and outer surface are marked by a *dotted line*. As an example, individual infected cells are outlined with a *solid line* in each organoid. Individual green infected cells are outlined with a *solid line* in each organoid showing diffuse cytoplasmic (*arrowheads*) and punctate vesicular GFP patterns. Scale bars, 100㎜.

Age	Sex	PPI Use	Biopsy Location	Diagnosis	ACE2 Score (Metaplasia)	ACE2 Score (Adjacent Tissue)	TMPRSS2 Score (Metaplasia)	TMPRSS2 Score (Adjacent Tissue)
57	M	Yes	Esophagus	Barrett's without dysplasia	1	0	1	0
82	M	Yes	Esophagus	Barrett's without dysplasia	2	0	1	0
63	M	No	Esophagus	Barrett's without dysplasia	2	0	1	0
78	M	Yes	Esophagus	Barrett's without dysplasia	1	1	1	0
75	M	Yes	GE Junction	Barrett's without dysplasia	2	0	1	0
76	M	Yes	Esophagus	Barrett's without dysplasia	1	0	1	0
60	F	Yes	GE Junction	Barrett's without dysplasia	1	0	2	0
57	M	Yes	Esophagus	Barrett's without dysplasia	2	N/A	1	N/A
66	M	Yes	Esophagus	Barrett's without dysplasia	2	0	0	0
68	M	No	Esophagus	Barrett's without dysplasia	2	0	1	0
59	M	No	Esophagus	Barrett's without dysplasia	2	0	1	0
71	M	Yes	Esophagus	Barrett's without dysplasia	2	0	1	0
75	M	Yes	GE Junction	Barrett's without dysplasia	2	0	1	0
66	M	Yes	Esophagus	Barrett's with Low-grade dysplasia	2	N/A	1	N/A
84	M	Yes	Esophagus	Barrett's with Low-grade dysplasia	2	0	1	0
66	M	Yes	Esophagus	Barrett's with Low-grade dysplasia	2	0	2	0
54	F	Yes	Esophagus	Barrett's with High-grade dysplasia	2	0	1	0
67	M	Yes	Esophagus	Barrett's with High-grade dysplasia	2	0	2	0
71	M	No	Esophagus	Barrett's with High-grade dysplasia	2	0	1	0
60	M	No	Esophagus	Barrett's with High-grade dysplasia	1	0	1	0
53	M	Yes	GE Junction	Barrett's with High-grade dysplasia	2	0	2	0
60	F	Yes	GE Junction	Barrett's with High-grade dysplasia	2	0	2	0
78	M	Yes	Esophagus	Barrett's with High-grade dysplasia	2	0	1	0
60	F	No	Esophagus	Barrett's with High-grade dysplasia	2	0	1	0
65	M	No	Esophagus	Barrett's with High-grade dysplasia	2	0	1	0
51	M	No	Esophagus	Barrett's with High-grade dysplasia	2	0	2	0
54	M	Yes	Gastric	Intestinal Metaplasia	1	0	0	0
49	F	No	Gastric	Intestinal Metaplasia	2	0	1	0
73	M	Yes	Gastric	Intestinal Metaplasia	2	N/A	1	N/A
76	M	Yes	Gastric	Intestinal Metaplasia	2	0	1	0
69	M	No	Gastric	Intestinal Metaplasia	1	0	1	0

Supplementary Table 1. Barrett's esophagus and gastric intestinal metaplasia express ACE-2 and TMPRSS2. Patient age, sex, protein pump inhibitor (PPI) use, biopsy location (esophagus, gastroesophageal junction, stomach), pathologic diagnosis, and quantification of ACE-2 and TMPRSS2 immunohistochemical staining in human tissue specimens of Barrett's esophagus (Barrett's without dysplasia, Barrett's with low-grade dysplasia, Barrett's with high-grade dysplasia) and gastric intestinal metaplasia. Scoring system: 0¼ no apical staining; 1¼ <50% of apical staining, 2¼>50% apical staining in 20× fields of view in areas of Barrett's esophagus or gastric intestinal metaplasia and adjacent tissue controls. N/A, areas without adjacent tissue controls.

ATF3 induces RAB7 to govern autodegradation in paligenosis, a conserved cell plasticity program

Authors: Megan D. Radyk[1], Lillian B. Spatz[1], Bianca L. Peña[1], Jeffrey W. Brown[1], Joseph Burclaff[1], Charles J. Cho[1], Yan Kefalov[1], Chien-Cheng Shih[2], James A.J. Fitzpatrick[2,3,4], Jason C. Mills[†1,5,6,7]

[1]Division of Gastroenterology, Department of Medicine, Washington University School of Medicine

[2]Washington University Center for Cellular Imaging, Washington University School of Medicine

[3]Departments of Neuroscience and Cell Biology & Physiology, Washington University School of Medicine

[4]Department of Biomedical Engineering, Washington University in St. Louis

[5]Department of Developmental Biology, Washington University School of Medicine

[6]Department of Pathology and Immunology, Washington University School of Medicine

[7]Current address and affiliation: Section of Gastroenterology and Hepatology, Departments of Medicine and Pathology, Baylor College of Medicine, Houston, TX

†**Correspondence:**

Jason C. Mills
Baylor College of Medicine
Houston, TX 77030
314-362-4213
314-362-7487 (fax)
jmills@wustl.edu

Key Words: Plasticity, Spasmolytic Polypeptide Expressing Metaplasia (SPEM), Acinar-Ductal Metaplasia (ADM), BHLHA15, RAB5

ABSTRACT (175 words)

Differentiated cells across multiple species and organs can reenter the cell cycle to aid in injury-induced tissue regeneration by a cellular program called paligenosis. Here we show that Activating Transcription Factor 3 (ATF3) is induced early during paligenosis in multiple cellular contexts, transcriptionally activating the lysosomal trafficking gene *Rab7b*. ATF3 and RAB7B are upregulated in gastric and pancreatic digestive-enzyme-secreting cells at the onset of paligenosis Stage 1, when cells massively induce autophagic and lysosomal machinery to dismantle differentiated cell morphological features. Their expression later ebbs before cells enter mitosis during Stage 3. *Atf3*$^{-/-}$ mice fail to induce RAB7-positive autophagic and lysosomal vesicles, eventually causing increased death of cells *en route* to Stage 3. Finally, we observe that ATF3 is expressed in human gastric metaplasia and during paligenotic injury across multiple other organs and species. Thus, our findings indicate *ATF3* is an evolutionarily conserved gene orchestrating the early paligenotic autodegradative events that must occur before cells are poised to proliferate and contribute to tissue repair.

INTRODUCTION

Injury in adult organisms can trigger differentiated cells to reprogram to an embryonic-like, progenitor state. The change from a differentiated cell to a proliferating progenitor-like cell has been shown in nearly every organ, for example: kidney (Kusaba *et al*, 2014), lung (Hong *et al*, 2001; Tata *et al*, 2013), stomach (Nam *et al*, 2010; Leushacke *et al*, 2017; Radyk *et al*, 2018; Willet *et al*, 2018; Meyer *et al*, 2019), pancreas (Mills & Sansom, 2015; Willet *et al.*, 2018), intestine (van Es *et al*, 2012; Jones *et al*, 2019), and liver (Raven *et al*, 2017; Chen *et al*, 2020). As early as 1900, it was proposed that such cellular retooling was a fundamental feature shared by cells, suggesting an evolutionarily conserved program that mature cells could invoke to reroute their energy from performing differentiated cell functions (like secretion of digestive enzymes) to instead undergo mitosis (Adami, 1900).

In the last few years, we have begun to delineate the shared features of injury-induced conversion of mature cells to regenerating proliferative cells (a process termed paligenosis) (Willet *et al.*, 2018). Paligenosis progresses via three distinct, sequential stages: 1) Autodegradation of mature cell structures via lysosomal and autophagy pathways, 2) Shift to expression of a progenitor or embryonic gene network, 3) Re-entry into the cell cycle. Much evidence indicates metaplasias largely arise via cell plasticity (often paligenosis), in particular Spasmolytic Polypeptide-Expressing Metaplasia (SPEM) in the stomach and Acinar-to-Ductal Metaplasia (ADM) in the pancreas (Storz, 2017; Burclaff & Mills, 2018; Meyer & Goldenring, 2018). Metaplasia is a lesion characterized by expression of progenitor/embryonic genes, often with increased proliferation, ultimately leading to increased risk for tumorigenesis. Recently, it has become clear that metaplasia in healthy organisms is an evolutionarily conserved injury response that is usually simply a transient, regenerative state that allows tissue to recruit mature cells to help repair injury after large-scale damage (Goldenring, 2018; Saenz & Mills, 2018; Saenz *et al*, 2018; Burclaff *et al*, 2020). It is likely that increased cancer risk occurs when

metaplasia is chronic and/or with repeated injury (Amieva & Peek, 2016; Giroux & Rustgi, 2017; Storz, 2017; Jin & Mills, 2019; Wroblewski *et al*, 2019). Accordingly, loss of a key paligenosis gene, *Ddit4*, increases tumorigenesis by allowing cells to proliferate even with DNA damage present (Miao *et al*, 2021). This further demonstrates the need to better understand paligenosis as a process that guards against cancer initiation.

Given the evolutionarily conserved role of paligenosis as a mechanism underlying both regeneration and tumorigenesis, we attempted to identify the core set of genes that might be largely dedicated to executing paligenosis. Such paligenosis genes would be expected to be evolutionarily conserved, shared across all tissue types, and required only for injury-induced proliferation of differentiated cells but not in dedicated stem cells or during embryonic development. We recently showed that two genes meeting those criteria are *Ddit4* (mentioned above) and *Ifrd1*. DDIT4 is invoked early in paligenosis to quench mTORC1, which must be shut off for the massive autophagy and lysosomal activity of Stage 1, while IFRD1 is essential to restore mTORC1 activity for entry into S phase (Miao *et al*, 2020b).

Here we dissect the conserved genetic program that drives the activation of the autodegradation activity in Stage 1. We focus on mechanisms conserved across two exocrine cell populations in two different organs: gastric zymogenic chief cells (ZCs) and pancreatic acinar cells (ACs). These, almost entirely postmitotic, cells live months to years in the absence of injury. ZCs and ACs have large, polarized morphologies with abundant rough endoplasmic reticulum (rER) and numerous, large secretory granules. Their secretory architecture is maintained almost entirely by a two-step transcriptional regulation program with X-box-binding protein 1 (Huh *et al*, 2010; Hess *et al*, 2011) transcriptionally activating the secretory granule trafficking transcription factor MIST1 (encoded by *Bhlha15*) (Pin *et al*, 2001; Ramsey *et al*, 2007; Lo *et al*, 2017; Dekaney *et al*, 2019). MIST1 induces and maintains expression of numerous transcriptional targets whose gene products in turn coordinate cellular organization, vesicular

trafficking, and stress responses (Kowalik *et al*, 2007). For example, MIST1 binds to and directly upregulates the pro exocrine secretory apparatus Rab proteins RAB26 and RAB3D by direct transcriptional upregulation of their genes (Tian *et al*, 2010; Mills & Taghert, 2012; Jin & Mills, 2014). MIST1 is an unusual transcription factor, in that it acts as a scaling factor for cell architecture and maturity by regulating abundance of cell trafficking proteins (Mills & Taghert, 2012).

Rab proteins, like RAB26, RAB3D and RAB27, are important in gastric zymogenic chief cells and pancreatic acinar cells because they help maintain secretory cell function and cell state (Ohnishi *et al*, 1996; Tian *et al.*, 2010; Jin & Mills, 2014; Hou *et al*, 2015; Lo *et al.*, 2017). Other Rab GTPases, like RAB5, RAB7, and RAB9 organize the endolysosomal system. RAB5 traffics the early endosome, RAB7 traffics the late endosome, lysosome, and autophagosome, and RAB9 traffics late endosomes as they transition to the trans-golgi network (Wandinger-Ness & Zerial, 2014; Langemeyer *et al*, 2018). There are over 70 human Rab GTPases which exhibit some overlap in function but can also exhibit distinct functions based on intrinsic characteristics or through protein cofactors. For example, RAB7A and RAB7B are both known to control late endosome maturation and lysosome biogenesis (Guerra & Bucci, 2016); however, they cannot be defined as isoforms because they do not share conserved motifs (Pereira-Leal & Seabra, 2000). The function of RAB7A is generally restricted to late endosomes and facilitates the transition to lysosomes (Bucci *et al*, 2000), while RAB7B can control endosomal transport to the trans-golgi network (Guerra & Bucci, 2016) and can interact with cystine protease ATG4B to modulate autophagy (Kjos *et al*, 2017).

We will show that Activating Transcription Factor 3 (ATF3) is induced during paligenotic injury in diverse organs, working to reverse the MIST1 cell maturation program early in Stage 1. ATF3 is a highly conserved transcription factor with clear orthologues even in primitive multicellular organisms like sea anemones (*Nematostella vectensis*;

https://omabrowser.org/oma/) (Altenhoff *et al*, 2018). It is rapidly induced following injury, and *Atf3* loss in multiple organisms and tissues generally exhibits phenotypes after injury (Hartman *et al*, 2004; Li *et al*, 2010; Wang *et al*, 2012; Brooks *et al*, 2015; Gey *et al*, 2016; Fazio *et al*, 2017; Zhao *et al*, 2017; Zhu *et al*, 2018). It has also been shown to transcriptionally repress MIST1 (Fazio *et al.*, 2017).

Here we show that ATF3 also has a surprising role in vesicle trafficking: it binds to and transcriptionally activates *Rab7b* (also previously identified as *Rab42* (Itoh et al, 2006; Marubashi & Fukuda, 2020)), which helps govern the maturation of late endosomes to lysosomes (Yang *et al*, 2004; Progida *et al*, 2010; Stroupe, 2018). We show RAB7 expression increases dramatically in early paligenotic exocrine cells, forming large accumulations of vesicles and co-labeling, as expected, with autophagic and lysosomal vesicles. Using *ATF3* overexpression and knockdown constructs in human epithelial cells and *Atf3* $^{-/-}$ mice, we show that autodegradative machinery depends on ATF3, partly through transcriptional regulation of *Rab7b.* Owing to failed degradation in Stage 1, *Atf3*$^{-/-}$ mice also have markedly aberrant later stages of paligenosis with increased cell death and decreased proliferation and regeneration in paligenosis Stage 3. We also find ATF3 expression focally in human SPEM, suggesting ATF3 is a staple in early transitions to metaplasia. These data indicate that ATF3 is a key evolutionarily conserved paligenosis gene that acts as one of the first proteins activated in paligenotic injury. It works principally to induce autodegradation, in part, by increasing the lysosome and autophagy coordinator *Rab7b.*

RESULTS

Degradation of specialized cell features follows exocrine cell injury

To better characterize the early, autodegradation phase of paligenosis at ultrastructural resolution, we identified the organelles and trafficking features that characterize the earliest morphological changes after injury. To induce stomach injury, we used high-dose tamoxifen (HDT), which has been described by our lab and others to quickly and synchronously elicit a stomach injury and induce SPEM independent of estrogen receptor activity or sex of mice (Huh *et al*, 2012; Saenz *et al*, 2016; Leushacke *et al.*, 2017; Keeley *et al*, 2019). To induce pancreas injury, we repeatedly treated with the secretagogue cerulein, which has long been described to cause damage to the exocrine pancreas (Adler *et al*, 1985; Niederau *et al*, 1985; Saluja *et al*, 1985; Willet *et al.*, 2018). Injury timelines and how the time points correspond to paligenosis stages are indicated in Figure EV1A-B.

We analyzed the initial downscaling stage of paligenosis via focused ion beam-scanning electron microscopy (FIB-SEM;) three-dimensional (3D) nanotomography (Figure 1A and Movie EV1-4). FIB-SEM of vehicle-treated ZCs compared to 24h HDT-treated ZCs revealed a dense accumulation of lysosomes and autolysosomes in the basal region of the cell, where the cell's rER network and many mitochondria are concentrated. In addition to loss of rER, we saw exocrine granule degradation as well as swelling and fragmenting of mitochondria. The ultrastructural changes were corroborated by immunofluorescence at 6 and 24h HDT showing gradual loss of GIF^+ exocrine granules coincident with increased $LAMP1^+$ lysosomes (Figure 1B). Transmission electron microscopy (tEM) showed that ZCs following 24h HDT injury harbored increased lysosomes and double-membrane bound vesicles (consistent with autophagosomes) filled with cell components, such as granules, ER, and cytosol (Figure 1C). Granular census was also reduced (Figure 1D), consistent with downscaling of mature cell architecture and an increase in single- and double- membraned vesicles which we summarize

and quantify as autodegradation events (Figure 1E). Similarly, we saw a trend towards decreased granule number and significantly increased autodegradation events in pancreatic ACs following repeated cerulein (CER) injury for one day (Figures 1F-H). These results support our initial description (Willet *et al.*, 2018) that Stage 1 of paligenosis consists of an increase in both lysosomal and autophagic degradation pathways and further clarifies which organelles are targeted for degradation.

We wanted to determine if lysosomes and autophagosomes are required for paligenosis progression in the stomach, so we treated mice with hydroxychloroquine (HCQ; 60mg/kg/day). Intraperitoneal injection of HCQ. dampens autophagic activity by blocking autophagosome-lysosome fusion (Rosenfeldt *et al*, 2013; Cao *et al*, 2017). A 3-day course of HCQ significantly decreased the fraction of stomach units that exhibit SPEM (Figure EV1C-F). We also saw many ZCs that appeared to never downscale their granules (meaning they did not undergo the autodegradative processes Stage 1), as marked by sustained GIF expression and residually large apical cytoplasms (Figure EV1D-F). Thus, lysosomes and autophagosomes are necessary for Stage 1 of paligenosis and, consequently, for subsequent progression of cells to Stage 2, which is characterized by induction of SPEM markers.

The massive degradation events occurring early in paligenosis indicated that cellular membrane trafficking was dramatically altered and pointed to alterations in the Rab family of small GTPases. RABs facilitate vesicle and organelle movement and are especially important for cells with secretory functions, like exocrine cells in the stomach and pancreas (Johnson *et al*, 2004; Faust *et al*, 2008; Fukuda, 2008; Tian *et al.*, 2010; Jin & Mills, 2014; Takahashi *et al*, 2017). RAB function can be regulated at the transcriptional level in exocrine cells (Johnson *et al.*, 2004; Tian *et al.*, 2010). Accordingly, we found a significant increase in *Rab7b* (though not *Rab5*, *Rab7a*, *Rab9*) mRNA at 12h HDT treatment: the time when the majority of ZCs are in Stage 1 of paligenosis (Figure 1I). Our analysis of a previously published dataset (Kowalik *et al.*,

2007) also suggests that *Rab7b* is expressed in pancreatic acinar cells following cerulein-induced pancreatitis. Together thefindings suggest that, like *Rab26* and *Rab3d*, *Rab7b* is transcriptionally controlled in exocrine cells.

163163

ATF3 binds to and directly induces the Rab7b gene during paligenotic downscaling

While there was little RAB7 expression in vehicle-treated stomach and pancreas, we observed large balloons and crescents of RAB7+ vesicles during stage 1 of paligenosis in stomach and pancreas (Figure 2A, 2D). Note that we have not found an antibody that can distinguish RAB7B from RAB7A in tissue sections, so we used total RAB7 antibody for these immunostaining studies. However, we favor the interpretation that the majority of the RAB7+ vesicles are likely RAB7B vesicles, given qRT-PCR and western blot showed only *Rab7b* mRNA and RAB7B protein are induced consistently after paligenotic injury in pancreas and stomach (Figure EV2A-B). In contrast, there was no consistent pattern of increased expression in any of the following paligenotic injury scenarios in pancreas and stomach: total RAB7 protein by western blot of whole tissue (Figure EV2A-B), *Rab7a* mRNA by qRT-PCR from whole tissue (Fig. 1I), and RAB7A protein by western blot of whole tissue (Figure EV2A-B).

We reasoned that the transcriptional upregulation of *Rab7b* specifically within early paligenosis might give us a route to identify, for the first time, early transcriptional regulators of the paligenosis process. Our previous work showed that MIST1 activates *Rab* transcription (eg *Rab3d* and *Rab26*) by binding within well-conserved *cis*-regulatory regions within the first intron. Thus, we used the MEME Suite web server (Bailey *et al*, 2009) and FIMO (Find Individual Motif Occurrences) software (Grant *et al*, 2011) to identify transcription factor binding sites within the first intron of *Rab7b*. A putative ATF3 binding motif was identified within this region. More detailed analysis using Contra v3 (Kreft *et al*, 2017) (http://bioit2.irc.ugent.be/contra/v3) (Figure EV3A-C) further corroborated that a potential ATF3 site was highly evolutionarily conserved

across mammals. ATF3 was previously characterized in the very early stages of cerulein-induced pancreatitis in mice (Fazio *et al.*, 2017; Data ref: Fazio *et al.*, 2017) and our *in-silico*-predicted ATF3 binding site matched a site from Chromatin Immunoprecipitation-sequencing (ChIP-Seq) analysis of genomic ATF3 binding early after cerulein injury from the published dataset (Figure EV3A-C). ATF3 was also an appealing target because it was previously described as one of the most highly upregulated genes in a mouse model of SPEM (Nozaki *et al*, 2008; Miao *et al.*, 2020b). Thus, the data pointed to ATF3 as a key transcription factor early in paligenosis, potentially activating *Rab7* to facilitate the massive autophagic changes in Stage 1.

Accordingly, ATF3 was rapidly induced specifically within ZCs and ACs following injury (Figure 2A, D), and *Atf3* transcript and ATF3 protein were also both increased in whole tissue analysis of the stomach and pancreas (Figure 2B-C). Specifically, ATF3 was dramatically increased early in paligenosis Stage 1, but its expression returned to almost homeostatic levels in paligenosis Stage 3. Moreover, ATF3 binding to the *Rab7b* gene in stomach tissue was confirmed using ChIP (Figure 2E) with primers designed to amplify genomic DNA including the consensus ATF3 intronic binding site described above (Fazio *et al.*, 2017). We used an equivalent intronic region in the *Rab9a* gene (which has similar function and gene structure) (Mackiewicz & Wyroba, 2009) as a negative control and a previously identified ATF3 binding site within the *Atf3* gene as a positive control (as ATF3 can transcriptionally regulate itself (Inoue *et al*, 2004)). As predicted, ATF3 specifically bound both to *Atf3* and *Rab7b* (vs. non-specific IgG and *Rab9* negative controls) with binding greatly increased very early (6h) after injury. Thus, induction of ATF3 activity and the consequent activation of *Rab7* occurs very early following injury; indeed, it is the earliest conserved molecular event we have so far identified in paligenosis.

ATF3 can act as a transcriptional activator or repressor depending on the gene and the context (Hai *et al*, 1999). To confirm that ATF3 activated *Rab7b* and to test if their molecular interaction was conserved across species, we used AGS cells (a human gastric epithelial line) to generate stable cell clones that overexpressed ATF3 or stably repressed *ATF3* using shRNAs. AGS cells did not express substantial endogenous ATF3, though cells expressing anti-*ATF3* shRNA (*ATF3*-KD) still expressed less (Figure 3A). *ATF3*-KD caused statistically significant decrease in *RAB7B* mRNA and fewer cells with detectable RAB7 protein, and conversely when ATF3 protein was overexpressed (ATF3-OE), we saw an induction of RAB7 protein and mRNA (Figure 3A-B). Of note, many of the ATF3-OE cells showed large $RAB7^{+}$ globular- and crescentic vesicular formations phenocopying those seen *in vivo* in paligenotic murine cells (Figure 3C). Our *in vivo* data suggested that ATF3 could induce autophagy in part via directly increasing RAB7 abundance. Supporting that hypothesis, we noted increased Cathepsin D (CTSD)-positive lysosomes in cells with higher expression of ATF3 correlating consequently with increased *RAB7B* (Figure 3C). To determine if RAB7B was sufficient, even in the absence of ATF3, to induce these large vesicles observed *in vivo* and *in vitro*, we forced expression of FLAG-tagged, WT RAB7B in *ATF3*-KD cells. Figure 3D shows the large vesicular phenotype is even more dramatic with RAB7B overexpression. On the other hand, transfection with $RAB7B^{T22N}$, a GTPase-dead RAB7B mutant (GTPase cycling is critical for RABs to traffic and maintain vesicular compartments), abrogated the phenotype (Figure 3D). These results are consistent with previous reports that $RAB7B^{T22N}$ impairs endolysosomal trafficking necessary for maturation of Cathepsin D, which is activated in its pro-form in the lysosome (Progida *et al.*, 2010). Taken together, ATF3 is sufficient to transcriptionally activate *RAB7B,* and RAB7B itself (whether ATF3-induced or transfected) is sufficient to activate the endolysosomal pathway to facilitate cell autodegradation. While ATF3, a transcription factor, may also induce other genes that activate autodegradation pathways, our results indicate *RAB7B* appears to be a principal target in paligenosis.

235235

Atf3 *is required for massive lysosome and autophagy induction in Stage 1 of paligenosis*

To determine if loss of *Atf3* results in decreased *Rab7 in vivo*, we studied paligenosis in stomach and pancreas of *Atf3*$^{-/-}$ mice (Hartman *et al.*, 2004). It is important to note that these mice have a global loss of *Atf3*, meaning *Atf3* is neither in differentiated nor progenitor cells. However, since we only see ATF3 induction in differentiated cells after injury, *Atf3's* main role is primarily in differentiated cells. In addition, we observed ATF3 induction in ACs in the pancreas, where there is no adult stem cell population, again suggesting that ATF3 mainly functions in differentiated cells after injury. In WT mice, we observed scant RAB7 in vehicle tissue of the stomach or pancreas, but following injury in WT animals, we saw the previously observed RAB7^{+} vesicles and large circular aggregates. Many of the large RAB7 were lysosomes or autolysosomes as indicated by enclosed CTSD (Figure 4A-B). Although, low-abundance RAB7 could still be detected in ZCs and ACs of *Atf3*$^{-/-}$ mice, the large RAB7-positive vesicles were predominantly lacking. Injury induced RAB7+ vesicles in WT mice, but in *Atf3*$^{-/-}$ mice, we did not observe upregulation of large RAB7+ vesicles (Figure 4A-B).

CTSD is a marker of both lysosomes and autolysosomes, so we next examined if loss of ATF3 and RAB7 affected autophagic trafficking. We observed that the autophagic vesicle marker MAP1LC3B (LC3) was induced in Stage 1 of paligenosis in the stomach, consistent with previous work and our EM analysis indicating increased autophagic trafficking (Willet *et al.*, 2018; Meyer *et al.*, 2019) (Figure 4C). Such LC3^{+} autophagic puncta were not induced in the absence of ATF3. We confirmed ATF3-dependent induction of lysosomes and autophagosomes using TEM (Figure 4D-E).

The results indicate ATF3 is induced rapidly in paligenosis and is required for RAB7-associated autophagy/lysosomal trafficking. Thus, ATF3 is both necessary and sufficient to induce the endolysosome-trafficking protein RAB7 and is critical for the massive induction of

autodegradative machinery that cells use in Stage 1 of paligenosis to downscale much of their mature cell architecture.

Atf3 *loss results in less repair and more cell death after secretory cell injury*

Paligenosis is a stepwise process, progression through which can be inhibited between each stage. We have previously shown that blocking autodegradative function during paligenosis impairs regeneration (Willet *et al.*, 2018). We reasoned the aberrant induction of autodegradation in the absence of ATF3 would affect the fraction of cells able to progress to Stage 2 (expressing metaplastic/progenitor genes) and Stage 3 (entering the cell cycle). Stage 2 is easily measured by induction of the epitope for the lectin GS-II in ZCs, with the resultant cells (known as SPEM cells) co-labeling with GS-II and ZC markers (like PGC or GIF). *Atf3*$^{-/-}$ mice showed profound loss of progression to Stage 2, with only rare SPEM cells (Figure 5A, EV4A-C). Stage 2 failure was corroborated by a second SPEM marker CD44v (Figure EV4A) (Khurana *et al*, 2013; Engevik *et al*, 2016; Meyer *et al.*, 2019). Moreover, the failure to produce Stage 2 SPEM cells correlated with reduced proliferation (Figure 5B-C; Figure EV4D). Note that progenitors higher up in the gastric unit (in the isthmus and neck) are induced to proliferate via a non-paligenotic mechanism (Willet *et al.*, 2018; Choi *et al*, 2019; Miao *et al*, 2020a; Miao *et al.*, 2020b). As expected, those non-paligenotic cells were still induced to proliferate after injury, so overall proliferation in the injured stomach was less affected by loss of ATF3 than paligenotic proliferation specifically (Figure EV4D; cf: Figure 5B vs. 5C showing basal, paligenotic proliferation).

We noticed that the lack of paligenotic progression to Stage 2 and 3 did not indicate mature cells were delayed in the paligenotic process, as many of the bases of gastric units, where ZCs or their paligenotic progeny should be, were simply missing, indicating dropout of whole gastric unit bases, a phenomenon we have previously described when there is a failure to

progress through paligenosis (Willet *et al.*, 2018; Miao *et al.*, 2020b). Inability to complete paligenosis resulted in marked base dropout with approximately 1/3rd of gastric unit bases missing (Figure 5D). As might be expected, the increased base dropout in *Atf3*$^{-/-}$ correlated with significantly increased Cleaved-CASP3 positivity, indicating cell death by apoptosis (Figure EV4E-F). In the pancreas, ATF3 was also required for paligenosis progression, as *Atf3*$^{-/-}$ACs had significantly higher Cleaved-CASP3 expression (Figure 5E-F) as well as decreased Stage 3 proliferation induction (Figure 5G-H)

Overall, the results indicate that the failure to upregulate autodegradation in Stage 1, in the absence of *Atf3,* led to the failure to progress through Stage 2 of paligenosis and finally resulted in increased cell death in Stage 3, in two both the stomach and pancreas.

ATF3 is critical for injury responses across organs

Our mouse and human work showed that ATF3 could regulate autodegradative activity in a conserved way across tissue and species by regulating RAB7. In addition, loss of ATF3 caused the same Stage 1 failure with associated overall paligenosis failure in two different organs, suggesting that early ATF3 induction might be a conserved feature of paligenosis. HDT injury producing SPEM in mice is a model of the SPEM that occurs in chronic atrophic gastritis in humans (Petersen *et al*, 2017). Using human stomach samples of tissue adjacent to gastric tumor tissue, we have previously extensively characterized (Lennerz *et al*, 2010; Radyk *et al.*, 2018; Willet *et al.*, 2018), we observed expression of ATF3 in SPEM. However, as might be expected, given ATF3 expression was early and transient following injury in mice, and most SPEM is chronic and mitotically quiescent in humans (Willet *et al.*, 2018; Burclaff *et al.*, 2020), only scattered, potentially transitional SPEM cells were ATF3-positive (Figure 6). Morphologically normal human gastric epithelial cells lacked ATF3 expression (Figure 6).

As ATF3 is highly conserved, we took advantage of a previously published Axolotl single-cell RNA sequencing analysis of limb regeneration (Gerber *et al*, 2018; Data ref: Gerber *et al*., 2018) that shows high correlation with gene expression in mouse paligenosis (Miao *et al.*, 2020b). We found that, like the previously identified paligenosis gene IFRD1, ATF3 is induced during limb regeneration. RAB7B is induced at the next time point after ATF3 (Figure EV5A), as represented by the fraction of cells that express these genes throughout the course of repair after limb amputation. We previously showed that regenerative proliferation in kidney and liver occurs by paligenosis (Willet *et al.*, 2018), and activation of muscle satellite cells following injury (Yue *et al*, 2020) also appears to involve a paligenosis-like process involving emergence from quiescence. We assayed genes whose expression was increased after paligenotic injury in all 5 organs: stomach, pancreas, liver, kidney, muscle to determine potential core paligenosis genes (Figure EV5B). We found only 7 genes were upregulated in all 5 datasets: *Atf3*, *Cebpb, Hmox1, Ier3, Ifrd1* (Data ref: Fahling *et al*., 2013; Data ref: Kowalik *et al*., 2007; Data ref: Moore *et al*., 2015; Data ref: Out *et al*., 2007; Data ref: Yue *et al*., 2020), *Junb,* and *Zfp36*. Thus, the results indicate *Atf3* may play a conserved role in mediating paligenosis across multiple tissues and species.

DISCUSSION

Our work here shows that ATF3, induced early in Stage 1 of paligenosis, is required for induction of the autodegradative machinery. Though there are likely additional targets critical for ATF3 actions in paligenosis, we show both in mouse paligenosis models and in human epithelial cells, that ATF3 binds and activates *Rab7b*, which encodes a protein critical in turn for trafficking autophagic vesicles and lysosomes. ATF3 is necessary for RAB7 induction and for induction of a large complement of autophagolysosomes. ATF3 induction after paligenotic injury is conserved across tissues and species with ATF3 increased even in human metaplasia.

The concept of an evolutionarily conserved program, paligenosis, which mechanizes cell plasticity for mature cells, like pancreatic or gastric exocrine cells is recent. Paligenosis, as originally defined, is a stepwise program that retools cell architecture to convert a mature cell to a regenerative, progenitor-like phenotype. The three paligenosis stages (1. Autodegradation, 2. Increased progenitor/metaplastic expression, 3. Cell cycle re-entry) can be genetically and morphologically defined, and progression from stage to stage can be blocked by inhibitors or deletion of key genes (Figure 7). The stepwise, conserved nature of the program allows us to determine if there are dedicated, paligenosis genes and genetic machinery, independent of tissue and conserved across evolutionary phyla, as is the case with other cellular programs like apoptosis. We recently identified *Ifrd1* and *Ddit4* as paligenosis-governing genes and proposed that paligenosis genes in general would be: 1) largely dispensable for normal development or proliferative activity; 2) activated primarily during regeneration-inducing injury; 3) highly evolutionarily conserved. We argue here that ATF3 is a similar such gene required for paligenosis. It is induced early in paligenosis in multiple tissues, is known to be induced by injury, is conserved from sea anemones to humans, and, in general, organisms null for ATF3 have phenotypes only after injury. Furthermore, we show evidence here that ATF3 is induced during transition to human metaplasia, which is representative of a much larger cohort (>500)

that we are currently analyzing for expression of paligenosis genes. We observe 11% of human metaplastic lesions have focal ATF3 in non-proliferative foci, consistent with ATF3 being upstream of the decision for cells to proliferation.

We describe a model (Figure 7) in which ATF3 is induced early after injury to help transcriptionally upregulate *Rab7b* and other genes important for autophagy and lysosomal induction during paligenosis Stage 1. During this time ATF3 also likely transcriptionally represses genes involved in cell differentiation/maturation like MIST1, a relationship that has been shown before in pancreas (Fazio *et al.*, 2017). Shortly after Stage 1, ATF3 decreases, and the cell progresses through the remainder of paligenosis. Without *Atf3*, the defects in Stage 1 (Autodegradation) obstruct the cell's ability to become regenerative, metaplastic cells. A greater proportion of cells die, and tissue repair is compromised. In addition, we describe a new signaling axis for injury-induced cell plasticity by ATF3 transcriptional regulation of *Rab7b* during paligenosis.

Atf3 joins the aforementioned *Ddit4* and *Ifrd1* as paligenosis-governing genes (Miao *et al.*, 2020b). At the tissue level, loss of *Atf3* appears most similar to loss of *Ifrd1* as lack of either gene leads to increased cell death in paligenosis Stage 3. While IFRD1 functions to suppress p53-mediated repression of mTORC1, allowing proliferation in Stage 3, ATF3 instead activates autodegradation pathways for proper clearance of differentiated/specialized cell features. Though both ATF3 and IFRD1 have different mechanisms to govern paligenosis, it is clear that failure to clear paligenosis checkpoints, either by inability to upregulate autodegradation ($Atf3^{-/-}$) or by inability to re-activate mTORC1 ($Ifrd1^{-/-}$) leads to decreased tissue recovery after injury. ATF3 and DDIT4 both function in Stage 1 to control autodegradation. Unlike *Atf3*, however, $Ddit4^{-/-}$ mice have increased proliferation. DDIT4 functions during initial stages to deactivate mTORC1; hence, $Ddit4^{-/-}$ mice express constitutively high mTORC1 throughout paligenosis, which overrides a checkpoint (Miao *et al.*, 2020b). Additionally, loss of *Ddit4* and induction of

metaplasia increases tumorigenesis in an N-methyl-N-nitrosourea spontaneous gastric cancer model (Miao *et al.*, 2021).

ATF3 is a member of the ATF/CREB family of transcription factors and shares similar binding sites with AP-1 (also from the ATF/CREB and c-Fos/c-Jun families), which regulates immediate early genes following stress/injury. *Atf3* has been implicated in injury settings in many organs including cerebral ischemia (Wang *et al.*, 2012), axon regeneration (Hunt *et al*, 2012; Gey *et al.*, 2016), acute lung injury (Zhao *et al.*, 2017), heart failure (Brooks *et al.*, 2015), alcohol liver damage (Tsai *et al*, 2015), liver ischemia-reperfusion injury (Zhu *et al.*, 2018), stress-induced β-cell apoptosis (Hartman *et al.*, 2004), ADM (Fazio *et al.*, 2017), and acute kidney injury (Li *et al.*, 2010). ATF3 is also important for injury responses in *Drosophila* (Zhou *et al*, 2017) and Axolotl (Gerber *et al.*, 2018). In all those cases, *Atf3* loss exacerbates the injury phenotype but is dispensable for homeostasis and embryonic development, just as we observed here in stomach and pancreas injury.

It has not been previously reported that injury-responsive ATF3 accumulation induces autophagy and lysosomal activity, but ATF3 has been reported to interact with individual autophagy pathway members. For example, ATF3 regulates *Beclin-1* (Lin *et al*, 2014) and *Atg5* (Sood *et al*, 2017). There may also exist an autophagy-ATF3 feedback loop because defective autophagy (*Atg4b* loss) impairs ATF3 activity in a mouse lung injury model (Aguirre *et al*, 2014).

To our knowledge there are no previous reports of ATF transcription factors transcriptionally regulating any Rabs, though potential ATF binding sites have been described to be present in the 5'-flanking region of *Rab7* (Bhattacharya *et al*, 2006). In fact, in general, transcriptional regulation of RABs or regulation of RAB function via titrating protein abundance is usually not studied, with some few exceptions such as MIST1 scaling RABs, and a report of c-Myc helping drive melanoma by activating *Rab7* (Alonso-Curbelo *et al*, 2014). However, an ATF-related protein, AP-1, regulates *Rab11a* in B cells in mice (Lizundia *et al*, 2007),

suggesting that ATF/CREB transcription factors may have an underappreciated and understudied role in transcriptionally regulating RABs.

RAB7A and RAB7B are regulators of endosomal trafficking and maturation. RAB7 proteins are largely localized to late endosomes and lysosomes to aid in the autophagosome-lysosome fusion and mitochondrion-lysosome contacts (Stroupe, 2018), events undoubtedly important during Stage 1 of paligenosis. As such, complete *Rab7* loss in pancreatic acinar cells impairs autophagic and endocytic pathways in mouse models of pancreatitis (Takahashi *et al.*, 2017). Here we show that *Atf3*-loss impairs autophagic and lysosomal pathways, further supporting the notion of ATF3 function through *Rab7b* during paligenosis and injury. There are few studies specifically focused on RAB7B, identified because of its size and sequence similarity to RAB7A. RAB7B has similar functions as RAB7A and was, accordingly, first observed to be associated with lysosomes in monocytes (Yang *et al.*, 2004). More recently, RAB7B has been shown to interact with ATG4B on vesicles and negatively regulate autophagy (Kjos *et al.*, 2017), indicating it also, like RAB7A, regulates autophagic trafficking. There may not be complete concordance between the two RAB7 proteins, however, as RAB7B may have an added function in some circumstances of aiding retrograde transport from late endosomes or lysosomes to the Golgi (Progida *et al.*, 2010).

Using AGS cells, we demonstrated that expression of RAB7B was sufficient to form the large vesicular compartments observed following injury in murine tissue. This effect was independent of *ATF3* expression, as vesicles were readily observed with *ATF3* knockdown and RAB7B overexpression. In addition, vesicle formation was dependent on RAB7B's GTPase activity, as no vesicles were observed with the $RAB7B^{T22N}$ mutant, even with overexpression of ATF3.

Recent studies have shown the importance of degradation and autophagy in regulating cell plasticity in several organs (Saera-Vila *et al*, 2016; Call & Nichenko, 2020; Li *et al*, 2020;

Romermann *et al*, 2020). We speculate that Stage 1 of paligenosis is not only required to change the cell structure to one that is more physiologically progenitor-like but also to generate enough energy for DNA replication and cell division. Ribosomes are an enormous pool for nucleotides, which may be one reason we see so much degradation machinery accumulate in the rER portion of the cell, where there may be release of nucleotides from ribosomes. As mentioned above, functional degradation machinery may also act as a checkpoint indicating a cell is healthy enough to commit to cell cycle re-entry. This was the case when we administered hydroxychloroquine to inhibit lysosome-autophagosome fusion (Figure EV1C-F) and when we blocked lysosome activity during paligenosis (Willet *et al.*, 2018) which, like *Atf3* and *Ifrd1* loss, also ultimately led to increased cell death.

ATF3 may transcriptionally regulate other targets during Stage 1 that do not control degradation. ATF3 can repress *Mist1*, the secretory cell scaling factor expressed only in mature ZCs and ACs; *Mist1* downregulation is a key early step in ZC and AC paligenosis (Kowalik *et al.*, 2007; Nozaki *et al.*, 2008; Lennerz *et al.*, 2010; Karki *et al*, 2015; Meyer *et al.*, 2019). It also represses *Sox9* (Fazio *et al.*, 2017), a metaplastic gene whose induction defines transition from Stage 1 to Stage 2, supporting the hypothesis that ATF3 plays several roles in Stage 1 of paligenosis. It is not clear how ATF3 is upregulated for paligenosis and metaplasia initiation, but once accumulated, ATF3 acts in a positive feedback loop to regulate itself. Reactive oxygen species are also induced *en route* to SPEM and may contribute to autodegradation and antioxidant pathway activation, as shown by the induction of antioxidant gene xCT, a cysteine/glutamate transporter in SPEM (Meyer *et al.*, 2019). Likewise, reactive oxygen species are important for ADM induction and progression to pancreatic adenocarcinoma (Liou *et al*, 2016; Cheung *et al*, 2020).

The current study stimulates several important questions. First, how does metabolic control affect the cell fate transitions in paligenosis? We saw dramatic structural changes in

mitochondria during paligenosis, which likely reflect changes in metabolism; however, the metabolism of cells as they transition from their normal state to a metaplastic state is not well characterized. We showed a dependency on dynamic mTORC1 activity during metaplasia (Willet *et al.*, 2018) and recent studies show acetyl-CoA metabolism contributes to cell plasticity in the pancreas and potentially tumorigenesis via epigenetic regulation (Carrer *et al*, 2019). Epigenetics also plays a role in SPEM initiation, most recently shown by miR148a repression of DNA methylating gene DNMT1, a pro-metaplasia gene (Shimizu *et al*, 2020). Second, which cells are poised to undergo paligenosis and become metaplastic? Not all mature cells in a tissue may have the ability to re-enter the cell cycle after injury, but organs experiencing chronic damage (like GI organs) harbor cells that act as facultative progenitors if the injury is severe enough, though the age of cells in the GI system is a factor for their ability to contribute to plasticity (Engevik *et al.*, 2016; Weis *et al*, 2017) and some cell types like acid-secreting parietal cells seem unable to return to the cell cycle. Further study of general, conserved genes that govern paligenosis in diverse contexts should help us have a better understanding of regeneration, tumorigenesis, and also potentially how plasticity arose as a way for multicellular organisms to use cells for both specialized, differentiated function and as progenitors after damage.

MATERIALS AND METHODS

Animal Studies and reagents

All experiments involving animals were performed according to protocols approved by the Washington University School of Medicine Animal Studies Committee. Mice were maintained in a specified pathogen-free barrier facility under a 12-hour light cycle. All mice used in experiments were 6−8 weeks old. Male and female mice were used for each experiment and we

did not note any differences due to sex. Statistical justification for animal numbers is based on our previous experience, consultation with biostatisticians, and using the sampling power analysis approach. Animals were randomized when allocating into each treatment groups. Experimental cohorts were randomly designated at birth for specific animals to minimize bias. Wild-type *C57BL/6* mice were purchased from Jackson Laboratories (Bar Harbor, ME). *Atf3*$^{-/-}$ mice were bred onto a *C57BL/6* background and received from Dr. Tsonwin Hai at the Ohio State University Medical Center. *Atf3*$^{-/-}$ mice were first described in (Hartman *et al.*, 2004).

Tamoxifen (250 mg/kg body weight; Toronto Research Chemicals, Inc, Toronto, Canada) was administered by intraperitoneal (IP) injection to induce SPEM in the stomach (See Figure EV1 for timeline (Saenz *et al.*, 2016)). Tamoxifen was prepared in a 10% ethanol and 90% sunflower oil solution by sonication (Sigma, St Louis, MO).

Pancreatitis was induced by 6 hourly IP injections of 50 µg/kg (in 0.9% saline) cerulein (Sigma-Aldrich) given every other day for up to 7 days (See Figure EV1 for timeline). Mice were sacrificed 24 h after the final cerulein injection.

Hydroxychloroquine sulfate (Acros Organics) was dissolved in PBS and administered by intraperitoneal injection at a dose of 60mg/kg/day (Rosenfeldt *et al.*, 2013). See Figure EV1C for injection timeline.

All mice were given an intraperitoneal injection containing BrdU (120 mg/kg) and 5-fluoro-2′deoxyuridine (12 mg/kg) 90 minutes before sacrifice to capture cells in S phase at the experimental endpoint.

Immunofluorescence and Immunohistochemistry

Mouse tissues were excised, flushed with phosphate-buffered saline (PBS), and then inflated with freshly prepared 4% paraformaldehyde. The stomach was clamped and suspended in fixative in a 50-mL conical overnight, followed by rinses in PBS and 70% ethanol, arrangement in 3% agar in a tissue cassette, and paraffin processing. Sections (5 µm) were cut, deparaffinized, and rehydrated with graded Histo-Clear (National Diagnostics), ethanol, and water, then antigen-retrieved in sodium citrate buffer (2.94 g sodium citrate, 500 uL Tween 20, pH 6.0) using a pressure cooker. Slides were blocked in 5% normal serum, 0.2% Triton-X 100, in PBS. Slides were incubated overnight at 4°C in primary antibodies (see Reagent Table), then rinsed in PBS, incubated 1 hour at room temperature in secondary antibodies and/or fluorescently labeled lectin rinsed in PBS, mounted in ProLong Gold Antifade Mountant with 4′6-diamidino-2-phenylindole (DAPI) (Molecular Probes).

For immunohistochemistry, steps were identical except the following. An extra quenching step was performed for 15 minutes in a methanol solution containing 1.5% H_2O_2 before antigen retrieval. Substrate reaction and detection was performed using ImmPACT VIP Peroxidase (horseradish peroxidase) Substrate Kit (Vector Laboratories, Burlingame, CA) as detailed per the manufacturer's protocol and sections were developed with DAB for desired time and counterstained with hematoxylin and/or eosin. Slides were mounted in Permount Mounting Medium.

514514

Western Blot

Approximately 75mg mouse corpus stomach or pancreas tissue were sonicated in RIPA buffer with 1x protease inhibitor cocktail (Thermo). Protein was separated using NuPAGE 10% Bis-Tris gels and transferred to an Invitrogen nitrocellulose membrane. Membranes were then blocked with 3% Bovine serum albumin (BSA) and incubated overnight at 4°C with primary antibodies

(see Reagent Table for antibodies). The membranes were rinsed in tris-buffered saline (TBS) pH 8.0, incubated 1 hour at room temperature in secondary antibody in 5% low-fat milk. Actin antibody was used as a control to ensure equal loading of protein in each gel lane. Secondary antibody signals were imaged and detected by SuperSignal West Pico PLUS Chemiluminescent Substrate Kit.

525525

Imaging and Quantifications

Fluorescence microscopy was performed using a Zeiss Axiovert 200 microscope with an Axiocam MRM camera and Apotome II instrument for grid-based optical sectioning. Post-imaging adjustments, including contrast, fluorescent channel overlay, and pseudo-coloring, were performed with Axiovision and Adobe Photoshop CS6. Histology of stomach and immunohistochemistry were imaged using an Olympus BX51 light microscope and Olympus SZX12 dissecting microscope w/12 MPixel Olympus DP70 camera. Images were analyzed and post-imaging adjustments were performed with Adobe Photoshop CS6.

Quantification of BrdU proliferation rates was done by counting 5 or more 20x fields from a whole-slide scanned images from the Hamamatsu Nanozoomer 2.0-HT system.

536536

FIB-SEM 3D Nanotomography

Performed as described in (Lo *et al.*, 2017). Mouse gastric tissues were bisected into fixative containing 2.5% glutaraldehyde and 2% paraformaldehyde in 0.15 M cacodylate buffer containing 2 mM CaCl2 (pH 7.4), fixed for 15 min at 37°C and then overnight at 4°C, sliced into ~1.5-mm-thick pieces, rinsed in cacodylate buffer for 10 min at room temperature, and subjected to secondary fixation in 1% osmium tetroxide/0.3% potassium ferrocyanide in

cacodylate buffer for 1 h on ice. The samples were then washed in ultrapure water and stained *en bloc* in 2% aqueous uranyl acetate for 1 h. After staining, samples were briefly washed in ultrapure water, dehydrated in a graded acetone series, and infiltrated with microwave assistance (Pelco BioWave Pro) into LX112 resin, which was cured in an oven for 48 h at 60°C. Cured blocks were trimmed and mounted onto SEM pins with silver epoxy and faced with a diamond knife. Toluidine blue-stained sections (300 nm thick) were used to locate a region of interest. Blocks were sputter-coated with 10 nm of iridium (Leica, ACE 600) with rotation on a planetary stage to ensure saturation. Regions of interest on a FIB-SEM (Zeiss, Crossbeam 540) were located by secondary electron imaging at 10 KeV. Once a region was found, the sample was prepared using the ATLAS (Fibics) 3D nanotomography engine. In short, a platinum pad was deposited on a 40-µm × 40-µm region of interest with the FIB set to 30 KeV and 1.5 nA. Three vertical lines for focus and sigmation and two angled lines for z-tracking were milled into the platinum pad at 50 pA, and a protective pad of carbon was deposited on top of the milled platinum at 1.5 nA. Following this, a rough trench 50 µm wide and 55 µm deep was milled at 30 nA and polished at 7 nA. Once polishing of the block face was complete, face detection, focusing, and ztracking were all performed on the fiducial marks that were milled into the platinum pad. Imaging was performed at 2 KeV and 1.1 nA using the EsB (energy selective backscatter) detector with a grid voltage of 1100 V. The block was milled at a current of 700 pA with 20-nm slices, and 2000 × 1750 pixel images were acquired at a resolution of 20 nm/pixel with a dwell of 8 or 10 µsec and a line average of 3 for a total z-depth of 35 µm.

3D reconstruction

Performed as described in (Lo *et al.*, 2017). All EM serial images were imported into the Amira 6 3D software package for 3D reconstruction. Areas of interest were manually segmented into data objects with intervening unsegmented slices (“X”) based on object volume. For organelles

with suboptimal contrast, the thresholding function was used for manual segmentation. The interpolation function was used to highlight areas of interest between manually segmented slices. 3D models were generated from labeled objects. The “Smooth” and “Simplify” functions were used for model generation, and pseudocoloring was used to enhance visualization for each organelle. Animations were created with the Animation Director in the software.

Electron Microscopy

For TEM, stomachs were fixed, sectioned, stained, and imaged as previously described (Willet *et al.*, 2018). Briefly, tissue was collected as described above, fixed overnight at 4˚C in modified Karnovsky’s fixative, and sectioned. Tissue was processed by the Washington University in St. Louis Department of Pathology and Immunology Electron Microscopy Facility.

Human cancer cell culture

AGS cells (ATCC) were grown under standard conditions (Advanced DMEM/F12, 10% FBS, Nonessential amino acids, and Pen/Strep at 37ºC and 5% CO_2) and were cotransfected with a transposon expressing shRNA against *ATF3* (TRCN0000329691) under a U6 promoter as well as a homemade plasmid expressing hyperactive PiggyBac transposase to generate stable incorporation of the vector into the genome. After selection with puromycin, passaged cells were obtained for experiments within the first 10 passages. To generate *ATF3* overexpression lines, the human *ATF3* sequence was cloned from Addgene #26115 and inserted into a homemade PiggyBac transposon vector for overexpression.

Following selection of stable ATF3 overexpression or *ATF3* knockdown constructs, the cells were transfected with transposons containing either *wild-type* or T22N point mutant of RAB7B containing an N-terminal 3x-FlagTag. RAB7B template was purchased from Origene (Catalog #RC202283) and the mutant was generated by amplifying a truncated C-terminal domain and a three-part ligation using oligos encoding the mutant N-terminal domain. All sequences were confirmed by sanger sequencing services provided by Genewiz. 2 days after transfection with RAB7B constructs the cells were fixed and stained with an anti-FLAG antibody, which permitted specific identification of those doubly transfected cells and to determine the cellular localization of mutated $RAB7B^{T22N}$.

For immunofluorescence experiments, cells were grown on cover slips and blocking and staining was completed in 12-well culture plates. For imaging, the coverslips were mounted onto slides with ProLong Gold Antifade Mountant with 4′6-diamidino-2-phenylindole (DAPI) (Molecular Probes).

603603

qRT-PCR

RNA was isolated using RNeasy (Qiagen) per the manufacturer's protocol. The integrity of the mRNA was verified with a BioTek Take3 spectrophotometer and electrophoresis on a 2% agarose gel. RNA was treated with DNase I (Invitrogen), and 1 µg of RNA was reverse-transcribed with SuperScript III (Invitrogen) following the manufacture's protocol. Measurements of cDNA abundance were performed by qRT–PCR using Applied Biosystems QuantStudio 3 Real-time PCR system. Power SYBR Green master mix (Thermo Scientific) fluorescence was used to quantify the relative amplicon amounts of each gene. Primer sequences are located in Table EV1.

ChIP-PCR

Approximately 25mg of stomach corpus tissue was flash frozen in liquid nitrogen until IP was performed. The SimpleChIP Plus Enzymatic Chromatic IP Kit (Cell Signaling Technology) was used for tissue prep and IP per the manufacturer's protocol (see Reagent table for antibody concentrations). Tissue was fixed with PFA for 20 minutes and disaggregated with a Medimachine (BD Biosciences). Standard PCR was used to determine ATF3 binding at the *Rab7b* first intron (see Table EV2 for primer sequences).

Human Patient Samples

Human gastric pathological tissue specimens were obtained with approval by the Institutional Review Board of Washington University School of Medicine. Samples used are deidentified tissues archived from standard-of-care procedures. Informed consent was received from all patients for the use of their tissue and experiments conformed to the principles set out in the WMA Declaration of Helsinki and the Department of Health and Human Services Belmont Report. Our research team does not have contact with patients and patient information is deidentified. All specimens are stored behind double-locked doors and only approved members of the research team have access. Gastric clinical samples have been previously described in (Lennerz *et al.*, 2010; Capoccia *et al*, 2013; Radyk *et al.*, 2018; Willet *et al.*, 2018).

Graphing and Statistical Analysis

Graphs and statistics were done with GraphPad Prism (La Jolla, CA). In cases involving more than two samples to compare, significance was determined using ANOVA with post-hoc correction: Tukey was used to assess statistical significance if multiple conditions were

compared; Dunnett post-hoc when comparing multiple samples to a single control. Otherwise, unpaired, two-tailed Student's *t*-test was used to determine significance. Data that would violate normalcy by study design were analyzed by nonparametric Mann-Whitney U test. Most data (e.g. cell counts) were first analyzed as mean values of measurements from multiple fields across multiple sections of an organ for each animal, and then the mean of those means was plotted. A p-value of ≤0.05 was considered significant. Samples were randomized, and measurements were blinded to prevent the introduction of experimental bias. Formal tests for normalcy were not performed. At least the minimum numbers of animals are used to achieve statistical significance in any determinations.

ACKNOWLEDGMENTS

We thank Dr. Tsonwin Hai at the Ohio State University for the *Atf3*$^{-/-}$ mice. We thank Karen Green, Lisa Snipes, and Kevin Boyer of the Department of Pathology Electron Microscopy Center. We acknowledge the AITAC of the Washington University Digestive Disease Center (DDRCC: P30 DK052574) and the NIH Shared Instrumentation Grant S10RR0227552 (for Nanozoomer slide scanning). FIB-SEM nanotomography was performed in the Washington University Center for Cellular Imaging (WUCCI) which is funded, in part by the Children's Discovery Institute of Washington University and St. Louis Children's Hospital (CDI-CORE-2015-505 and CDI-CORE-2019-813), the Foundation for Barnes-Jewish Hospital (3770) and Siteman Cancer Center (P30CA091842). MDR was funded by F31CA236506-01 (NIH NCI), the Philip and Sima Needleman Student Fellowship in Regenerative Medicine, and 5T32GM007067-43 (NIH); LBS was supported by Siteman Cancer Center Cancer Pathway Program (P30 CA091842 and T32CA113275). BLP by Washington University Biology Summer Undergraduate Research Fellowship Program (BioSURF) and the Children's Discovery Institute of Washington University and St. Louis Children's Hospital; JWB was supported by the Department of Defense, through

the PRCRP program under Award No. W81XWH2010630 (USAMRAA), T32-DK007130 (NIH NIDDK), the Digestive Disease Research Core Centers Pilot and Feasibility Grant as part of P30 DK05257, NIH R21 AI156236, and the American Gastroenterological Association AGA2021-5101; J.B. was supported by National Institutes of Health (NIH) training grant (GM007067) and the Philip and Sima Needleman Student Fellowship in Regenerative Medicine; CJC by T32-CA009547 (NIH NCI); JCM by the National Institute of Diabetes and Digestive and Kidney Diseases (R21 DK111369, R01DK094989, R01DK105129, R01DK110406 R01120680), The National Institutes of Health National Cancer Institute (P30 CA09182, R01 CA239645, R01 CA246208), and the BETRNet (U54 CA163060).

AUTHOR CONTRIBUTIONS

MDR designed and performed experiments, analyzed, and interpreted data, performed statistical analyses, and drafted and revised the manuscript; LBS and BLP designed and performed experiments, analyzed and interpreted data, performed statistical analyses, and drafted the manuscript; JWB, JB, CJC, and YK designed and performed experiments. C-CS and JAJF designed the experiments. JCM designed the experiments, provided funding for the study, generated data, performed bioinformatics analyses, and drafted and revised the manuscript.

CONFLICTS OF INTEREST

The authors declare that they have no conflicts of interest.

REFERENCES

683 Adami JG (1900) On Growth and Overgrowth. In: *"Festschrift" in Honor of Abraham Jacobi, MD,*
684 *LLD: To Commemorate the Seventieth Anniversary of His Birth, May Sixth, 1900*, pp.
685 422-432. Knickerbocker Press:

686 Adler G, Hahn C, Kern HF, Rao KN (1985) Cerulein-induced pancreatitis in rats: increased
687 lysosomal enzyme activity and autophagocytosis. *Digestion* 32: 10-18

688 Aguirre A, Lopez-Alonso I, Gonzalez-Lopez A, Amado-Rodriguez L, Batalla-Solis E, Astudillo A,
689 Blazquez-Prieto J, Fernandez AF, Galvan JA, dos Santos CC *et al* (2014) Defective
690 autophagy impairs ATF3 activity and worsens lung injury during endotoxemia. *J Mol Med*
691 *(Berl)* 92: 665-676

692 Alonso-Curbelo D, Riveiro-Falkenbach E, Perez-Guijarro E, Cifdaloz M, Karras P, Osterloh L,
693 Megias D, Canon E, Calvo TG, Olmeda D *et al* (2014) RAB7 controls melanoma
694 progression by exploiting a lineage-specific wiring of the endolysosomal pathway.
695 *Cancer Cell* 26: 61-76

696 Altenhoff AM, Glover NM, Train CM, Kaleb K, Warwick Vesztrocy A, Dylus D, de Farias TM, Zile
697 K, Stevenson C, Long J *et al* (2018) The OMA orthology database in 2018: retrieving
698 evolutionary relationships among all domains of life through richer web and
699 programmatic interfaces. *Nucleic Acids Res* 46: D477-D485

700 Amieva M, Peek RM, Jr. (2016) Pathobiology of Helicobacter pylori-Induced Gastric Cancer.
701 *Gastroenterology* 150: 64-78

702 Bailey TL, Boden M, Buske FA, Frith M, Grant CE, Clementi L, Ren J, Li WW, Noble WS (2009)
703 MEME SUITE: tools for motif discovery and searching. *Nucleic Acids Res* 37: W202-208

704 Bhattacharya M, Ojha N, Solanki S, Mukhopadhyay CK, Madan R, Patel N, Krishnamurthy G,
705 Kumar S, Basu SK, Mukhopadhyay A (2006) IL-6 and IL-12 specifically regulate the
706 expression of Rab5 and Rab7 via distinct signaling pathways. *EMBO J* 25: 2878-2888

Brooks AC, DeMartino AM, Brainard RE, Brittian KR, Bhatnagar A, Jones SP (2015) Induction of activating transcription factor 3 limits survival following infarct-induced heart failure in mice. *Am J Physiol Heart Circ Physiol* 309: H1326-1335

Bucci C, Thomsen P, Nicoziani P, McCarthy J, van Deurs B (2000) Rab7: a key to lysosome biogenesis. *Mol Biol Cell* 11: 467-480

Burclaff J, Mills JC (2018) Plasticity of differentiated cells in wound repair and tumorigenesis, part II: skin and intestine. *Dis Model Mech* 11

Burclaff J, Willet SG, Saenz JB, Mills JC (2020) Proliferation and Differentiation of Gastric Mucous Neck and Chief Cells During Homeostasis and Injury-induced Metaplasia. *Gastroenterology* 158: 598-609 e595

Call JA, Nichenko AS (2020) Autophagy: an essential but limited cellular process for timely skeletal muscle recovery from injury. *Autophagy* 16: 1344-1347

Cao B, Parnell LA, Diamond MS, Mysorekar IU (2017) Inhibition of autophagy limits vertical transmission of Zika virus in pregnant mice. *J Exp Med* 214: 2303-2313

Capoccia BJ, Jin RU, Kong YY, Peek RM, Jr., Fassan M, Rugge M, Mills JC (2013) The ubiquitin ligase Mindbomb 1 coordinates gastrointestinal secretory cell maturation. *J Clin Invest* 123: 1475-1491

Carrer A, Trefely S, Zhao S, Campbell SL, Norgard RJ, Schultz KC, Sidoli S, Parris JLD, Affronti HC, Sivanand S *et al* (2019) Acetyl-CoA Metabolism Supports Multistep Pancreatic Tumorigenesis. *Cancer Discov* 9: 416-435

Chen T, Oh S, Gregory S, Shen X, Diehl AM (2020) Single-cell omics analysis reveals functional diversification of hepatocytes during liver regeneration. *JCI Insight* 5

Cheung EC, DeNicola GM, Nixon C, Blyth K, Labuschagne CF, Tuveson DA, Vousden KH (2020) Dynamic ROS Control by TIGAR Regulates the Initiation and Progression of Pancreatic Cancer. *Cancer Cell* 37: 168-182 e164

Choi E, Means AL, Coffey RJ, Goldenring JR (2019) Active Kras Expression in Gastric Isthmal Progenitor Cells Induces Foveolar Hyperplasia but Not Metaplasia. *Cell Mol Gastroenterol Hepatol* 7: 251-253 e251

Dekaney CM, King S, Sheahan B, Cortes JE (2019) Mist1 Expression Is Required for Paneth Cell Maturation. *Cell Mol Gastroenterol Hepatol* 8: 549-560

Engevik AC, Feng R, Choi E, White S, Bertaux-Skeirik N, Li J, Mahe MM, Aihara E, Yang L, DiPasquale B *et al* (2016) The Development of Spasmolytic Polypeptide/TFF2-Expressing Metaplasia (SPEM) During Gastric Repair Is Absent in the Aged Stomach. *Cell Mol Gastroenterol Hepatol* 2: 605-624

Fahling M, Mathia S, Paliege A, Koesters R, Mrowka R, Peters H, Persson PB, Neumayer HH, Bachmann S, Rosenberger C (2013) Gene Expression Omnibus GSE44925 (https://www.ncbi.nlm.nih.gov/geo/query/acc.cgi?acc=GSE44925). [DATASET]

Fahling M, Mathia S, Paliege A, Koesters R, Mrowka R, Peters H, Persson PB, Neumayer HH, Bachmann S, Rosenberger C (2013) Tubular von Hippel-Lindau knockout protects against rhabdomyolysis-induced AKI. *J Am Soc Nephrol* 24: 1806-1819

Faust F, Gomez-Lazaro M, Borta H, Agricola B, Schrader M (2008) Rab8 is involved in zymogen granule formation in pancreatic acinar AR42J cells. *Traffic* 9: 964-979

Fazio EN, Young CC, Toma J, Levy M, Berger KR, Johnson CL, Mehmood R, Swan P, Chu A, Cregan SP *et al* (2017). Gene Expression Omnibus GSE60250 (https://www.ncbi.nlm.nih.gov/geo/query/acc.cgi?acc=GSE60250). [DATASET]

Fazio EN, Young CC, Toma J, Levy M, Berger KR, Johnson CL, Mehmood R, Swan P, Chu A, Cregan SP *et al* (2017) Activating transcription factor 3 promotes loss of the acinar cell phenotype in response to cerulein-induced pancreatitis in mice. *Mol Biol Cell* 28: 2347-2359

Fukuda M (2008) Regulation of secretory vesicle traffic by Rab small GTPases. *Cell Mol Life Sci* 65: 2801-2813

Gerber T, Murawala P, Knapp D, Masselink W, Schuez M, Hermann S, Gac-Santel M, Nowoshilow S, Kageyama J, Khattak S *et al* (2018). Gene Expression Omnibus GSE106269 (https://www.ncbi.nlm.nih.gov/geo/query/acc.cgi?acc=GSE106269). [DATASET]

Gerber T, Murawala P, Knapp D, Masselink W, Schuez M, Hermann S, Gac-Santel M, Nowoshilow S, Kageyama J, Khattak S *et al* (2018) Single-cell analysis uncovers convergence of cell identities during axolotl limb regeneration. *Science* 362

Gey M, Wanner R, Schilling C, Pedro MT, Sinske D, Knoll B (2016) Atf3 mutant mice show reduced axon regeneration and impaired regeneration-associated gene induction after peripheral nerve injury. *Open Biol* 6

Giroux V, Rustgi AK (2017) Metaplasia: tissue injury adaptation and a precursor to the dysplasia-cancer sequence. *Nat Rev Cancer*

Goldenring JR (2018) Pyloric metaplasia, pseudopyloric metaplasia, ulcer-associated cell lineage and spasmolytic polypeptide-expressing metaplasia: reparative lineages in the gastrointestinal mucosa. *J Pathol* 245: 132-137

Grant CE, Bailey TL, Noble WS (2011) FIMO: scanning for occurrences of a given motif. *Bioinformatics* 27: 1017-1018

Guerra F, Bucci C (2016) Multiple Roles of the Small GTPase Rab7. *Cells* 5

Hai T, Wolfgang CD, Marsee DK, Allen AE, Sivaprasad U (1999) ATF3 and stress responses. *Gene Expr* 7: 321-335

Hartman MG, Lu D, Kim ML, Kociba GJ, Shukri T, Buteau J, Wang X, Frankel WL, Guttridge D, Prentki M *et al* (2004) Role for activating transcription factor 3 in stress-induced beta-cell apoptosis. *Mol Cell Biol* 24: 5721-5732

Hess DA, Humphrey SE, Ishibashi J, Damsz B, Lee AH, Glimcher LH, Konieczny SF (2011) Extensive pancreas regeneration following acinar-specific disruption of Xbp1 in mice. *Gastroenterology* 141: 1463-1472

784 Hong KU, Reynolds SD, Giangreco A, Hurley CM, Stripp BR (2001) Clara cell secretory protein-
785 expressing cells of the airway neuroepithelial body microenvironment include a label-
786 retaining subset and are critical for epithelial renewal after progenitor cell depletion. *Am*
787 *J Respir Cell Mol Biol* 24: 671-681
788 Hou Y, Ernst SA, Stuenkel EL, Lentz SI, Williams JA (2015) Rab27A Is Present in Mouse
789 Pancreatic Acinar Cells and Is Required for Digestive Enzyme Secretion. *PLoS One* 10:
790 e0125596
791 Huh WJ, Esen E, Geahlen JH, Bredemeyer AJ, Lee AH, Shi G, Konieczny SF, Glimcher LH,
792 Mills JC (2010) XBP1 controls maturation of gastric zymogenic cells by induction of
793 MIST1 and expansion of the rough endoplasmic reticulum. *Gastroenterology* 139: 2038-
794 2049
795 Huh WJ, Khurana SS, Geahlen JH, Kohli K, Waller RA, Mills JC (2012) Tamoxifen induces
796 rapid, reversible atrophy, and metaplasia in mouse stomach. *Gastroenterology* 142: 21-
797 24 e27
798 Hunt D, Raivich G, Anderson PN (2012) Activating transcription factor 3 and the nervous
799 system. *Front Mol Neurosci* 5: 7
800 Inoue K, Zama T, Kamimoto T, Aoki R, Ikeda Y, Kimura H, Hagiwara M (2004) TNFalpha-
801 induced ATF3 expression is bidirectionally regulated by the JNK and ERK pathways in
802 vascular endothelial cells. *Genes Cells* 9: 59-70
803 Itoh T, Satoh M, Kanno E, Fukuda M (2006) Screening for target Rabs of TBC (Tre-
804 2/Bub2/Cdc16) domain-containing proteins based on their Rab-binding activity. *Genes*
805 *Cells* 11: 1023-1037
806 Jin RU, Mills JC (2014) RAB26 coordinates lysosome traffic and mitochondrial localization. *J*
807 *Cell Sci* 127: 1018-1032

Jin RU, Mills JC (2019) The cyclical hit model: how paligenosis might establish the mutational landscape in Barrett's esophagus and esophageal adenocarcinoma. *Curr Opin Gastroenterol*

Johnson CL, Kowalik AS, Rajakumar N, Pin CL (2004) Mist1 is necessary for the establishment of granule organization in serous exocrine cells of the gastrointestinal tract. *Mech Dev* 121: 261-272

Jones JC, Brindley CD, Elder NH, Myers MG, Jr., Rajala MW, Dekaney CM, McNamee EN, Frey MR, Shroyer NF, Dempsey PJ (2019) Cellular Plasticity of Defa4(Cre)-Expressing Paneth Cells in Response to Notch Activation and Intestinal Injury. *Cell Mol Gastroenterol Hepatol* 7: 533-554

Karki A, Humphrey SE, Steele RE, Hess DA, Taparowsky EJ, Konieczny SF (2015) Silencing Mist1 Gene Expression Is Essential for Recovery from Acute Pancreatitis. *PLoS One* 10: e0145724

Keeley TM, Horita N, Samuelson LC (2019) Tamoxifen-Induced Gastric Injury: Effects of Dose and Method of Administration. *Cell Mol Gastroenterol Hepatol* 8: 365-367

Khurana SS, Riehl TE, Moore BD, Fassan M, Rugge M, Romero-Gallo J, Noto J, Peek RM, Jr., Stenson WF, Mills JC (2013) The hyaluronic acid receptor CD44 coordinates normal and metaplastic gastric epithelial progenitor cell proliferation. *J Biol Chem* 288: 16085-16097

Kjos I, Borg Distefano M, Saetre F, Repnik U, Holland P, Jones AT, Engedal N, Simonsen A, Bakke O, Progida C (2017) Rab7b modulates autophagic flux by interacting with Atg4B. *EMBO Rep* 18: 1727-1739

Kowalik AS, Johnson CL, Chadi SA, Weston JY, Fazio EN, Pin CL (2007) Gene Expression Omnibus GSE3644 (https://www.ncbi.nlm.nih.gov/geo/query/acc.cgi?acc=GSE3644). [DATASET]

Kowalik AS, Johnson CL, Chadi SA, Weston JY, Fazio EN, Pin CL (2007) Mice lacking the transcription factor Mist1 exhibit an altered stress response and increased sensitivity to

caerulein-induced pancreatitis. *Am J Physiol Gastrointest Liver Physiol* 292: G1123-1132

Kreft L, Soete A, Hulpiau P, Botzki A, Saeys Y, De Bleser P (2017) ConTra v3: a tool to identify transcription factor binding sites across species, update 2017. *Nucleic Acids Res* 45: W490-W494

Kusaba T, Lalli M, Kramann R, Kobayashi A, Humphreys BD (2014) Differentiated kidney epithelial cells repair injured proximal tubule. *Proc Natl Acad Sci U S A* 111: 1527-1532

Langemeyer L, Frohlich F, Ungermann C (2018) Rab GTPase Function in Endosome and Lysosome Biogenesis. *Trends Cell Biol* 28: 957-970

Lennerz JK, Kim SH, Oates EL, Huh WJ, Doherty JM, Tian X, Bredemeyer AJ, Goldenring JR, Lauwers GY, Shin YK *et al* (2010) The transcription factor MIST1 is a novel human gastric chief cell marker whose expression is lost in metaplasia, dysplasia, and carcinoma. *Am J Pathol* 177: 1514-1533

Leushacke M, Tan SH, Wong A, Swathi Y, Hajamohideen A, Tan LT, Goh J, Wong E, Denil S, Murakami K *et al* (2017) Lgr5-expressing chief cells drive epithelial regeneration and cancer in the oxyntic stomach. *Nat Cell Biol* 19: 774-786

Li HF, Cheng CF, Liao WJ, Lin H, Yang RB (2010) ATF3-mediated epigenetic regulation protects against acute kidney injury. *J Am Soc Nephrol* 21: 1003-1013

Li X, Wu J, Sun X, Wu Q, Li Y, Li K, Zhang Q, Li Y, Abel ED, Chen H (2020) Autophagy Reprograms Alveolar Progenitor Cell Metabolism in Response to Lung Injury. *Stem Cell Reports* 14: 420-432

Lin H, Li HF, Chen HH, Lai PF, Juan SH, Chen JJ, Cheng CF (2014) Activating transcription factor 3 protects against pressure-overload heart failure via the autophagy molecule Beclin-1 pathway. *Mol Pharmacol* 85: 682-691

Liou GY, Doppler H, DelGiorno KE, Zhang L, Leitges M, Crawford HC, Murphy MP, Storz P (2016) Mutant KRas-Induced Mitochondrial Oxidative Stress in Acinar Cells Upregulates

EGFR Signaling to Drive Formation of Pancreatic Precancerous Lesions. *Cell Rep* 14: 2325-2336

Lizundia R, Chaussepied M, Naissant B, Masse GX, Quevillon E, Michel F, Monier S, Weitzman JB, Langsley G (2007) The JNK/AP-1 pathway upregulates expression of the recycling endosome rab11a gene in B cells transformed by Theileria. *Cell Microbiol* 9: 1936-1945

Lo HG, Jin RU, Sibbel G, Liu D, Karki A, Joens MS, Madison BB, Zhang B, Blanc V, Fitzpatrick JA *et al* (2017) A single transcription factor is sufficient to induce and maintain secretory cell architecture. *Genes Dev* 31: 154-171

Mackiewicz P, Wyroba E (2009) Phylogeny and evolution of Rab7 and Rab9 proteins. *BMC Evol Biol* 9: 101

Marubashi S, Fukuda M (2020) Rab7B/42 Is Functionally Involved in Protein Degradation on Melanosomes in Keratinocytes. *Cell Struct Funct* 45: 45-55

Meyer AR, Engevik AC, Willet SG, Williams JA, Zou Y, Massion PP, Mills JC, Choi E, Goldenring JR (2019) Cystine/Glutamate Antiporter (xCT) Is Required for Chief Cell Plasticity After Gastric Injury. *Cell Mol Gastroenterol Hepatol* 8: 379-405

Meyer AR, Goldenring JR (2018) Injury, repair, inflammation and metaplasia in the stomach. *J Physiol* 596: 3861-3867

Miao ZF, Adkins-Threats M, Burclaff JR, Osaki LH, Sun JX, Kefalov Y, He Z, Wang ZN, Mills JC (2020a) A Metformin-Responsive Metabolic Pathway Controls Distinct Steps in Gastric Progenitor Fate Decisions and Maturation. *Cell Stem Cell* 26: 910-925 e916

Miao ZF, Lewis MA, Cho CJ, Adkins-Threats M, Park D, Brown JW, Sun JX, Burclaff JR, Kennedy S, Lu J *et al* (2020b) A Dedicated Evolutionarily Conserved Molecular Network Licenses Differentiated Cells to Return to the Cell Cycle. *Dev Cell*

Miao ZF, Sun JX, Adkins-Threats M, Pang MJ, Zhao JH, Wang X, Tang KW, Wang ZN, Mills JC (2021) DDIT4 Licenses Only Healthy Cells to Proliferate During Injury-induced Metaplasia. *Gastroenterology* 160: 260-271 e210

Mills JC, Sansom OJ (2015) Reserve stem cells: Differentiated cells reprogram to fuel repair, metaplasia, and neoplasia in the adult gastrointestinal tract. *Sci Signal* 8: re8

Mills JC, Taghert PH (2012) Scaling factors: transcription factors regulating subcellular domains. *Bioessays* 34: 10-16

Moore BD, Jin RU, Osaki L, Romero-Gallo J, Noto J, Peek RK, Mills JC (2015) Gene Expression Omnibus GSE71580 (https://www.ncbi.nlm.nih.gov/geo/query/acc.cgi?acc=GSE71580). [DATASET]

Moore BD, Jin RU, Osaki L, Romero-Gallo J, Noto J, Peek RK, Mills JC (2015) Identification of alanyl aminopeptidase (CD13) as a surface marker for isolation of mature gastric zymogenic chief cells. *Am J Physiol Gastrointest Liver Physiol* 309: G955-G964

Nam KT, Lee HJ, Sousa JF, Weis VG, O'Neal RL, Finke PE, Romero-Gallo J, Shi G, Mills JC, Peek RM, Jr. *et al* (2010) Mature chief cells are cryptic progenitors for metaplasia in the stomach. *Gastroenterology* 139: 2028-2037 e2029

Niederau C, Ferrell LD, Grendell JH (1985) Caerulein-induced acute necrotizing pancreatitis in mice: protective effects of proglumide, benzotript, and secretin. *Gastroenterology* 88: 1192-1204

Nozaki K, Ogawa M, Williams JA, Lafleur BJ, Ng V, Drapkin RI, Mills JC, Konieczny SF, Nomura S, Goldenring JR (2008) A molecular signature of gastric metaplasia arising in response to acute parietal cell loss. *Gastroenterology* 134: 511-522

Ohnishi H, Ernst SA, Wys N, McNiven M, Williams JA (1996) Rab3D localizes to zymogen granules in rat pancreatic acini and other exocrine glands. *Am J Physiol* 271: G531-538

Otu HH, Naxerova K, Ho K, Can H, Nesbitt N, Libermann TA, Karp SJ (2007) Gene Expression Omnibus GSE6998 (https://www.ncbi.nlm.nih.gov/geo/query/acc.cgi?acc=GSE6998). [DATASET]

910 Otu HH, Naxerova K, Ho K, Can H, Nesbitt N, Libermann TA, Karp SJ (2007) Restoration of
911 liver mass after injury requires proliferative and not embryonic transcriptional patterns. *J*
912 *Biol Chem* 282: 11197-11204
913 Pereira-Leal JB, Seabra MC (2000) The mammalian Rab family of small GTPases: definition of
914 family and subfamily sequence motifs suggests a mechanism for functional specificity in
915 the Ras superfamily. *J Mol Biol* 301: 1077-1087
916 Petersen CP, Mills JC, Goldenring JR (2017) Murine Models of Gastric Corpus Preneoplasia.
917 *Cell Mol Gastroenterol Hepatol* 3: 11-26
918 Pin CL, Rukstalis JM, Johnson C, Konieczny SF (2001) The bHLH transcription factor Mist1 is
919 required to maintain exocrine pancreas cell organization and acinar cell identity. *J Cell*
920 *Biol* 155: 519-530
921 Progida C, Cogli L, Piro F, De Luca A, Bakke O, Bucci C (2010) Rab7b controls trafficking from
922 endosomes to the TGN. *J Cell Sci* 123: 1480-1491
923 Radyk MD, Burclaff J, Willet SG, Mills JC (2018) Metaplastic Cells in the Stomach Arise,
924 Independently of Stem Cells, via Dedifferentiation or Transdifferentiation of Chief Cells.
925 *Gastroenterology* 154: 839-843 e832
926 Ramsey VG, Doherty JM, Chen CC, Stappenbeck TS, Konieczny SF, Mills JC (2007) The
927 maturation of mucus-secreting gastric epithelial progenitors into digestive-enzyme 928
secreting zymogenic cells requires Mist1. *Development* 134: 211-222
929 Raven A, Lu WY, Man TY, Ferreira-Gonzalez S, O'Duibhir E, Dwyer BJ, Thomson JP, Meehan
930 RR, Bogorad R, Koteliansky V *et al* (2017) Cholangiocytes act as facultative liver stem
931 cells during impaired hepatocyte regeneration. *Nature* 547: 350-354
932 Romermann D, Ansari N, Schultz-Moreira AR, Michael A, Marhenke S, Hardtke-Wolenski M,
933 Longerich T, Manns MP, Wedemeyer H, Vogel A *et al* (2020) Absence of Atg7 in the
934 liver disturbed hepatic regeneration after liver injury. *Liver Int* 40: 1225-1238

Rosenfeldt MT, O'Prey J, Morton JP, Nixon C, MacKay G, Mrowinska A, Au A, Rai TS, Zheng L, Ridgway R *et al* (2013) p53 status determines the role of autophagy in pancreatic tumour development. *Nature* 504: 296-300

Saenz JB, Burclaff J, Mills JC (2016) Modeling Murine Gastric Metaplasia Through Tamoxifen-Induced Acute Parietal Cell Loss. *Methods Mol Biol* 1422: 329-339

Saenz JB, Mills JC (2018) Acid and the basis for cellular plasticity and reprogramming in gastric repair and cancer. *Nat Rev Gastroenterol Hepatol* 15: 257-273

Saenz JB, Vargas N, Mills JC (2018) Tropism for Spasmolytic Polypeptide-Expressing Metaplasia Allows Helicobacter pylori to Expand Its Intragastric Niche. *Gastroenterology* 944

Saera-Vila A, Kish PE, Louie KW, Grzegorski SJ, Klionsky DJ, Kahana A (2016) Autophagy regulates cytoplasmic remodeling during cell reprogramming in a zebrafish model of muscle regeneration. *Autophagy* 12: 1864-1875

Saluja A, Saito I, Saluja M, Houlihan MJ, Powers RE, Meldolesi J, Steer M (1985) In vivo rat pancreatic acinar cell function during supramaximal stimulation with caerulein. *Am J Physiol* 249: G702-710

Shimizu T, Sohn Y, Choi E, Petersen CP, Prasad N, Goldenring JR (2020) Decrease in MiR-148a Expression During Initiation of Chief Cell Transdifferentiation. *Cell Mol Gastroenterol Hepatol* 9: 61-78

Sood V, Sharma KB, Gupta V, Saha D, Dhapola P, Sharma M, Sen U, Kitajima S, Chowdhury S, Kalia M *et al* (2017) ATF3 negatively regulates cellular antiviral signaling and autophagy in the absence of type I interferons. *Sci Rep* 7: 8789

Storz P (2017) Acinar cell plasticity and development of pancreatic ductal adenocarcinoma. *Nat Rev Gastroenterol Hepatol* 14: 296-304

Stroupe C (2018) This Is the End: Regulation of Rab7 Nucleotide Binding in Endolysosomal Trafficking and Autophagy. *Frontiers in Cell and Developmental Biology* 6

960 Takahashi K, Mashima H, Miura K, Maeda D, Goto A, Goto T, Sun-Wada GH, Wada Y, Ohnishi
961 H (2017) Disruption of Small GTPase Rab7 Exacerbates the Severity of Acute
962 Pancreatitis in Experimental Mouse Models. *Sci Rep* 7: 2817
963 Tata PR, Mou H, Pardo-Saganta A, Zhao R, Prabhu M, Law BM, Vinarsky V, Cho JL, Breton S,
964 Sahay A *et al* (2013) Dedifferentiation of committed epithelial cells into stem cells in vivo. 965
Nature 503: 218-223
966 Tian X, Jin RU, Bredemeyer AJ, Oates EJ, Blazewska KM, McKenna CE, Mills JC (2010)
967 RAB26 and RAB3D are direct transcriptional targets of MIST1 that regulate exocrine
968 granule maturation. *Mol Cell Biol* 30: 1269-1284
969 Tsai WW, Matsumura S, Liu W, Phillips NG, Sonntag T, Hao E, Lee S, Hai T, Montminy M
970 (2015) ATF3 mediates inhibitory effects of ethanol on hepatic gluconeogenesis. *Proc*
971 *Natl Acad Sci U S A* 112: 2699-2704
972 van Es JH, Sato T, van de Wetering M, Lyubimova A, Yee Nee AN, Gregorieff A, Sasaki N,
973 Zeinstra L, van den Born M, Korving J *et al* (2012) Dll1+ secretory progenitor cells revert
974 to stem cells upon crypt damage. *Nat Cell Biol* 14: 1099-1104
975 Wandinger-Ness A, Zerial M (2014) Rab proteins and the compartmentalization of the
976 endosomal system. *Cold Spring Harb Perspect Biol* 6: a022616
977 Wang L, Deng S, Lu Y, Zhang Y, Yang L, Guan Y, Jiang H, Li H (2012) Increased inflammation
978 and brain injury after transient focal cerebral ischemia in activating transcription factor 3 979
knockout mice. *Neuroscience* 220: 100-108
980 Weis VG, Petersen CP, Weis JA, Meyer AR, Choi E, Mills JC, Goldenring JR (2017) Maturity
981 and age influence chief cell ability to transdifferentiate into metaplasia. *Am J Physiol*
982 *Gastrointest Liver Physiol* 312: G67-G76
983 Willet SG, Lewis MA, Miao ZF, Liu D, Radyk MD, Cunningham RL, Burclaff J, Sibbel G, Lo HG,
984 Blanc V *et al* (2018) Regenerative proliferation of differentiated cells by mTORC1-
985 dependent paligenosis. *EMBO J* 37

Wroblewski LE, Choi E, Petersen C, Delgado AG, Piazuelo MB, Romero-Gallo J, Lantz TL, Zavros Y, Coffey RJ, Goldenring JR *et al* (2019) Targeted mobilization of Lrig1(+) gastric epithelial stem cell populations by a carcinogenic Helicobacter pylori type IV secretion system. *Proc Natl Acad Sci U S A* 116: 19652-19658

Yang M, Chen T, Han C, Li N, Wan T, Cao X (2004) Rab7b, a novel lysosome-associated small GTPase, is involved in monocytic differentiation of human acute promyelocytic leukemia cells. *Biochem Biophys Res Commun* 318: 792-799

Yue L, Wan R, Luan S, Zeng W, Cheung TH (2020) Gene Expression Omnibus GSE113631 (https://www.ncbi.nlm.nih.gov/geo/query/acc.cgi?acc=GSE113631). [DATASET]

Yue L, Wan R, Luan S, Zeng W, Cheung TH (2020) Dek Modulates Global Intron Retention during Muscle Stem Cells Quiescence Exit. *Dev Cell* 53: 661-676 e666

Zhao Y, Wu X, Qian L, Guo L, Liao J, Wu X (2017) Activating transcription factor 3 protects mice against pseudomonas aeruginosa-induced acute lung injury by interacting with lipopolysaccharide binding protein. *Mol Immunol* 90: 27-32

Zhou J, Edgar BA, Boutros M (2017) ATF3 acts as a rheostat to control JNK signalling during intestinal regeneration. *Nat Commun* 8: 14289

Zhu Q, Wang H, Jiang B, Ni X, Jiang L, Li C, Wang X, Zhang F, Ke B, Lu L (2018) Loss of ATF3 exacerbates liver damage through the activation of mTOR/p70S6K/ HIF-1alpha signaling pathway in liver inflammatory injury. *Cell Death Dis* 9: 910

FIGURE LEGENDS

Figure 1. Secretory cell structure is dismantled rapidly and in a choreographed pattern in paligenosis

A. *Left* – Single-level electron micrograph images of zymogenic chief cells (ZCs) after 24h vehicle or high-dose tamoxifen (HDT) treatment from FIB-SEM 3D tomography. G = representative secretory granules; N = nuclei. Scale bar, 2μm. *Right* - Stacked EM images rendered into 3D projections using Amira software. Cells outlined by dashed yellow line.

B. Representative immunofluorescence images of stomach unit bases at homeostasis, 6 hour, and 24h HDT stained with GIF (red, granules) and LAMP1 (green, lysosomes) Scale bar, 25μm. Stomach unit base outlined by dashed white line.

C. Representative TEM images of normal and injured ZCs (scale bar, 2μm). *Right* (insets)- higher magnification images of boxed regions from left show emergence of double-membraned autophagic vesicles engulfing mature granules, mitochondria, and rough ER 24h after HDT injury. Scale bar, 500nm. Arrowheads mark vesicular degradation events in the cell lacking double membranes. Cells outlined by dashed yellow line.

D. Graph of the number of zymogenic chief cell granules per cell in vehicle vs. 24h HDT treatment. Each data point=total granules in a cell in a single TEM section with cells from 2 separate mice plotted together (each cell is a data point; cells from the same mouse are grouped by color shade). Red line indicates mean across all the mice.

E. Graph of the number of degradation events scored as in D. A degradation event was counted if electron dense-cargo or organelles were surrounded by a single membrane (lysosome) or double membrane (autophagosome). Red line indicates mean across all the mice.

F. Representative TEM images of normal and injured acinar cells. Scale bar, 2μm. *Right* (insets)- higher magnification images of boxed regions from left show emergence of double-membraned autophagic vesicles engulfing mature granules, mitochondria, and rough ER 24h after cerulein (CER) injury. Scale bar, 500nm. Arrowheads mark degradation events without double membranes.

G. Graph of the number of acinar cell granules per cell in vehicle vs. 24h CER treatment. Each data point=total granules in a cell in a single cell counted from one mouse. Red line indicates mean.

H. Graph of the number of degradation events scored in vehicle vs. 24h CER treatment. Each data point=total events in a cell in a single cell counted from one mouse. Red line indicates mean.

I. mRNA expression by qRT-PCR of *Rab5*, *Rab7a*, *Rab7b*, and *Rab9*. Significance determined by one-way ANOVA, Tukey post hoc. Each data point represents the mean of triplicate technical replicates from a single mouse, n=3-4 mice in independent experiments. Error bars denote standard deviation.

Figure 2. ATF3 transcriptionally upregulates *Rab7b* early in paligenosis, and RAB7 protein is associated with large lysosomal aggregates

A. *Top* – Representative RAB7 expression in base of stomach units (ZCs) in vehicle or 24h HDT by immunohistochemistry. Arrowheads point to RAB7 vesicle aggregates. Scale bar 20μm. *Bottom* – Representative ATF3 expression in base of stomach units (ZCs) by immunohistochemistry. ATF3 appears in nuclei following 24h high-dose tamoxifen (HDT). Scale bar 20μm. Stomach unit base outlined by dashed black line.

B. *Atf3* mRNA expression by qRT-PCR in vehicle, 6 hour, 24 hour, and 72 hour HDT treatment. Each data point represents the mean of triplicate technical replicates from a single mouse, n=3-4 mice in independent experiments. Significance determined by One-way ANOVA, Tukey. Error bars denote standard deviation.

C. Western blot of ATF3 expression over HDT and CER timecourses with β-Actin loading control.

D. *Top* – Representative RAB7 staining in pancreatic acinar cells. Arrowheads indicate RAB7 vesicles. Scale bar 20μm. *Bottom* – Representative ATF3 expression in pancreatic acinar cells. Nuclei express ATF3 after 24h cerulein (CER) injury. Scale bar 20μm.

E. ChIP-PCR on mouse stomach tissue at vehicle and 6 hour HDT. Chromatin probed with ATF3, Histone H3 antibodies, or a Rabbit IgG control. Also included is the 2% chromatin input and water to control for DNA contamination. *Rab7b* amplicon is from a conserved, putative ATF3-binding site in the first intron. Amplicon from *Atf3* is a positive control from a previously characterized ATF3-binding site; negative control is from a site in *Rab9a* lacking putative ATF3 binding motifs.

Figure 3. ATF3 transcriptionally upregulates *RAB7B in vitro* to govern formation of autodegradative vesicles

A. mRNA expression of *ATF3* by qRT-PCR in control, *ATF3* knockdown (KD), and ATF3 overexpression (OE) AGS cell lines generated using a Piggybac™ transposon system. Significance by one-way ANOVA, Dunnett post-hoc. Datapoint = mean of technical triplicates in a single mouse. n=3 mice. Error bars denote standard deviation.

B. mRNA expression of *RAB7B* by qRT-PCR in AGS cell lines from 3A. Statistics and plotting as for panel A.

C. *Top* – Immunofluorescence for RAB7 (red) and DAPI (blue, nuclei) in control, *ATF3* knockdown (KD), and ATF3 overexpression (OE) AGS cells. Arrowhead indicates aggregated

RAB7 vesicular formation similar to those observed in tissue. *Bottom* – Immunofluorescence for ATF3 (purple) and Cathepsin D (CTSD, green, lysosomes) in AGS cells. Scale bar, 20μm.

D. *Left* - Immunofluorescence for anti-FLAG (RAB7B) (red) and DAPI (blue, nuclei) in *ATF3* knockdown; RAB7B overexpression (*ATF3*-KD RAB7B-OE) AGS cells show large vesicular structures. *Right* - Immunofluorescence for anti-FLAG (RAB7B) (red) and DAPI (blue, nuclei) in ATF3 overexpression; RAB7B GTPase mutant (ATF3-OE $RAB7B^{T22N}$) AGS cells fail to make vesicles. Scale bar, 20μm.

Figure 4. *Atf3* coordinates cellular autodegradation after injury in paligenosis stage I

A. Representative immunofluorescence images of pancreatic acinar cells after vehicle or 24h cerulein (CER) treatment stained for RAB7 (red) and Cathepsin D (CTSD, green, lysosomes). Top row is wild-type, bottom row is $Atf3^{-/-}$. Yellow arrowhead highlights RAB7 and CTSD co-expression. White arrowhead points to an area of RAB7 expression only. Scale bar, 20μm.

B. Representative immunofluorescence images of gastric chief cells after vehicle or 24h high-dose tamoxifen (HDT) treatment stained for RAB7 (red) and Cathepsin D (CTSD, green, lysosomes). Top row is wild-type, bottom row is $Atf3^{-/-}$. Yellow arrowhead highlights RAB7 and CTSD co-expression. White arrowhead points to an area of RAB7 expression only. Scale bars 20μm. Stomach unit base outlined by dashed white line.

C. Representative immunofluorescence images of gastric chief cells after vehicle or 24h HDT treatment stained for Pepsinogen C (PGC, red, granules) and MAP1LC3B (green, autophagy marker). Top row is wild-type, bottom row is $Atf3^{-/-}$. Scale bar, 50μm. Stomach unit base outlined by dashed white line.

D. Transmission electron micrograph images of zymogenic chief cells (ZCs) after 24h vehicle or HDT treatment in WT (top) and *Atf3*$^{-/-}$ mice (bottom). Scale bar, 1μm. Arrowheads indicate cell components being degraded.

E. Quantification of degradation events per cell counted from EM images of ZCs after 24h HDT treatment in WT and *Atf3*$^{-/-}$mice as shown in panel 3D. Each data point=total granules in a cell in a single TEM section with cells from 2 separate mice plotted together (data point colors indicate cells from a single mouse). Red line indicates mean across all the mice.

Figure 5. *Atf3* loss increases cell death and reduces proliferation after paligenotic injury

A. Representative immunofluorescence images of gastric units after vehicle or 72h high-dose tamoxifen (HDT) treatment stained for GIF (red, granules), GSII (green, neck cells and SPEM marker), BRDU (white, proliferation) and DAPI (blue, nuclei). Top row is wild-type, bottom row is *Atf3*$^{-/-}$. Yellow arrowheads point to areas of base dropout where ZCs have been lost. Scale bar, 50μm. Stomach units outlined by dashed white line.

B. Proliferation as quantified by number of BrdU^{+} cells per unit in WT and *Atf3*$^{-/-}$vehicle±HDT. Each data point = mean of counts from 40-50 gastric glands from an individual mouse, n=3-4 mice per treatment group. Significance by unpaired two-tailed t-test. Error bars denote standard deviation.

C. Plot and statistical analysis as for Panel B but quantifying BrdU^{+} cells only in the bottom 1/3 of the unit, which are derived mostly from paligenosis and not from isthmal and neck stem and progenitor cells.

D. Death of ZCs after injury plotted by quantifying the base dropout rate, which is the fraction of glands that do not reach the muscularis mucosa from the lumen. Each data point is the mean of

80-100 glands from an individual mouse, n=4 mice per treatment group. Significance by unpaired two-tailed t-test. Error bars denote standard deviation.

E. Representative immunohistochemistry of Cleaved-Caspase 3 in pancreatic acinar cells marking apoptosis in vehicle or 24h cerulein (CER) treatment. Top row is WT, bottom row is *Atf3*$^{-/-}$. Scale bar, 50μm.

F. Apoptosis quantified following 24h CER injury by the number of Cleaved-Caspase 3^{+} cells from a 40x field. Each data point is mean of positive cells in 4-5 40x fields in an individual mouse, n=3 mice per treatment group. Significance by unpaired two-tailed t-test. Error bars denote standard deviation.

G. Representative immunohistochemistry of BrdU in pancreatic acinar cells marking proliferation in vehicle or 7 days of repeated cerulein injury. Top row is WT, bottom row is *Atf3*$^{-/-}$. Scale bar, 50μm.

H. Quantification of proliferation at peak ADM as counted by the number of BrdU^{+} cells from a 20x field following 7D cerulein treatment. Plotting and statistical analysis as per panel F.

Figure 6. ATF3 is expressed in human SPEM

Serial sections of human tissue. Representative immunohistochemistry of GSII (top; spasmolytic polypeptide-expressing metaplasia [SPEM] marker and neck cells) counterstained with hematoxylin (blue) and eosin (pink). Representative staining of ATF3 (bottom) counterstained with eosin (pink). Tissue was taken from regions adjacent to gastric adenocarcinoma. Scale bars *left* - 50μm *right* - 20μm. Arrowheads indicate strongly expressing ATF3 cells and the corresponding region in the same gland labeled with GSII in a serial tissue section. GSII at the base of gastric glands in the body of the stomach indicate transition to SPEM.

Figure 7. Model of ATF3 function in paligenosis

ATF3 peaks early after injury and helps to coordinate the induction of autodegradation by transcriptionally activating *Rab7b* and other targets to increase the number of lysosomes and induce autophagy. ATF3 also functions at this same time (Stage 1) to repress scaling and maturation factor *Mist1*.

EXTENDED VIEW FIGURE LEGENDS

Figure EV1. Schemes for gastric and pancreatic injury treatments, and hydroxychloroquine treatment in stomach tissue to inhibit paligenosis.

A. Scheme of tamoxifen treatment timeline. Mice were administered high-dose tamoxifen (HDT; 5 mg/20 g body weight) by intraperitoneal injection up to two times and stomachs were harvested at the respective/indicated timepoint as per the experimental details. Day 3 of timeline is when peak SPEM is observed. Orange bars indicate each stage of paligenosis and where they correspond in the treatment timeline.

B. Scheme of cerulein (CER) treatment timeline to induce pancreatitis. Mice were administered repeated cerulein injections by intraperitoneal injection. Six hourly injections of cerulein (50μg/kg) were given every other day for up to 7 days (peak ADM). Orange bars indicate each stage of paligenosis and where they correspond in the treatment timeline.

C. Scheme of hydroxychloroquine (HCQ) treatment timeline. Mice were pretreated with 60mg/kg HCQ (or PBS) one day prior to high-dose tamoxifen (HDT) administration alongside HCQ (60mg/kg/day). Stomachs were harvested at Day 3 (72 hours) when peak SPEM is normally observed.

D. Immunohistochemistry for GSII in gastric units to mark normal mucous neck cells (vehicle) and SPEM cells (72h HDT) in mice treated with Vehicle, HDT, HCQ, or HDT+HCQ. Scale bars 20μm. Counterstained with hematoxylin. Arrows mark GSII at the base of the stomach unit indicating SPEM.

E. Quantification of the fraction of gastric units exhibiting SPEM (from EV1D). Each data point = mean of counts from 40-50 gastric glands from an individual mouse, n=4-6 mice per treatment group; black line = mean of means from each mouse ± SEM. Significance by nonparametric two-tailed t-test.

F. Immunofluorescence of gastric units; nuclei (DAPI, blue), chief cells (GIF, red), progenitor/metaplastic cells (GSII green + red GIF) and proliferative cells (BrdU, white) after treatment with HDT or HDT+HCQ for 72 hours. 72h HDT units exhibit SPEM (GSII and GIF overlap), while 72h HDT+HCQ units show scant SPEM and full chief cell cytoplasm packed with GIF secretory granules. Scale bars 50μm. Stomach unit base outlined by dashed white line.

Figure EV2. Protein expression of RABs in stomach and pancreas.

A. RAB7A, RAB7B, RAB7 expression by Western blot in stomachs treated with high-dose tamoxifen (HDT) compared to ACTIN loading control.

B. RAB7A, RAB7B, RAB7 expression by Western blot in pancreata treated with cerulein (CER) compared to ACTIN loading control.

Figure EV3. Analysis of ATF3 binding sites in the mouse *Rab7b* first intron.

A. Mouse *Rab7b* gene alignment using UCSC genome browser (NCBI37/mm9).

B. Regions of predicted conserved ATF3 binding derived from ConTra v3. Orange indicates conserved ATF3 sites in one region of *Rab7b* and blue indicates a second region of conserved ATF3 sites downstream, but still in the first intron. Highlighted regions are aligned to the gene in (A). TFBS = transcription factor binding sites.

C. Alignment of ATF3 ChIP-seq analysis from 4h Cerulein treated mouse pancreas published in Fazio *et al*., 2017 GEO accession GSE60250. ChIP-seq peaks aligned to gene in (A).

Figure EV4. Markers of Spasmolytic Polypeptide-Expressing Metaplasia, cell proliferation, and cell death in the stomach following injury.

A. Representative immunofluorescence of gastric units stained for DAPI (blue), gastric intrinsic factor (GIF, cyan), and CD44v (marker of spasmolytic polypeptide-expressing metaplasia [SPEM] when expressed in cells at the unit base, red). WT (top) and *Atf3*$^{-/-}$ (bottom) mice were treated with 72h high-dose tamoxifen (HDT). Arrowhead indicates base dropout in *Atf3*$^{-/-}$stomach. Scale bars 20μm. Stomach units outlined by dashed yellow line.

B. Representative immunohistochemistry of GSII in gastric units to mark normal mucous neck cells (vehicle) and SPEM cells (72h HDT) in WT (top) and *Atf3*$^{-/-}$ (bottom) mice. Scale bars 50μm. Counterstained with hematoxylin. Stomach units outlined by dashed black line.

C. Quantification of the percent of gastric units exhibiting SPEM as counted by the number of units with GSII at the unit base over the number of units total. Each data point = mean of counts from 40-50 gastric glands from an individual mouse, n=5 mice per treatment group. Significance by nonparametric two-tailed t-test. Error bars denote standard deviation.

D. Representative immunohistochemistry of BrdU in WT (top) and *Atf3*KO (bottom) gastric units with vehicle or 72h high-dose tamoxifen (HDT) treatment. BrdU administered 90 minutes prior to sacrifice to capture cells in S phase. Eosin counterstain. Scale bars 50μm. Stomach units outlined by dashed black line.

E. Representative immunohistochemistry of Cleaved-Caspase 3 in gastric units of WT (top) and *Atf3*KO (bottom) mice when treated with vehicle or 72h high-dose tamoxifen (HDT). Counterstained with eosin. Arrowheads point to ZCs with high expression of Cleaved-CASP3. Scale bars 50μm. Stomach units outlined by dashed black line.

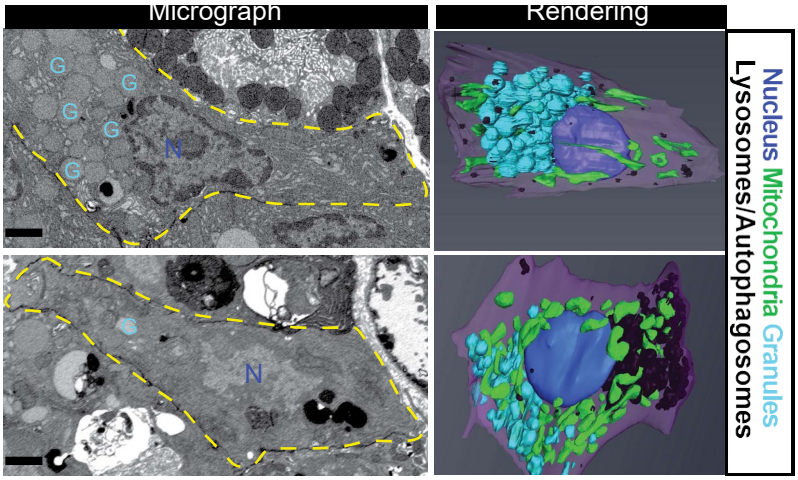
F. Graph of the apoptosis rate following 72h HDT injury as counted by the number of Cleaved-Caspase 3+ cells from a 40x field. Each data point = mean of counts from 40-50 gastric glands

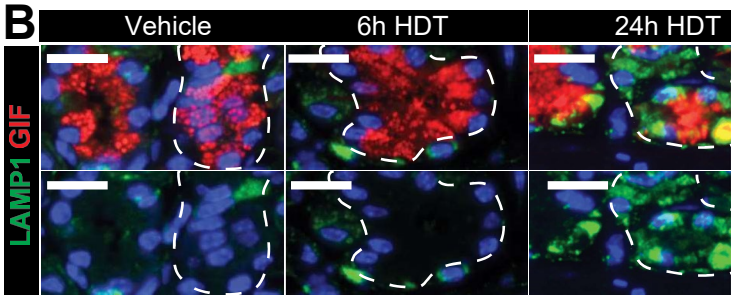
from an individual mouse, n=4 mice per treatment group. Significance by nonparametric two-tailed t-test. Error bars denote standard deviation.

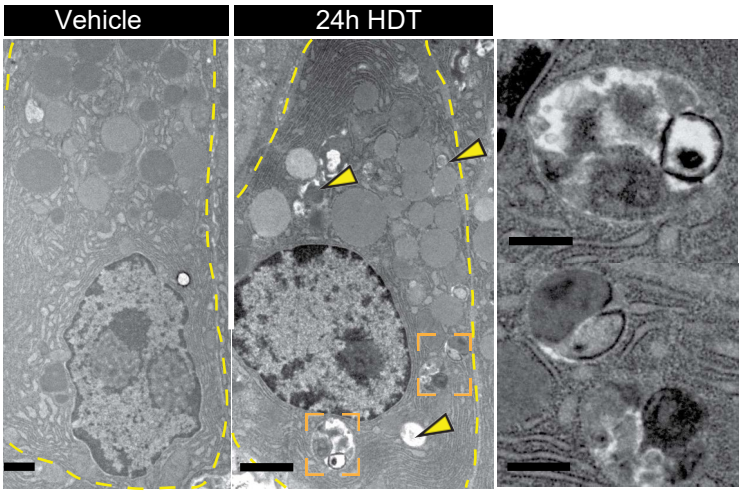
Figure EV5. Conservation of *Atf3* expression across tissues after injury.

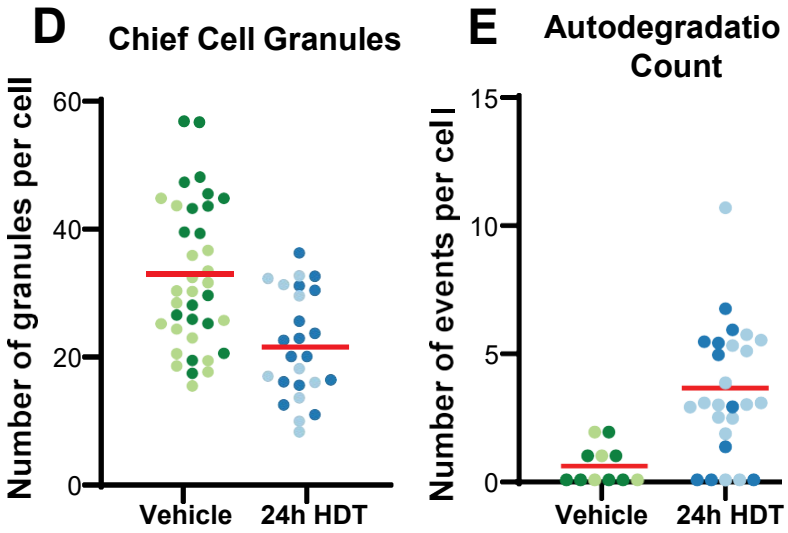
A. Fraction of cells expressing ATF3, RAB7B, and IFRD1 in previously published single-cell RNA-sequencing of regenerating cells after axolotl limb amputation. IFRD1 is a previously published paligenosis gene known to be activated during Stage 1.

B. Intersection of transcripts upregulated by paligenotic injury in 5 tissues. Only intersections of gene sets ≥4 and transcripts unique for that intersection are depicted. Unique genes from each intersection are listed above the UpSet plot depicting the intersection combination, the number of overlapping genes, and the total number of genes in the dataset.

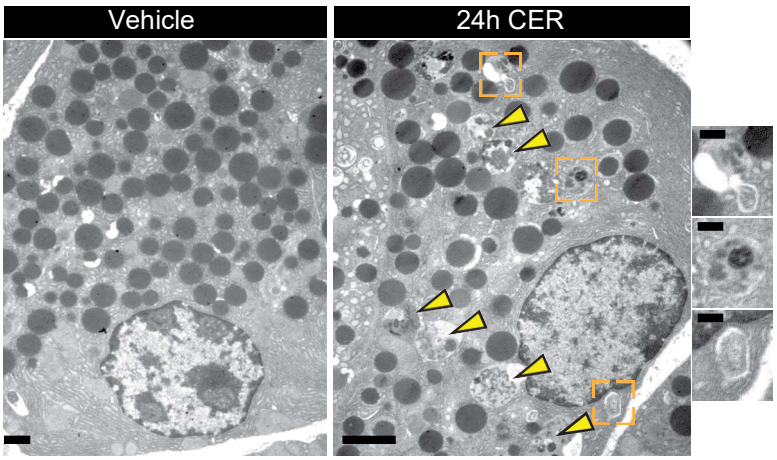


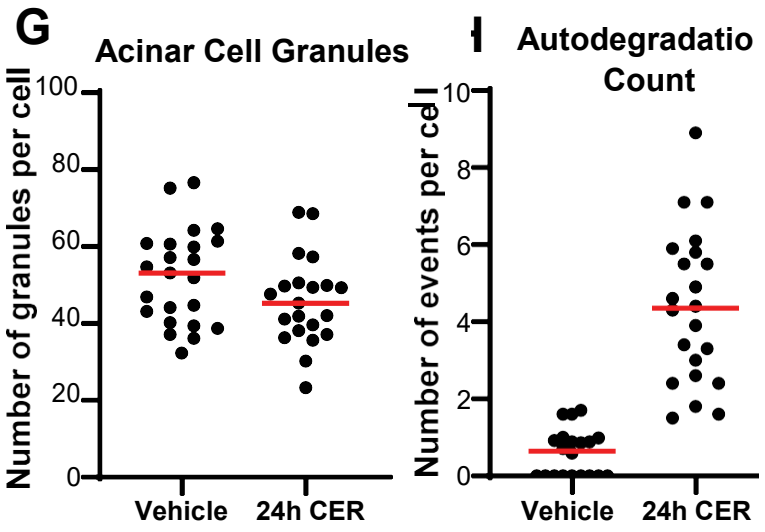




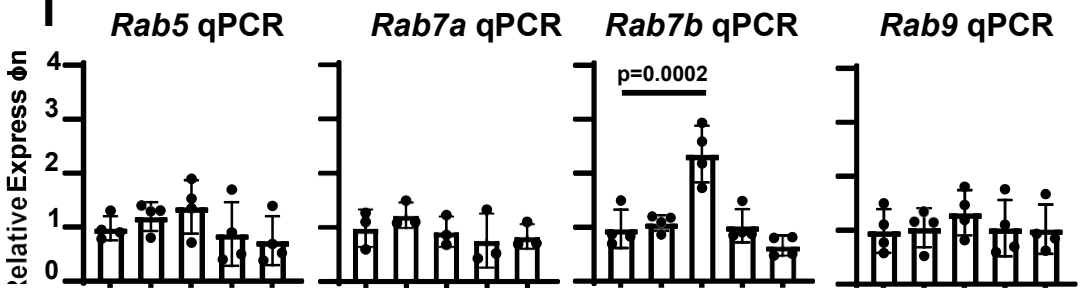


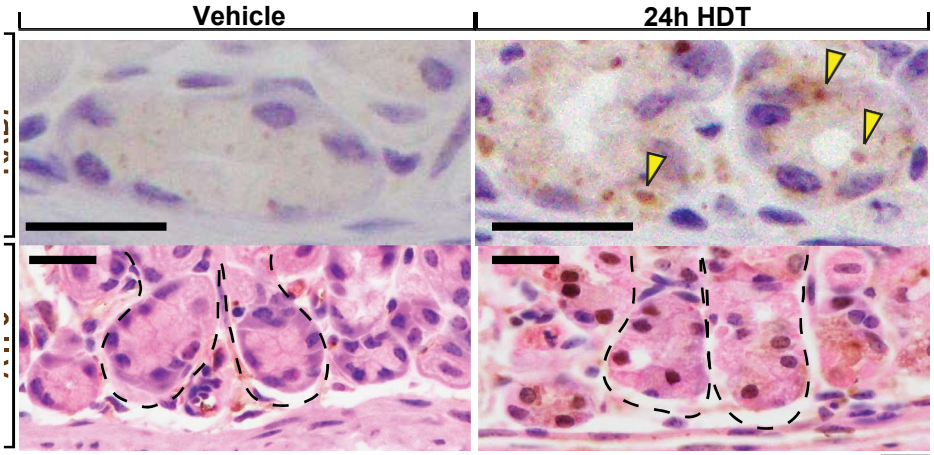
Pancreas

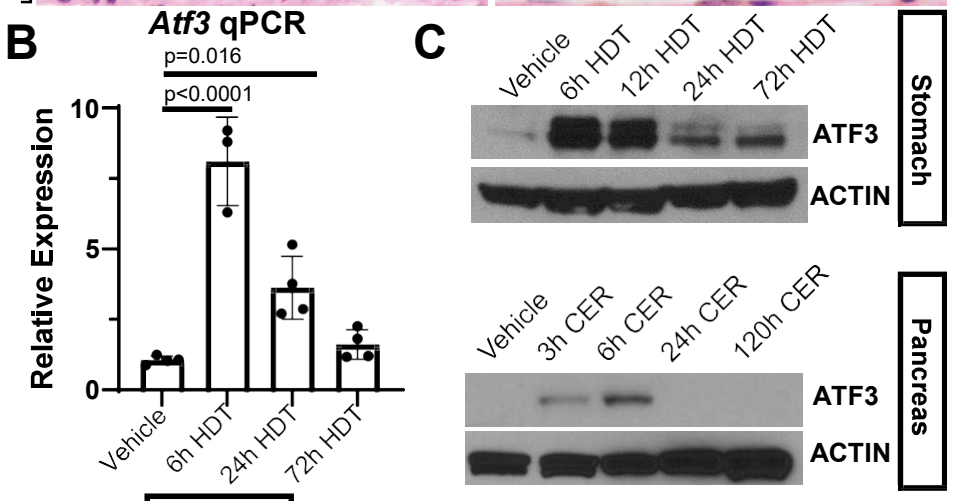




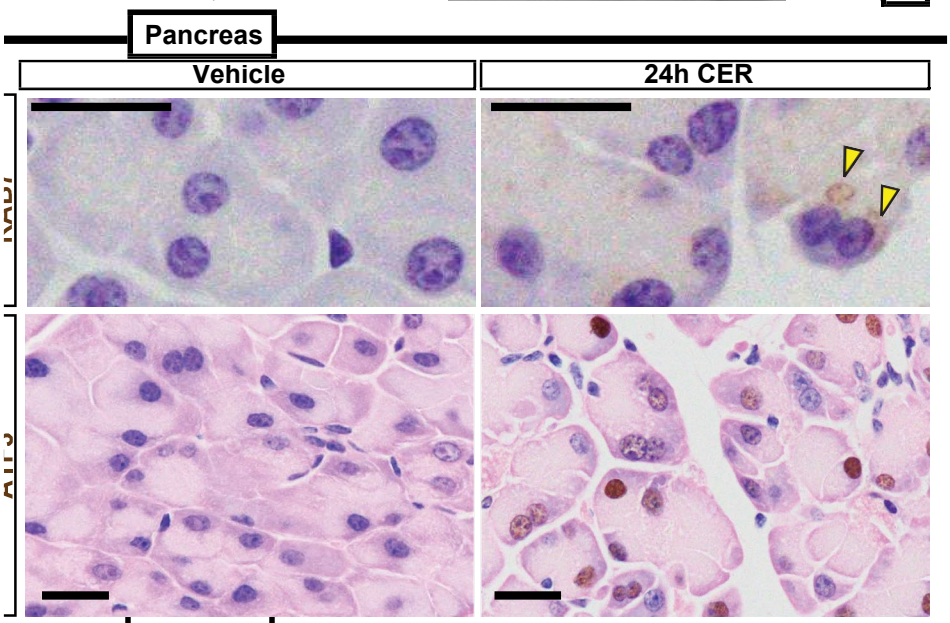
Stomach

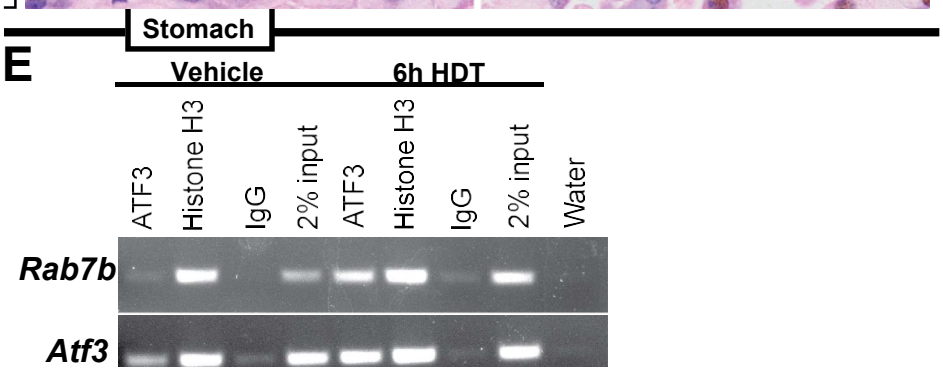


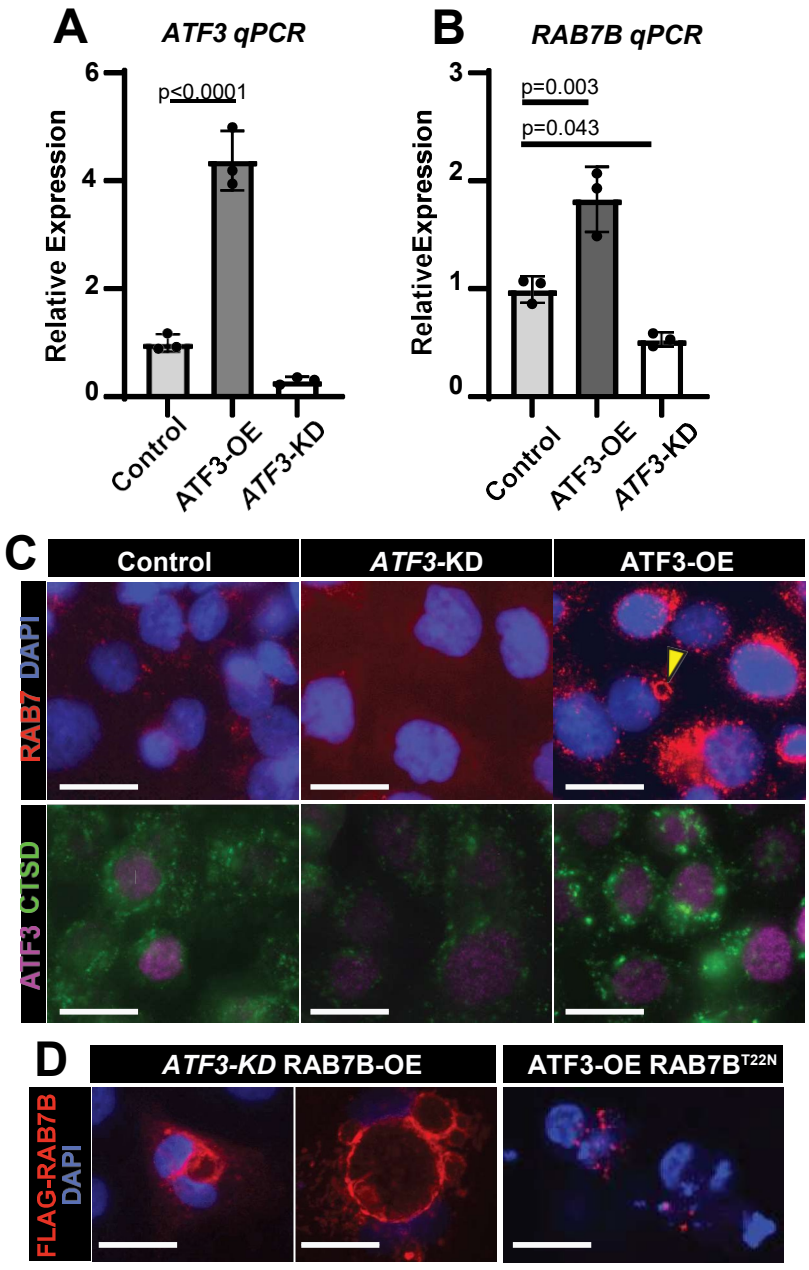

Vehicle
24h HDT

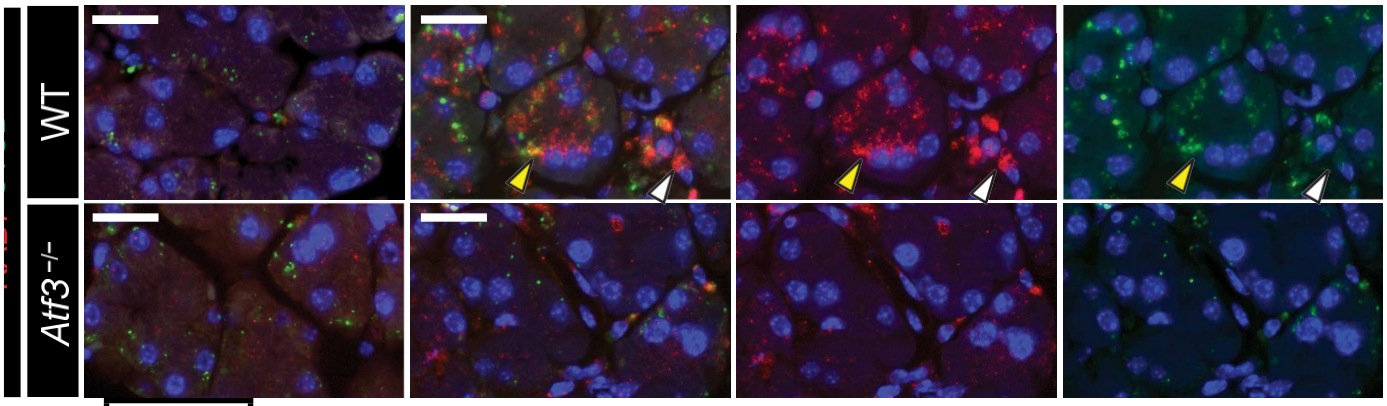

B
Atf3 qPCR
p=0.016
p<0.0001
Relative Expression
10
5
0
Vehicle
6h HDT
24h HDT
72h HDT

C
Vehicle
6h HDT
12h HDT
24h HDT
72h HDT
ATF3
ACTIN
Stomach
Vehicle
3h CER
6h CER
24h CER
120h CER
ATF3
ACTIN
Pancreas

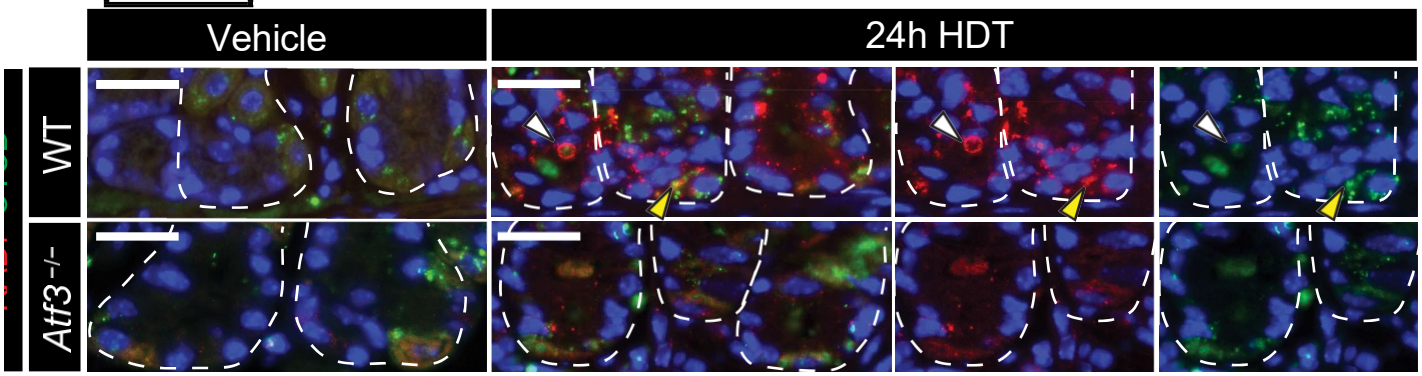

Pancreas
Vehicle
24h CER

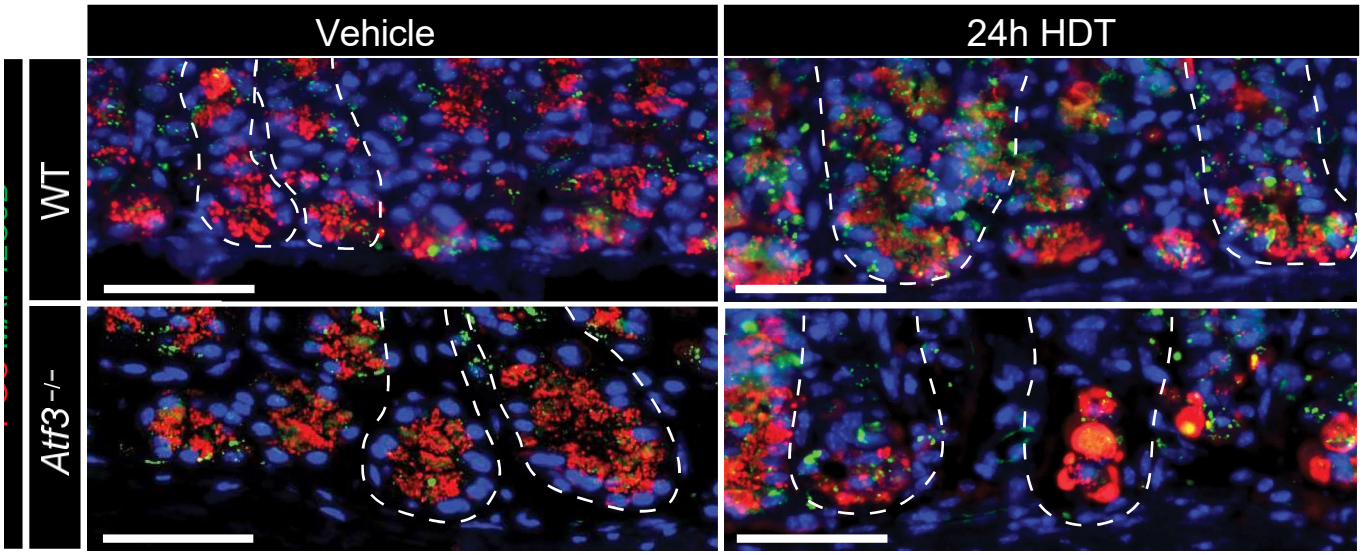

Stomach
E
Vehicle
6h HDT
ATF3
Histone H3
IgG
2% input
ATF3
Histone H3
IgG
2% input
Water
Rab7b
Atf3


A
ATF3 qPCR
p<0.0001
Relative Expression
6
4
2
0
Control
ATF3-OE
ATF3-KD
B
RAB7B qPCR
p=0.003
p=0.043
RelativeExpression
3
2
1
0
Control
ATF3-OE
ATF3-KD
C
Control
ATF3-KD
ATF3-OE
RAB7 DAPI
ATF3 CTSD
D
ATF3-KD RAB7B-OE
ATF3-OE RAB7B T22N
FLAG-RAB7B
DAPI

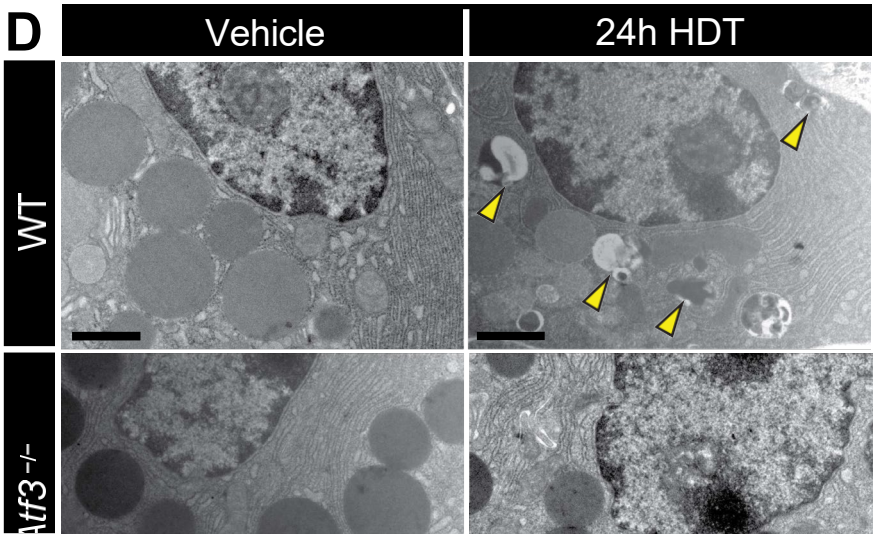

WT
Atf3 -/-

Stomach

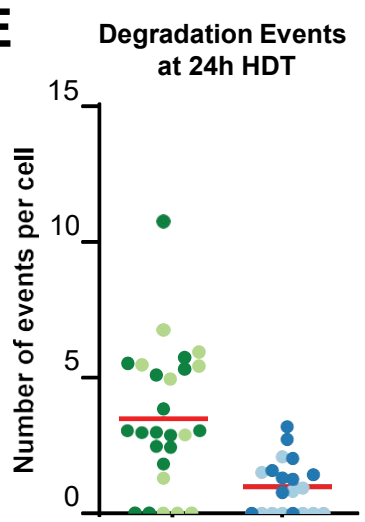

Vehicle
24h HDT
WT
Atf3 -/-

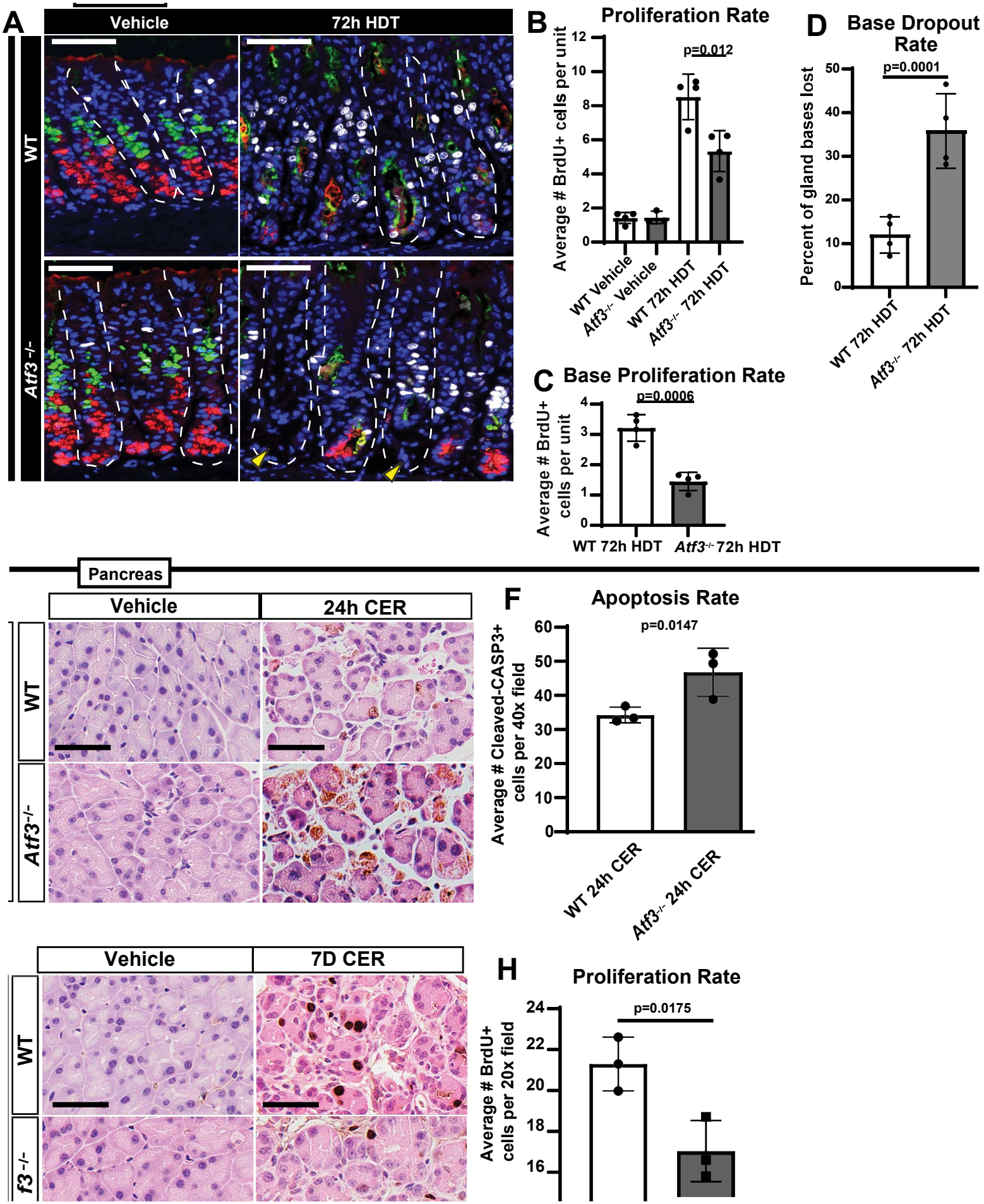

Vehicle
24h HDT
WT
Atf3 -/-

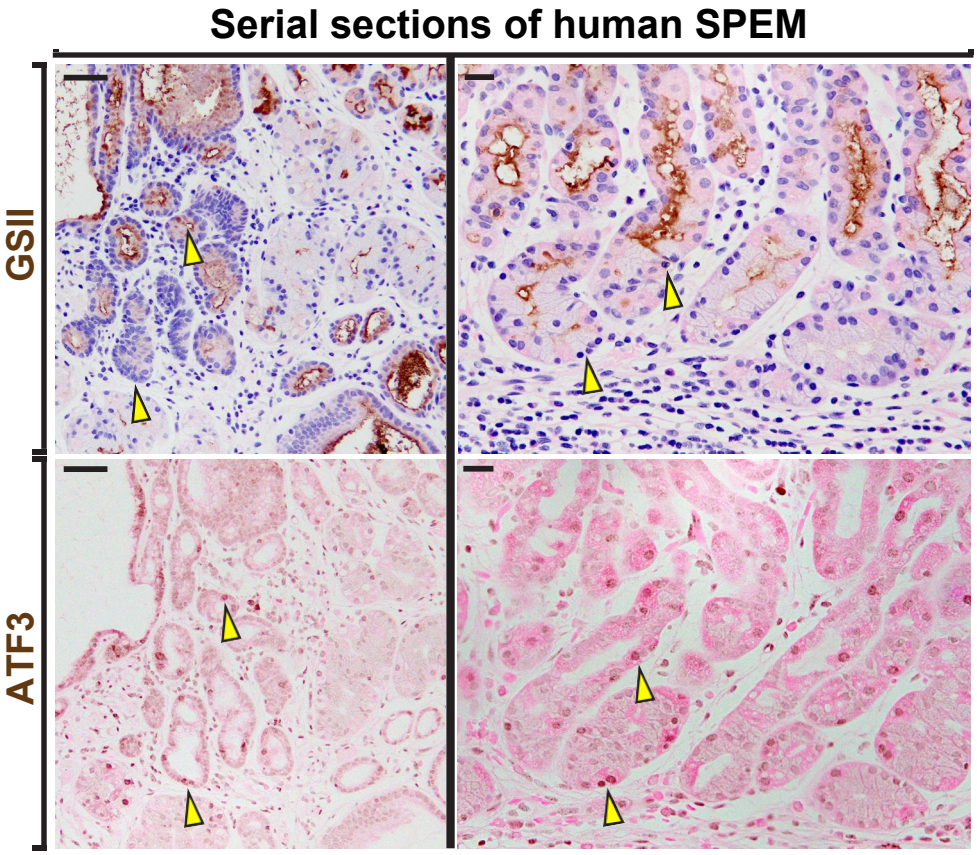
D

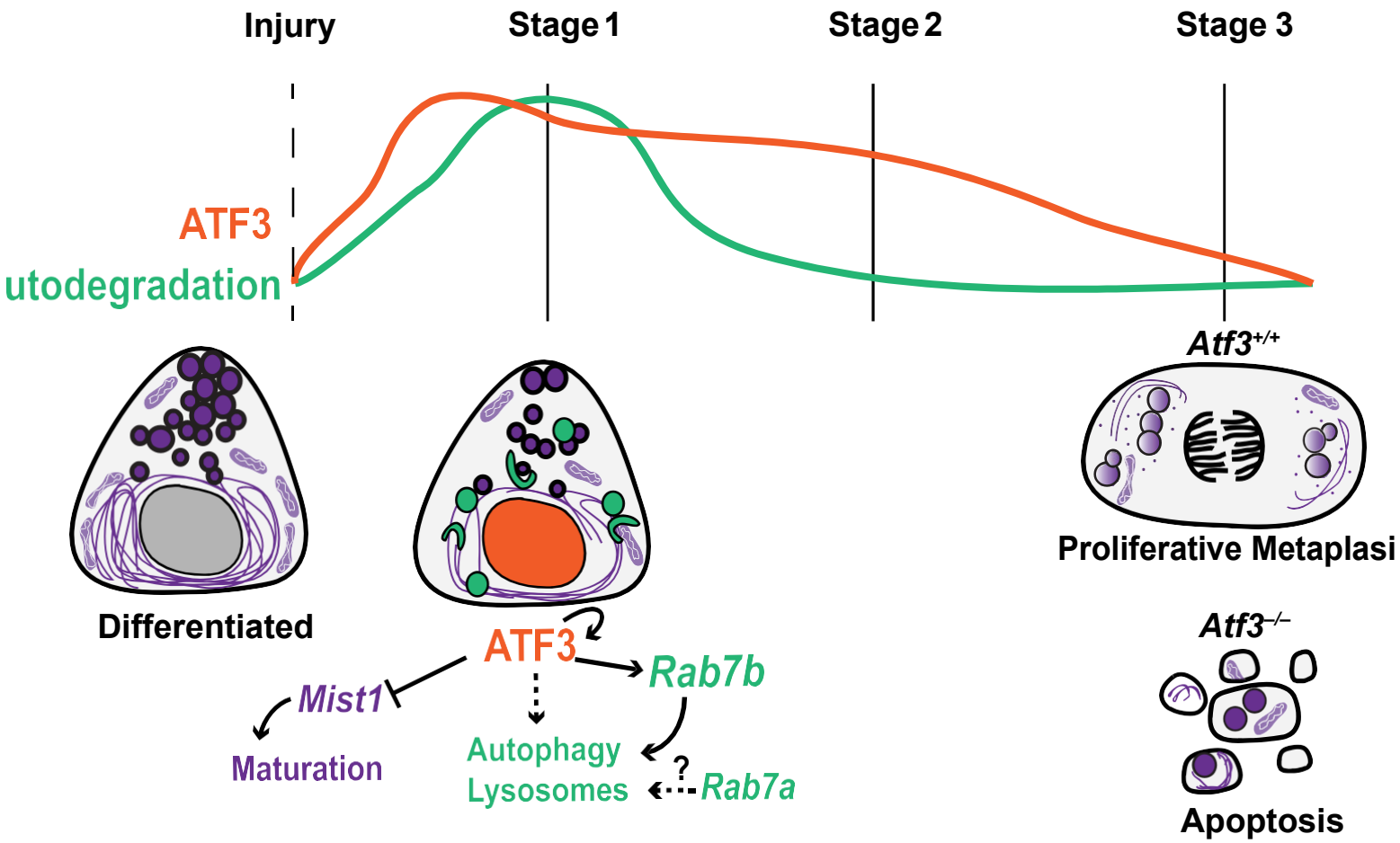

Vehicle
24h HDT
WT
Atf3 -/-

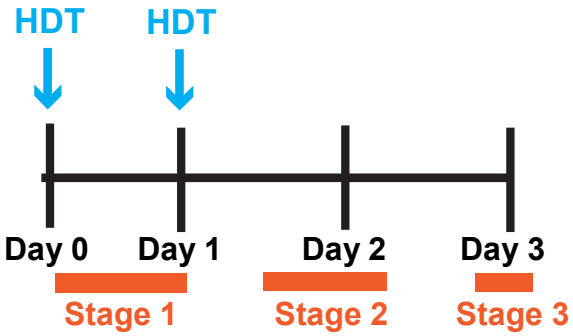
E


Degradation Events at 24h HDT
Number of events per cell
15
10
5
0

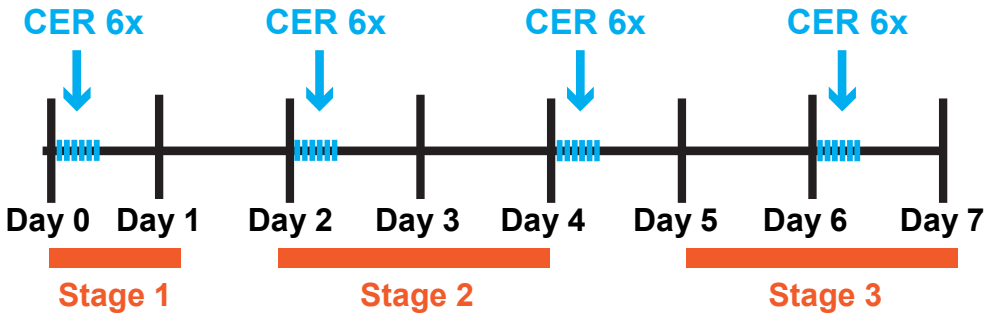

A
Vehicle
72h HDT
WT
Atf3 -/-
B
Proliferation Rate
p=0.012
Average # BrdU+ cells per unit
WT Vehicle
Atf3-/- Vehicle
WT 72h HDT
Atf3-/- 72h HDT
D
Base Dropout Rate
p=0.0001
Percent of gland bases lost
WT 72h HDT
Atf3-/- 72h HDT
C
Base Proliferation Rate
p=0.0006
Average # BrdU+ cells per unit
WT 72h HDT
Atf3-/- 72h HDT
Pancreas
Vehicle
24h CER
WT
Atf3-/-
F
Apoptosis Rate
p=0.0147
Average # Cleaved-CASP3+ cells per 40x field
WT 24h CER
Atf3-/- 24h CER
Vehicle
7D CER
WT
f3 -/-
H
Proliferation Rate
p=0.0175
Average # BrdU+ cells per 20x field


Serial sections of human SPEM
GSII
ATF3

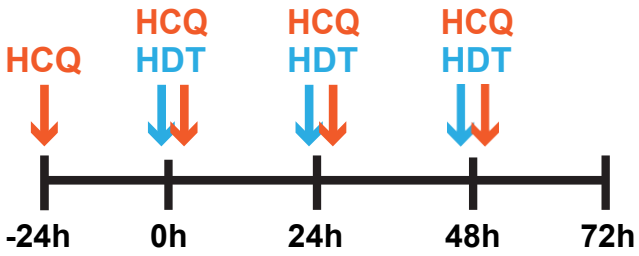

Injury
Stage 1
Stage 2
Stage 3
ATF3
utodegradation
Differentiated
ATF3
Mist1
Maturation
Rab7b
Autophagy
Lysosomes
?
Rab7a
Atf3+/+
Proliferative Metaplasi
Atf3−/−
Apoptosis



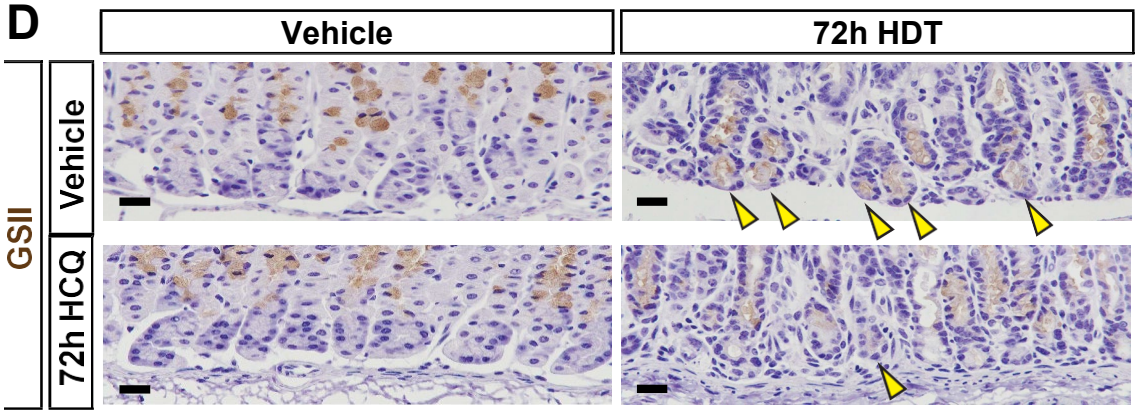
B Cerulein Treatment Timeline



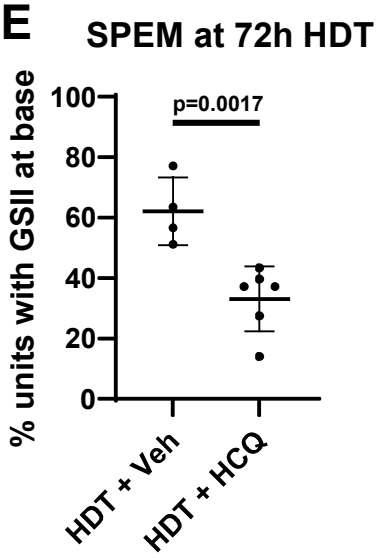
C



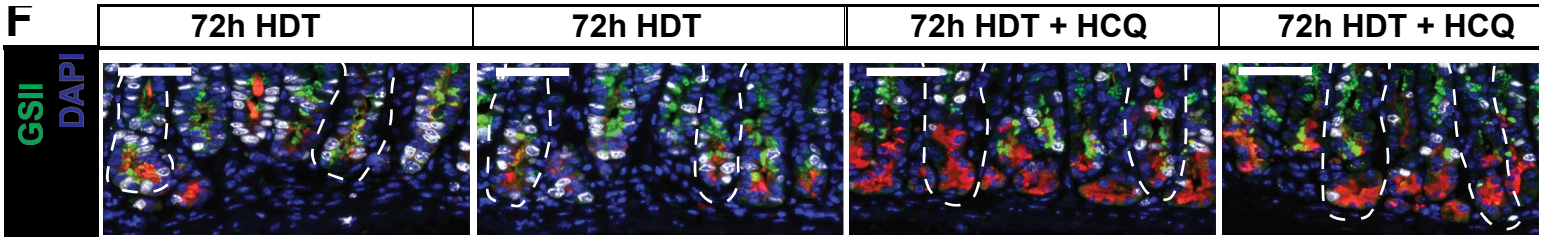
D

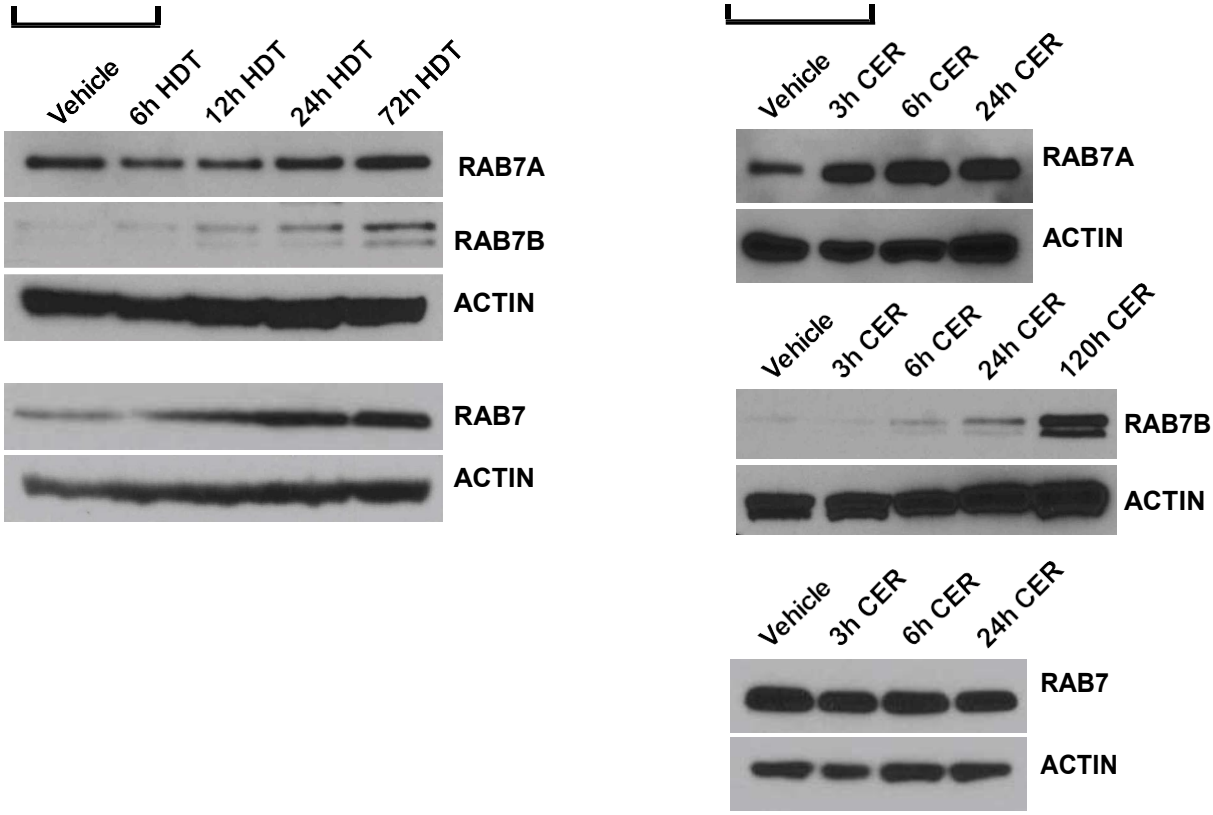


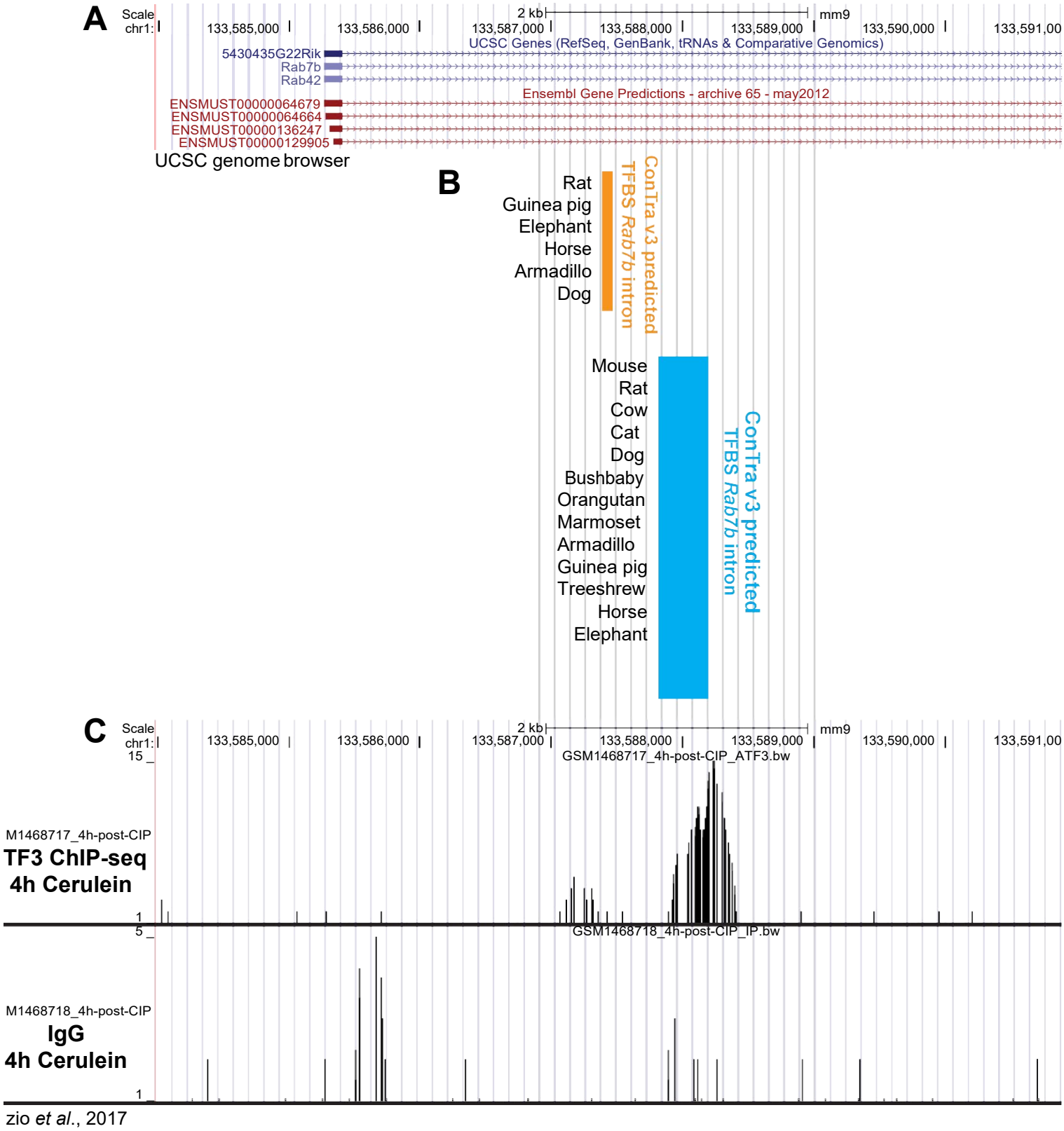
E



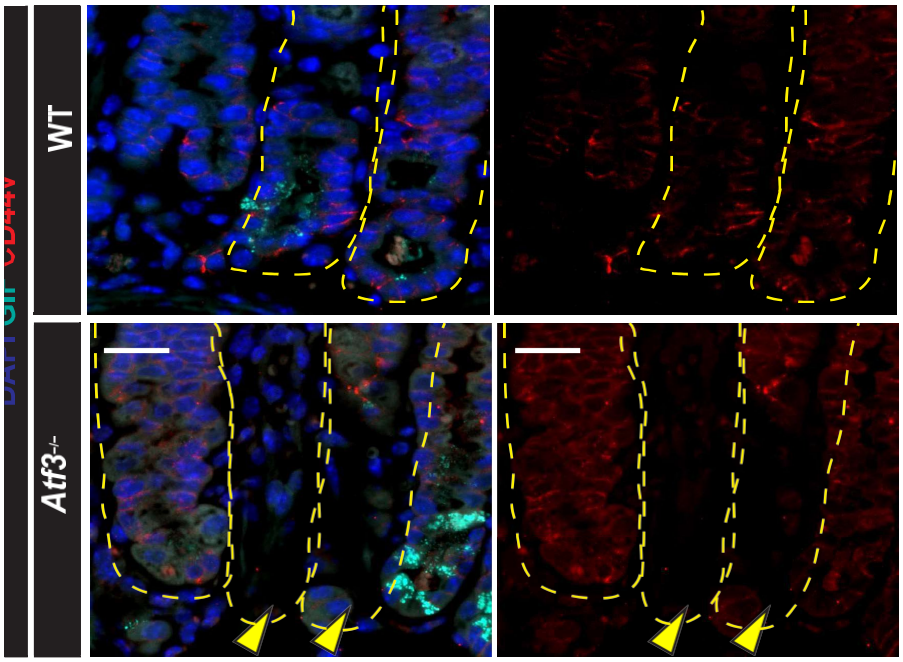
F

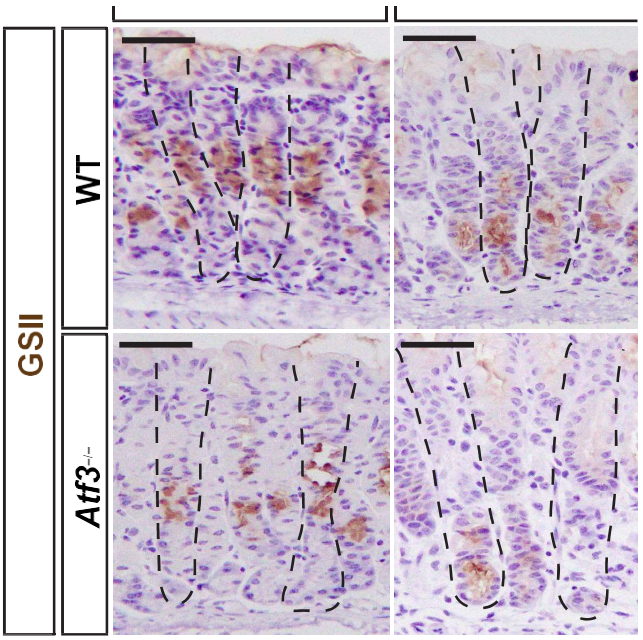



Vehicle
6h HDT
12h HDT
24h HDT
72h HDT
RAB7A
RAB7B
ACTIN
RAB7
ACTIN
Vehicle
3h CER
6h CER
24h CER
RAB7A
ACTIN
Vehicle
3h CER
6h CER
24h CER
120h CER
RAB7B
ACTIN
Vehicle
3h CER
6h CER
24h CER
RAB7
ACTIN

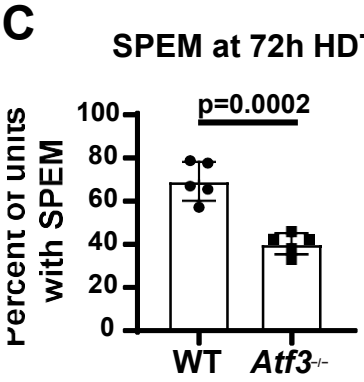


zio *et al.*, 2017

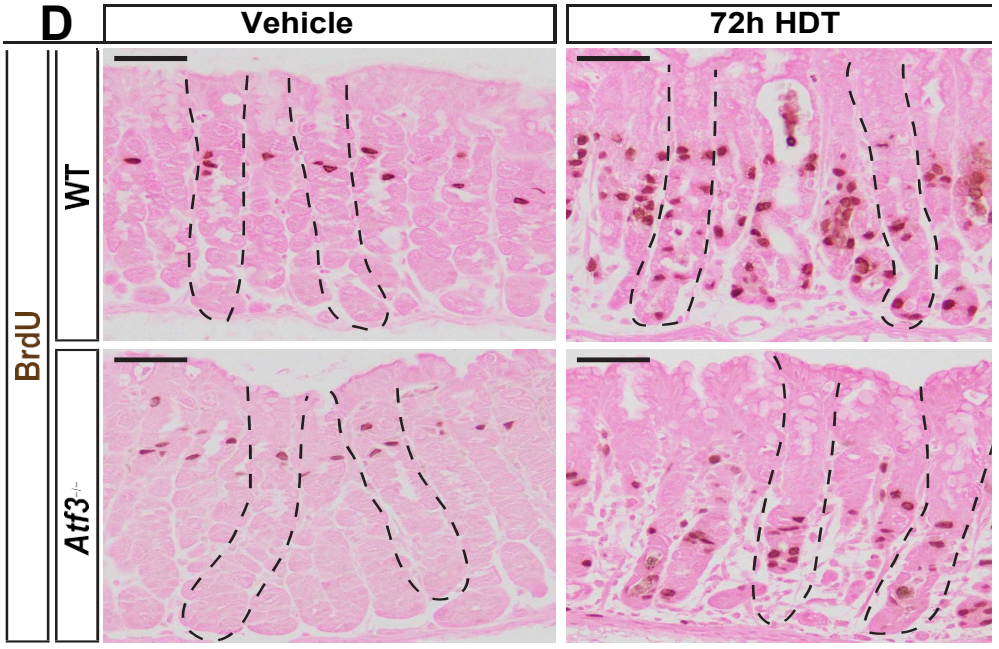

WT
Atf3-/-


GSII
WT
Atf3-/-

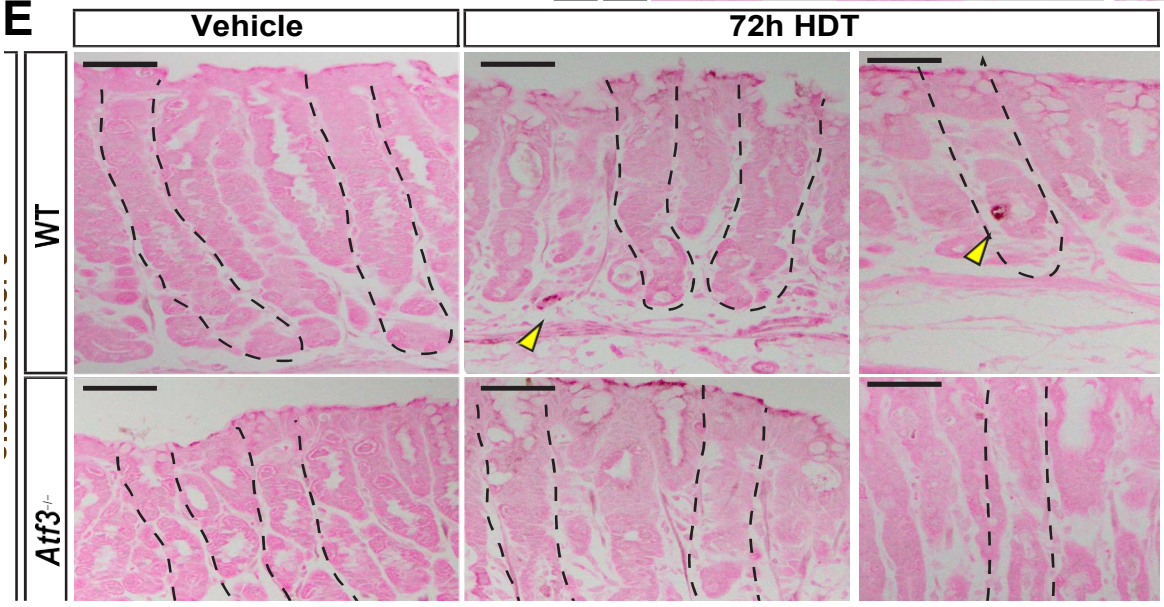
C


SPEM at 72h HDT
p=0.0002
Percent of units with SPEM
100
80
60
40
20
0
WT
Atf3-/-

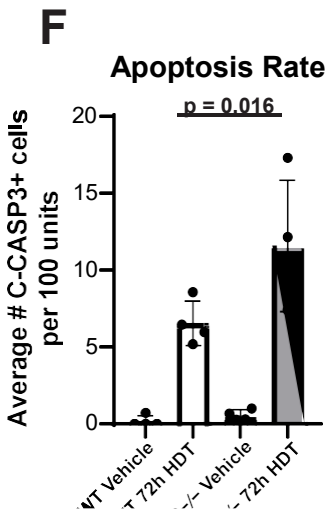
D


Vehicle
72h HDT
BrdU
WT
Atf3-/-

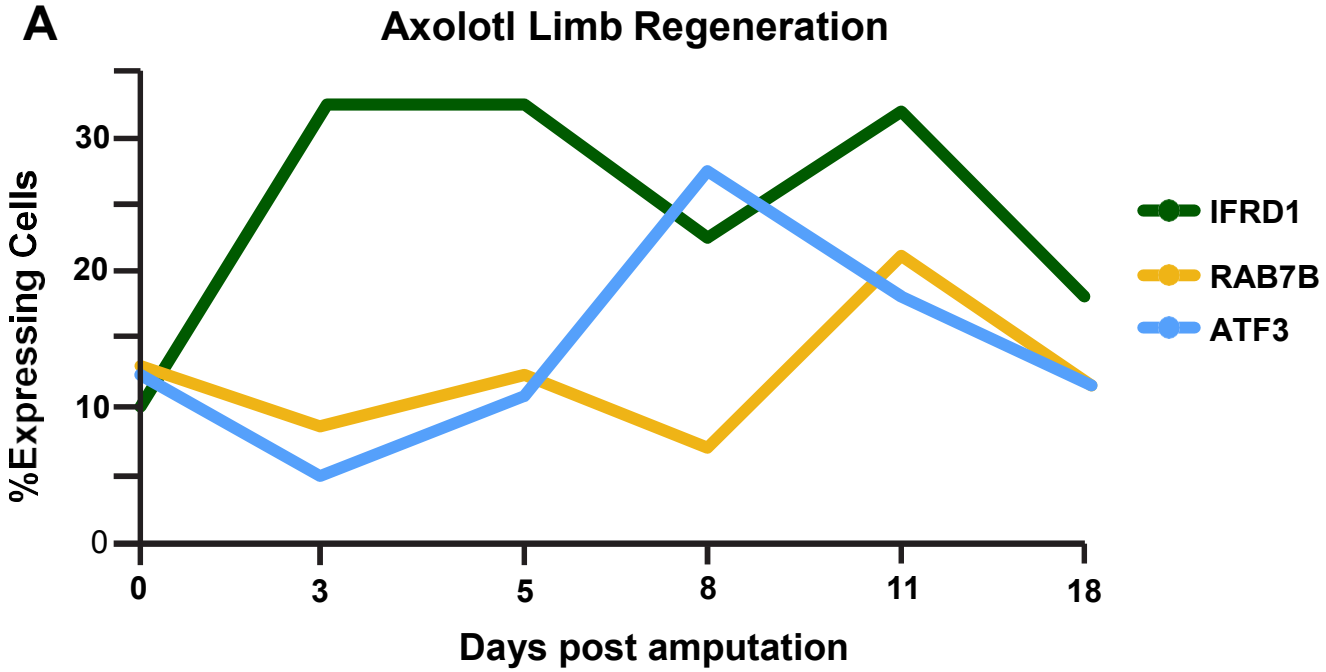
E


Vehicle
72h HDT
WT
Atf3-/-

F

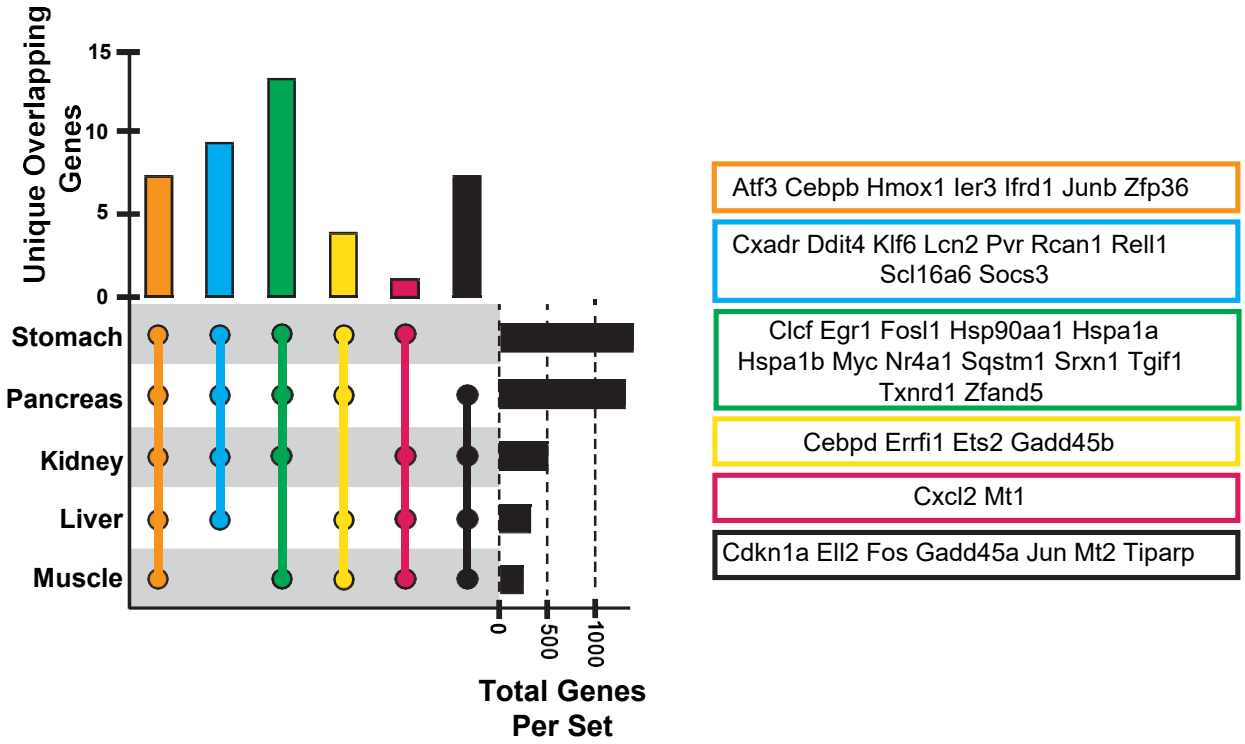

Apoptosis Rate
p = 0.016
Average # C-CASP3+ cells per 100 units
20
15
10
5
0
Vehicle
72h HDT
Vehicle
72h HDT

A



Dataset from Gerber *et al.*, 2018

B



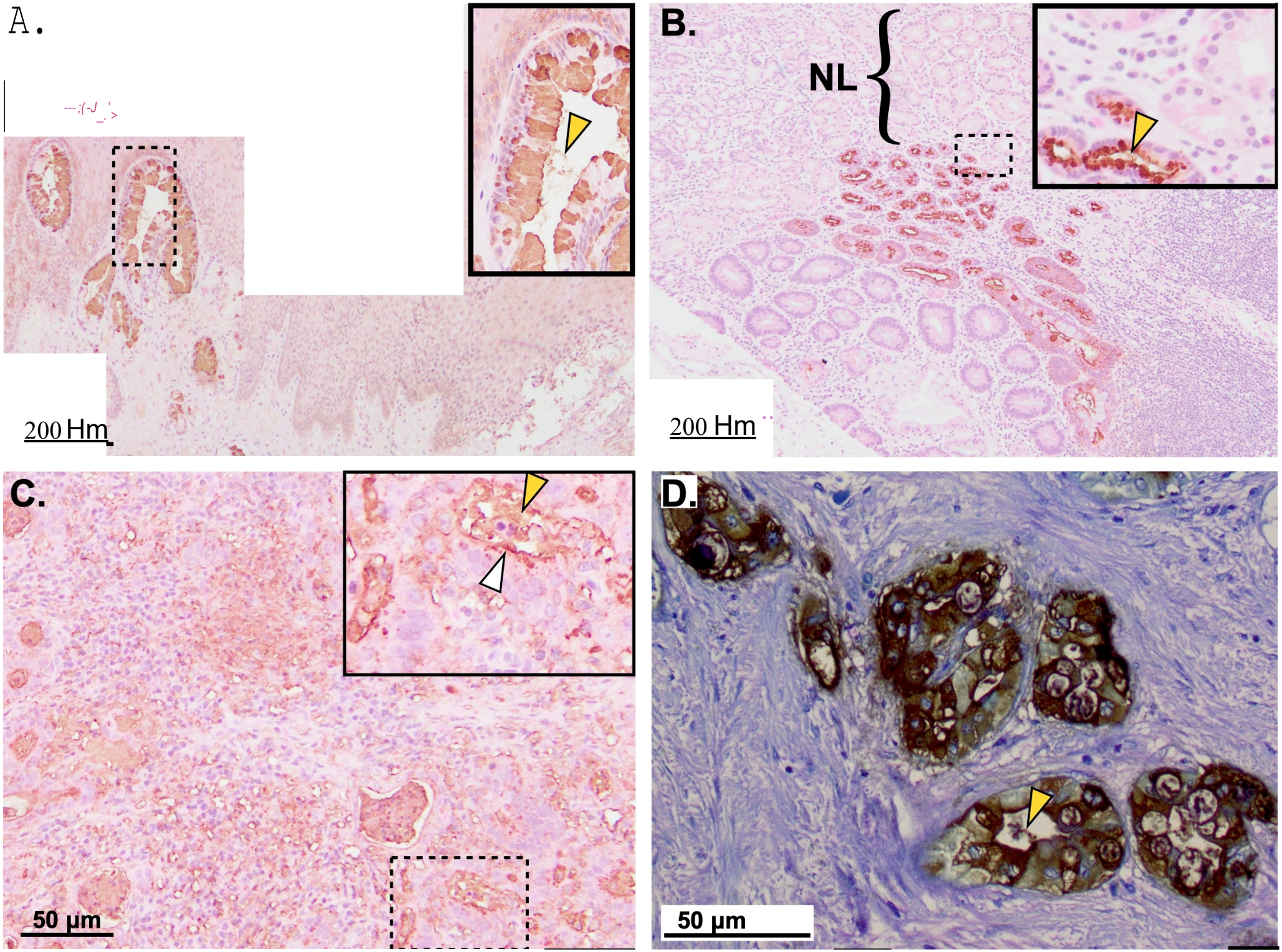
bioRxiv preprint doi: https://doi.org/10.1101/2021.03.17.435789; this version posted March 17, 2021. The copyright holder for this preprint (which was not certified by peer review) is the author/funder. All rights reserved. No reuse allowed without permission.

JWB, KKD, VK, JCM: Conceived of the project, funded the research, performed experiments, analyzed data, and wrote the manuscript

KMD: Provided essential reagents, funded the research, and edited the manuscript.

STATEMENT OF ETHICAL ASSURANCE

JWB & JCM is the guarantor of this work and, as such, had full access to all of the data in the study and takes responsibility for the integrity of the data and the accuracy of the data analysis.


A.
200 Hm
B.
NL
200 Hm
C.
50 µm
D.
50 µm

A.

B.

TFMS

- +

171000 11300

- +

12300 1910

250 KDa

148 KDa

98 KD

bioRxiv preprint doi: https://doi.org/10.1101/2021.03.17.435789; this version posted March 17, 2021. The copyright holder for this preprint (which was not certified by peer review) is the author/funder. All rights reserved. No reuse allowed without permission.

64KDa

50KDa

36KDa

22KDa

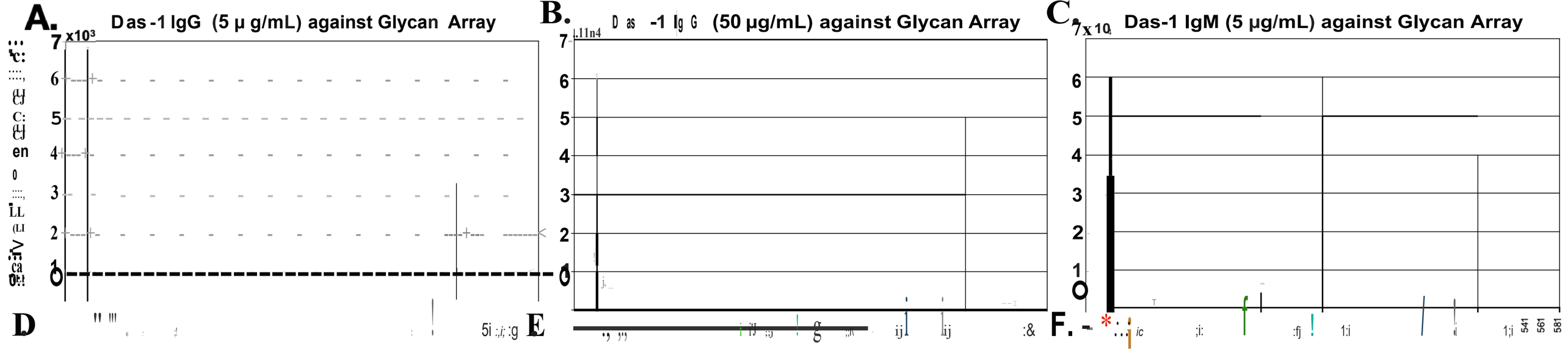
16KDa

6KDa

4KDa

Das-1 IgM

Das-1 IgG



IgG Affinities (5 ug/mL)

Rank	ID	Glycan	RFA	SD
1	28	(3S)Galb1-3(Fuca1-4)GlcNAcb-Sp8	6738	115
2	484	(3S)Galb1-3(Fuca1-4)GlcNAcb-SpO	2936	329
3	30	(3S)Galb1-3GlcNAcb-Sp0	1532	164
4	26	(3S)Galb1-4(6S)Glcb-Sp0	211	14
5	34	(3S)Galb1-4(6S)GlcNAcb-SpO	189	16
6	27	(3S)Galb1-4(6S)Glcb-Sp8	92	14
7	38	(3S)Galb-Sp8	82	10
8	29	(3S)Galb1-3GalNAca-Sp8	51	6
9	37	(3S)Galb1-4GlcNAcb-Sp8	48	7
10	356	Fuca1-2Galb1-4(Fuca1-3)GlcNAcb1-2Mana1-6(Fuca1-2Galb1-4(Fuca1-3)GlcNAcb1-2Mana1-3)Manb1-4GlcNAcb-1-4GlcNAb-Sp20	47	3
11	84	(3S)Galb1-4(Fuca1-3)Glcb-Sp0	47	1
12	285	Galb1-3GlcNAcb1-3Galb1-3GlcNAcb-SpO	42	1
13	293	(6S)Galb1-4(6S)GlcNAcb-SpO	41	5
14	295	Neu5Aca2-3Galb1-4(Fuca1-31GlcNAcb1-6(Galb1-3)GalNAca-Sp14	41	2
15	24	(3S)Galb1-4(Fuca1-3)(6S)Glc-SpO	41	2
16	135	Neu5Aca2-6{Galb1-3)GalNAca-Sp8	41	1
17	44	(6S)Galb1-4GlcNAcb-Sp8	40	5
18	34	(3S)Galb1-4(6S)GlcNAcb-SpO	39	2
19	22	6S(3S)Galb1-4(6S)GlcNAcb-SpO	39	3
20	40	(4S)Galb1-4GlcNAcb-Sp8	39	6
91	246	Neu5Aca2-3Galb1-3GlcNAcb-SpO	24	3
98	436	(6S)Galb1-3GlcNAcb-SpO	24	5
107	250	Neu5Aca2-3Galb1-4(Fuca1-3)GlcNAcb-Sp0	23	5
120	251	Neu5Aca2-3Galb1-4(Fuca1-3)GlcNAcb-Sp8	21	3
270	149	Galb1-3GlcNAcb-SpO	10	4
318	41	(6P)Mana-Sp8	7	3
325	236	Neu5Aca2-3Galb1-3(Fuca1-4)GlcNAcb-Sp8	6	3
329	128	Galb1-3(Fuca1-4)GlcNAc-SpO	6	3
340	102	Gala1-3(Fuca1-2)Galb1-3GlcNAcb-Sp8	6	3
417	129	Galb1-3(Fuca1-4)GlcNAc-Sp8	3	1

bioRxiv preprint doi: https://doi.org/10.1101/2021.03.17.435789; this version posted March 17, 2021. The copyright holder for this preprint (which was not certified by peer review) is the author/funder. All rights reserved. No reuse allowed without permission.

IgG Affinities (50 pg/ml)

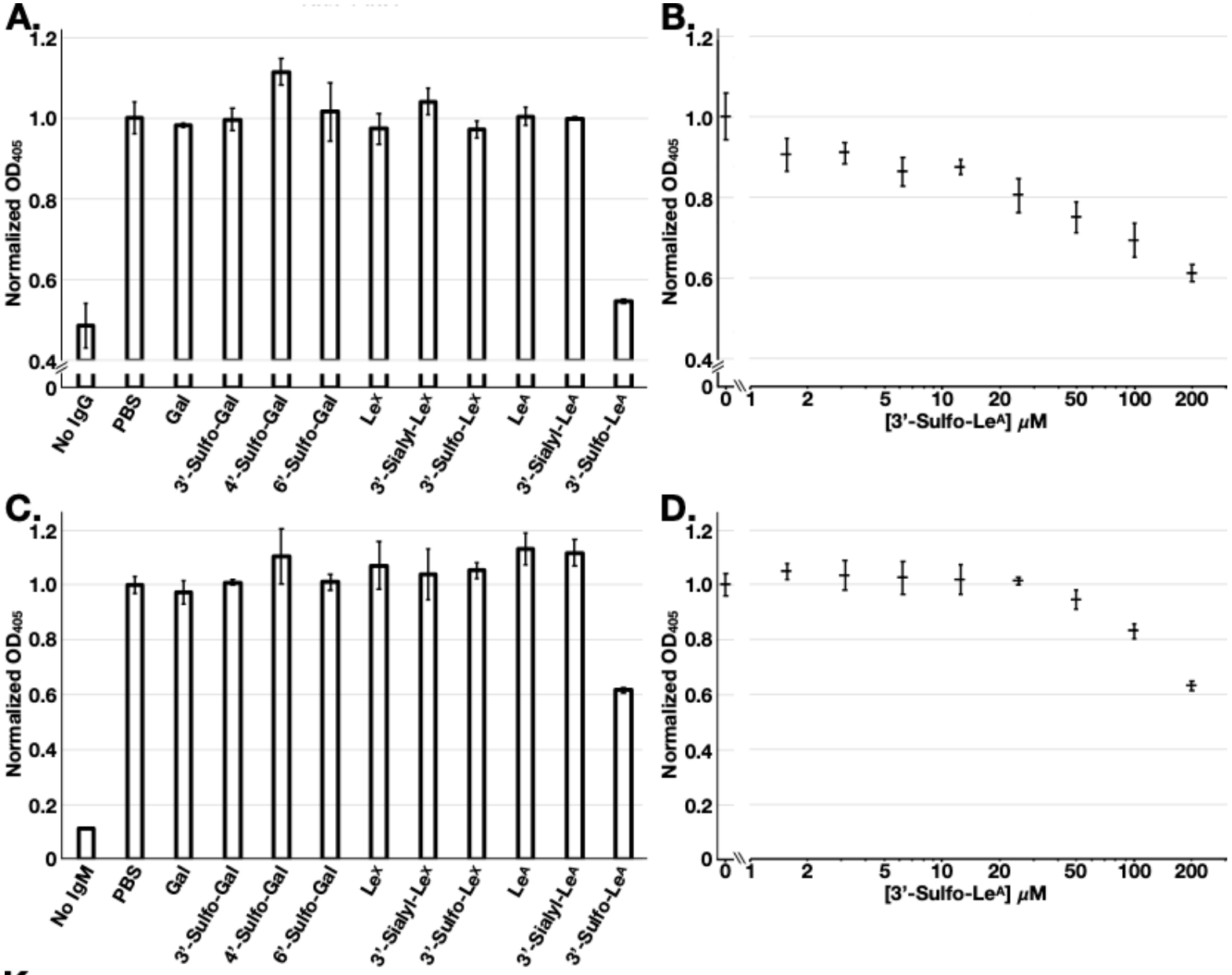
Rank	ID	Glycan	RFA	SD
1	28	(3S)Galb1-3(Fuca1-4)GlcNAcb-Sp8	58890	3160
2	484	(3S)Galb1-3(Fuca1-4)GlcNAcb-SpO	44494	1393
3	30	(3S)Galb1-3GlcNAcb-Sp0	24516	16706
4	26	(3S)Galb1-4(6S)Glcb-Sp0	12734	1905
5	31	(3S)Galb1-3GlcNAcb-Sp8	12514	2166
6	27	(3S)Galb1-4(6S)Glcb-Sp8	6189	1011
7	34	(3S)Galb1-4(6S)GlcNAcb-SpO	3287	217
8	29	(3S)Galb1-3GalNAca-Sp8	3269	246
9	35	(3S)Galb1-4(6S)GlcNAcb-Sp8	2626	303
10	545	Glc!NAcb1-3Galb1-4GlcNAcb1-6(GlcNAcb1-3Galb1-4GlcNAcb1-2)Mana1-6(GlcNAcb1-3Galb1-4GlcNAcb1-2Mana1-3)Manb1-4GlcNAcb1-4GlcNAc-Sp24	1442	651
11	38	(3S)Galb-Sp8	1438	118
12	531	Glc!NAcb1-3Galb1-4GlcNAcb1-2Mana1-6(GlcNAcb1-3Galb1-4GlcNAcb1-2Mana1-3jManb1-4GlcNAcb1-4GlcNAcb-Sp12	1079	116
13	45	(6S)Galb1-4(6S)Glcb-Sp8	978	48
14	537	Galb1-4GlcNAcb1-3Galb1-4GlcNAcb1-3Galb1-4GlcNAcb1-2Mana1-6(Galb1-4GlcNAcb1-3Galb1-4GlcNAcb1-3Galb1-4GlcNAcb1-2Man a1-3)Manb1-4GlcNAcb1-4GlcNAcb-Sp12	796	250
15	293	(6S)Galb1-4(6S)GlcNAcb-SpO	654	37
16	22	68(38)Galb1-4(6S)GlcNAcb-8pO	629	20
17	84	(3S)Galb1-4(Fuca1-3)Glcb-Sp0	433	28
18	37	(3S)Galb1-4GlcNAcb-Sp8	430	24
19	25	(3S)Galb1-4Glcb-Sp8	424	32
20	562	Galb1-4GlcNAcb1-3Galb1-4GlcNAcb1-6(Galb1-4GlcNAcb1-3Galb1-4GlcNAb1-2jMana1-6(Galb1-4GlcNAcb1-3Galb1-4GlcNAcb1-2Man a1-3)Manb1-4GlcNAcb1-4(Fuca1-6)GlcNAcb-Sp24	277	84
57	44	(6S)Galb1-4GlcNAcb-Sp8	36	5
82	436	(6S)Galb1-3GlcNAcb-SpO	25	3
96	246	Neu5Aca2-3Galb1-3GlcNAcb-SpO	2.2	2
160	41	(6P)Mana-Sp8	17	5
247	128	Galb1-3(Fuca1-4)GlcNAc-SpO	13	2
251	250	Neu5Aca2-3Galb1-4(Fuca1-3)GlcNAcb-SpO	13	1
305	251	Neu5Aca2-3Galb1-4(Fuca1-3)GlcNAcb-Sp8	12	1

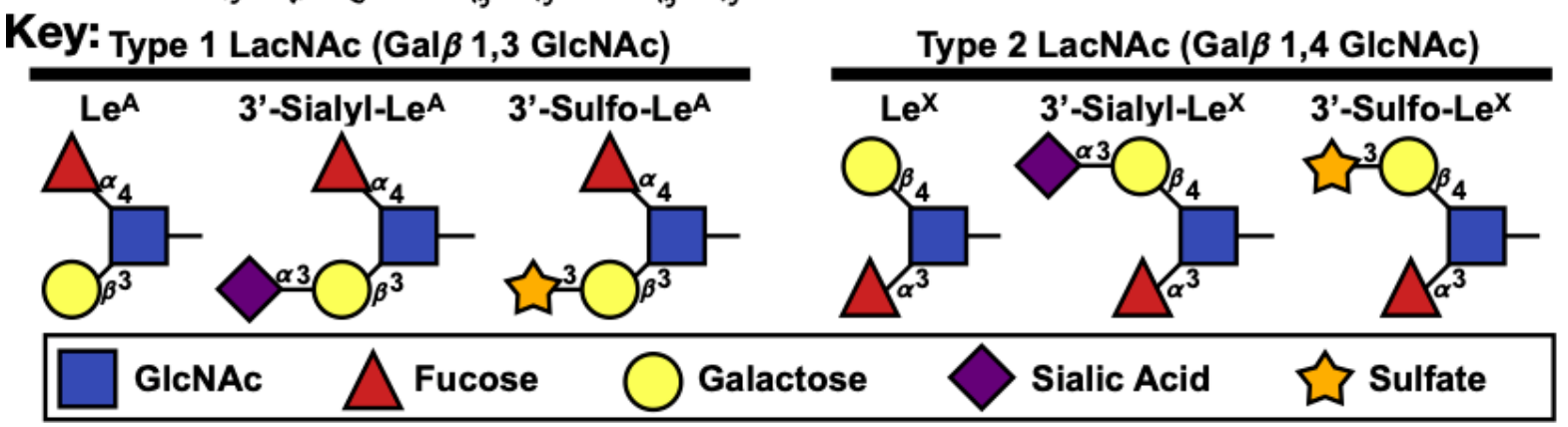
IgM Affinities (5 ug/mL)

Rank	ID	Glycan	RFA	SD
1	293	(6S)Galb1-4(6S)GlcNAcb-SpO	52774	4529
2	30	(3S)Galb1-3GlcNAcb-SpO	53365	6565
3	28	(3S)Galb1-3(Fuca1-4)GlcNAcb-Sp8	52578	6381
4	26	(3S)Galb1-4(6S)Glcb-Sp0	44761	2990
5	34	(3S)Galb1-4(6S)GlcNAcb-SpO	37881	1585
6	484	(3S)Galb1-3(Fuca1-4)GlcNAcb-SpO	36012	2788
7	31	(3S)Galb1-3GlcNAcb-Sp8	35173	1694
8	27	(3S)Galb1-4(6S)Glcb-Sp8	34384	4456
9	45	(6S)Galb1-4(6S)Glcb-Sp8	34222	2681
10	22	6S(3S)Galb1-4(6S)GlcNAcb-SpO	34066	1021
11	35	(3S)Galb1-4(6S)GlcNAcb-Sp8	30024	2.286
12	38	(3S)Galb-Sp8	28471	2188
13	29	(3S)Galb1-3GalNAca-Sp8	28315	1943
14	25	(3S)Galb1-4Glcb-Sp8	6633	967
15	217	(3S)Galb1-4(Fuca1-3)(6S)GlcNAcb-Sp8	6250	849
16	37	(3S)Galb1-4GlcNAcb-Sp8	2454	405
17	84	(38)Galb1-4(Fuca1-3)Glcb-8p0	219.2	1 42
18	437	(6S)Galb1-3(6S)GlcNAc-SpO	390	15
19	36	(3S)Galb1-4GlcNAcb-SpO	372	52
20	187	GlcNAcb1-6(GlcNAcb1-4)GalNAca-Sp8	239	14
27	44	(6S)Galb1-4GlcNAcb-Sp8	44	2
60	436	(6S)Galb1-3GlcNAcb-SpO	23	4
85	246	Neu5Aca2-3Galb1-3GlcNAcb-SpO	4	
124	250	Neu5Aca2-3Galb1-4(Fuca1-3)GlcNAcb-Sp0	15	2
237	41	(6P)Mana-Sp8	8	1
314	128	Galb1-3(Fuca1-4)GlcNAc-SpO	6	1
317	236	Neu5Aca2-3Galb1-3(Fuca1-4)GlcNAcb-Sp8	6	1
318	251	Neu5Aca2-3Galb1-4(Fuca1-3)GlcNAcb-Sp8	6	2
329	149	Galb1-3GlcNAcb-SpO	5	2
423	129	Galb1-3(Fuca1-4)GlcNAc-Sp8	4	2
464	102	Gala1-3(Fuca1-2)Galb1-3GlcNAcb-Sp8	3	1

311	236	Neu5Aca2-3Galb1-3(Fuca 1-4)GlcNAcb-Sp8	11	2
324	149	Galb1-3GlcNAcb-SpO	10	1
487	129	Galb1-3(Fuca 1-4)GlcNAc-Sp8	5	1
488	150	Galb1-3GlcNAcb-Sp8	5	1

bioRxiv preprint doi: https://doi.org/10.1101/2021.03.17.435789; this version posted March 17, 2021. The copyright holder for this preprint (which was not certified by peer review) is the author/funder. All rights reserved. No reuse allowed without permission.





suppressed YTN-16 tumor growth *in vivo*, with a greater effect in wildtype mice as compared to NSG mice, implying a role of YTHDF1 in antitumor immunity. Moreover, YTHDF1 knockout in YTN-16 tumors induced the maturation of dendritic cells in the peri-tumoral microenvironment, which in turn promoted $CD4^+$ and $CD8^+$ T- cells infiltration together with increased interferon-*y* (IFN-*y*) and tumor necrosis factor-α (TNF-α) secretion. Concomitantly, immune suppressive myeloid-derived suppressor cells (MDSCs) were induced. Dual injection of wildtype and YTHDF1 knockout YTN-16 cells compromised antitumor immunity against the YTHDF1 knockout tumor leading to increased tumor growth. On the contrary, pre-emptive exposure of YTHDF1 knockout YTN-16 tumors triggered a potent antitumor immune response upon re-challenge with wildtype YTN-16 cells, implying that YTHDF1 mediates systemic immune suppression in GC.
Conclusion: YTHDF1 is overexpressed in GC and exerts a pro-tumorigenic role. YTHDF1 suppresses tumor immune microenvironment by inhibiting maturation of dendritic cells, subsequently reducing infiltration and activation of anti-tumor $CD4^+$ and $CD8^+$ T cells, but inducing MDSCs.

367

IL-13 IS CRITICAL FOR METAPLASIA DEVELOPMENT DURING CHRONIC ATROPHIC GASTRITIS

Christine Noto, Kevin Bockerstett, Nicholas M. Jackson, Eric L. Ford, Richard J. Dipaolo

Background: Metaplasia is a precancerous lesion that often develops in a setting of chronic inflammation. In the stomach, both *Helicobacter pylori* infection and autoimmune gastritis can cause gastric metaplasia and increase the risk of gastric cancer. The type 2 cytokines IL-4 and IL-13 have recently been shown to play a role in drug- and inflammation-induced metaplasia but the mechanisms by which these cytokines promote metaplasia are poorly understood. These studies determined the cellular and molecular underpinnings by which IL-4/IL-13 regulate metaplasia development caused by chronic atrophic gastritis. **Methods:** Using a mouse model of inflammation-induced metaplasia, we identified IL-4/IL-13-producing immune cells in the chronically inflamed gastric mucosa. Mouse and human gastric organoids were cultured with and without IL-4 or IL-13 and analyzed using histopathological, immunological, and molecular assays to determine how IL-4/IL-13 regulate gastric epithelial cell growth, survival, and metaplasia-associated gene expression. To determine the role of IL-4/IL-13 *in vivo*, we generated a line of mice with chronic gastritis deficient in IL-4/IL-13 signaling (*Il4ra*$^{-/-}$). Furthermore, cytokine neutralization studies in mice with chronic gastritis were performed to determine if neutralizing IL-4 and/or IL-13 inhibited metaplasia development. **Results:** Histopathological analyses of stomach tissue sections have identified a population of infiltrating mast cells in the chronically inflamed stomach. Additionally, flow cytometric analysis of IL-13-producing immune cells identified mast cells as the largest producers of IL-13 in mice with gastritis. 3-D gastric organoid cultures revealed that IL-13 increases organoid size (proliferation), viability, and expression of *Muc6*, three features of gastric metaplasia. Notably, mice with chronic gastritis deficient in IL-4/IL-13 signaling do not develop metaplasia and neutralization of IL-13 in mice with gastritis significantly reduced metaplasia development in the inflamed gastric corpus. **Conclusion:** These studies identified an important role for IL-13, and possibly IL-13-producing mast cells, in the development of gastric metaplasia. Furthermore, IL-13 acts directly on gastric epithelial cells to promote a metaplastic phenotype. Together, these novel findings provide insight into the pathophysiology of gastric metaplasia and identify potential therapeutic targets for the prevention of metaplasia and gastric cancer development.

368

3′-SULFATED LEWIS A IS A BIOMARKER FOR METAPLASTIC AND CARCINOMATOUS TRANSFORMATION OF SEVERAL GASTROINTESTINAL EPITHELIA

Jeffrey W. Brown, Koushik K. Das, Vasilios Kalas, Kiron M. Das, Jason Mills

Multiple previous studies have shown the monoclonal antibody Das-1 (formerly called $7E_{12}H_{12}$) recognizes specifically metaplastic and carcinomatous lesions in multiple organs of the gastrointestinal system (e.g. Barrett's esophagus, intestinal-type metaplasia of the stomach, gastric adenocarcinoma, high-grade pancreatic intraepithelial neoplasm, and pancreatic ductal adenocarcinoma) as well as in other organs (bladder and lung carcinomas). Beyond its proven utility as a tissue biomarker, we have recently showed that a Das-1 sandwich ELISA assay of pancreatic cyst fluid was significantly more accurate than current paradigms for identifying those cysts harboring advanced neoplasia. Though this antibody has been used extensively for clinical, basic science, and translational applications for decades, its epitope has remained elusive. Here, we report our discovery that the diagnostically important epitope for this antibody is the glycan, 3'-Sulfated Lewis A (3'-Sulfo-Le^A). Further, we show that this epitope, which is resistant to digestion by lysosomal arylsulfatase, can be used to track membranes through the lysosome and then out of the cell during the process of paligenosis. We call this undescribed cellular process cathartocytosis [Greek: Cellular Cleansing] and believe that it is an efficient means of eliminating membranes that were previously used for differentiated subcellular structures (vesicles, abundant ER, mitochondria, specialized apical membrane, etc) but now superfluous to the metaplastic dedifferentiated cells. We believe that the near universal expression of 3'-Sulfo-Le^A in metaplasias and cancer of the foregut and elsewhere occur because these cells utilize cathartocytosis to dedifferentiate in order to augment plasticity and change cell state. We are working towards demonstrating the necessity/sufficiency of this epitope to metaplastic dedifferentiation as inhibiting its synthesis may represent a novel therapeutic strategy for these lethal cellular transformations.

369

IBD PREDICTION AND TREATMENT: MULTI-POPULATION RISK SCORES AND RARE VEO-IBD VARIANTS

Kyle Gettler, Rachel Levantovsky, Judy H. Cho

Background Polygenic risk scores (PRS) may soon be used to predict inflammatory bowel disease (IBD) risk in prevention efforts and more personalized treatments can be informed by high-impact rare variants. We leveraged exome-sequence and SNP array data from individuals in a multi-ethnic, randomly-ascertained health system-based BioMe biobank to calculate multi-population PRS and to define the effects of rare variants in genes associated with very early onset IBD (VEO-IBD) on disease prediction and pathophysiology. **Methods** PRS were calculated from European, African-American, and Ashkenazi Jewish (AJ) reference case-control studies, and a meta-GWAS run using all three association datasets. PRS were then combined using regression to assess which combination of scores best predicted IBD status in European, AJ, Hispanic, and African American cohorts in BioMe and UK Biobank. Rare variants were assessed in genes associated with VEO-IBD by estimating the genetic penetrance in 29,358 individuals from BioMe (European, African, and Hispanic), measured according to the percentage of individuals who were either heterozygous or homozygous for each that developed IBD. After identifying a LRBA variant of particular interest in African Americans, we also tested for differences in expression of both LRBA and CTLA-4 in 2 carriers of the SNP relative to 10 non-carriers. **Results** Combining risk scores based on association data from distinct ancestral populations improved IBD prediction for every population in BioMe (Figure 1A) and significantly improved prediction among European ancestry UK Biobank individuals (Figure 1B). We found several variants in VEO-IBD related genes that had high penetrance values, many of which also had high CADD and GERP scores - suggesting potential impacts on protein function (Figure 2A). One variant of particular interest in LRBA was also found to be associated with modified expression levels of both LRBA and CTLA-4, and to show partial rescue after hydroxychloroquine treatment (Figure 2B and 2C). **Conclusions** Greater genetic diversity in African populations improves prediction across populations, and generalizes some VEO-IBD genes. Increasing African-American IBD case-collections should be prioritized to reduce health disparities and enhance pathophysiologic insight. The rare, African-American predominant variants in the VEO-IBD genes ADAM17 and LRBA could lead to more personalized treatment options for IBD, as expression of CTLA-4 has been shown to be increased by chloroquine treatment in vitro.

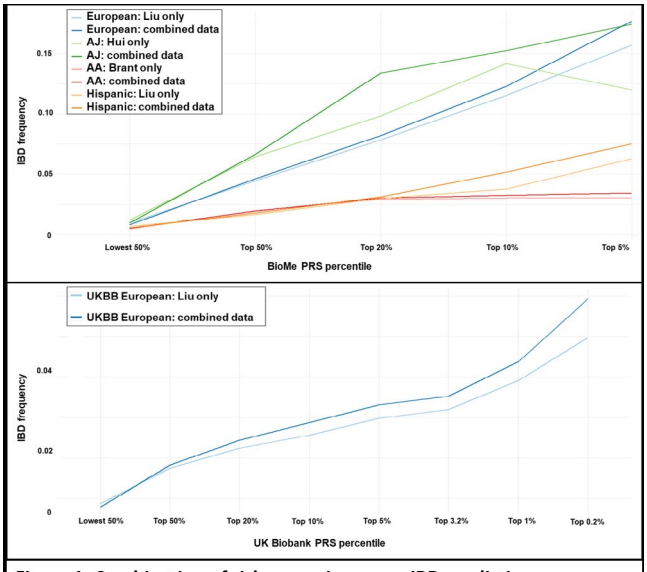


Figure 1: Combination of risk scores improves IBD prediction across BioMe racial populations. A. BioMe individuals with higher risk scores have a higher rate of IBD regardless of ancestry. Integration of association data from multiple populations also increases IBD prediction in every population, though IBD prediction is more challenging in African Americans. B. Replication in UK Biobank individuals of European ancestry shows similar improvement.

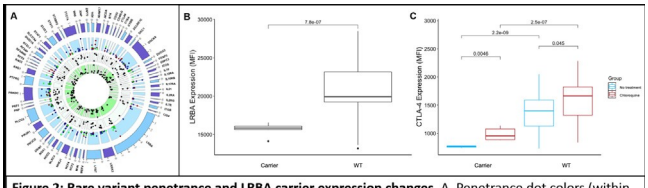


Figure 2: Rare variant penetrance and LRBA carrier expression changes. A. Penetrance dot colors (within light blue layer) reflect ancestry: blue = European, red = AA, green = Hispanic. AJ individuals are included as European-ancestry. Penetrance points plotted if TotalHet # > 10, HetCases > 1, and penetrance > 1. Max penetrance values for the light blue layer: Eur = 21.43, Afr = 10.53, His = 9.09. White layer = GERP scores > 3 and green layer = CADD scores > 10. Outer ticks represent 100kb in gene region. B. Mean intracellular expression of LRBA. C. Mean extracellular expression of CTLA-4, with and without 18-hour chloroquine treatment. All conditions were performed in triplicate. P-values calculated using Welch's t-test. MFI, mean fluorescence intensity.

We found that transcripts associated with stratified squamous epithelial cells were down-regulated in GATA4-expressing cells, including critical markers such as *p63*, *SOX2, SOX7, BMP7, KRT4*, *KRT5*, *KRT14*, *KRT15,* and *IVL.* Conversely, transcripts associated with columnar epithelial cells were up-regulated, such as *KRT8, KRT18,* and *MUC1*, as were transcripts encoding the gastric columnar epithelial cell markers *PPARG*, *CLDN18,* and *PGC*. Moreover, genes differentially expressed in GATA4-expressing esophageal cells overlapped with genes differentially expressed in BE. Finally, we identified GATA4 binding sites in differentially expressed genes suggesting direct regulation of gene expression, either positively or negatively, by GATA4. **Conclusions**: GATA4 expression in normal human adult esophageal cells alters cell identity from squamous toward columnar. Gene expression changes, in part, mimicked those observed in BE. Future analysis will define GATA4 direct targets in esophageal cells using Cut and Tag. The long-term goal is to identify mechanisms through which GATA4, directly and indirectly, promotes columnar cell identity in esophageal cells and to apply this knowledge to BE and EAC.

Sa125

DIFFERENTIAL TNFSF14/LIGHT-RECEPTOR-MEDIATED PATHWAYS SHAPE THE BALANCE BETWEEN INFLAMMATORY AND REGENERATIVE FIBROBLASTS IN EOSINOPHILIC ESOPHAGITIS

Mario C. Manresa, Elaine Pham, Loan D. Duong, Kevin Okamoto, Haruka Miki, Michael Croft, Seema S. Aceves

Rationale: Fibroblasts (FBL) mediate tissue remodeling in eosinophilic esophagitis (EoE), a chronic allergen-driven inflammatory pathology. The presence of diverse FBL subtypes with inflammatory or regenerative profiles has been recognized in various diseases and tissues. However, the mediators controlling FBL differentiation into novel subtypes remain unknown. We recently defined a putative role of the cytokine TNFSF14/LIGHT as a promoter of an inflammatory esophageal FBL. Herein we investigated the involvement of the LIGHT-receptors herpes virus entry mediator (HVEM) and lymphotoxin-beta receptor (LTβR) in LIGHT-induced and repressed gene expression and the downstream pathways activated by LIGHT.
Methods: Esophageal FBL were isolated from healthy donors and pediatric active and inactive EoE patients. siRNAs were used to silence HVEM and LTβR expression. RNA sequencing (RNAseq), qRT-PCR, flow cytometry, immunofluorescence, and immunoblots were used to investigate molecular pathways activated by LIGHT and the contribution of each receptor to the LIGHT transcriptome.
Results: siRNA-mediated knock-down of LIGHT receptors demonstrated that HVEM regulates a defined subset of LIGHT targets including ICAM-1 and IL-32. In contrast, silencing of LTβR has a general regulatory effect on the LIGHT-induced inflammatory transcriptome. Analysis of the LIGHT-repressed transcriptome showed down-regulation of genes involved in the maintenance of epithelial homeostasis such as, WNT5a, WNT2b or type 3 semaphorins, in a manner that was both HVEM and LTβR-dependent. LIGHT strongly induced the activation of both canonical p65-mediated and alternative p52-dependent NF-κB pathways. Pharmacologic blockade of the alternative pathway with a small molecule inhibitor had a potent silencing effect on the LIGHT-induced transcriptome and partially restored the expression of LIGHT-repressed genes in esophageal FBL. Comparison of the protein expression level of HVEM and LTβR between active and inactive EoE FBL demonstrated higher basal levels of LTβR than HVEM expression. Interestingly, the frequency of HVEM+ FBL was higher in active than inactive EoE but LTβR expression was similar in FBL from active and inactive EoE biopsies.
Conclusions: Our current and past studies reveal the ability of LIGHT to promote differentiation of esophageal FBL toward an inflammatory phenotype and a dominant role of the LTβR-p52 pathway in EoE FBL. HVEM shows an inducible profile and participates in the expression of specific inflammatory-FBL markers and may "fine tune" LIGHT signals in EoE FBL. These pathways may be potential therapeutic targets in EoE.

Sa126

TROPISM OF SARS-COV-2 FOR BARRETT'S ESOPHAGUS MAY INCREASE SUSCEPTIBILITY TO DEVELOPING COVID-19

Ramon Jin, Jeffrey W. Brown, Alan Meeker, Qing K. Li, Peter Bayguinov, Jean S. Wang, James A. Fitzpatrick, Sean Whelan, Jason Mills

Background and Aims: In addition to pulmonary and thrombotic sequalae, gastrointestinal (GI) manifestations of COVID-19 are common. Although enterocytes express ACE2 and TMPRSS2, the proteins that determine SARS-CoV-2 tropism, prior studies have suggested that the virus is inactivated by gastric acid and other luminal fluids as it transits the gastrointestinal tract. However, we reason here that individuals with intestinal metaplasia of the esophagus and stomach might have ectopic, proximal SARS-CoV-2 receptor expression that would predispose them to infection from ingested oral secretions or respiratory sputum.
Methods: Histology, immunohistochemistry, and immunofluorescence were performed on human tissue and organoid cultures derived from biopsied human Barrett's esophagus. Organoid cultures were infected with a chimeric virus expressing the SARS-CoV-2 spike protein (rVSV-eGFP-SARS-CoV-2). Both fixed and live cells were imaged by light, epifluorescence, and live confocal microscopy.
Results: Unlike normal esophagus and stomach, Barrett's esophagus and gastric intestinal metaplasia both strongly express apical ACE2 and TMPRSS2 at the protein level. Organoids derived from Barrett's esophagus are readily infected by the chimeric rVSV-eGFP-SARS-CoV-2 virus as demonstrated by the GFP fluorescence observed in both epifluorescence as well as three-dimensional, time-lapse confocal imaging of live infected organoids. We observed that fluorescence persisted for greater than 2 weeks in culture suggesting ongoing viral infection and intestinal identity correlated with increased viral entry.
Conclusions: SARS-CoV-2 has a previously undescribed tropism for Barrett's esophagus and gastric intestinal metaplasia, placing these individuals at higher risk of infection via the orogastric route.

Sa127

AN IBD-RISK VARIANT IN PTPN2 PROMOTES CELLULAR UPTAKE OF SARS-COV-2, WHICH IS MITIGATED BY THE JAK INHIBITOR TOFACITINIB

Marianne Spalinger, Rong Hai, Jiang Li, Tara M. Nordgren, Michel L Tremblay, Lars Eckmann, Elaine M. Hanson, Michael M. Scharl, Xiwei Wu, Brigid Boland, Declan F. McCole

Background and aims: Since the start of the coronavirus disease (COVID-19) pandemic, its causative agent, SARS-CoV-2, has affected over 60 million individuals and claimed more than 1.4 million lives. While fatality rates are higher among the elderly and those with underlying comorbidities, host factors that promote susceptibility to SARS-CoV-2 infection and severe COVID-19 are poorly understood. Exacerbated cytokine signaling, termed 'cytokine storm' contributes to severe COVID-19. Many of those cytokines act through Janus kinase (JAK)-signaling transducer and activator of transcription (STAT) pathways, and clinical trials indicate that treatment with a JAK inhibitor might reduce COVID-19 severity and hospitalization time. Protein tyrosine phosphatase non-receptor type 2 (PTPN2) is a ubiquitously expressed intracellular regulator of cytokine-induced JAK signaling, and loss-of-function variants in the *PTPN2* gene are associated with autoimmune and auto-inflammatory disorders, including IBD. The aim of our study was to investigate whether loss of functional PTPN2 affects viral uptake and whether treatment with the JAK-inhibitor tofacitinib could restrict viral uptake in PTPN2-deficient/loss-of-function cells. **Methods:** ACE2 expression was investigated in intestinal biopsies and peripheral blood mononuclear cells (PBMC) from *PTPN2*-variant carrying IBD patients, intestinal, lung and heart samples from PTPN2-deficient mice, and PTPN2-knockdown intestinal (Caco-2, HT-29) and lung (A549) epithelial cell lines (mRNA, protein). Uptake of SARS-CoV-2 S-protein expressing virus like particles (SARS-CoV-2 VLPs) was measured in these cells. In some experiments, cells were pre-treated with 50 mM tofacitinib. **Results:** IBD patients carrying the rs1893217 risk PTPN2-variant expressed higher levels of ACE2 (heterozygous: $p<0.05$, homozygous $p<0.001$), and uptake of SARS-CoV-2 VLPs was elevated in PBMCs from variant carriers ($p<0.001$). ACE2 levels were increased in intestinal, heart and lung tissue from PTPN2-deficient mice ($p<0.01$, each), and PTPN2-knockdown intestinal and lung epithelial cells expressed higher ACE2 levels ($p<0.05$, each) and were more susceptible to SARS-CoV-2 VLP entry ($p<0.01$, each). ACE2 expression and viral entry was further increased by interferon-g (1000 U/ml; 24 h), but normalized by STAT1 siRNA. ACE2-dependency of the elevated SARS-CoV-2 VLP uptake was confirmed with an ACE2-blocking antibody. Inhibition of JAK-signaling by tofacitinib normalized ACE2 expression in PTPN2-variant and PTPN2-deficient cells and reduced SARS-CoV-2 entry in PTPN2-wild-type and variant cells. **Conclusion:** Our findings describe that the IBD- and autoimmunity-associated variant in PTPN2 might be a risk factor for increased SARS-CoV-2 invasion (entry) likely promoting severe COVID-19, but also identify that the clinically-approved drug tofacitinib could mitigate this risk.

Sa128

CYTOGLOBIN IMPAIRS PANCREATIC CANCER GROWTH *IN VITRO* AND *IN VIVO*

Viet Hoang Dinh, Thi Thanh Thuy Le, Hoang Hai, Quoc Dat Ninh, Ngoc Hieu Vu, Huu Hoang Truong, Minh Phuong Dong, Vinh Hanh Ngo, Yoshihiro Ikura, Kenjiro Kimura, Shoji Kubo, Norifumi Kawada

Background and Aims Pancreatic cancer (PC) represents the most challenging malignancies with the poorest prognosis, and lowest survival rate. Cytoglobin (CYGB), a hemeprotein presenting in pericytes of all organs, has been involved in suppressing liver fibrosis and cancers but there is no report in PC. This study aims to explore the effects of CYGB on the development of PC. **Methods** Expression of CYGB in 32 specimens from human pancreatic cancer patients were analyzed. Cygb overexpressing mice with their wild-type (WT) counterparts were induced PC using 7,12-Dimethylbenz[a]anthracene (DMBA) directly injected in mouse pancreas and sacrificed at different time-points. *In vitro CYGB* overexpression in human pancreatic stellate cells (PSCs), and MIA PaCa-2 cancer cells, or siRNA were performed. Human recombinant CYGB (rhCYGB) protein was produced and applied in vitro. RNA sequencing, flow cytometry, immunoblots, immunofluorescence, and reverse transcription polymerase chain reaction were implemented. **Results** In 32 specimens from human PC, expression of CYGB was found dominantly surrounding the adenocarcinoma area and negatively correlated with the size of tumors. The more CYGB expression, the smaller the size of tumors. DMBA administration time-dependently induced severe pancreatic inflammation, and fibrosis development which were attenuated in Cygb overexpressing mice. Interestingly, tumor incidence was 93% in WT mice compared to 55% in Cygb overexpressed mice, $p<0.05$. *In vitro* overexpression of *CYGB* in PSCs significantly suppressed their activation and collagen production, while *CYGB* siRNA reverted these effects. MIA Paca-2 cells were either overexpressed *CYGB* or cultured in conditioned medium from *CYGB* overexpressed PSCs exhibited reduction of cell proliferation via cell cycle arrest at G1/S phase. Similarly, rhCYGB treated MIA Paca-2 cells inhibited cell growth, migration, and colony formation time and dose-dependently. RNA sequencing in MIA Paca-2 cells treated with rhCYGB in comparison with non-treated group revealed the most enriched KEGG pathways of metabolism, MAPK, cell cycle, and p53 signaling. Among 1708 differential expressed genes, the most significant up-regulated genes are cellular growth arrest GADD45 (+70.9 folds), and DNA damage inducible transcript 3 (DDIT3, +14 folds) which promotes apoptosis, but down-regulated genes which inhibited cell cycle including E2F transcription factor 1 (-9.4 folds), Cyclin E2 (-5.9 folds), and Cyclin A2 (-3 folds). **Conclusion**s Cytoglobin suppressed activation of PSCs, pancreatic fibrosis, and tumor growth *in vivo* and *in vitro* which open its potential therapeutic application.